Radiant and mass fluxes in multi-platform, multi-payload satellite-based volcano monitoring

Thesis

Radiant and mass fluxes in multi-platform, multi-payload satellite-based volcano monitoring

A thesis presented for the degree of Doctor of Philosophy

Nikola Rogic

B.Sc (Hons), The Open University (2014); M.Sc, University College London (2015)

School of Environment, Earth and Ecosystem Sciences

The Open University

September 2020

Abstract

The enormous amount of remote sensing (RS) data available today at a range of temporal and spatial resolutions aid emergency management in volcanic crises. RS provides a technological solution for bridging critical gaps in volcanic hazard assessment and risk mitigation. Detection and measurement of high-temperature thermal anomalies enable eruption monitoring and new lava flow propagation forecasts, for example. The accuracy of such thermal estimates relies on the knowledge of input parameters, such as emissivity - the efficiency with which surfaces radiate thermal energy at various wavelengths and temperatures. Emissivity is directly linked to the measurement of radiant flux and therefore affects the mass flux estimate as well as any model-based prediction of lava flow behaviour.

Emissivity is not commonly measured across the range of volcanic lava compositions and temperatures, and it is generally assumed to have a constant value between 1.0 and 0.80 for basaltic lava. There is a lack of field and laboratory-based emissivity data for robust, more realistic modelling. To address this deficit, experiments on 'aa' lava samples were performed using data from Mount Etna (Italy), representing the range of its eruptive behaviour. In three sequential stages, emissivity was measured over the widest range of temperatures (294 – 1373 K) and wavelengths (2.17 - 15.0 μm) executable in the laboratory environment.

The results show that emissivity is temperature, composition and wavelength dependent. Measured emissivity increases non-linearly with temperature decrease (cooling), exhibiting significant variations above 900 K with values considerably lower than the typically assumed 0.80. The measured and modelled emissivity values were applied to various remote sensing applications as input parameters for physical modelling of lava flows. This new evidence has significant impact on the computation of radiant heat flux from spaceborne data, as well as on modelling of lava flow 'distance-to-run' simulations. Furnished with improved input parameters (multicomponent emissivity), the novel approach developed here can be used to test an improved version of an unsupervised multi-platform, multi-payload volcano monitoring system.

Acknowledgements

So many people have helped in the completion of this thesis over the last four years. First, I would like to thank Hazel Rymer, Fabrizio Ferrucci and Stephen Blake for being great supervisors, as well as Anne Jay for supporting me with my project and for providing a wonderful opportunity to teach. They all endured enormous amount of pestering on my part but always came back with great suggestions and ways out of trouble. In the last few months, they have also read and corrected several (very messy) drafts, which were swiftly returned.

The project was funded by the Open University studentship. The Natural Environment Research Council (NERC) has also granted funding in 2017 to access the Field Spectroscopy Facility at University of Edinburgh, U.K. (C. McLellan and A. Grey). Special thanks to Clarendon Laboratory, University of Oxford, U.K. (N. Bowles), the Planetary Spectroscopy Laboratory (PSL) of the German Aerospace Center (DLR), Berlin, Germany (A. Maturilli) and the Image Visualization and Infrared Spectroscopy (IVIS) Laboratory, at the University of Pittsburgh, Pennsylvania, U.S.A. (M. Ramsey and J. O. Thompson) for accommodating FTIR pilot and extended studies and helpful discussions.

Many more people provided external collaboration and data, without which I could not achieve what was needed. A big thanks to the University of Calabria, Rende, (CS), Italy for providing a remote sensing workshops (C. Di Bartola), the Istituto Nazionale di Geofisica e Vulcanologia, Osservatorio Etneo, Catania, Italy (A. Cappello, G. Ganci, G. Bilotta and C. Del Negro) for collaboration and data validation, as well as J. Murray for the exceptional geodetic field trip to my beloved Mt Etna in 2019 to collect much needed samples. I must not forget J. Fraser, S. Eriksen and particularly B. Hirn for providing instrumental guidance and support with coding. Your expertise and patience were very much appreciated, as “hello world” approach is certainly not my forte.

Within the department I am grateful to Yasmin (Such Fun!) for putting up with me on a professional and personal level (‘I can’t believe you’ve done this!’), as well as Arlene, Clare, Tom and Rick for the advice and much needed moral support. Also, in the 2020, Greg and Sav (+ Ollie) were ideal housemates and great friends, responsible for keeping me sane during the tough 6+ months of unprecedented lockdown times.

Finally, the biggest thanks are reserved for my family – Mum and my big brother (and Milo) deserve special mention for supporting me unconditionally, as without your help I wouldn’t be able to take all the opportunities that have come my way. This is for you!

Table of Contents

List of Figures

List of Tables

1 Passive Remote Sensing of active volcanoes

1.1 Introduction

Since the late 1960s, satellite remote sensing (RS), has become an established technological solution for bridging critical gaps in volcanic hazard assessment and risk mitigation. The Earth Resource Technology Satellite (ERTS), launched by the U.S.A. in 1972 (later renamed Landsat-1), was followed by the first Geostationary Operational Environmental satellite (GOES) in 1974; this arguably marked the start of a modern era of RS. It is important to note that none of the sensors employed to date were specifically designed to monitor active volcanoes. However, despite their primary purpose being focused on meteorological, agricultural or environmental observations, spaceborne data are successfully utilized in a wide range of volcano related research. Early examples of spaceborne detection of volcanic thermal anomalies span back to the late 1970s when National Oceanic and Atmospheric Administration - 5 satellite (NOAA-5) detected the 1978 eruption of Mt Etna or when the Landsat-3 produced its first high-resolution imagery of Siera Negra volcano (Galapagos) lava flow in 1979 (Rothery et al., 1988).

The enormous amount of RS data available today at a range of temporal and spatial resolutions can aid standard monitoring in ‘peace time’ as well as emergency management in volcanic crises involving very-high temperature thermal events. In this thesis, the primary focus will be on lava flows with surfaces ranging up to 1350 K in temperature, detected and measured using thermal remote sensing techniques.

Almost 1500 active subaerial volcanoes around the world are known to have erupted in the last 10000 years (the Holocene Era), of which 700 have erupted at least once in historical times; every year about 60 volcanoes erupt on land (Sigurdsson et al., 2015; Siebert et al., 2010). Considering that fewer than 10% of active subaerial volcanoes are monitored regularly on the ground, RS provides an opportunity to increase coverage, providing a cost-effective global surveillance. For remote or inaccessible sites, RS may be the only form of surveillance that is practical and safe.

Satellite RS can either be passive or active. While the former provides a direct measurement of physical parameters (mainly linked to hot radiating bodies and rock textures or their proxies), the latter is used for observing geomorphological features and measuring near-vertical ground deformation.

A good example of a synoptic view available using satellite data are geostationary platforms, which maintain their position relative to the Earth's surface at an approximate altitude of 36000 km. These can be used to detect short-lived effusive events and it has been demonstrated to be a valuable volcano monitoring tool (Harris et al., 2001, 1997). In contrast, most Low Earth Orbit (LEO) satellites are in sun-synchronous polar-orbits at heights of 600-800 km, allowing for Earth observation (EO) at higher spatial resolutions, but at the expense of significantly poorer temporal resolution.

Cloud cover permitting, both platforms play an important role even at the best monitored active volcanoes worldwide (e.g., Mt Etna in Italy and Kilauea in Hawaii), as well as providing data for remote volcanoes that are impossible to obtain using ground-based networks and/or methods due to accessibility or safety reasons.

1.2 Thermal remote sensing of volcanic activity: background and theory

Passive RS exploits the natural sources of external (mainly the Sun) and internal (thermal) radiation, within specific atmospheric windows (Table 1.1). Indeed, the Earth's atmosphere is not transparent to electro-magnetic radiation at all wavelengths; it has absorption windows of high transmissivity, separated by regions of low transmissivity associated with the various atmospheric gases and aerosols.

Table 1.1. Location of atmospheric windows and average transmissivity

Atmospheric Window Location	**Exploitable Wavelengths (μm)**	**Average transmissivity $\tau(\lambda)$**
Near Infra-Red (NIR)	0.7-0.89	0.90
	1.0-1.1	0.94
Short Wavelength Infra-Red (SWIR)	1.18-1.31	0.94
	1.51-1.76	0.96
	2.03-2.36	0.96
Mid-Infra-Red (MIR)	3.44-4.13	0.94
Thermal Infra-Red (TIR)	8.6-12.2	0.92

*Wavelengths (μm) are used in this thesis **Atmospheric windows beyond 15 μm are not considered here

The mean spectral radiance (R_λ) is the central parameter measured by the satellite's radiometer and it is linearly related to Digital Numbers (DN), where DN values in each band are 'translated' into the spectral radiance received at-satellite:

$$R_\lambda = S_\lambda DN_\lambda + I_\lambda \quad (1)$$

where R_λ is at-satellite radiance, DN_λ is digital number, S_λ is slope and I_λ is intercept for spectral band with central wavelength, so total at-satellite radiance can be written as:

$$R_\lambda = \tau_\lambda(\varepsilon_\lambda R_{\lambda S} + \rho_\lambda R_{\lambda D}) + R_{\lambda U} + R_{\lambda sp} \quad (2)$$

in which τ_λ, ε_λ and ρ_λ are atmospheric transmissivity, emissivity of the surface and spectral reflectivity of the surface at wavelength λ respectively; $R_{\lambda S}$ is surface radiation, $R_{\lambda D}$ and $R_{\lambda U}$ are the downwelling and upwelling atmospheric radiances, and $R_{\lambda sp}$ is the space contribution (generally ignored as insignificant).

Therefore, R_λ is composed of the surface reflected radiance $R_{\lambda D}$, the upwelling path radiance $R_{\lambda U}$ and the surface thermal radiance $L\ (\lambda, T)$

$$\begin{aligned} R_\lambda &= \tau_\lambda L(\lambda, T) + \tau_\lambda \rho_\lambda R_{\lambda,D} + R_{\lambda,U} \\ &= R_{\lambda,thermal} + R_{\lambda,nonthermal} \end{aligned} \quad (3)$$

where, τ_λ is the atmospheric spectral transmission coefficient; ρ_λ is the spectral reflectivity of the target; $R_{\lambda,thermal}$ is composed of $\tau_\lambda L(\lambda, T)$ and $R_{\lambda,nonthermal}$ is composed of $\tau_\lambda \rho_\lambda R_{\lambda,D} + R_{\lambda,U}$.

What can be 'seen' by spaceborne sensors and in which wavelength, essentially depends on three fundamental laws: Planck, Stefan-Boltzmann and Wien.

These laws demonstrate that surfaces radiate in different regions of the electro-magnetic spectrum, depending on their temperature. Planck's radiation law defines the radiation released by a perfect radiator, a blackbody, and it can be calculated from the body's surface temperature (Fig. 1.2):

$$M_\lambda = \frac{2\pi hc^2}{\lambda^5 (e^{\frac{hc}{\lambda kT}} - 1)} \quad (4)$$

In Equation (Eq. 4), M_λ is spectral radiant exitance (W $m^{-2}\mu m^{-1}$), h is Planck's constant (6.626×10^{-34} J s), c is the speed of light (2.9979246×10^8 m s^{-1}), k is Stefan-Boltzmann's constant (1.3806×10^{-23} JK^{-1}), T is absolute temperature (K) and λ is the wavelength (μm).

An emitted spectral radiance exists at all wavelengths. The wavelength at which blackbody temperature curve reaches a maximum (λ_{max}) is defined by Wien's Displacement Law (Eq. 5 and Fig. 1.1, dotted line).

$$\lambda_{max} = \frac{b}{T} \quad (5)$$

where T is the absolute temperature in K, b is a constant of proportionality, known as Wien's displacement constant, equal to 2.898×10^{-3} m K.

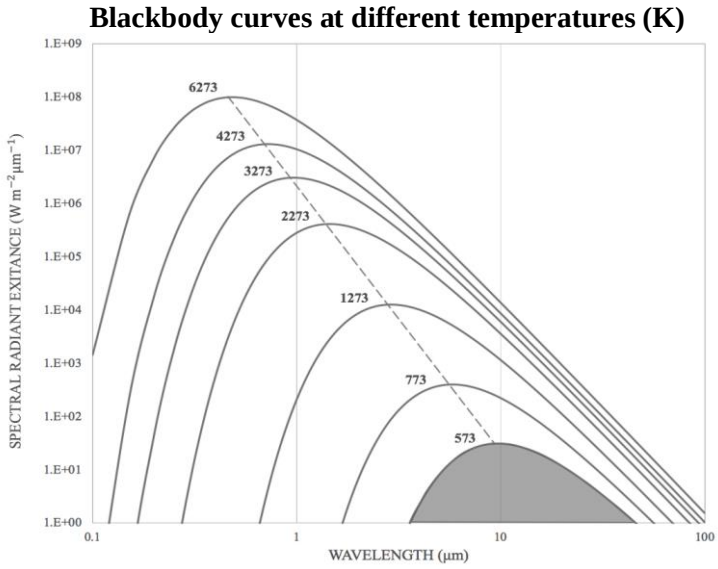

Figure 1.1 Blackbody curves at different temperatures (573-6273 K), derived from Eq. (4). The laws of Planck, Stefan-Boltzmann (shaded area under 573 K curve) and Wien (dotted line) are illustrated in this figure.

These relationships mean that in shortwave infrared (SWIR) wavelengths $R_{\lambda S}$ will make a significant measurable contribution to R_{λ}, which is true for magmatic (and hot fumarole) temperatures. Coincidence of the SWIR window with λ_{max} for bodies at magmatic temperatures (~1100-1400 K) will contribute measurable $R_{\lambda S}$ (Fig. 1.2). Coincidence of the midinfrared (MIR) window λ_{max} for bodies at ~500-1000 K makes these wavebands sensitive to thermal emittance from high temperature bodies, such as lava flows.

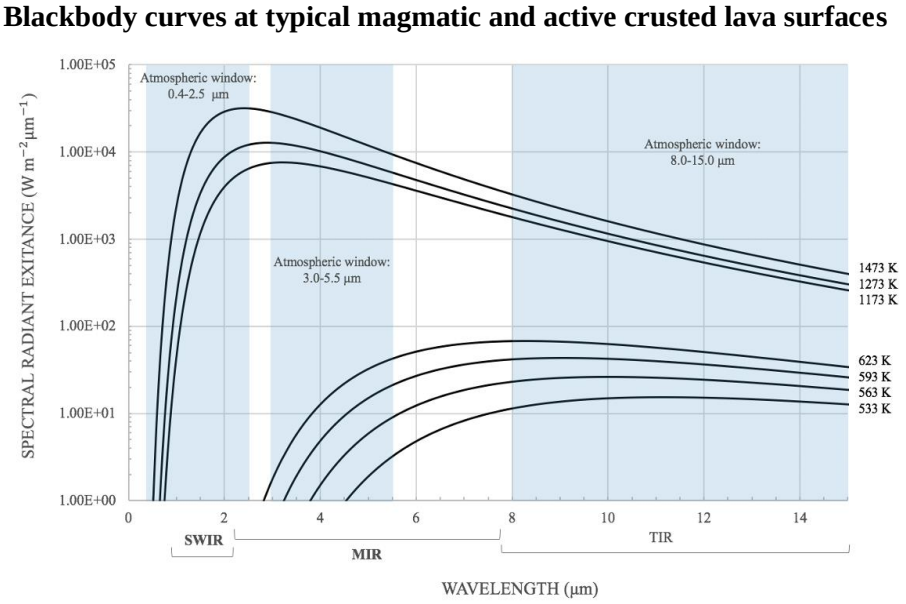

Figure 1.2 Blackbody curves derived from Eq. (4), at typical magmatic (1073-1473 K) and active crusted lava surface temperatures (533-1073K).

While daytime $R_{\lambda S}$ is mixed with reflected radiance in both SWIR and MIR, coincidence of the thermal infrared (TIR) window with λ_{max} for bodies at typical Earth ambient temperatures have negligible contribution of $\rho_\lambda R_{\lambda D}$, which makes this waveband useful for measuring $R_{\lambda S}$ from ambient temperatures.

The reason for the direct relationship between thermal emission and volcanic activity is that all objects above absolute zero (0 K) emit electromagnetic radiation at a wavelength and intensity that are each function of the surface temperature and emissivity (radiating efficiency):

$$E = \sigma \varepsilon T^4 \tag{6}$$

where σ is Stefan-Boltzmann constant and ε is emissivity. According to the Stefan-Boltzmann Law in Equation (Eq. 6) and Figure 1.1 (shaded area under 573 K curve), the radiance emitted by the surface will increase, as the temperature of the surface rises (fourth power of its temperature). As a hotter volcanic surface will radiate more energy and higher radiant flux density, and any variation in observed radiance will reflect a variation in volcanic activity on the ground. Therefore, these fundamental laws and their relationships in a volcanological context may demonstrate (Fig. 1.1) that surfaces of similar temperatures to the Sun (i.e., ~6273 K) will radiate most strongly in the visible region (VIS), whereas a high-temperature (e.g., 1100-1400 K) thermal anomaly (active lava flow) will radiate most strongly in the SWIR region, and much cooler surfaces (e.g., solar heated ground) will radiate most strongly in TIR.

However, a precise retrieval of the temperature and/or emissivity from the measured radiation data, using RS approach, reveals a non-linear relationship between the two (Rolim et al., 2016). When a pixel is composed of two or more areas that differ in respect to temperature, then the average is composed of several different values (Harris, 2013a). Therefore, the single DN that represent the pixel does not accurately represent the values present. As a result, over a mixed pixel, spectral response will be integrated to form a pixel integrated temperature, that does not match the pure signature of the sub-pixel feature we wish to analyse (Harris, 2013a). Therefore, an effective temperature is needed (Eq. 9).

Based on Planck's radiation law, the spectral radiance ($\mathrm{W\,m^{-2}ster^{-1}\mu m^{-1}}$) of a pixel $L(\lambda, T)$ is a function of its integrated temperature (T_i):

$$L(\lambda, T) = \frac{\varepsilon_\lambda c_1 \lambda^{-5}}{\pi \left[\exp\left(\frac{c_2}{\lambda T_i}\right) - 1\right]} \tag{7}$$

where c_1 and c_2 are related constants; $c_1 = 1.19 \times 10^{-16}$ W m^{-2} sr^{-1} and $c_2 = 1.44 \times 10^{-2}$ m K, respectively. $c_1 = 2\pi\, h\, c^2$ where h is Planck's constant and c is the speed of light; $c_2 = h\frac{c}{k}$ where k is the Stefan-Boltzmann constant; λ is the wavelength in μm; ε_λ is the emissivity of the radiative surface, and T_i is the pixel integrated temperature at a specific wavelength.

Removing the effects of the atmosphere is the essential step necessary to use spaceborne imagery for absolute temperature studies. The emitted signal leaving a target on the ground is both attenuated and enhanced by the atmosphere. Therefore, an appropriate knowledge of the atmosphere is needed for specific dates, location and altitude, so that a radiative transfer model can be used to estimate the transmission, upwelling and downwelling radiance (Barsi et al., 2003). Obtaining these parameters for each date and location for scene analysed, the space-reaching radiance can be converted to a surface-leaving radiance:

$$L_{TOA} = \tau\, \varepsilon\, L_T + L_u + (1 - \varepsilon)\, L_d \tag{8}$$

where τ is the atmospheric transmission, ε is the emissivity of the surface, L_T is the radiance of a blackbody target of kinetic temperature T, L_u is the upwelling or atmospheric path radiance, L_d is the downwelling (sky radiance), and L_{TOA} is the space-reaching top of the atmosphere (TOA) radiance measured by the instrument. Radiances are in units of W/m^2 ster μm and the transmission and emissivity are unitless. Radiance to temperature conversions are made using the Planck Equation (Eq. 4). The TOA temperature is not a good estimate of surface temperature, as neglecting the atmospheric correction will result in systematic errors in the predicted surface temperature.

Assuming that the pixel is thermally pure (i.e., isothermal surface), the pixel integrated temperature should be the temperature of the target surface after being corrected for emissivity, atmospheric, and sensor response effects. However, a scene recorded over an active lava flow surface may contain a wide range of temperatures (and emissivities), so a single pixel will be a mixture of several thermal components. The pixel integrated temperature in Equation (Eq. 7) accounts for 'static' (constant) emissivity ε_λ of the radiative surface at specific wavelength (not accounting for emissivity variation with temperature). In this thesis, a novel technique was used (Chapters 3 and 4), where traditional ε_λ is replaced with $\varepsilon_{\lambda,T}$, which represent a multicomponent emissivity, variable with temperature (Chapter 2), before applying fundamentals of 'dual-band' approaches (Harris, 2013a; Oppenheimer,

1993; Dozier, 1981; Matson and Dozier, 1981) to derive the so-called Effective Temperature (T_e):

$$T_e = [f_h \, {T_h}^4 + (1 - f_h){T_c}^4]^{\frac{1}{4}} \quad (9)$$

In Equation (Eq. 9), pixel radiance values are computed as the weighted average of subpixel radiance emitted by two distinctly different temperature components: the 'hot' component at T_h representing melt, occupying a surface fraction f_h of the pixel, and the cooling 'crust' component, at temperature T_c, occupying the rest 1-f_h of the pixel.

Using T_e for each radiant pixel the remotely sensed radiant heat flux (Q_{R_calc}) can be acquired (Wright and Pilger, 2008; Pieri et al., 1990):

$$Q_{R_{calc}} = A \, \varepsilon_{\lambda,T} \, \sigma \, \tau \left({T_e}^4 - {T_a}^4\right) \quad (10)$$

where, A is the pixel surface area, $\varepsilon_{\lambda,T}$ is emissivity (wavelength and temperature dependent), σ is Stefan-Boltzmann constant, τ is atmospheric transmissivity, ${T_e}^4$ is the effective temperature to the fourth power, and the ${T_a}^4$ is the ambient temperature to the fourth power. The $Q_{R_{calc}}$ data is often used to calculate lava effusion rates (Hirn et al., 2009; Harris et al., 2007; Wright et al., 2001; Harris et al., 1997; Pieri and Baloga, 1986) from which lava flow 'distance-to-run' could be empirically estimated (Kilburn, 2015, 1996; Calvari and Pinkerton, 1998).

A complete and comprehensive review of the main models and techniques on thermal RS of active volcanoes can be found in (Blackett, 2017; Harris, 2013a), among others.

1.2.1 Uncertainty: Non-uniform emissivity

The calculated temperature and radiant heat flux depend mainly on two factors: the wavelength λ of observation, and the emissivity ε of the material. For these reasons, the real surface emissivity is required for accurate computation of surface energy budgets.

Emissivity values are often assumed to be close to 1.0, which would reveal the 'brightness temperature' (i.e., blackbody) and not the real surface temperature. A non-unity constant emissivity assumption (e.g., 0.80) may provide an improved first order approximation (Table 1.2) but could additionally introduce systematic errors if applied uniformly.

Table 1.2 Emissivity table of some common urban and natural materials. This is not a comprehensive list and should be taken as a reference only (Harris, 2013a; Jin and Liang, 2006)

*Material	ε	**Material	ε
Asphalt (paving)	0.97	Basalt (polished)	0.90
Brick (red-rough)	0.93	Basalt (rough)	0.95
Brick (silica -unglazed rough)	0.80	Olivine basalt	0.93-0.95
Glass (smooth)	0.94	Andesite	0.91-0.94
Gold (pure highly polished)	0.02	Rhyolite	0.94-0.95
Granite (polished)	0.85	Rhyolitic obsidian	0.87-0.90

*(Jin and Liang, 2006) **(Harris, 2013a)

Emissivity values are often taken from spectral libraries (laboratory or spaceborne) and used for identification and compositional discrimination of various materials (Hulley et al., 2015; Kotthaus et al., 2014; Gillespie et al., 1998). However, libraries usually refer to measurements carried out in standard or near-standard temperature and pressure conditions and are often constant average values.

Recent development of multispectral thermal emission spectroscopy allows direct quantitative comparison between laboratory and RS data sets (Maturilli and Helbert, 2014). To extract reliable information about the surface composition from spaceborne data, a detailed laboratory spectroscopic study of Etnean lava flow samples' spectral behaviour at a range of wavelengths and temperatures was performed. It was deemed necessary to obtain the information on wavelength position, shape and contrasts of reflectance and emission bands of volcanic rock minerals analysed here at the widest range of wavelengths (2.17-15.0 μm) and temperatures (294-1373 K) achievable in a laboratory environment (Chapter 2). This would allow surface compositional emissivity variation to be determined (Chapters 2 and 5), as well as establish the degree of possible distinction between target(s) used in RS applications (Chapter 3).

1.3 Application of Thermal Remote Sensing in Volcanology

Using RS instruments to observe and monitor volcanoes has many advantages but one of major problems encountered when conducting RS of a volcanic target or set of targets is that associated with sensor saturation (Harris, 2013b). Saturation may occur when the amount of detected electromagnetic radiation from the observed high-temperature thermal anomaly (e.g., active lava flow) exceeds the instrument's limit to record a meaningful value. Since none of the satellites launched to date were specifically designed to monitor volcanic features but intended for weather observation, this is expected.

In application to volcanic, high-temperature features, SWIR channels are appropriate to measure the thermal emission peak, as according to the Planck's and the Wien's laws (Figs. 1.1 and 1.2), the ideal wavelength to observe a lava flow with initial surface temperature between ~900 to 1400 K would be at approximately 2.20 μm (SWIR).

As the majority of RS instruments were designed to track weather patterns or intended to measure surface features using reflected solar radiation, many sensors are unable to cope with the amount of emitted radiation in SWIR from high-temperature volcanic features and become saturated. In the absence of SWIR data due to saturation, spaceborne TIR bands (8.0-15.0 μm) can been employed to constrain thermal anomaly features (Harris, 2013a). This approach however, results in severe limitations in accurately deriving apparent lava surface temperatures, due to the position of TIR bands in the electromagnetic spectrum, as they are not as sensitive to high temperatures.

Additionally, many of the satellite instruments are of a coarse spatial resolution, which may be sufficient to monitor weather patterns but may be of insufficient resolution (≥1 km pixel) to track the dynamic development of an active lava flow in detail, for example.

It has been widely recognized that satellite thermal RS offers major benefits to volcano monitoring, such as global synoptic coverage, repeat and spectral capabilities with continuity of data acquisition from safe, reusable platforms. Several examples of such platforms available today to detect, map and assess active lava flows at a range of spectral, spatial and temporal resolutions are shown in Table 1.3

Table 1.3 Selection of current optical satellite payloads suitable for lava observation

Feature	Need	Resolution	Observable	Required	Payload	Mission	Pixel (m)
Magma at surface	Detection and location	High temporal (15 min to twice daily)	Radiance	TIR, MIR, SWIR	SEVIRI MODIS VIIRS	MSG Terra/Aqua NOAA	3000 1000 375-750
Lava flows	Flow mapping	High spatial (5-16 days)	Radiance*	TIR, MIR, SWIR, NIR	ETM+ OLI Sentinel-2 TIRS	Lansat-7 Landsat-8 MSI Landsat-8	30 30 20 100
	Effusion rate monitoring	High temporal (15 min to twice daily)	Radiance*	TIR, MIR, SWIR	SEVIRI MODIS VIIRS	MSG Terra/Aqua NOAA	3000 1000 375-750

*Advanced post-processing required

1.3.1 High temperature thermal anomalies: lava flows

It has been established that the Earth's surface temperature and its composition can be derived from IR radiances measured by multispectral spaceborne instruments (Nash et al., 1993). Since early spaceborne missions were launched to study weather patterns, thermal anomalies have been identified at active volcanoes (Francis and Rothery, 2000). The most obvious application of measuring high-temperature thermal anomalies is to identify the hottest (most active) parts of a lava flow, which are potentially the most hazardous features. In addition to observable surface lava flows (or lakes), it has been indicated that spaceborne data can locate and identify the surface thermal expression of active sub-surface lava tubes (Flynn et al., 2001; Harris et al., 1998), the type of lava involved ('pahoehoe', 'aa' or 'blocky'), can contribute significantly to the final lengths during an effusive event. This is significant for civil protection, as some of world's most active volcanoes are located in close proximity to high urban-density settlements (e.g., Mt Etna and Mt Vesuvius, Italy and Mt Merapi, Java, Indonesia). To ensure that meaningful temperatures are collected, satellite thermal data must be corrected for instrumental errors (USGS, 2019), atmospheric attenuation (Barsi et al., 2005, 2003) and emissivity of the surface (Chapters 2-5). This information can be used to extract both qualitative and quantitative information of the volcanic activity, which is crucial to constrain more advanced spaceborne data applications (Chapters 3 and 4) and for lava flow models validation (Chapters 3 and 5).

It is widely recognized that RS data can be integrated with ground-based observations during volcanic crises to facilitate the estimation of thermal anomalies, and depending on spatial and temporal resolutions, forecast the progression of active lava flows. However, a developing lava flow is a complex surface to observe using either ground-based, as well as remote techniques, due to the presence of moving material at a range of temperatures, textures, vesicularities (Michael S. Ramsey and Fink, 1999), as well as variations that depend on viewing angles (Ball and Pinkerton, 2006).

Several automated processes for detection and measurement of volcanic 'hot-spots', such as VAST (Higgins and Harris, 1997), MODVOLC (Wright et al., 2004, 2002), RAT (Di Bello et al., 2004), MyVOLC and MyMOD (Barbara Hirn et al., 2008b), among others, have been developed, tested and run to date. In particular, three projects have marked the development and awareness for a complete and global monitoring capacity: (i) the European Space Agency's (ESA) pilot project GLOBVOLCANO (2008-2011), using high-spatial resolution RS (Borgström et al., 2008); (ii) the European Commission's European Volcano Observatory Space Services (EVOSS, 2010-2016), centred on high-to very-high temporal

resolutions (Tait and Ferrucci, 2013), and (iii) the Disaster Risk Management volcano pilot project of the Committee on Earth Observation Satellite (CEOS), focusing on continuous monitoring of volcanic activity in the whole of Latin America and Caribbean (USGS, n.d.). These projects, among others, have demonstrated how access to RS data over volcanic regions can benefit the understanding of volcanic activity, enabling hazard mitigation and identification of developing trends in volcanic activity.

Spaceborne RS may be considered as an exceptional tool in studying active volcanoes globally, as a single satellite image, depending on the orbit and resolution, may provide hundreds of square kilometres coverage, allowing assessment of the entire volcano and a record of volcanic activity (cloud cover permitting for optical instruments). Nonetheless, limiting either or both the temporal and spatial resolutions could prove to be disadvantageous in some cases, depending on the (spatial and temporal) dimensions of the target. For example, a lava flow may be only tens of metres wide and may progress at a rate of a few kilometres per hour. So, for effective monitoring, involving measurement and interpretation of volcanic behaviour, both high-spatial and high-temporal resolutions are required (Chapter 6).

1.3.2 A question of resolution: spatial and temporal

A number of studies focus on high -spatial resolution ($\leq$ 0.1 km) satellite imagery (Marchese et al., 2018; Hirn et al., 2008), whereas others exploit lower spatial resolution ($\geq$ 1.0 km) but high temporal RS data (Ferrucci and Hirn, 2016; Hirn et al., 2008; Harris et al., 2001; Oppenheimer, 1998).

Whereas weather satellites are intended to cover large areas as frequently as possible, Low Earth Orbit (LEO) instruments, provide images of higher resolution and greater detail.

The time taken for a particular instrument to image the entire Earth's surface is a function of the orbit and swath width of the instrument. For example, the Landsat series instrument (USGS, 2019) passes over the exact same location every 16 days, whereas instruments with a wider swath will complete the entire cycle in a shorter period. Moderate-resolution Imaging Spectro-radiometer (MODIS) onboard the National Aeronautics and Space Administration (NASA) Earth Observation Systems, Terra and Aqua (WMO, n.d.), has a swath width of 2230 km and provides global coverage once (short-wave channels) or twice daily (long-wave channels). The higher-temporal resolution of MODIS (1-2 a day) in comparison to Landsat (16 days) had to be compromised with a lower-spatial resolution, as MODIS imagery has a scaled pixel area of 1.0 km^2. Whilst the Landsat family is a good example of high-spatial resolution (30-100 m) land surface data acquisition, spanning almost

half of a century, it is now accompanied by the Copernicus Multi-Spectral Imager (WMO, n.d.) for Sentinel-2 pair (A and B), bringing the frequency of revisit down to as low as 5 days.

As hotter volcanic surfaces will radiate more energy and higher radiant flux density, any variation in observed radiance will reflect a variation in volcanic activity on the ground. Sensors having channels in MIR and TIR bands (e.g., MODIS) have been used widely for decades to detect volcanic thermal anomalies (Solikhin et al., 2012; Ramsey and Dehn, 2004) and have proven to be a valuable tool for identifying general trends (derived from radiant heat and mass flux) and monitor broad volcanic activity (Ramsey et al., 2019; Harris, 2013a; Harris et al., 2011; Hirn et al., 2008a; Wright et al., 2004; Wooster and Rothery, 1997; Oppenheimer, 1993; Rothery et al., 1988). On the other hand, sensors such as the MSI (Sentinel-2) and Landsat-8 (OLI), having channels in NIR and SWIR, providing data at high-spatial resolution, enable better identification detail of high-temperature thermal anomalies (e.g., lava flows) (Marchese et al., 2018; Hirn et al., 2008).

1.4 Mount Etna, Italy: A Natural Laboratory

The geological history of one of the most active basaltic volcanoes worldwide and the most active volcano in Europe, Mt Etna (3340 m a.s.l.) spans over 500 ka. Located along the Ionic coast of eastern Sicily (Italy), this large composite volcano has a maximum diameter of ~45 km and it covers an area of 1250 km^2. The geology of Mt Etna volcano has been studied since the 19^{th} century and suggests a complex evolution (Branca et al., 2011).

Due to its persistent activity and relatively easy access, Mt Etna has been frequently targeted for studies involving ground-based investigations and applications of RS data to detect high-temperature thermal features and measure eruptive products, using various volcano monitoring approaches. Mt Etna has been displaying a quasi-continuous activity recently, at different locations on the volcanic edifice (e.g., summit, flanks) (Corradino et al., 2019; Acocella et al., 2016; Kahl et al., 2014; Cappello et al., 2013).

The past two decades on Mt Etna have seen a range of summit and flank eruptions (Cappello et al., 2019), which appears to occur in a cyclic manner (Allard et al., 2006), exposing the large communities living in close proximity to the volcano (almost one million people) to a significant risk (Negro et al., 2013). Since the year 2000, Mt Etna has produced both short-lived and longer lasting destructive lava flow fields, which caused major damage to the local economy and nearby tourist facilities, situated on southern and northern flanks of Mt Etna (Neri et al., 2005). In 2004, 2006 and 2008–2009 several flank eruptions occurred

from fissures at the eastern base of the Southeast Crater. This effusive activity was directed towards the uninhabited Valle del Bove, a wide depression at the eastern flank of Mt Etna. Following the 2008–2009 eruption, which was the longest flank eruption since the 1991–1993 event and the second longest since the 17th century (Behncke et al., 2016), Mt Etna developed more explosive behaviour (Ganci et al., 2012), characterized by a growing number of paroxysmal eruptions at the summit craters (Ganci et al., 2019). In just seven years (2011-2018), fifty-seven eruptive events occurred, characterized by lava fountaining, pyroclastic material, and short-lived lava flows (Cappello et al., 2019; Vicari et al., 2011), suggesting higher risk than previously anticipated (Negro et al., 2013).

In this thesis, three distinct Mt Etna effusive events were investigated, occurring in 2001, 2002-2003 and 2017 (Fig.1.3 and Table 1.4).

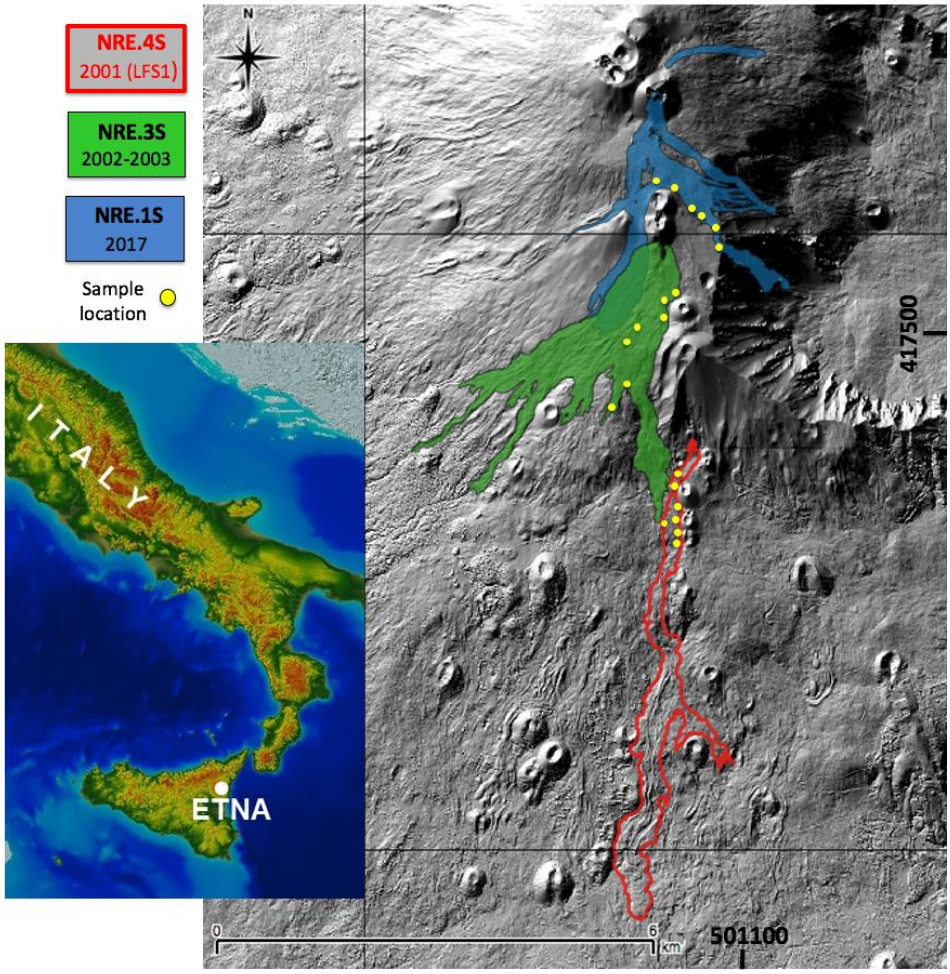

Figure 1.3 (main) The location and actual extent of the 2001 (red), 2002-2003 (green) and 2017 (blue) lava flows are shown on Mt Etna Digital Elevation Model (DEM); **(inset)** a geological map of Sicily, Italy (Tarquini et al., 2007) and the location of Mt Etna volcano. Approximate location of collected samples (NRE.1S, NRE.3S and NRE.4S) are indicated with filled yellow circles. Note that only LFS1 (Coltelli et al., 2007), individual lava flow (18 July-09 August 2001) was used for the 2001 eruption analysis.

Table 1.4 Summary of the 2001, 2002-2003 and 2017 Mt Etna eruptions

Eruption	Location	Start Date (dd-mm-yy)	Stop Date (dd-mm-yy)	Duration (days)	Volume ($\times 10^6$ m^3)	*Previous work
2001	S flank	18/07/01	09/08/01	23	21.4-38	1, 2, 4, 5
2002-2003	NE flank	27/10/02	05/11/02	9	11.8	3, 4, 5
	S flank	27/10/02	29/01/03	94	32.7	3, 4, 5
2017	SEC	15/03/17	09/04/17	26	7.96	6

*Source: 1 (Coltelli et al., 2007); 2 (Behncke and Neri, 2003); 3 (Andronico et al., 2005); 4, (Harris et al., 2011); 5 (Allard et al., 2006); 6 (Cappello et al., 2018)

Previous research on Mt Etna has revealed that during the 20th century two main eruptive trends occurred; (i) 1900-1971 characterised with a moderate eruptive frequency and an average eruption rate of 0.2 m^3s^{-1}; and (ii) 1971-1999 characterised with a significant increase in eruption frequency with an average eruption rate of 0.8 m^3s^{-1} (Allard et al., 2006; Andronico and Lodato, 2005; Wadge, 1981; Wadge and Guest, 1981). The former period (i) produced a cumulative lava volume of 436×10^6 m^3, whereas the latter (ii) produced 767×10^6 m^3 (Andronico and Lodato, 2005).

However, the 2001 flank eccentric eruption displayed an anomalous degree of explosivity, which was followed by another highly explosive eccentric eruption in 2002 (Spampinato et al., 2008), suggesting that eruption dynamics have changed on Mt Etna, triggered by the 2001 eruption (Allard et al., 2006; Behncke and Neri, 2003). This claim was evaluated using a multidecadal (1971-2010) assessment to define volumetric behaviour of this persistently active system (Harris et al., 2011). The study concluded that there was a variation in terms of frequency and duration of effusive activity. However, on a decadal scale volumes and mean output rate (~0.8 m^3s^{-1}) were in line with the typical rate for Mt Etna prior to the 2001 eruption (Harris et al., 2011). Furthermore, they argue that, although some changes have occurred in the shallow system which reflect on the eruption style producing short-duration high effusive phases, the output rates, controlled by supply from the deep system remained unchanged.

The 2001 eruption, despite lasting only 23 days, gave rise to seven distinct fast-developing lava flows (Coltelli et al., 2007). Although the 2001 eruption produced seven different lava flows, focus will be on the individual flow (LFS1) produced between 18 July and 9 August 2001 (Coltelli et al., 2007). It has been indicated that the total lava flow volume is significant in the recent eruptive history of Mt Etna (Coltelli et al., 2007), and the key

aspect for selecting it for RS analysis is that despite being almost two decades old at the time of writing, this eruption could be observed by three high spatial resolution multispectral payloads (TM onboard Landsat-5, ETM+ onboard Landsat-7, and ASTER onboard Terra).

The 2002-2003 Mt Etna flank eruption occurred in two distinct locations, the North-East rift (27 October to 04 November 2002) and two episodes at the South-East rift (28 to 31 October 2002 and 13 November 2002 to 28 January 2003). This eruption apparently shared several features with the 2001 event (Andronico et al., 2005), such as south flank activity and a strongly explosive style. Magma viscosity is thought to be the key property (Giordano and Dingwell, 2003) driving magmatic processes (formation, transport, crystallization), which is closely associated with the type of volcanic activity (effusive and/or explosive). Both the 2002-2003 and 2001 flank eruptions occurred along the Etnean southern rift, exhibiting unusual explosivity due to the rise of volatile-rich magma reaching the surface bypassing the central conduits and producing eccentric eruptions (Spampinato et al., 2008; Guest and Duncan, 1981).

The 2017 event is the most recent effusive event investigated in this thesis. It started at the old 'saddle' (Fig. 1.3), between the South-East Crater (SEC) and the New South-East Crater (NSEC) on the morning of 15 March 2017. The lava flow expanded to both the southeast and southwest, diverted by the eruptive cones during the 2002-2003 flank eruption. At the beginning of April 2017, the lava started flowing from two ephemeral vents that opened downstream. This eruption, which ended on 9 April 2017, emitted an estimated 7.96 $\times 10^6 m^3$ of lava (Cappello et al., 2018) over an area of 1.78 km^2.

The selected effusive events (Table 1.4) are used as case studies based on their diverse temporal advance (i.e., short-lived and long-term activity) and lava volumes produced, which are significant for Etnean recent eruptive history. Twenty samples (Fig. 1.3 and Table 1.5) were collected for emissivity studies, representing Mt Etna's 2001 (NRE.4S), 2002-2003 (NRE.3S) and 2017 (NRE.1S) effusive events, in a grid scaled to dimensions in line with high-spatial resolution satellite sensors (~100 m). Moreover, spaceborne data was acquired by several high-spatial multispectral instruments and is accessible for assessment of representative sample collections.

Sample series are colour coded according to the Figure 1.3 (i.e., NRE.1S - blue, NRE.3S - green and NRE.4S - red) and will be referred to according that colour-code throughout this thesis.

Table 1.5 Summary of sample locations from eruptions analysed

2001 eruption Sample ID #	Location Lat/Lon	**2002-03** eruption Sample ID #	Location Lat/Lon	**2017** eruption Sample ID #	Location Lat/Lon
NRE.4.0	37°41’51.12’’N 14°59’43.11’’E	NRE.3.11	37°43’16.06’’N 15°0’2.51’’E	NRE.1.0	37°44’17.21’’N 15°0’3.68’’E
NRE.4.1	37°41’55.71’’N 14°59’52.28’’E	NRE.3.12	37°43’8.97’’N 14°59’44.29’’E	NRE.1.1	37°44’12.70’’N 15°0’12.94’’E
NRE.4.2	37°41’55.96’’N 14°59’58.68’’E	NRE.3.14	37°43’27.05’’N 15°0’12.42’’E	NRE.1.2	37°43’59.50’’N 15°0’24.02’’E
NRE.4.3	37°42’3.07’’N 15°0’4.08’’E	NRE.3.15	37°43’24.26’’N 15°0’8.17’’E	NRE.1.3	37°43’57.00’’N 15°0’26.27’’E
NRE.4.4	37°42’8.33’’N 15°0’8.57’’E	NRE.3.16	37°43’14.75’’N 14°59’51.77’’E	NRE.1.4	37°43’55.47’’N 15°0’30.07’’E
NRE.4.5	37°42’10.08’’N 15°0’10.99’’E	NRE.3.18	37°42’47.62’’N 14°59’41.37’’E	NRE.1.5	37°43’52.62’’N 15°0’32.11’’E
NRE.4.6	37°41’59.21’’N 15°0’10.86’’E	NRE.3.20	37°43’36.38’’N 14°59’31.92’’E		

The XRF analysis of samples I collected, further provided the opportunity to determine the geochemical ‘uniqueness’of each sample to better determine the composition of erupted material (Table 1.6). Major elements of my samples were determined using fused glass beads, prepared from ignited powders sample to flux ratio 1:5, 80 % Li metaborate: 20 % Li tetraborate flux using X-Ray Fluorescence (XRF) technique on University of Leicester, Department of Geology PANanalytical AXios Advanced XRF spectrometer (Table 1.6).

Table 1.6 XRF major elements content, as a component oxide weight percent (wt.%)

Major elements	**NRE.1S**	**NRE.3S**	**NRE.4S**
SiO_2	47.49	47.85	48.15
TiO_2	1.63	1.53	1.53
Al_2O_3	17.71	17.41	16.49
Fe_2O_3	11.26	10.99	11.19
MnO	0.17	0.17	0.17
MgO	4.81	4.84	5.71
CaO	10.36	9.73	10.48
Na_2O	3.65	3.77	3.52
K_2O	1.72	1.85	1.70
P_2O_5	0.55	0.58	0.53
SO_3	0.005	0.004	0.005
LOl	-0.35	-0.41	-0.30
Total	99.02	98.37	99.14

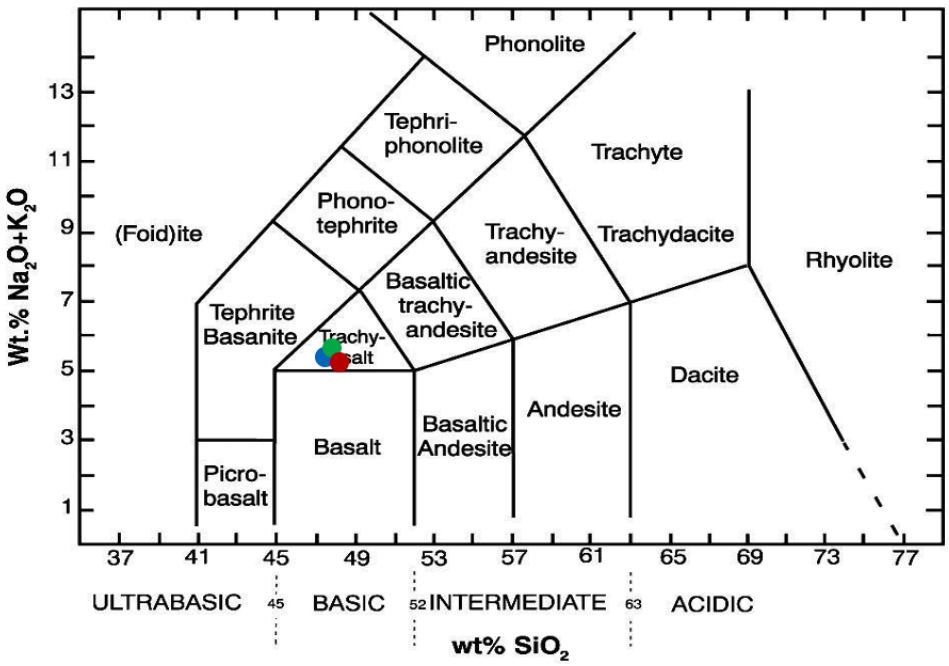

Figure 1.4 Derived Total Alkalis Silica (TAS) plot for the 3-eruption series analysed, superimposed on the standard field boundaries for igneous rocks (LeMaitre et al., 1989).

XRF results indicate silica (SiO_2) and alkali ($Na_2O + K_2O$) contents, consistent with previous research on Etnean lavas (Giordano and Dingwell, 2003), categorizing them all as trachy-basalts. The compositions (Table 1.6 and Fig. 1.4) for samples analysed here for each Mt Etna eruption are geochemically very simillar, plotting closely together and in the same field (trachybasalt) on the Total Alkali Silica (TAS) graph.

1.5 Aim and structure of this thesis

As indicated previously, spectral emissivity is not commonly measured for a range of materials and temperatures, and it is generally assumed to have a constant value between 1.0 and 0.80 for basaltic lava (Harris, 2013a).

Nonetheless, emissivity of molten basalts is recognised to be significantly lower than those of fully cooled counterparts (Thompson and Ramsey, 2020; Ramsey et al., 2019; Lee et al., 2013). Since there is a lack of laboratory-based data for robust inverse and/or forward modelling, this thesis addresses this deficit (Chapter 2). This involves a thorough experiment on ‘aa’ lava samples from three significant eruptions on Mt. Etna, which are representative of the range of its eruptive behaviour(s) (Cappello et al., 2019). Emissivity of samples is measured over the widest range of temperatures (~294-1373 K) and wavelengths (0.66-15.0 µm) executable in laboratory environment to establish the role of emissivity in estimates from spaceborne data.

The thesis falls into two main sections. The first deals with past and current approaches to RS data processing and the need for laboratory-based data (Chapter 2) to determine the relevance of laboratory measured emissivity to the spectral radiance, a central parameter measured by the satellite sensor. Therefore, the aim in this thesis is to highlight the need for detailed emissivity assessment and relate the results and their physical meaning in terms of 'at-satellite' spectral radiance and its relationship to derived apparent lava surface temperatures, radiant heat flux and subsequent analyses that rely on the accuracy of this measurement. The net result is to establish how applicable these measurements (i.e., role of emissivity) may be to calibrate the target signal and to 'ground-truth' the RS data.

The second section centres on testing emissivity-temperature 'trend(s)', as input parameters, derived from the laboratory data presented in Chapter 2 to quantify uncertainty in the current approaches and the novel multicomponent emissivity method introduced here is then applied to spaceborne and modelling applications (Chapters 3-5). Spaceborne data from OLI and Sentinel-2 onboard Landsat-8 and MSI, as well as MODIS onboard Terra and Aqua were exploited as the best candidates for RS analyses to provide the required spatial, temporal and spectral coverage (SWIR, MIR and TIR), in an attempt to extract accurate apparent lava surface temperatures. These have an inherent influence on the computation of radiant heat and mass fluxes, which impact directly on the prediction of lava flow 'distance-to-run' forecasts, as mass flux (effusion rate) estimates depend on measured radiant flux.

Research question, on how can detailed laboratory-measured data on emissivity-temperature trends (currently largely ignored) benefit spaceborne data analysis and interpretation to reduce uncertainty in calculated radiant heat flux has been discussed in this thesis. The main aim of this study is to answer this question through analysis of the role of emissivity in high-to-moderate spatial resolution satellite data, discussing implications of results for current modelling and spaceborne approaches and the selection of platforms for volcano monitoring. This may be summarised as:

(a) Laboratory-based FTIR data analyses. Data covering several spectroscopy methods with diverse sensitivities are analysed to derive (a) emissivities of basaltic rock and (b) what reliable emissivity-temperature trends can be extracted.

(b) Analysis of existing spaceborne emissivity data. Variation in emissivity acquired by ASTER GED, of the same target area is validated using laboratory measured data. Comparison of spectral signatures enable the value of this approach to be assessed.

(c) Use of measured emissivity-temperature trends as spaceborne data input parameters. Techniques are employed using well established approaches with the key

difference that emissivity is wavelength and temperature dependent (multicomponent), rather than ‘static’. The novel approach developed in this thesis has been validated by the Istituto Nazionale di Geofisica e Vulcanologia (INGV) in Catania, Italy with the expectation of it being implemented for future spaceborne and modelling applications to monitor Mt Etna.

(d) Wider application. Emissivity-temperature trends developed for Mt Etna are compared with values obtained for volcanoes in different setting (Lascar, Chile and Kilauea, Hawaii) which are also analysed in this study. This offers a complementary view on global application of such trends.

(e) Towards automation. Why and how can findings presented in this thesis be applied and incorporated into multi-platform, multi-payload automated system for volcano monitoring.

During this study, opportunities to work with external collaborators were embraced, which allowed access to several external facilities and resulted in several presentations at international and national conferences and peer reviewed publications. Papers published are presented here in Appendices. As first author for these collaborative papers there is necessarily some inevitable repetition in the main body of the thesis.

2 Spaceborne and laboratory measured emissivity results

Much of the material discussed in this chapter has been published in the papers by Rogic et al. (2019a) and Rogic et al. (2019b), which are reproduced in full as Appendices G and H.

2.1 Introduction

To measure the emissivity of the lava samples collected and analysed in this thesis, available satellite emissivity data from Advanced Spaceborne Thermal Emission and reflection Global emissivity Database (ASTER GED) and several Fourier Transform Infrared (FTIR) spectroscopy methods were used (Table 2.1). For clarity, different symbols are used (Table 2.1) to present results (Section 2.3) for each technique (e.g., empty circles for the FTIR analysis at 343 K).

Table 2.1 Summary of techniques used to measure and assess emissivity

Technique	Section	Symbol	Sample ID	Eruption	Sample size	*Temp. (K)	Wavelength (μm)
Spaceborne ASTER GED	2.2.1 2.3.1	◆	all (Table 1.5)	2001 2002-03 2017	100-m pixel	-	8.30, 8.65, 9.10. 10.60, 11.30
Laboratory-based FTIR (reflectance)	2.2.2 2.3.2	□	NRE.4.1; 4.4 NRE.3.11; 3.14 NRE.1.1; 1.5	2001 2002-03 2017	1000-3000 (μm)	294	0.66-16.0
Laboratory-based FTIR (radiance)	2.2.3 2.3.3	○	all (Table 1.5)	2001 2002-03 2017	Hand specimen ~8.0 cm	343	8.0-15.0
Laboratory-based FTIR (radiance)	2.2.4 2.3.4	■	NRE.4.1; 4.4 NRE.3.11; 3.14 NRE.1.1; 1.5	2001 2002-03 2017	1000-3000 (μm)	400-900	5.0-15.0
Laboratory-based FTIR (radiance)	2.2.5 2.3.5	▲	NRE.4.1; 4.4 NRE.3.11; 3.14 NRE.1.1; 1.5	2001 2002-03 2017	100-350 (μm)	737-1373	2.17-15.0

*Temperature in Kelvin (K)

An introduction to the theory and methods of Fourier Transform Infrared (FTIR) spectroscopy can be found in (King et al., 2004), among others.

The physical principle behind measuring emissivity from surface reflectance spectra (at ambient temperature) using the FTIR method is that ‘apparent’ emissivity values can be calculated from the measured reflectance (*R)* using Kirchhoff’s law (Korb et al., 1999). Source radiation from FTIR spectrometer was impinged on samples within an integrating sphere coated by a diffusely reflecting gold surface. By comparing reflected radiation from the sample, with that from a diffuse gold reference surface, directional hemispherical reflectance, and emissivity, through Kirchhoff’s law can be calculated.

Unlike the reflectance approach, retrieving ‘absolute’ emissivity from radiance does not require a separate source of infrared radiation; instead, the radiation emitted by the surface is compared with the amount of radiation emitted by a blackbody at the same kinetic temperature.

The Michelson interferometer is central to any FTIR spectrometer. The interferometer splits the beam of incoming radiation into two paths: one path travels to a fixed mirror, whereas the other path travels to a moving mirror. The two paths of radiation are recombined at the detector producing an interference pattern. The temporal coherence of the radiation is recorded as a function of mirror position (path difference) at discreet time intervals to produce an interferogram. A cosine Fourier transform of the interferogram will produce a spectrum of energy intensity as a function of wavelength. Corrections are applied to account for the resolution and field of view of the instrument, as detailed in Griffiths (1975).

The simplest approach (the ‘reference channel’ method) which assumes that target emissivity is equal to that of a blackbody (unity) at a given wavelength in the measured spectrum (Murcray et al., 1970). Given that target radiance and emissivity are known at a specific wavelength, it is possible to derive surface temperature and calculate emissivity at all other wavelengths. Another approach assumes a known emissivity maximum at a specified waveband, rather than a specific wavelength (Kahle and Alley, 1992), where the temperature of the Planck’s curve with the closest ‘blackbody fit’ to the specified maximum emissivity is used to calculate emissivity for the remainder of the spectrum. The blackbody calibration method is used in this chapter to derive ‘absolute’ emissivity in all radiance FTIR approaches at a range of temperature (343-1737 K).

2.2 Methods

2.2.1 Spaceborne emissivity retrieval: ASTER GED

The Global Emissivity Database (GED) built by NASA’s Jet Propulsion Laboratory (JPL) (Hulley and Hook, 2013) is currently the most detailed emissivity product available for Earth’s land surface, derived from spaceborne data. Emissivity, rescaled to 100 m from the original 90-m Advanced Spaceborne Thermal Emission and Reflection Radiometer (ASTER) TIR pixels, is an average of data acquired at five TIR central wavelengths (8.30 μm, 8.65 μm, 9.10 μm, 10.60 μm, and 11.30 μm) every 16 days, from 2000 to 2008. It was obtained by NASA JPL by combining temperature emissivity separation (TES) algorithms

and water vapor scaling (WVS) atmospheric corrections coincident with MODIS MOD07 atmospheric profiles and the MODTRAN 5.2 radiative transfer code (Hulley et al., 2015).

2.2.2 Emissivity from Surface Reflectance Spectra at 294 K

I measured reflectance spectra of samples measured at an ambient temperature (~294 K), collected at the Planetary Emissivity Laboratory (DLR, Germany) by the Bruker Vertex 80v FTIR spectrometer, using a gold integration sphere hemispherical reflectance accessory.

The 'apparent' emissivity (ε') values can be predicted from reflectance (R) derived from the FTIR measured reflectance data, using Kirchhoff's law (Eq. 11). This approach provides an expected result precision of 0.005 (Korb et al., 1999), and is typically simplified as:

$$\varepsilon' = 1 - R \tag{11}$$

It is important to note that Kirchhoff's law is only valid for hemispherical reflectance measurements, and is used to approximate emissivity from reflectance data (Korb et al., 1999); thus, the term 'apparent' emissivity (ε') is used here to contrast with the 'absolute' emissivity (ε) term used in radiance FTIR approaches.

The experimental setup (Fig. 2.1) in this study and in Maturilli et al. (2018) measures the reflectance of samples in the visible to near-infrared (V-NIR), and MIR wavelength range. Reflectance is converted into an 'apparent' emissivity using Equation (Eq. 11). For MIR measurements, a wide-range Mercury Cadmium Telluride (HgCdTe) detector is used ($1000 - 400\ \mathrm{cm}^{-1}$) in tandem with a wide-range germanium (Ge) on potassium bromide (KBr) beam splitter ($12500 - 420\ \mathrm{cm}^{-1}$). For V-NIR measurements, conversely, an InGaAs Diode detector was used ($12500 - 5800\ \mathrm{cm}^{-1}$) in tandem with a silicon (Si) on calcium fluoride (CaF_2) beam splitter ($15000 - 1200\ \mathrm{cm}^{-1}$).

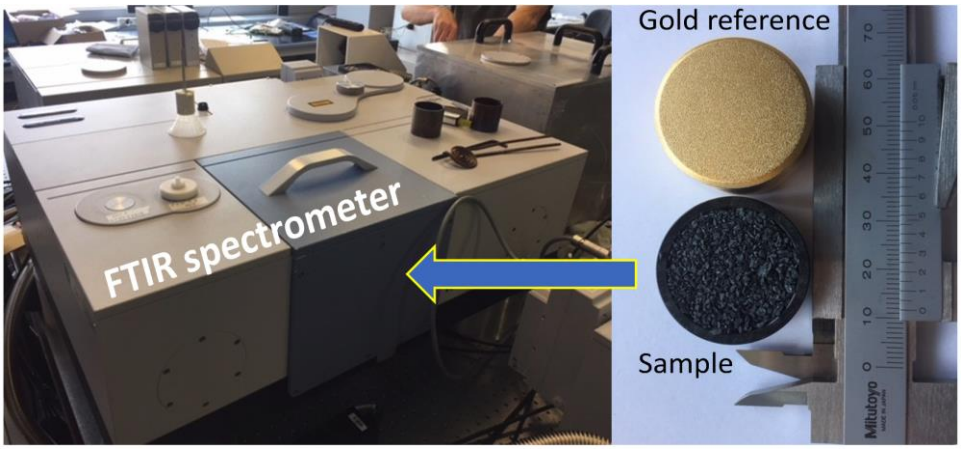

Figure 2.1 Reflectance FTIR experimental set-up (this study) to measure samples' reflectance at ambient temperature (~294 K). Reflectance data were converted to 'apparent' emissivity using Kirchhoff's Law (1-R).

Samples of 4 grams in particulate form (particle size 500–1000 μm) were placed into individual sample cups (2.5 cm diameter), which were positioned on the hemispherical reflectance accessory, and aligned. Prior to measuring samples, a gold reference target (Fig. 2.1) was used to calibrate the instrument. Finally, individual sample spectra were normalized to the gold reference target spectrum results to obtain reflectance values.

2.2.3 Emissivity from Surface Radiance Spectra at 343 K

I measured samples at the Natural Environment Research Council (NERC) Field Spectroscopy Facility at the University of Edinburgh, U.K., using a MIDAC M2000 spectrometer (MIDAC corporation, 2003).

The experimental setup is shown in Figure 2.2, where TIR measurements (8.0-15.0 μm) were taken at an approximate temperature of 343 ($\pm$10 K). The spectrometer is equipped with zinc selenide (ZnSe) optics and a mercury cadmium telluride (HgCdTe) sensor, giving a spectral range of a ~2.0-15.0 μm, with a selectable resolution of 32-0.5 cm^{-1}. A 75-mm gold front surface coated mirror attached on a rotary spindle is designed for viewing sample surfaces. The path from target to sensor was ~35 cm. A blackbody system built by Electron Systems is used for spectrometer calibration. The system consists of three blackbodies, two of which can be heated (or cooled) to user-selectable temperatures. Hemispheric down-welling radiance (DWR) measurements are made using diffuse gold highly reflective surface (InfraGold), with a reported emissivity of less than 0.06 (R>0.94). Prior to measuring the samples, a thermocouple was placed inside the spectrometer housing to monitor spectrometer temperature for 90 minutes. Solid samples (~8 cm) were grouped into two categories (i) naturally occurring 'rough' surface and (ii) cut 'smooth' surface (same sample sawn in half) and were heated to ~343 K ($\pm$10 K) using a convection oven to produce a spectral contrast with background radiation. The experimental step where samples were manually transferred from the oven to the measuring platform was less than ideal, as temperature stability (cooling) could not be controlled. The sample surface temperature was recorded using a contact temperature probe. Two blackbodies were set to 313 K (BB 1) and 353 K (BB2), to 'bracket' the sample temperature, and were kept at constant temperatures using a Dual (+1) IR-301 Blackbody controller powered by an external battery. The third blackbody (BB3) was kept at ambient temperature (~294 K).

Calibration spectra were firstly taken of two heated blackbodies (BB1 and BB2), followed by BB3 and a measurement of DWR using the InfraGold. Spectra were then collected for each sample. Each measurement co-added 32 spectra at a resolution of 2 cm^{-1}.

A measurement time of ~10 seconds per sample, encompassed measurement of the naturally occurring 'rough' surface sample (Fig. 2.2 b), instantly followed by a measurement of the cut 'smooth' sample surface (Fig. 2.2 c) to keep the sample temperature conditions identical during both measurements. Calibration and DWR measurements were repeated at regular intervals (every 60 minutes) to account for changes in background radiance and spectrometer temperature. Raw spectrometer data were converted to radiance and absolute emissivity based on the empirical conversion approach of (Ruff et al., 1997).

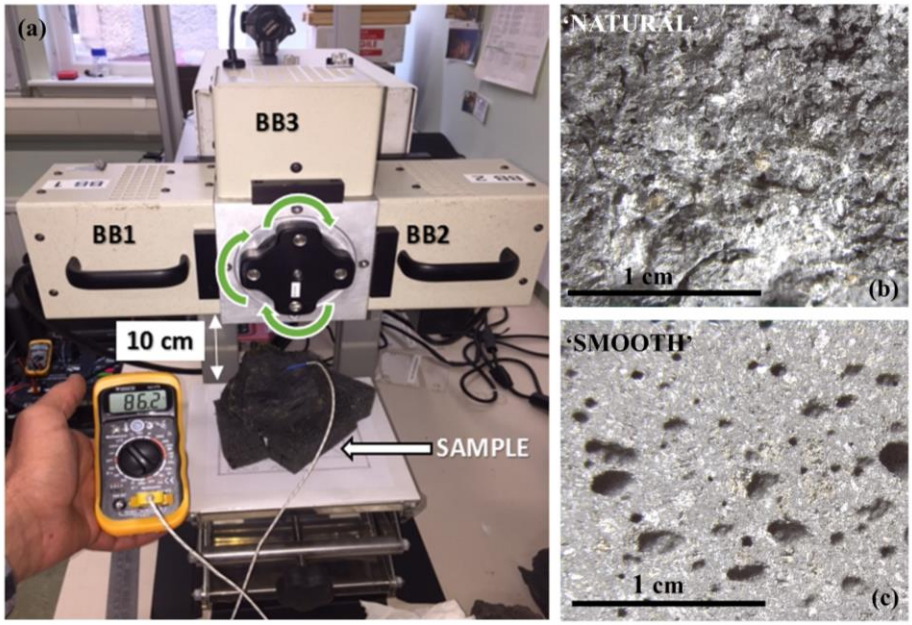

Figure 2.2 (**a)** Emission FTIR experimental set up at 343 K and 8.0-15.0 μm wavelength range, involved MIDAC M2000 spectrometer, including blackbody system consisting of 3 blackbodies (BB); BB1 at 313 K, BB2 at 353 K and BB3 at 294 K (ambient temperature), which were used for spectral calibration. Hemispheric down-welling radiance is measured using diffuse gold (InfraGold) highly reflective surface ($\boldsymbol{\varepsilon} < 0.06$). Samples were heated to ~343 K ($\pm 10\ K$) using convection oven, while sample surface temperature was recorded using a contact temperature probe; **(b)** An example of a naturally occurring 'rough' sample surface (NRE.1.4R) and **(c)** sample cut in half to reveal freshly cut interior sample surface is termed 'smooth' (NRE.1.4S).

2.2.4 Emissivity from Surface Radiance Spectra 400-900 K

I measured thermal emission spectra of the samples at the Planetary Spectroscopy Laboratory (PSL) of the German Aerospace Center (DLR) in Berlin (Germany), using a Bruker Vertex 80V FTIR spectrometer operating in vacuum, with a liquid nitrogen cooled mercury cadmium telluride (HgCdTe) detector and potassium bromide (KBr) beam splitter. 'Absolute' emissivity spectra were acquired between 5.0 and 15.0 μm, with a spectral resolution of 4 cm^{-1} and temperature range 400-900 K. The experimental setup (this study and (Maturilli et al., 2018; Maturilli and Helbert, 2014) uses an externally evacuated planetary 'simulation chamber', attached to the FTIR spectrometer (Fig. 2.3). The radiance

is collected by an Au-coated parabolic 90° off-axis mirror and reflected to the spectrometer. The emissivity chamber is equipped with an internal webcam and several temperature sensors to measure the sample/cup temperature, monitor the equipment, and record chamber temperatures. Both the cup and the sample in a particulate form (500–3000 μm) are heated uniformly by induction, and the temperature of the emitting surface is measured using a thermophile sensor in contact with the surface. Samples were heated successively from 400 K at 100 K temperature steps (i.e., 400, 600, 700 800 and 900 K) and once the temperature was stabilized (5 minutes dwell time), emissivity was measured while the temperature was held constant (10 seconds) under a low vacuum (0.7 mbar). The heating cycle between temperature steps (e.g., 600-700 K) took approximately 20 minutes, plus the additional 5 minutes dwell time. Cooling-test of the same samples was performed once the maximum temperature was reached (i.e., 900 K) where that temperature was held constant with 15 minutes dwell time before cooling-down measurements were taken (i.e., 900, 800, 700, 600 and 400 K). The resulting data are calibrated using the emissivity spectrum of the blackbody material (Ferrari et al., 2014; Maturilli and Helbert, 2014) to provide the set(s) of 'absolute' emissivity data.

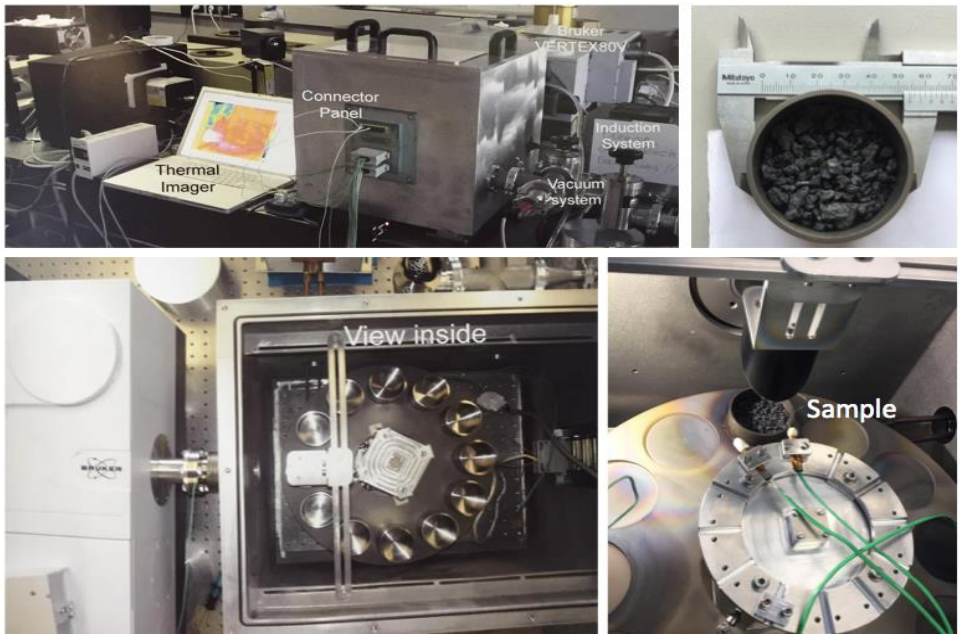

Figure 2.3 Emission FTIR experimental set-up (this study and (Maturilli et al., 2018)) measured 'absolute' emissivity 400-900 K temperature and 5.0-15.0 μm wavelength range, using Bruker VERTEX 80V instrument.

2.2.5 Emissivity from Surface Radiance Spectra 773-1373 K

I measured thermal emission spectra, collected in the Image Visualization and Infrared Spectroscopy (IVIS) Laboratory, at the University of Pittsburgh, Pennsylvania,

U.S.A. The experimental set up (Fig. 2.4) to measure 'absolute' emissivity at very-high temperature uses the Nicolet Nexus 870 FTIR spectrometer, equipped with a potassium bromide (KBr) beam splitter, and a mercury cadmium telluride (MCT-B) detector (cooled with liquid nitrogen) with a spectral range of 4608 - 400 cm^{-1} (2.17 - 25.0 μm). Emission spectra were collected over 8 scans, at a spectral resolution of 2 cm^{-1}, and averaged.

A 'glovebox' adjacent to the spectrometer contains a custom-made furnace (University of Pittsburgh machine shop) and sample measuring apparatus. The 'glovebox' and spectrometer temperature and humidity are carefully monitored, resulting in high-precision emissivity spectra. Both the spectrometer and the attached 'glovebox' are purged with dry air to limit spectral obscuration by H_2O and CO_2. Due to the time limitations and access to this external facility, a total of seven samples (two representative samples from each Mt Etna eruption and an additional sample erupted in 1993 at Lascar, in Chile, discussed in Chapter 5) were prepared for this analysis. All samples were crushed and sieved into ~100-350 μm size fractions. Approximately 1 gram of sample was poured into a 3.0 cm-diameter platinum cup (to ~3 mm depth), which was manually placed into the furnace, located in a glovebox adjacent to the spectrometer and covered with a furnace lid (with viewing opening) and kept there for the duration of the experiment to maintain constant conditions.

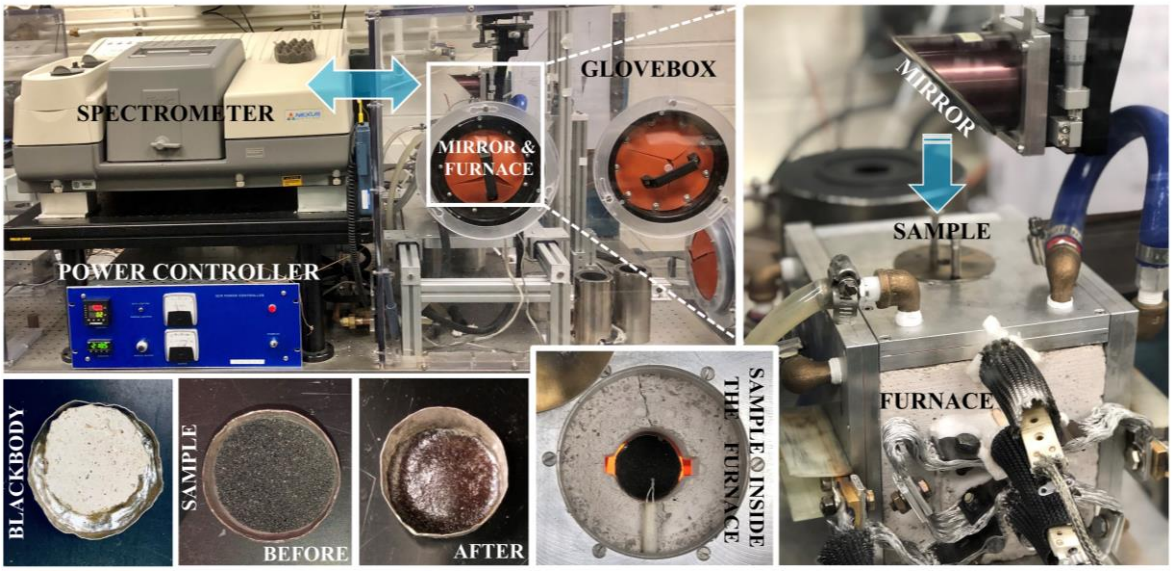

Figure 2.4 Experimental set up to measure emissivity at IVIS Laboratory, at the University of Pittsburgh (U.S.A.) at 773-1373 K and 2.17-15.0 μm wavelength range, shows **(top left)** a power controller unit and Nicolet Nexus 870 FTIR spectrometer and **(right)** adjacent to the 'glovebox', which contains the furnace and sample measuring apparatus. Sample before and after measurement is shown **(bottom left)**, as well as the blackbody used to calibrate the results.

The methodology used here relies on the energy from the heated sample as the source to obtain sample emittance. The IVIS Laboratory instrument measurements, by default will record temperatures in ℃, whereas in this thesis all temperatures are shown in K. For consistency and direct comparison, all temperatures were converted to K in the results section (Section 2.3). Sample measurement steps in both directions, heating-up (773 K to 1373 K) and cooling-down (1373 K to 773 K) were set at 50 K intervals (e.g., 773 K, 823 K, 873 K, 923 K) using a SCR power controller (Fig. 2.3), providing two sets of data for each sample. A four minutes dwell time was applied at each temperature step, to allow equilibration prior of the collection of the spectra (10 seconds), which is an important factor in attaining accurate emissivity spectra.

Prior to the analysis, spectra were acquired from blackbody sources (Fig. 2.3) that are precision controlled to 50 K either side of sample measurement steps, also at 50 K intervals. The spectra of the blackbody targets allow for the instrument and environmental emission to be quantified and removed (Ruff et al., 1997). Measured radiance from the laboratory blackbody was subtracted from that of a calculated (theoretical) blackbody emitter. Calibration and conversion of raw data to absolute emissivity was carried out following the approach of (Ruff et al., 1997) and using an IDL code written by Thompson J.O. (University of Pittsburgh, U.S.A). Experimental error is reported in Appendix B.

2.3 Results

2.3.1 Spaceborne emissivity data: ASTER GED

I downloaded twelve $1° \times 1°$ ASTER GEDv3 datasets (‘tiles’) from the NASA EOSDIS Land Processes DAAC (Hulley and Hook, 2013), centred on Sicily and Mount Etna (Section 2.2.1).

I used existing spaceborne ASTER gedV3 data (Hulley and Hook, 2013) to create the emissivity map (Fig. 2.5) of Sicily (Italy), including Mt Etna. Conversion of downloaded Hierarchical Data Format Files (HDF), a standardised format for scientific data storage to georeferenced (GeoTiff) files, allowed extraction of emissivity values for targets analysed. The highest emissivities are shown in dark blue (~0.95-1.0); these correspond to the volcanic region of Mt Etna, which is consistent with the emissivity signatures relating to basaltic volcanic surfaces (Harris, 2013a). Sicily is geologically complex due to its regional tectonics; thus, green and red areas on the map with lower emissivities would represent compositionally different units of non-volcanic origin.

Mean spaceborne emissivity results (Table 2.2) for the location of all samples analysed, derived from 100 m spatial resolution product ASTER GEDv3 are shown in Figure 2.6. ASTER GED mean emissivity values range from 0.90 to 0.96 in the TIR (8.30-11.30 μm) wavelength range. It is important to note that the ASTER GED emissivity values for the sample locations analysed here are nine-year average (2000-2008) at 100-m resolution. This may have resulted in inclusion of background emissivity, bordering with the target (specific lava flow) within the individual pixel. Furthermore, data on new lava may be averaged out against emissivities of underlying rock before the eruption occurred.

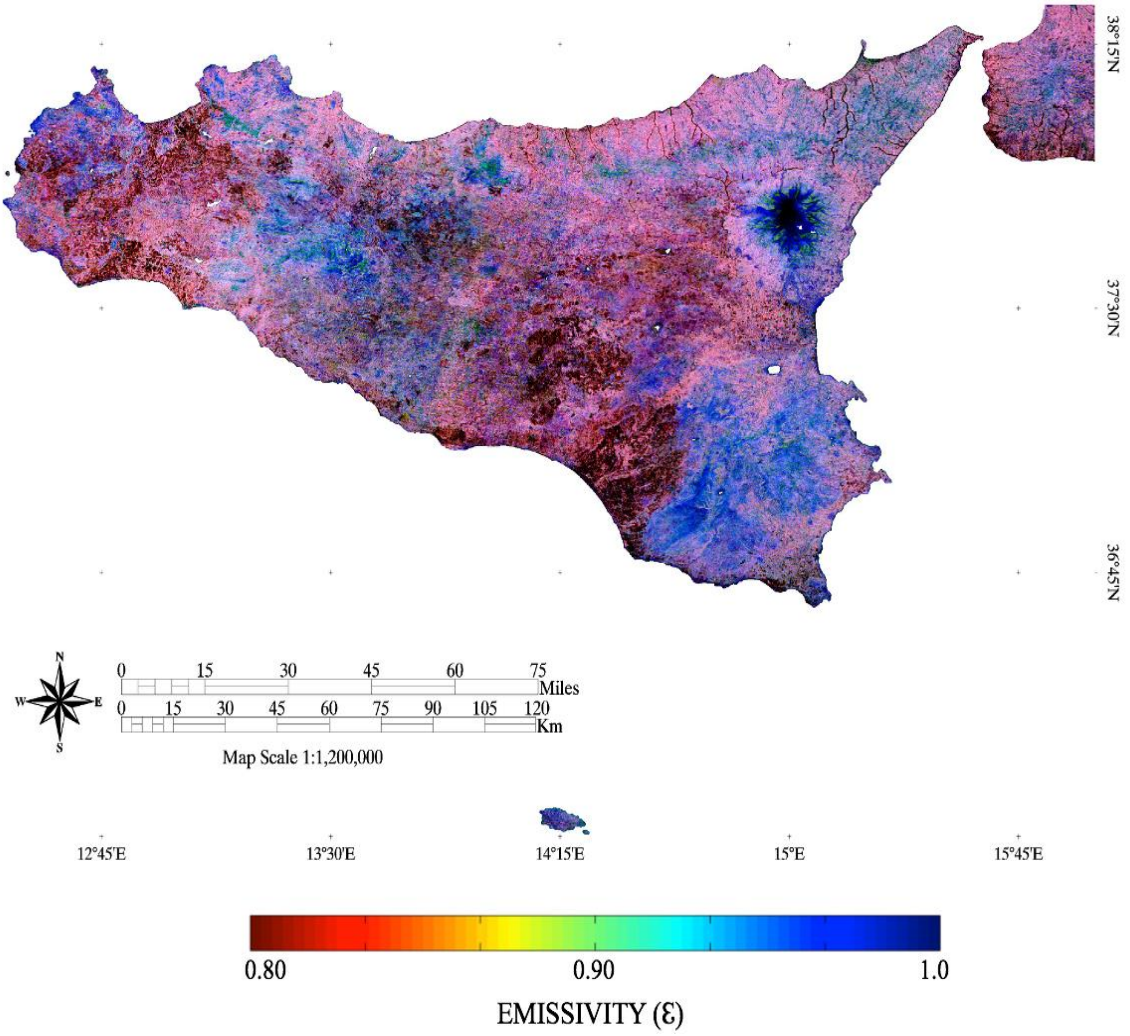

Figure 2.5 ASTER GED emissivity map over Sicily, Italy at 100-m pixel resolution at 10.60 μm and 4-3-1 band red-green-blue (RGB) view. The colour ramp specifies the emissivity values (0.80-1.0). The highest emissivities are shown in dark blue (~0.95-1.0); which correspond to volcanic region of Mt Etna.

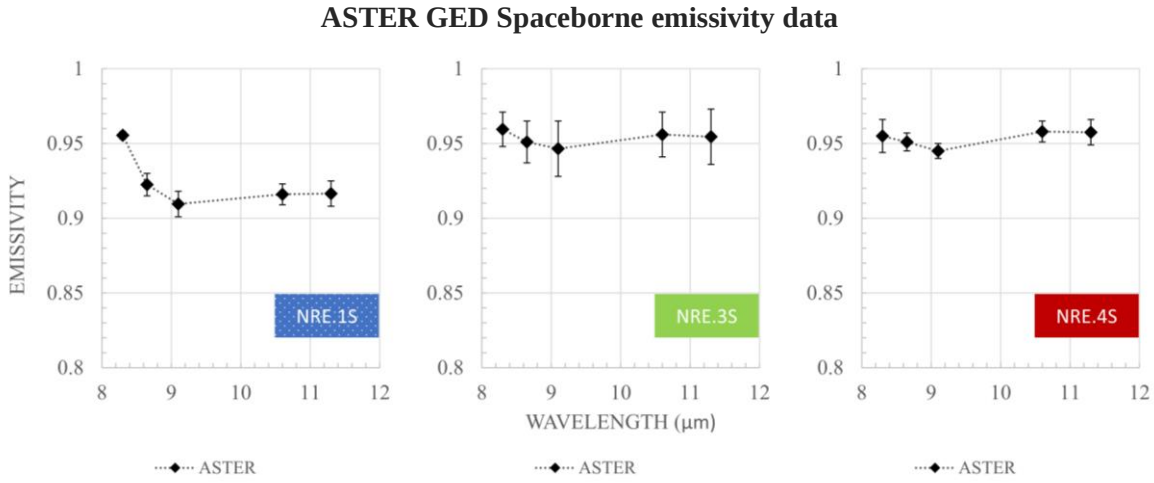

Figure 2.6 Mean spaceborne emissivity results for the 3-eruption sample series location, derived from 100-m spatial resolution product ASTER GEDv3. (Fig. 2.5). Results for each sample series are shown at five ASTER TIR bands (8.30, 8.65, 9.10, 10.60 and 11.30 μm).

Table 2.2 ASTER GED mean emissivity at ASTER TIR bands for sample locations

ASTER TIR bands	8.30 μm	8.65 μm	9.10 μm	10.60 μm	11.30 μm
ASTER GED NRE.1S	0.955	0.923	0.909	0.916	0.916
ASTER GED error	0.002	0.008	0.009	0.007	0.009
ASTER GED NRE.3S	0.959	0.951	0.947	0.956	0.955
ASTER GED error	0.015	0.014	0.018	0.015	0.019
ASTER GED NRE.4S	0.955	0.951	0.945	0.958	0.958
ASTER GED error	0.011	0.006	0.005	0.007	0.008

2.3.2 Emissivity from Reflectance at 294 K

Since the IR emission spectroscopy (εFTIR) is complementary to the reflectance spectroscopy (R FTIR), this special relationship has been applied (Ruff et al., 1997) by use of Kirchhoff's Law, where the central contrast between the two methods is in the source of IR energy (in εFTIR, the heated sample becomes the IR source). This rule generally holds (Korb et al., 1999; Henderson et al., 1996).

Reflectance data measured at ambient temperature may be regarded as a preliminary estimate (first approximation) of surface emissivity. To extend the observable spectral range, two detectors (KBr at 0.66 to 2.50 μm and MCT at 2.50 to 16.00 μm) were used, so that the data could be merged at 2.63 μm to provide the best signal-to-noise (STN) ratio result for the entire range from V-NIR to TIR. The maximum difference in emissivity at any wavelength 0.66-14.0 μm, between the three-sample series is ≤0.03.

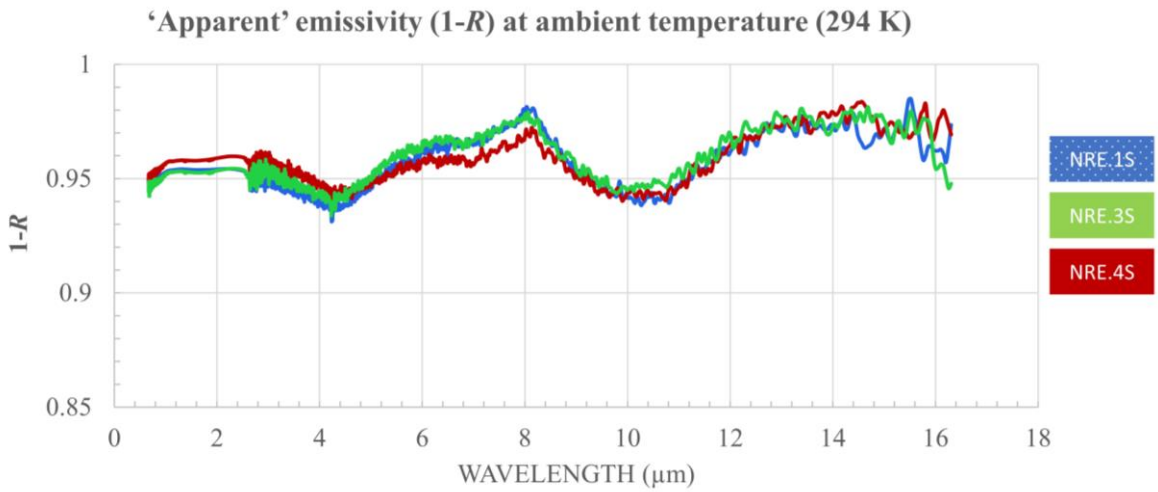

Figure 2.7 'Apparent' emissivity results from reflectance data at 294 K (ambient temperature) and 0.66 μm to 16.3 μm wavelength range. 'Apparent' emissivity was derived from reflectance data using Kirchhoff's Law (1-R).

However, it is important to note that there are several drawbacks in using reflectance measurements compared to emission measurements. For example, the temperature of the sample is not considered, and an isothermal sample is assumed, without accounting for its thermal gradient behaviour. Kirchhoff's Law is used to approximate the emissivity of the sample, where the packing fraction of the particulate sample is also not considered. The incident rays from the spectrometer only interact with the surface layer, so it may not be representative of the bulk composition, and sample preparation may also influence the result.

2.3.3 Emissivity from radiance data at 343 K

Unlike the reflectance approach, retrieving emissivity from radiance does not require a separate source of IR radiation; instead, the radiation emitted by the samples' surface is compared (calibrated) with the amount of radiation emitted by a blackbody at the same kinetic temperature.

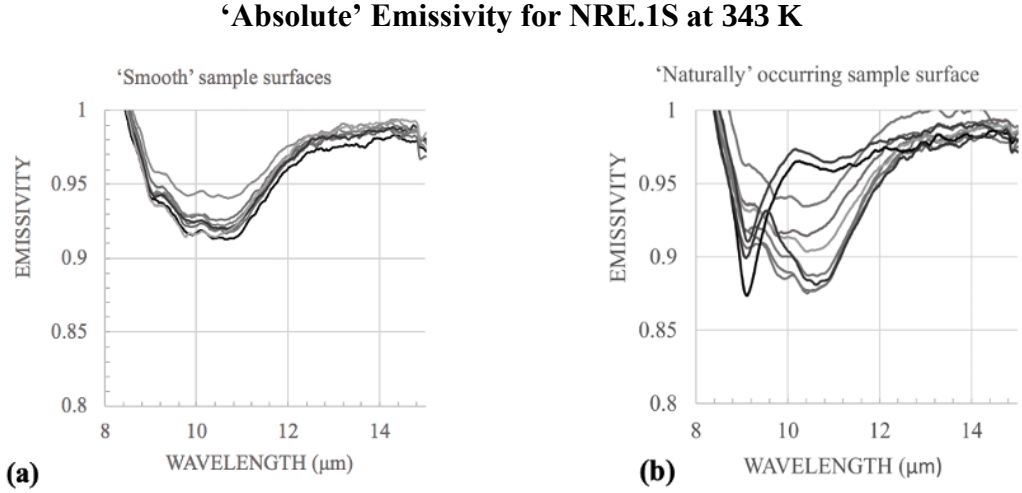

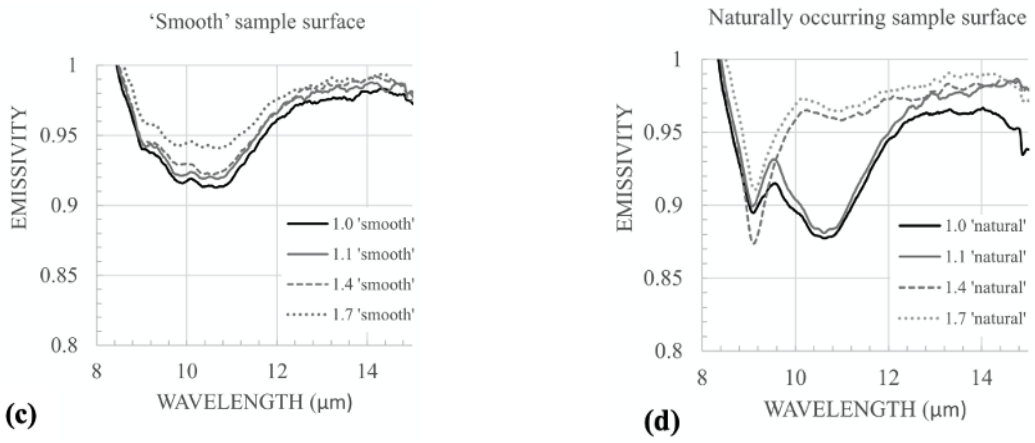

Figure 2.8 Emissivity spectral signature results variation for **(a & c)** cut 'smooth' and **(b & d)** naturally occurring 'rough' sample surfaces, where 'naturally rough' surface samples display a range of spectral contrast (lower emissivity) and different spectral signature shapes from that of their cut 'smooth' counterparts. The example shown here **(a & b)** is for NRE.1 sample series, whereas examples shown in **(c & d)** are four select samples, exhibiting extreme variation between 'naturally rough' and cut 'smooth' results.

The results showed that there is a marked difference in the spectral signatures of measured emissivity between naturally occurring 'rough' (Fig. 2.8 b and d) and cut 'smooth' surface samples (Fig. 2.8 a and c).

All Mt Etna sample series show, to an extent, similar behaviour displayed in an example given in Figure 2.8 for NRE.1S, where several naturally occurring 'rough' surface samples (Fig. 2.8 d) display a range of spectral contrast (lower emissivity) and different spectral signature (shape) to that of its cut 'smooth' surface counterpart (Fig. 2.8 c).

A typical basalt in TIR (8.0-15.0 μm) is expected to have a 'U' shaped feature (Harris, 2013a), with the distribution of emissivity minima at a specific wavelength (~10.65 μm). This shape can be observed (Fig. 2.8 a & c) for all cut 'smooth' surface samples and some naturally occurring 'rough' samples but with higher spectral contrast and lower emissivity (Fig. 2.8 b & d). High SiO_2 glass, such as obsidian would have very prominent feature and defined emissivity low at ~9.10 μm wavelength, which coincides with the absorption band diagnostic of a glass (Harris, 2013a). Samples NRE.1.7 and NRE.1.4 exhibit this feature ('V' shape), whereas samples NRE.1.1 and 1.1 show different feature ('W' shape).

Etnean samples are not expected to be identical, as each eruption is compositionally unique, but they are of relatively similar chemical composition (Table 1.6 and Fig. 1.4), hence should produce comparable emissivity spectral signatures. Furthermore, this should hold true for the samples from the same eruption. This is the case for cut 'smooth' surface samples (Figs. 2.8 a & c), which show similar shapes ('U') for all samples. Considering that

inconsistent ‘V’ and ‘W’ shaped features can be observed in some naturally occurring ‘rough’ surface samples but none in the ‘cut surface’ range series, it should be investigated. These features identified only in ‘rough’ surface sample results may be due to a complex surface mineralogical variation, possibly related to lava cooling and solidification processes, identified by the high resolution FTIR instrument (6 cm field of view), involving ~35 cm path from target to sensor. Spaceborne instruments, such as ASTER (Section 2.3.1) may not record compositional detail seen here, due to its spatial resolution or pixel size (90 m in TIR) and data acquisition altitude (705 km), hence spaceborne results may be comparable to bulk compositional emissivity signatures, provided by the cut ‘smooth’ surface sample results. It has been previously suggested (Ramsey and Fink, 1999) that physical properties, such as vesicularity or cooling fractures, clast size, amount of glass on exposed surfaces may contribute to the impact magnitude of effects causing variation in the naturally occurring ‘rough’ surface emissivity results. However, these physical properties and their impacts on my results have not been assessed fully and/or accounted for in this basic analysis.

In an attempt to confirm this hypothesis (although beyond the scope of this thesis), thin sections for NRE.1.4 naturally occurring ‘rough’ and cut ‘smooth’ surface (Fig. 2.9 and Appendix A) were created to identify features that may cause this spectral discrepancy.

Thin sections were examined using the optical microscope (Leica Wild MZ8) equipped with polarizing filters and rotating stage for geological samples. It operates both in reflected and transmitted modes. The low power view in both plane-polarised light (Fig. 2.9 a-b) and cross-polarised light (Fig. 2.9 c-d) shows that this is a fine-grained rock with microphenocrysts (500-2000 μm) of plagioclase and olivine, enclosed in a fine-grained (< 500 μm) groundmass of minerals typical for basalt (plagioclase feldspar, clinopyroxene and olivine).

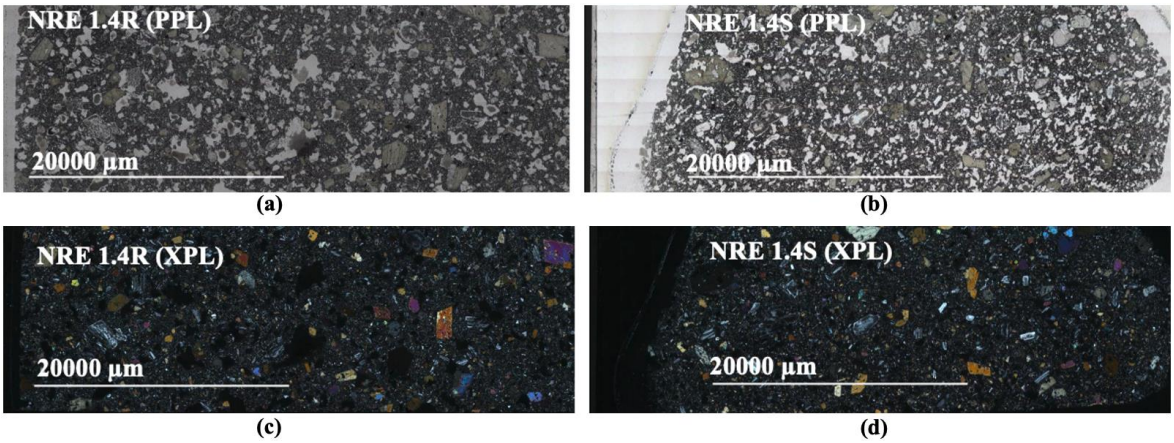

Figure 2.9 A thin section for NRE.1.4 sample, showing an example of **(a)** naturally occurring ‘rough’ and **(b)** cut ‘smooth’ sample surface in plane polarized light (PPL) and **(c-d)** in cross polarized light (XPL). Thin

sections were analysed using optical microscope Leica Wild MZ8, equipped with polarizing filters for geological samples.

Although this analysis could not confirm with confidence that the samples' surface mineralogical variation may be responsible for producing the features identified (Fig. 2.8 b & d), it is evident that the shape and position of spectral signatures are markedly different for the two types of surfaces.

For this reason, the naturally occurring 'rough' surface results were considered inadequate for the purpose of this study, due to significant discrepancies on several samples with inconclusive results, which could not be validated with confidence. Therefore, the cut 'smooth' surface samples were identified as the FTIR analysis representatives at 343 K and only these are referred to in this and the following chapters.

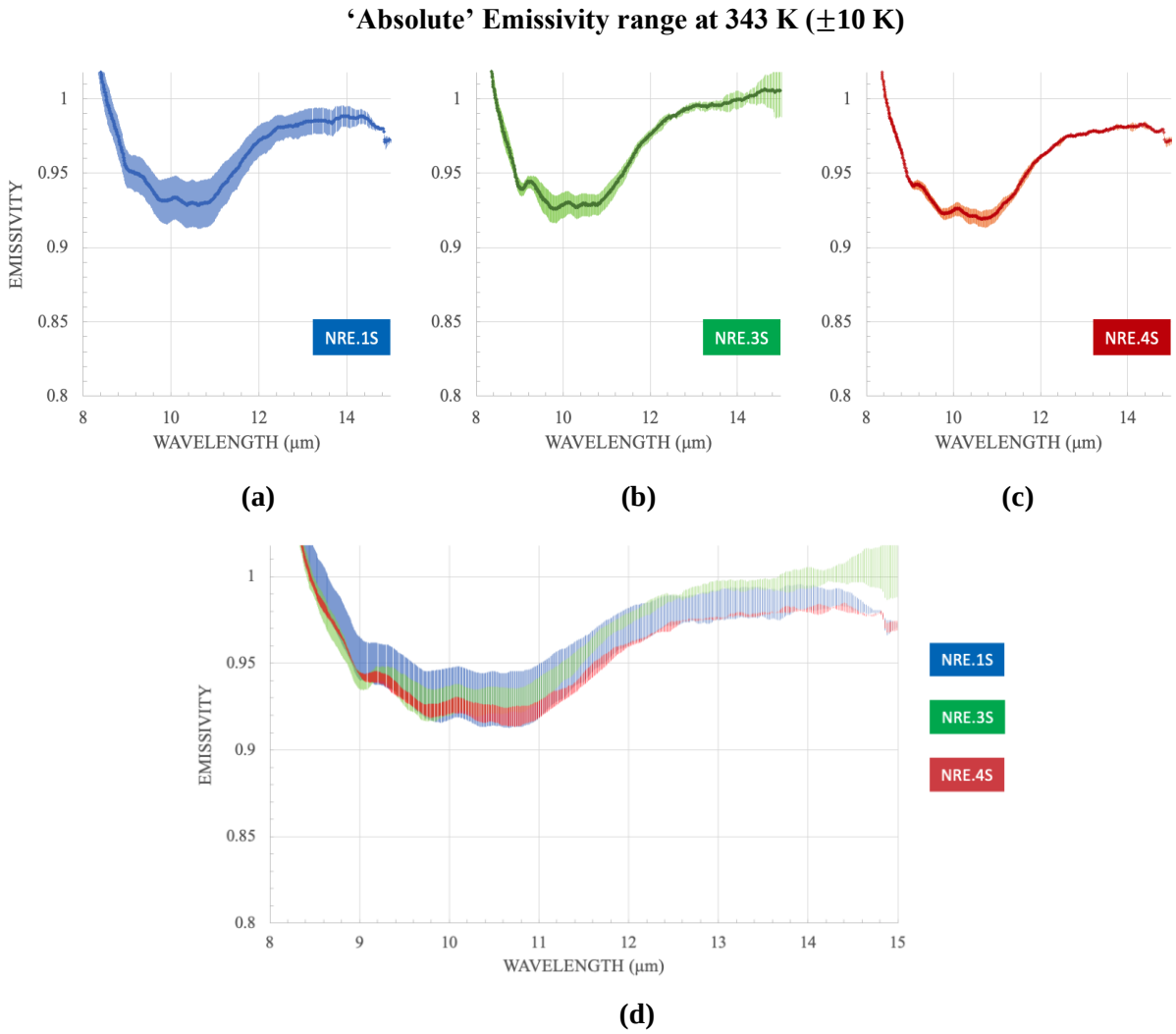

Figure 2.10 'Absolute' emissivity spectral signature range at 343 K (±10 K) for **(a)** NRE.1S (blue) **(b)** NRE.3S (green) and **(c)** NRE.4S (red), whereas **(d)** shows emissivity 'fields' for combined sample series range.

Emissivity results (Fig. 2.10) show a range of emissivity at the same temperature (343 K ± 10 K), which is particularly evident for the NRE.1 sample series. The spectral fields generated by several samples from the same eruption, show differences in emissivity of as large as 0.07.

The maximum difference in emissivity at any wavelength between the NRE.1S series samples was ≤0.07; ≤0.04 for NRE.3S and ≤ 0.03 for NRE.4S.

This difference (range) in results may be due to the samples' temperature stability issue during measurement, detailed in the experimental set up. An error of ± 10 K was allocated to account for this temperature instability. Nonetheless, the three-eruption series produced results with inconsistent emissivity values and considerable difference (uncertainty).

Previous research suggests that the emission maximum, the so-called 'Christiansen feature', should be located at ~8.5 μm (Hamilton et al., 2001) but due to either instrumental or calibration reasons, all samples at wavelengths less than 8.4 μm and more than 8.0 μm plot well above the expected emissivity maximum (i.e., 1.0), hence this feature could not be identified. These findings may affect the reliability of the results at 343 K.

2.3.4 Emissivity from radiance data 400-900 K

The spectral signatures for samples analysed using thermal emission analysis at 400 K (Fig. 2.11) display 'absolute' emissivity values consistent with the preliminary reflectance data (Fig. 2.7) in the TIR region (8.0–15.0 μm), with a significantly improved signal-to-noise (STN) ratio and optimal difference range (≤0.015) for the same series samples.

In contrast to 294 K and 343 K data (Figs. 2.7 and 2.10), results for 400-900 K (Fig. 2.11) show a steady decrease in emissivity with every temperature increase step (400–900 K), with more significant change in emissivity 700-900 K.

'Absolute' Emissivity variation at high temperature (400-900 K)

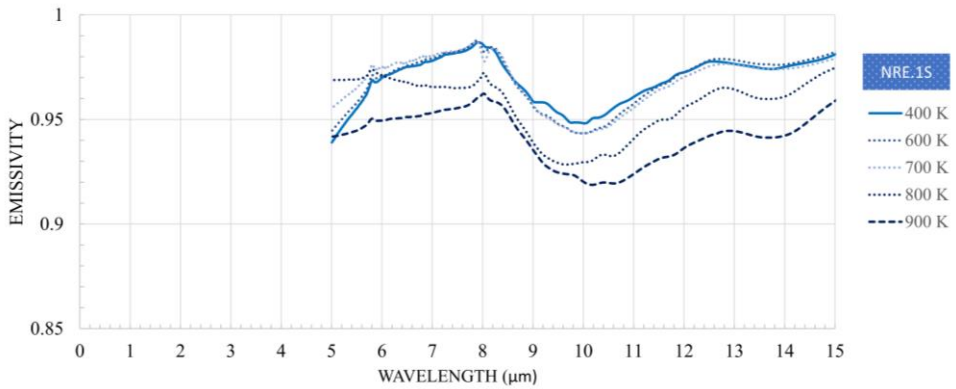

(a)

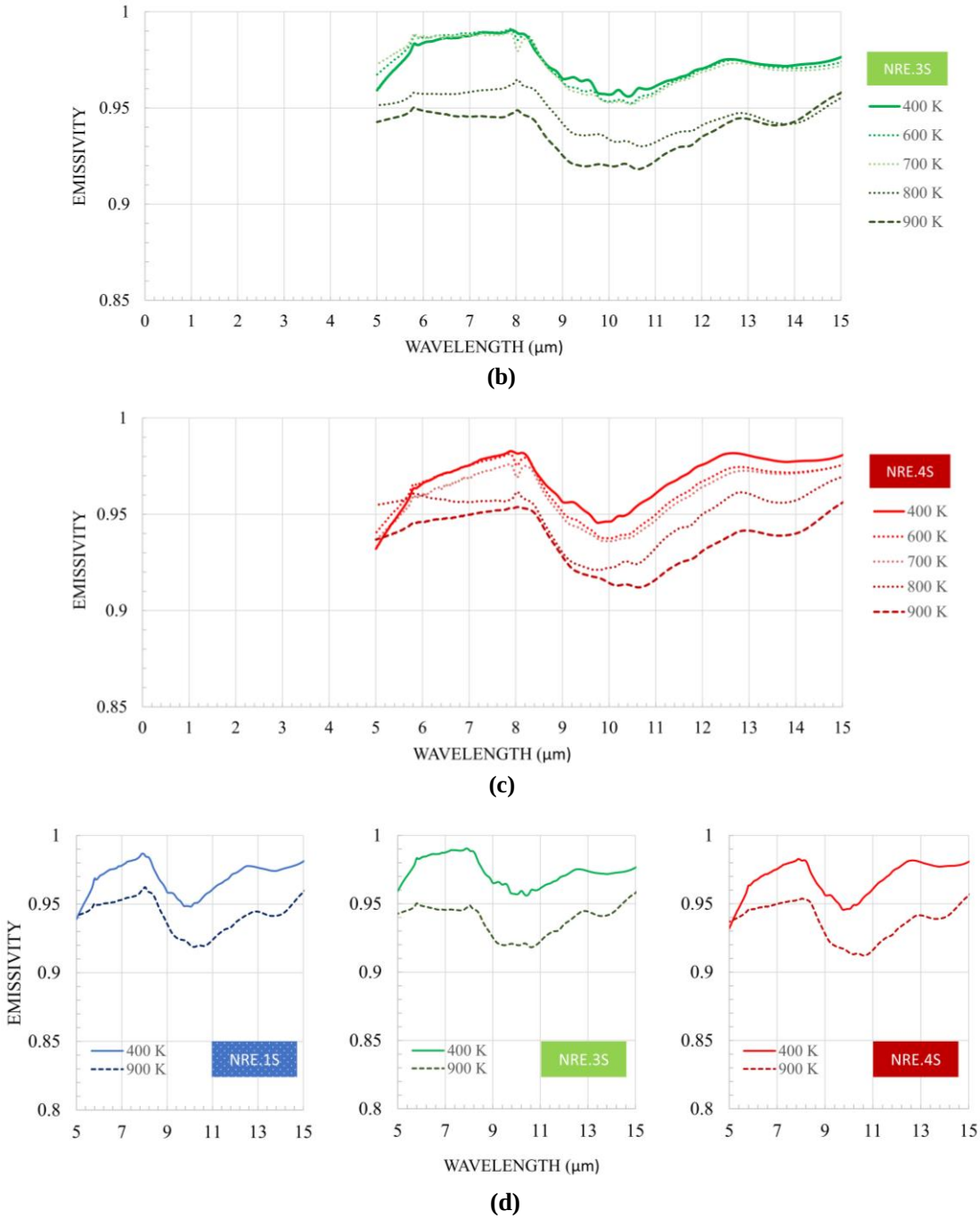

Figure 2.11 'Absolute' emissivity results at high temperature (400-900 K) for **(a)** NRE.1S (blue), **(b)** NRE.3S (green) and **(c)** NRE.4S at 5.0-15.0 μm and **(d)** emissivity difference with temperature change at 400 K (solid lines) and 900 K (dashed lines), the highest achieved temperature by the instrument.

However, this trend could not be observed between 5.0–6.0 μm. This is attributed to the instrument sensitivity limitations in that region and for this reason, the results in TIR wavelengths (8.0–15.0 μm) appear to be stable enough. An additional 'cooling test' was performed by measuring the emissivity of the same series in the opposite direction (cooling), by decreasing temperature steps (i.e., 900–400 K), maintaining consistent sample conditions. The variation in emissivity values during the temperature increase (heating-up), shown in

Figure 2.11 and same sample deviance for the temperature decrease (cooling-down) was ≤0.02 at all wavelengths (8.0-15.0 μm) and temperatures, with no hysteresis deviation trend(s) in either direction.

2.3.5 Emissivity from radiance data 773-1373 K

Hyperspectral emissivity derived for Etnean trachy-basaltic samples at the highest variety of sample temperatures and wavelengths using thermal emission FTIR spectroscopy show significantly more complete trends for emissivity's behaviour with temperature. Generally, the emissivity increased as the sample temperature decreased (cooling) and a glassy crust formed. The greatest and smallest increase in average emissivity were observed in MIR region (~30 %) and TIR region (~8 %), respectively, with the upper SWIR region having an increase of 15%.

Spectral signatures (Fig. 2.12) are consistent and relatively comparable with previous laboratory-based research of basaltic rocks (Hamilton et al., 2001) in TIR and low temperature. However, my new findings involve additional very-high temperatures and data in lower wavelengths (2.17-8.0 μm) that are not available in the literature and demonstrate that emissivity depends not only on wavelength, but also on temperature.

Observed trends in the upper SWIR (2.17–2.5 μm) and MIR (3.0–5.50 μm) show a marked difference and more complex spectral shapes (i.e., lower emissivity and different signature) from preliminary ambient temperature spectral signatures, obtained using the reflectance data approach (Fig. 2.7). This marked variation may be attributed to the instrument's sensitivity, where the very-high temperature instrument reveals exceptionally detailed trends, not observed in previous analyses performed in this thesis at shorter wavelengths of the electromagnetic spectrum.

Basalts generally have a SiO_2 content of 45-52 % and hence have spectra that are dominated by absorption features associated with SiO_2 bonds (vibrations and bending) (Lee et al., 2013, 2010). The strong absorption feature at ~4.0 μm is a result of silica overtone vibrations with the smaller feature at ~7.5 μm associated with *Al-O* bond vibrations. The main *Si-O-Si* bond vibration and bending results in the broad absorption feature between 8.0 and 12 μm. The increase in emissivity observed during cooling and crustal formation of these samples is a consequence of the decrease in SiO_2 bond vibrational and bending energy, reducing energy absorption by the sample (Lee et al., 2013, 2010).

'Absolute' Emissivity variation at very-high temperature (773-1373 K)

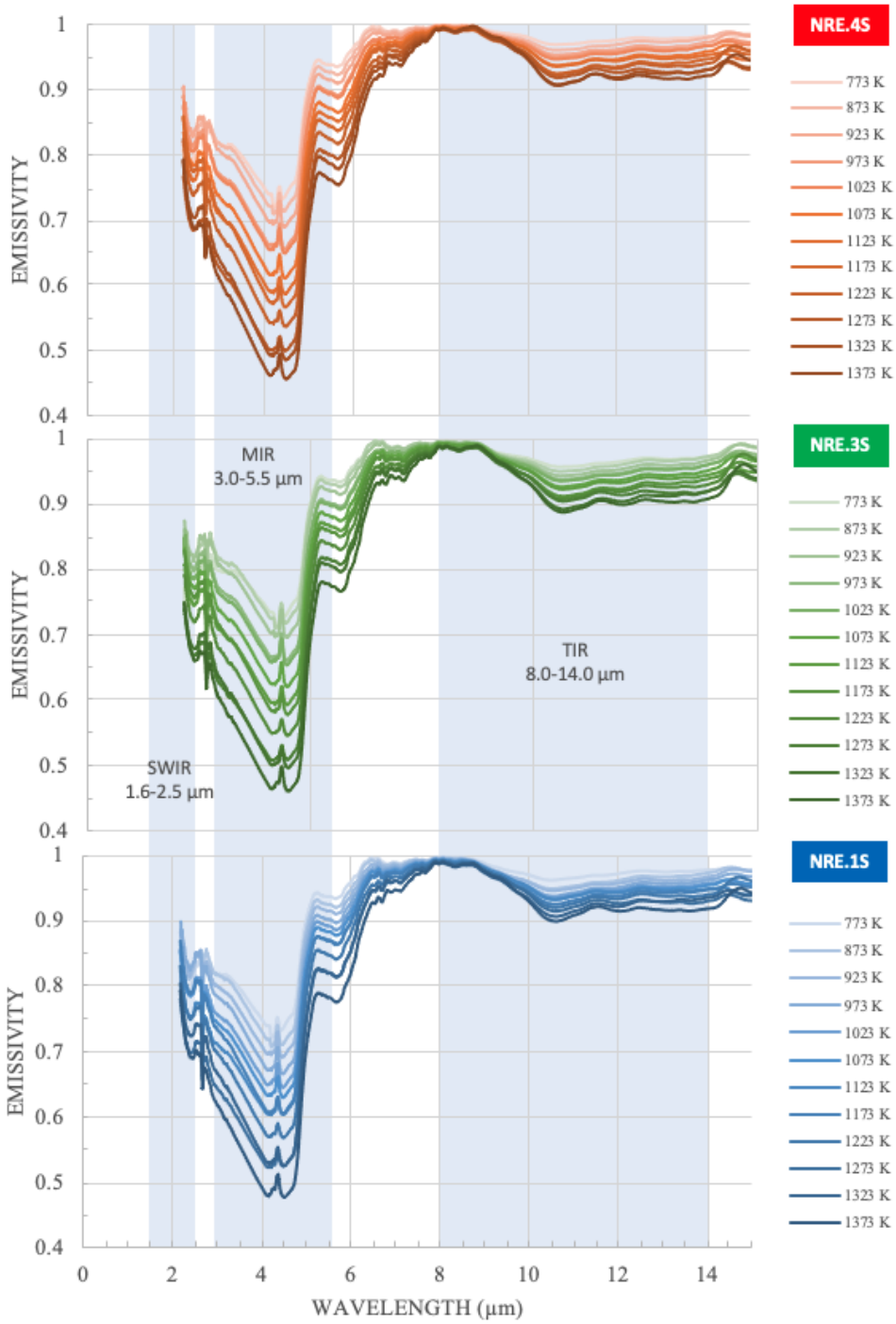

Figure 2.12 'Absolute' emissivity spectral signatures 773-1373 K for **(a)** NRE.4S (red) **(b)** NRE.3S (green) and **(c)** NRE.1S (blue). Data measured in upper SWIR (2.17-2.50 µm), MIR (3.0-5.50 µm) and TIR (8.0-14.0 µm) atmospheric windows, relevant for spaceborne applications are highlighted in grey.

2.3.6 Satellite data validation using laboratory measured emissivity

In this sub-section, the extracted ASTER GED spaceborne emissivity data for the eruptions investigated here (Fig. 2.6) and laboratory FTIR results (Figs. 2.7, 2.10, 2.11 &

2.12) of the same target area for all sample series are compared at ASTER TIR operating central-wavelength bands (8.30 µm, 8.65 µm, 9.10 µm, 10.60 µm, and 11.30 µm).

A comparable trend can be observed in 'apparent' emissivity (Fig. 2.13), for NRE.3S and NRE.4S exhibiting the best data fit at 9.10 µm (≤0.01) and data difference of ≤0.02 at other wavelengths. The NRE.1S FTIR data have larger data difference (≤0.04) when compared to ASTER GED. This is to be expected, since ASTER GED data were created from all available ASTER data between 2000 and 2008.

FTIR (1-*R*) results at 294 K and ASTER GED emissivity comparison

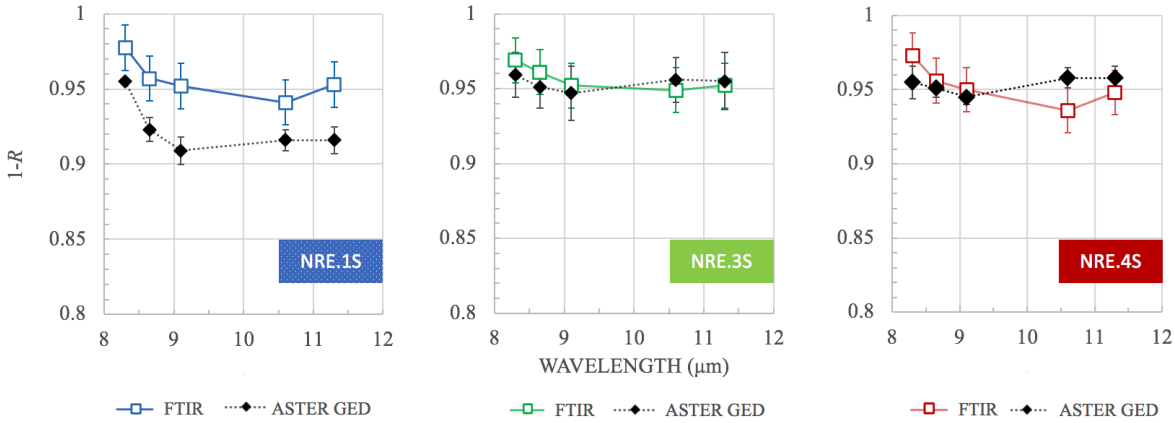

Figure 2.13 Comparison of reflectance FTIR derived 'apparent' emissivity results at 294 K (empty squares) with the spaceborne ASTER GED emissivity results for the same target area (black diamonds). A direct data comparison was made at five ASTER TIR bands.

FTIR results at 343 K and ASTER GED emissivity comparison

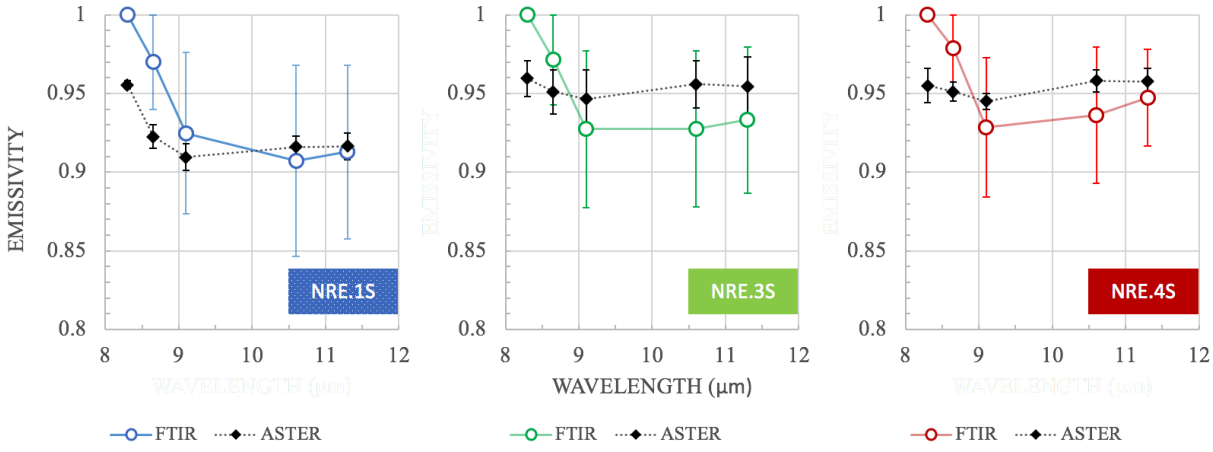

Figure 2.14 Comparison of FTIR derived 'absolute' emissivity results at 343 K (empty circles) with the spaceborne ASTER GED emissivity results for the same target area (black diamonds). A direct data comparison was made at five ASTER TIR bands. Error bars show data range for all samples analysed.

This means that NRE.3S and NRE.4S samples, representing the 2001 and 2002-2003 eruptions would be included in ASTER (9-year) dataset but the 2017 eruption would not. The emissivity recorded by ASTER at pixel locations of the NRE.1S targets, which was acquired prior to the 2017 eruption (ASTER data spans 2000-2008), does not show the target measured here, but it shows average emissivities of underlying rock before the 2017 eruption occurred. This is not the case for emissivity of NRE.3S and NRE.1S samples, which show reasonable similarities with ASTER data of the same target measured. The age of the surface that the 2017 lava was emplaced onto (recorded by ASTER GED for NRE.1S sample's locations) could not be verified with confidence.

The RS (ASTER GED) and 'ground-truth' (laboratory-based FTIR analyses) emissivities correspond reasonably well with the results from reflectance at 294 K, and emission at 343 K and 400 K (Figs. 2.13, 2.14 and 2.15a). It is evident that the emissivity at these (low) temperatures and spaceborne data appear to provide constant ('static') emissivity values, which may be related to the solidified (cooled) lava.

(a)

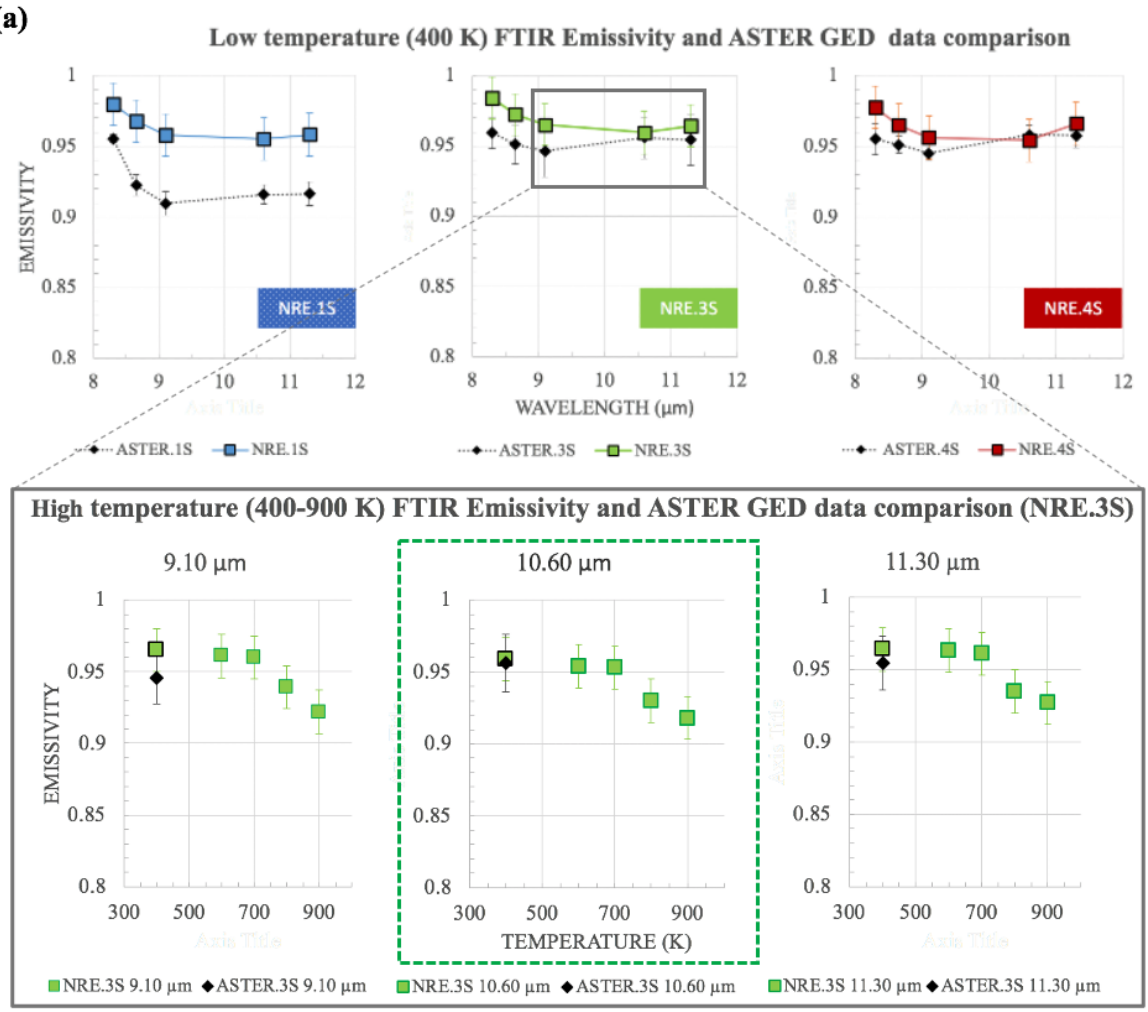

(b)

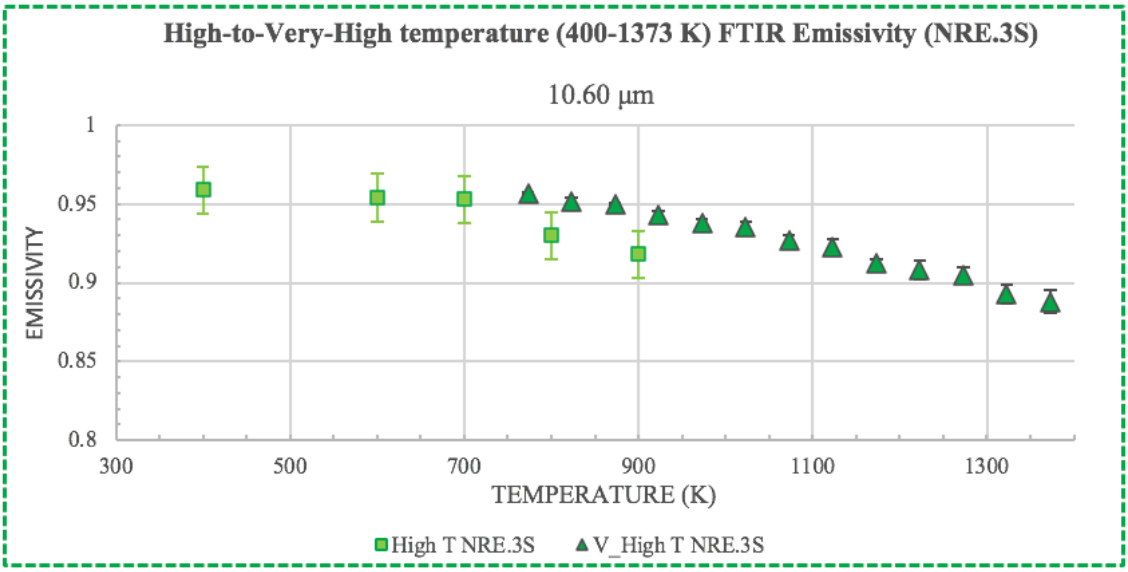

(c)

Figure 2.15 Comparison of FTIR derived 'absolute' emissivity results at (a) 400 K (filled squares) with the spaceborne ASTER GED emissivity results for the same target area (black diamonds). A direct comparison was made at five ASTER TIR bands. **(b)** FTIR measured emissivity 400-900 K comparison for NRE.3S (filled green squares) is shown with ASTER GED emissivity data (filled black diamonds) for the same target area at upper ASTER TIR bands (9.10, 10.60 and 11.30 µm). Whereas **(c)** is an example of emissivity temperature trends for NRE.3S at 400-900 K (filled green squares) and 773-1373 K (filled green triangles) at ASTER 10.60 µm band. Data uncertainty for each method is indicated by error bars.

However, Figures 2.15 b and c show that when thermal component is considered (i.e., temperature) emissivity increases at every measured temperature decrease (cooling), both 900-400 K and 1373-773 K measurement, demonstrating that emissivity is temperature dependent.

These findings are consistent with several thermal emission studies of silicate glasses and basaltic lavas, suggesting that the emissivity of molten material may be significantly lower than that of the same material in a solid state (Thompson and Ramsey, 2020; Lee et al., 2013).

Equally, the high-temperature thermal anomaly observed on Mt Etna for example, has an extrusion temperature of ~1350 K, so there is a need to account for changes in emissivity with temperature, as it is apparent from data above 900 K (Fig. 2.15 c) that emissivity increases further with continued temperature decrease (cooling). Therefore, based on the key findings (Table 2.3), only one approach, emissivity determined by means of radiance (Sections 2.2.5 and 2.3.5) can provide emissivity information at appropriate range of temperatures (773-1373 K) and wavelengths (2.17-15.0 µm) that may be stable enough for spaceborne and modelling applications.

Table 2.3 Summary of key results for various techniques used to measure emissivity

Technique	Section #	*Temp. (K)	Wavelength (μm)	Key Results	Comments
Spaceborne ASTER GED	2.2.1 2.3.1	-	8.30, 8.65, 9.10, 10.60 11.30	wavelength dependency evident	Single (’static‘) emissivity for 100 m pixel in TIR with no temperature component
Laboratory-based FTIR (reflectance)	2.2.2 2.3.2	294	0.66-16.0	wavelength dependency evident	Emissivity at full range of wavelengths but only at ambient temperature (’static‘)
Laboratory-based FTIR (radiance)	2.2.3 2.3.3	343	8.0-15.0	wavelength dependency evident	Emissivity inconsistent (error ≥0.07), poor temperature stability
Laboratory-based FTIR (radiance)	2.2.4 2.3.4	400-900	5.0-16.0	wavelength and temperature dependency evident	Data in TIR only, as 5.0-8.0 μm data unstable. Highest temperature not sufficient to assess eruptive temperatures
Laboratory-based FTIR (radiance)	2.2.5 2.3.5	773-1373	2.17-25.0	wavelength and temperature dependency evident	Data in upper SWIR, MIR and TIR and full range of temperatures found in an active lava flow (including eruptive temperature)

*Temperature in Kelvin (K)

2.4 Discussion and conclusions

The apparent land surface temperature derivation and the estimation of eruption rates from spaceborne data rely on accurate input parameters of lava flow emissivity. The majority of research on emissivity to date has been carried out on solid lava at ambient temperatures (Harris, 2013a), and it is anticipated that under certain conditions, target radiation emission in the TIR region of the electromagnetic spectrum is inversely proportional to its reflectance (Rolim et al., 2016). However, there are several drawbacks in using reflectance to derive emissivity values, as the temperature of the sample is not taken into account, and its spatial variation is not recorded. Nonetheless, ‘apparent’ emissivity data, calculated via Kirchhoff’s Law from laboratory-based reflectivity data has been used to provide a first approximation of emissivity estimate in the absence of ‘absolute’ emissivity information (Harris, 2013c).

Most geologic studies that used reflectance and/or emission FTIR methods have focussed on crystalline minerals, as they have unique and identifiable spectral features (Lee et al., 2010) and have been used to determine compositional (Hamilton et al., 2001; Hamilton and Christensen, 2000) and other physical properties (Wright and Ramsey, 2006; Michael S. Ramsey and Fink, 1999; Walter and Salisbury, 1989; Salisbury and Eastes, 1985).

It has been recognized that a wide range of geologic characteristics may influence identification and interpretation of reflectance and emission spectra of rocks, such as

variations in particle size, chemical composition and surface roughness, among many others (Osterloo et al., 2012). Therefore, spectral shape and depth presented here may be affected by one (or more) of these parameters, as well as range of methodologies used, which implicates an array of distinctive instrumental sensitivities and limitations.

The 'apparent' emissivity spectral signatures, derived from reflectance data at ambient temperature are generally comparable to those of 343 K and 400 K emission FTIR data, as well as ASTER GED data. The difference in emissivity of ≤0.03 at all TIR wavelengths considered here, is broadly consistent with previous research on basaltic rock spectral signatures (Hamilton et al., 2001) in TIR at low temperatures. A certain amount of spectral contrast is observed between 'particulate' and solid sample specimens for 343 K results and can be attributed to the instrument's sensitivity and/or the methodology used. This has been acknowledged in previous research (Sabol et al., 2009), suggesting the likely cause to be a result of the surface roughness (Danilina et al., 2009) and/or particle size and texture (Kirkland et al., 2003). It has also been recognised that absolute emissivity minima of roughened surface can be lower, with greater spectral contrast than that of the same sample in a particulate form (Osterloo et al., 2012). This spectral contrast trend has been interpreted as a decrease in scattering efficiency due to particle size, as well as porosity. Nonetheless, the results at 343 K produced a range of emissivity values with a difference of up to 0.07, which can be attributed to the samples' temperature stability issues. Therefore, the results for 343 K may be considered inadequate to be included in further analyses to produce accurate input parameters for spaceborne and/or modelling application.

The reflectance and emission FTIR results at ambient/low temperature, as well as ASTER GED data, correspond well for the same target area, with an exception of NRE.1S target (2017 Mt Etna eruption), since it occurred outside the range of ASTER GED measurement database (2000-2008). Nonetheless, the remaining sample series show good correlation at specific TIR wavelengths by exhibiting an emissivity difference of ≤0.03. However, this emissivity information is 'static', relating to the solidified (cooled) surface, not reflecting the range of temperatures involved in an active lava flow or the emissivity-temperature trends seen in high or very-high temperature FTIR results above 700 K.

The results from high and very-high temperature data suggest that it is essential to expand this study to assess the role and significance of emissivity, not only as a 'static' and uniform value across all wavelengths and temperatures, but also taking its response to thermal gradient and the emissivity-temperature link into account. This will determine the emissivity variation with temperature change, uncertainties and errors that may be

introduced relating to emissivity as an input parameter and will provoke further investigation into the role and impact of emissivity in lava flow dynamic modelling and hazard mitigation, using spaceborne data.

In order to make the emissivity a standard input parameter and develop a procedure for both spaceborne and modelling applications involving Mt Etna, 773-1373 K data is used in further analyses, as it appears to be most complete. It also covers the appropriate temperature and wavelength range used in RS. Therefore, 773-1373 K data were considered to be the most complete and sufficiently stable to support the development of ‘dynamic emissivity-temperature’ trends, ‘rules’ and ‘look-up’ tables for advanced monitoring applications (Chapters 3-5).

3 Spaceborne approach to energy fluxes

Much of the material discussed in this chapter has been published in the papers by Rogic et al. (2019a) and Rogic et al. (2019b), which are reproduced in full as Appendices G and H.

How eruptive behaviour varies temporally and spatially can be monitored and quantified, using the enormous amount of spaceborne data freely available today. There is wide variety in local practices used for volcano surveillance (Cigna et al., 2020; Ramsey and Harris, 2013a; Sparks et al., 2011), and only a small fraction of potentially active subaerial volcanoes worldwide are monitored with any quality, frequency, or timeliness (Sigurdsson et al., 2015; Tait and Ferrucci, 2013). The lack of monitoring poses an objective and significant threat to communities (Brown et al., 2015; Komorowski et al., 2013), especially in countries lacking in infrastructure and with limited financial resources (Pallister et al., 2019), creating a critical gap in hazard assessment and risk management (Hill et al., 2011).

Satellites offer cost effective global volcano surveillance at a wide range of spatial and temporal resolutions (Corradino et al., 2019; Ganci et al., 2019; Cappello et al., 2018; Ferrucci and Hirn, 2016). They can be used to contribute significantly to operational eruption forecasting and hazard assessment (Bilotta et al., 2016; Del Negro et al., 2016; Cappello et al., 2015b, 2015a; Negro et al., 2013).

Spaceborne TIR bands have been used widely for decades to monitor high-temperature thermally anomalous volcanic phenomena on the ground (Solikhin et al., 2012; Ramsey and Dehn, 2004; Glaze et al., 1989) and had proven valuable for identifying volcanic activity trends (Harris, 2013a; Murphy et al., 2013; Wright et al., 2004; Wooster and Rothery, 1997; Oppenheimer, 1993), and volcano monitoring (Hirn et al., 2008; Di Bello et al., 2004; Wright et al., 2004, 2002; Higgins and Harris, 1997). The TIR bands are particularly sensitive to surface temperatures of 320-350 K. As for molten lava temperatures (>900 K), which may be more significant when observing high-temperature thermal anomalies on the ground, data from lower MIR and upper SWIR would be more appropriate (Harris, 2013a; Hirn et al., 2008b). This approach is explored further in this study, using high-to-moderate spatial resolution data (Chapters 3 and 4).

To accurately compute the emissions of energy actually leaving surface, the radiant signal must also be corrected for the influence of the atmospheric transfer function (Barsi et al., 2005, 2003) and the emissivity of the radiating surface (Harris, 2013a). As characterised previously (Chapter 1), emissivity is defined as the ratio of the radiation emittance of a

surface to that of a same temperature blackbody. This parameter is not well quantified for molten materials and hot volcanic rocks, and the majority of authors adopt a constant value based on the rare published laboratory measurements and/or the TIR emissivity-temperature separation method (Sobrino et al., 2008), underlying the Advanced Spaceborne Thermal Emission and Reflection Radiometer Global Emissivity Database (ASTER GED)(Hulley et al., 2015), among others.

However, several recent thermal emission studies of silicate glasses and basaltic lavas (Thompson and Ramsey, 2020; Ramsey et al., 2019; Lee et al., 2013) suggest that the emissivity of molten material is significantly lower than that of the same material in its solid state.

Extensive laboratory measured emissivity analyses at very-high temperature presented in this thesis (Chapter 2) validate the argument that the emissivity of molten material is lower than that of the same material in its solid state. They also provide quantitative evidence that emissivity is not only wavelength dependent but can also be significantly temperature dependent, leading us to revisit its effect on experimental estimate of radiant heat fluxes. By applying multicomponent emissivity approach to modelling radiant heat flux, the uncertainty associated with ascribing a constant 'representative' emissivity can be established and quantified.

3.1 Spaceborne measured Emissivity

As established, emissivity of a target analysed can be extracted from existing global spaceborne libraries, such as ASTER GED (Hulley et al., 2015), or the NASA's LP DAAC, MODIS Land Surface Temperature and Emissivity Product (LP DAAC).

These libraries may only represent a 'static' mean emissivity value (Chapter 2). For example, the ASTER GED 100-meter pixel value is a nine-year average (2000-2008) and/or a larger (1000×1000 m) MODIS pixel would integrate values outside (background) the dimensions of the target investigated (i.e., lava flow), due its spatial resolution. These constant emissivity values, if applied uniformly, independent of the pixel size (i.e., independent of the nominal scale of observations) will produce variations in computed apparent surface temperatures and would not account for the range of temperatures (then, of emissivities) found in an active lava flow.

In addition to spectral libraries, emissivity (and kinetic temperature) can be derived using the temperature emissivity separation (TES) method, developed for ASTER data (Sabol et al., 2009; Gillespie et al., 1998). However, a recent study aiming to quantify uncertainty of remotely acquired TIR data (Thompson and Ramsey, 2020) argued that a

more appropriate minimum emissivity for molten basaltic surface should be 0.66 rather than the higher (1.0-0.95), often used in previous studies (Harris et al., 2010, 2005). Therefore, the computation of surface temperature from spaceborne data and models that rely on temperatures to track cooling with time, introduce errors due to uncertainty in emissivity as an input parameter. The need to quantify the role of emissivity-temperature relationship was illustrated using 'distance-to-run' simulations for the 2001 Mt Etna eruption (Rogic et al., 2019a). One of the limited number of studies investigating emissivity-temperature behaviour used thermo-rheological models to forecast lava flow emplacement (Ramsey et al., 2019), assumed the fraction of molten lava to cooled crust by using 'two-components' emissivity. The study made inference that the emissivity of molten lava could be as low as 0.60, while an emissivity of 0.95 corresponded to the computed, crusted fraction of the lava. A more sophisticated multicomponent approach, developed in this thesis, applies measured emissivity-temperature trends, using 'thresholding' approach (detailed in Section 3.2), to support computation of radiant heat fluxes from spaceborne data, acquired during the 2017 effusive event on Mt Etna (this chapter).

3.2 Methods

For this analysis, two platforms were selected (Tables 3.1 and 3.2), hosting decametric resolution sensors operating at the time of the eruption: the Landsat-8 (Landsat Continuity Mission), launched by National Aeronautics and Space Administration (NASA) in April 2013 (USGS, 2019; World Metheorological Organisation, n.d.), and the Copernicus MSI for Sentinel-2, launched by the European Space Agency (ESA) in June 2015 (WMO, n.d.).

Table 3.1 Characteristics of the Landsat-8 (OLI and TIRS) instrument

Instrument	Band	Spectral Range [μm]	Spatial resolution [m]
OLI	1	0.43-0.45	30
	2	0.45-0.51	30
	3	0.53-0.59	30
	4	0.64-0.67	30
	5	0.85-0.88	30
	6	1.57-1.65	30
	7	2.11-2.29	30
	8	0.50-0.68	15
	9	1.36-1.38	30
TIRS	10	10.60-11.19	100
	11	11.50-12.51	100

Placed on a sun-synchronous orbit at 705 km altitude, Landsat-8 hosts two payloads, the Operational Land Imager (OLI) and the Thermal Infrared Sensor (TIRS), with the overall capability of collecting data in 11 spectral bands (0.44-12.00 μm). They have 30 m to 100 m spatial resolution global coverage (15 m panchromatic channel 8), and equatorial repeat cycle of 16 days, using a pushbroom technology with a swath of 180 km. It's spectral response range in wavelengths (NIR and SWIR) relevant to this study is shown in Figure 3.1.

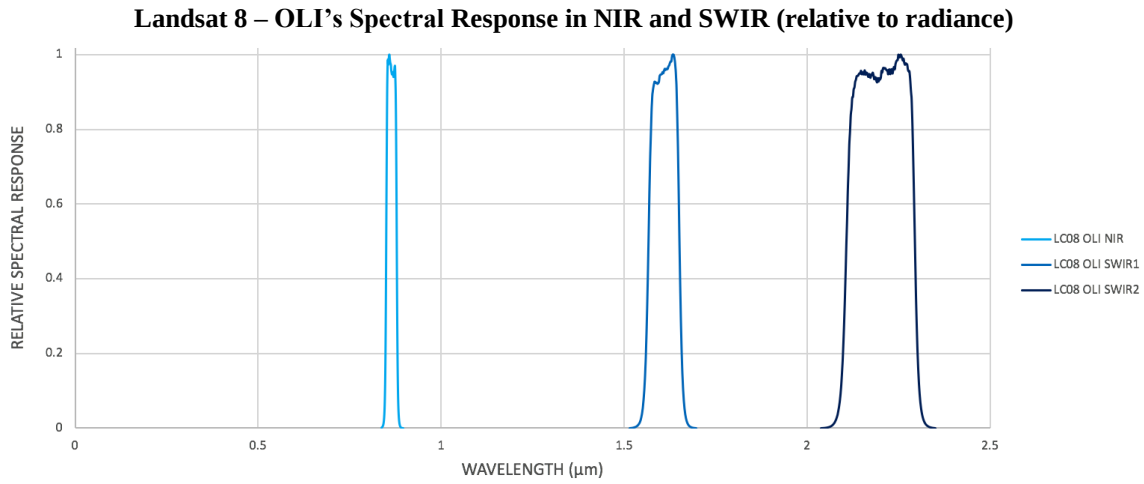

Figure 3.1 Landsat 8 – OLI's spectral response in NIR (0.85-0.88 μm) and SWIR (1.57-1.65 μm and 2.11-2.29 μm respectively).

Copernicus, the European Commission's (EC) Earth Observation Program launched the Sentinel-2A and Sentinel-2B satellites in 2015 and 2017, respectively. The Copernicus program, formerly called the Global Monitoring for Environment and Security (GMES), started in 1998 with the overarching aim to become Europe's operational Earth Observation monitoring system providing data and information services. An essential part of the program is the space component, which is managed by the ESA, responsible for the Copernicus Sentinel Satellite Constellations. One of them, the Copernicus Sentinel-2 optical mission (S2) systematically collects multispectral land surface imagery from two satellites with a revisit cycle of 5 days at 10 m, 20 m and 60 m spectral resolutions (Table 3.2). Their single instrument is the MSI that collects data in 13 spectral bands, using a pushbroom technology with a swath of 290 km. It's spectral response range in wavelengths relevant to this study is shown in Figure 3.2.

Table 3.2 Characteristics of the MSI (Sentinel-2A) instrument

Instrument	Band	Central wavelength [μm]	Spatial resolution [m]
MSI Sentinel 2A	1	0.443	60
	2	0.490	10
	3	0.560	10
	4	0.665	10
	5	0.705	20
	6	0.740	20
	7	0.783	20
	8	0.842	10
	8A	0.865	20
	9	0.945	60
	10	1.375	60
	11	1.610	20
	12	2.190	20

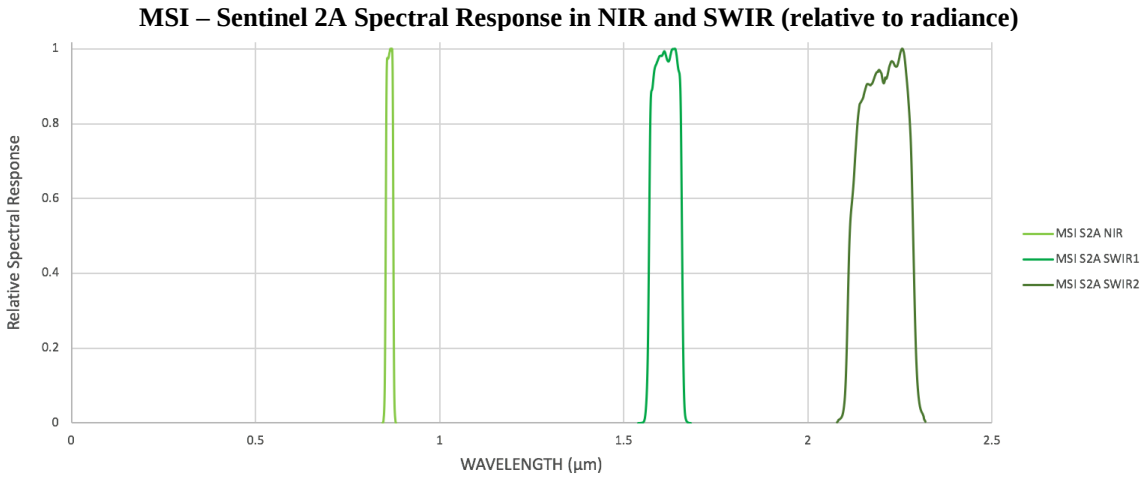

Figure 3.2 MSI for Sentinel 2A spectral response in NIR (0.85-0.88 μm) and SWIR (1.53-1.68 μm and 2.08-2.32 μm respectively).

Here, the specific, approach described in (Hirn et al., 2008b) was used, which is a systematized variant of the sub-resolution approaches (Dozier, 1981; Matson and Dozier, 1981), and their application to high-temperature volcanic features (Blackett, 2014; Oppenheimer, 1993; Rothery et al., 1988). This approach allows the relative size and temperature of these thermal components to be resolved, following solutions, which depend on data availability (saturation) in each band (Harris, 2013e, 2013d). The mean spectral radiance measured by a satellite sensor as a digital number (DN) is converted into 'at-satellite' spectral radiance R_λ (detailed in Chapter 1). It has been established that in the

SWIR region (1.5 and 2.5 μm) upwelling path radiance ($R_{\lambda,U}$) contribution is low (Harris, 2013a), whereas the surface reflected radiation $\left(R_{\lambda,D}\right)$ can be estimated by subtracting the mean spectral radiance (R_{λ}) value of surrounding, clearly non-volcanic background pixels ($\mathrm{bg}_{(\mathrm{band})}$) from the thermally anomalous pixels (Blackett, 2017, 2014). Therefore, for example, only pixels with radiance greater than $(3\times \mathrm{bg}_{7})+ \mathrm{bg}_{7}$ for OLI's SWIR Band 7 were extracted as thermally anomalous, within the region of interest. Same approach is applied to both SWIR OLI's bands (Band 6 and Band 7) and Sentinel-2A (Band 11 and Band 12). The background radiance values are also manually validated to ensure that pixels chosen for this purpose did not include the cooler volcanic plume and were truly representing the background. The total radiant heat fluxes (Q_{r_calc} in W), associated with the thermally anomalous pixels isolated were computed using the Stephan Boltzmann Equation (Eq. 10). Night-time images, not available in this study for the 2017 Etna eruption, would be preferable, as they contain only the thermal component. It is important to note that MSI has no capability to acquire data at night, whereas Landsat-8 does.

Here, all available (daytime) images acquired during the 2017 Mt Etna eruption were analysed, distributed by the Global Visualisation (GloVis) Viewer (U.S. Department of the Interior and U.S. Geological Survey, 2005) for Landsat-8, and Copernicus Open Access Hub (ESA, n.d.) for MSI Sentinel-2A to produce the time series of the radiant flux (Q_{r_calc}), retrieved by these two platforms between 16 March and 8 August 2017.

The motivation for the 2017 Mt Etna study is to assess the role of emissivity in the determination of radiant heat fluxes and uncertainty, obtained from multiplatform spaceborne data, using methodological innovation (multicomponent approach) compared to previous methods (Harris, 2013a; Hirn et al., 2008b).

To achieve this, the results from spaceborne data were compared, using three approaches; firstly, by applying a constant emissivity, where an assumed value (e.g., 0.95 or 0.60) is applied to the entire thermal anomaly; and secondly, multicomponent emissivity is used, derived from very-high temperature laboratory FTIR data, in SWIR (Chapter 2). Using different emissivities acknowledges that Etnean trachy-basalts re-emit only a percentage of radiance incident upon them (not unity). This percentage would be denoted by the emissivity term and although previously never proved to be temperature dependent, its behaviour with temperature has been questioned (Flynn et al., 2000).

It has been previously implied that volcanic anomalies are unlikely to entirely fill the 30-m SWIR pixel (e.g., OLI) with a single source at a specific temperature (Flynn et al., 2000), thus, two or more thermal components would likely be present and should be

accounted for. So, after radiometric and atmospheric data correction, procedures outlined in (Ferrucci and Hirn, 2016; Hirn et al., 2008b) and 'dual-band' approaches (Harris, 2013a; Flynn et al., 2001; Oppenheimer, 1993; Glaze et al., 1989; Rothery et al., 1988; Francis and Rothery, 1987; Dozier, 1981), applying modifications related to emissivity as input parameter were employed. Here, radiance data in SWIR (OLI's Bands 6, 7 and Sentinel-2 Bands 11, 12) are linked to an appropriate, measured emissivity value to compute pixel integrated temperature (T_i) for each band, enabling derivation of an effective temperature (T_e) for each radiant pixel of the high-temperature thermal anomaly analysed (Eq. 8). This 'thresholding' approach, detailed in Figure 3.3 (and Appendix D), uses radiant pixels segmentation to link specific radiance range to an appropriate emissivity value to compute pixel integrated temperature (T_i). Considering that emissivity also varies as a function of wavelength, the absence of FTIR data at 1.65 μm (due to instrument limitations) and the close proximity of OLI and Sentinel-2 SWIR bands (1.65 and 2.20 μm), similar behaviour is anticipated based on preliminary reflectance data (Fig. 2.7) and previous research (Flynn et al., 2000).

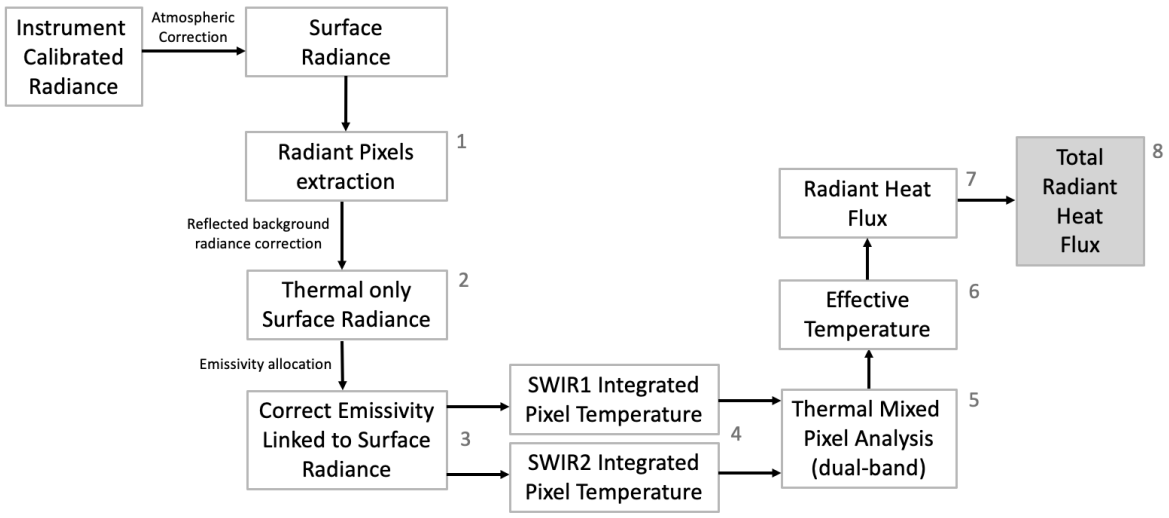

Figure 3.3 A flowchart illustrating the semi-automated (steps 1-8) methods used to derive total radiant heat flux using high-spatial resolution data in two SWIR bands (Appendix D).

Having obtained the Effective Temperature (T_e) for each radiant pixel, the remotely sensed radiant heat flux (Q_{r_calc}) was computed (Eq. 10) (Wright and Pilger, 2008; Pieri et al., 1990).

It is important to note that MSI for Sentinel 2A reflectance data was firstly converted to radiance (IDL code – courtesy of Hirn, personal communication), and the resulting radiance values from SWIR bands 11 (1.61 μm) and 12 (2.19 μm), extracted from thermally

anomalous pixels were exploited to compute total radiant heat flux for each scene analysed using both platforms.

3.3 Results: High-spatial resolution spaceborne data

Varying the emissivity and wavelength has an impact on the computation of pixel integrated temperatures (Eq. 8) and the consequent computation of total radiant heat flux (Eq. 10) of the high-temperature thermal anomaly investigated.

To perform a quantitative evaluation on the impact of emissivity, as an input parameter on computation of total radiant heat flux, seven high-spatial resolution scenes available for the 2017 Mt Etna eruption (Fig. 3.4) were selected and processed, acquired by Landsat 8 (OLI) and MSI (Sentinel 2A) in SWIR (Bands 6, 7, and Bands 11, 12 respectively), between 16 March and 08 April 2017. Panels are in chronological order (from left to right) for Landsat-8 (top panels) and MSI (bottom panels) scenes.

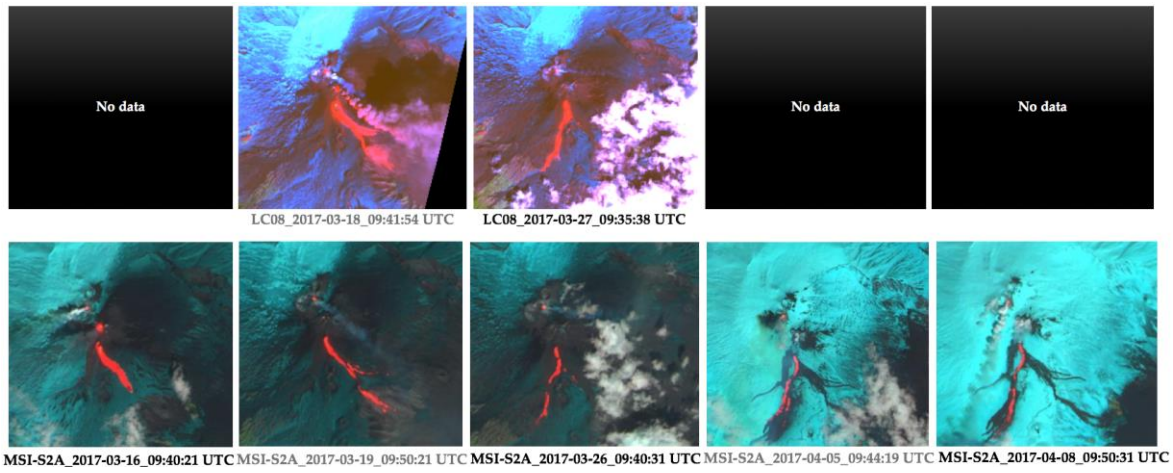

Figure 3.4 (top) Spaceborne scenes acquired by Landsat-8 (18/03/2017 and 27/03/2017) and **(bottom)** scenes acquired by MSI (16/03/2017, 19/03/2017, 26/03/2017, 05/04/2017 and 08/04/2017). Each panel displays an area of approximately 7 km^2.

The isolated thermally anomalous pixels, corresponding to recorded radiances in OLI's and Sentinel-2A SWIR bands (Appendix C) were used to compute total radiant heat flux following the method detailed in Figure 3.3 (and Appendix D).

Figure 3.5 shows emissivity-temperature trends in SWIR, both measured and modelled for NRE.1 sample Series (Chapter 2, Fig. 2.12), relevant for this eruption. Mean emissivity values were extracted for upper SWIR wavelength and averaged over the SWIR spectral response range available (2.17 μm to 2.30 μm), relating to the temperature and radiance. Values reported in Table 3.3 were used as spaceborne data input parameters. These emissivity-temperature modelled values (Fig. 3.5 right and Table 3.3) were applied to both

OLI and Sentinel-2 SWIR bands and used as input values for computation of pixel integrated temperatures, to derive radiant heat flux values for each scene (Table 3.7). Uniform emissivity values (0.95 and 0.60) were applied to all radiant pixels in high-temperature thermal anomalies analysed, while multicomponent emissivity was computed using emissivity-temperature-radiance link values reported in Table 3.3.

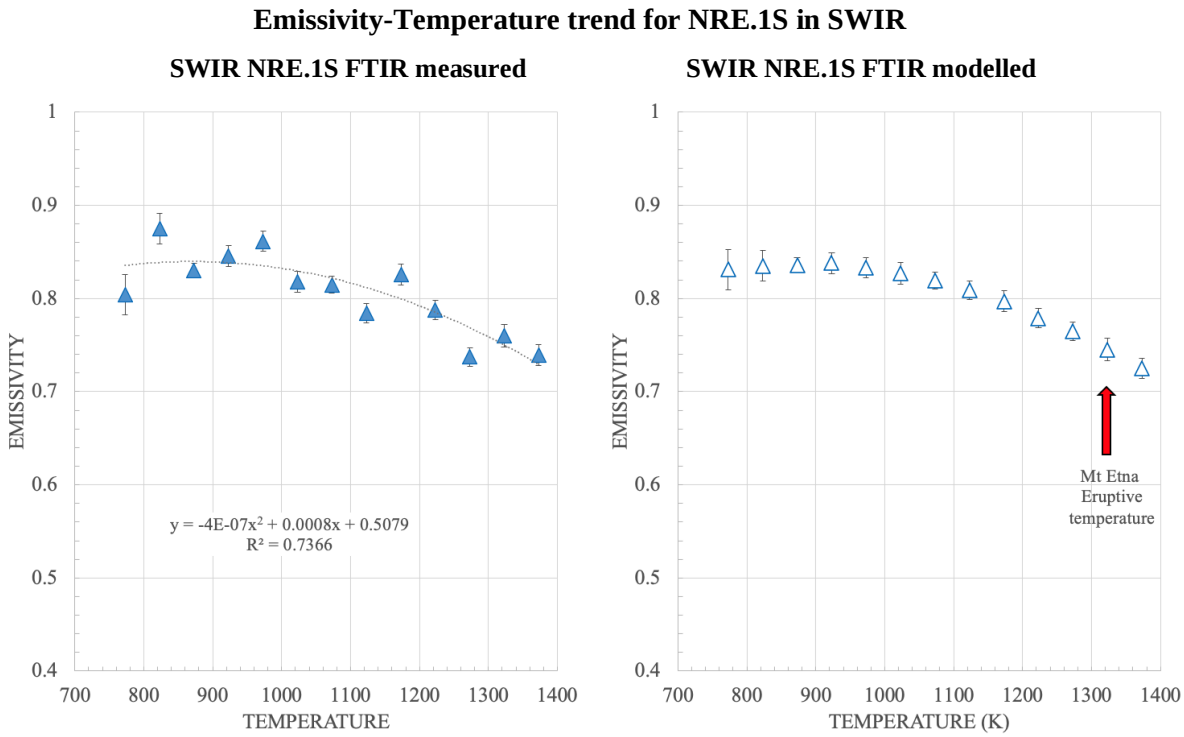

Figure 3.5 SWIR emissivity-temperature trend(s): **(left)** FTIR measured (2.17-2.30 µm and 773-1737 K) and **(right)** modelled data. Same emissivity values shown here are applied to both SWIR bands in computation of total radiant heat flux for each spaceborne scene analysed. Uncertainty is indicated by error bars. The best fit trendline used to model NRE.1S measured data is $y = -4 - 07x^2 + 0.0008x + 0.5079$ and $R^2 = 0.7366$.

Table 3.3 Landsat 8 (OLI) and MSI (Sentinel 2A) measured (ε FTIR) and modelled (ε model) emissivity data at OLI's channels 6 and 7 and Sentinel 2A channels 11 and 12. 'Rad' is predicted satellite measured spectral radiance.

λ (µm)	Mode	*773	823	873	923	973	1023	1073	1123	1173	1223	1273	1323	1373
1.65	εFTIR	0.80	0.87	0.83	0.84	0.86	0.81	0.81	0.78	0.82	0.78	0.73	0.76	0.73
	εmodel	**0.83**	**0.83**	**0.83**	**0.83**	**0.83**	**0.82**	**0.82**	**0.81**	**0.79**	**0.77**	**0.76**	**0.74**	**0.72**
	Error	0.02	0.05	0.01	0.01	0.01	0.01	0.01	0.01	0.01	0.01	0.01	0.01	0.01
	Rad	2.2	4.4	8.1	14.4	23.0	35.3	51.2	71.5	101.7	131.9	162.3	215.8	271.2
2.22	εFTIR	0.80	0.87	0.83	0.84	0.86	0.81	0.81	0.78	0.82	0.78	0.73	0.76	0.73
	εmodel	**0.83**	**0.83**	**0.83**	**0.83**	**0.83**	**0.82**	**0.81**	**0.80**	**0.79**	**0.77**	**0.76**	**0.74**	**0.72**
	Error	0.02	0.05	0.01	0.01	0.01	0.01	0.01	0.01	0.01	0.01	0.01	0.01	0.01
	Rad	4.3	7.6	11.4	17.5	25.4	33.4	44.8	56.3	75.8	90.5	104.4	130.8	151.3

*Temperature in Kelvin (K)

'Rad' is predicted satellite measured radiance

3.3.1 Radiant Heat Flux: Landsat 8 – OLI

Radiance data for both SWIR bands (6 and 7) were extracted for this analysis and appropriate emissivity was allocated (linked) to each radiant pixel, based on its calculated predicted radiance (Table 3.3) using 'thresholding' method, to compute pixel integrated temperatures. Non-thermal radiance marked as Background (bg_7=1.5) is related to daytime image reflectance and was subtracted from recorded radiance data to account for thermal component only. Same Background value was subtracted from SWIR Band 6 (bg_6=1.5).

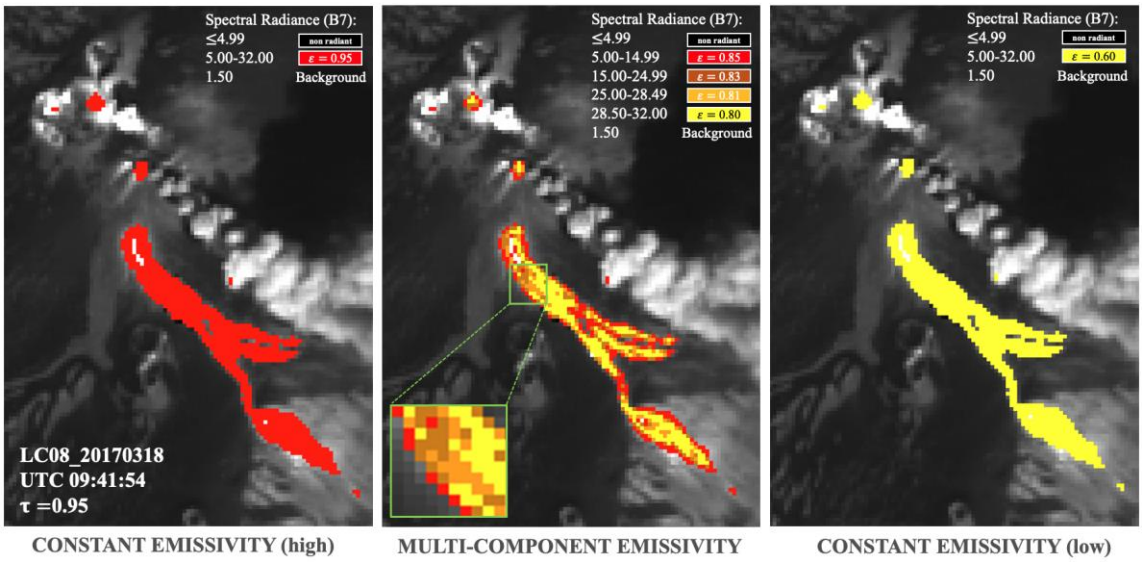

Figure 3.6 Landsat-8 scene (OLI's Band 7) acquired on 18 March 2017, showing all radiant pixels, with recorded spectral radiance (W μm^{-1}), used for computation of total radiant heat flux at constant emissivity **(left)** 0.95 and **(right)** 0.60, as well as the **(centre)** multi-component emissivity approach (dynamic). **Inset (centre):** distribution of radiant pixels within the thermal anomaly analysed, using multicomponent emissivity 'thresholding' approach.

853 radiant pixels extracted from the Landsat-8 scene, acquired on 18 March 2017 (Fig.3.6) were used to compute total radiant heat flux values of 3.02 GW and 3.57 GW for constant emissivity 0.95 and 0.60 respectively. In contrast, computation of total radiant heat flux using multicomponent emissivity, involved automatic allocation of correct emissivity values based on radiance thresholds indicated in Figure 3.6 centre, where emissivity of 0.85 was applied to 352 pixels, 0.83 to 164 pixels, 0.81 to 92 pixels and 0.80 to 245 pixels, producing 3.22 GW.

441 radiant pixels extracted from the Landsat-8 scene, acquired on 27 March 2017 (Fig.3.7) were used to compute total radiant heat flux values of 1.85 GW and 2.18 GW for constant emissivity 0.95 and 0.60 respectively. In contrast, computation of total radiant heat flux using multicomponent emissivity, involved automatic allocation of correct emissivity values based on radiance thresholds indicated in Figure 3.7 centre, where emissivity of 0.85

was applied to 170 pixels, 0.83 to 109 pixels, 0.81 to 48 pixels and 0.80 to 114 pixels, producing 1.95 GW.

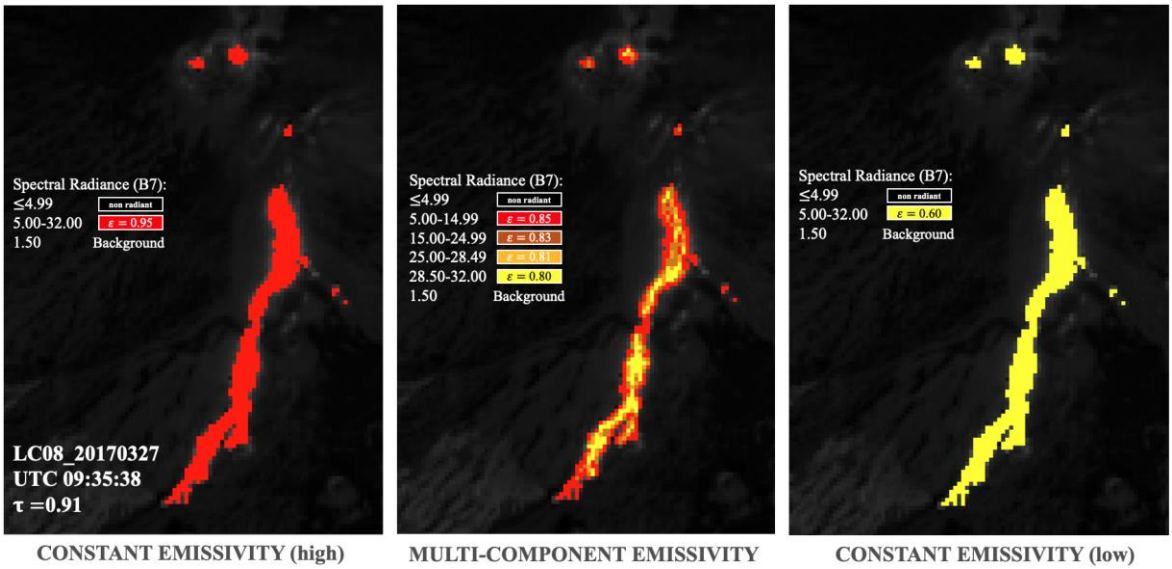

CONSTANT EMISSIVITY (high) MULTI-COMPONENT EMISSIVITY CONSTANT EMISSIVITY (low)

Figure 3.7 Landsat-8 scene (OLI's Band 7) acquired on 27 March 2017, showing all radiant pixels, with recorded spectral radiance (W μm^{-1}), used for computation of total radiant heat flux at constant emissivity **(left)** 0.95 and **(right)** 0.60, as well as the **(centre)** multi-component emissivity approach (dynamic).

3.3.2 Radiant Heat Flux: MSI – Sentinel 2A

Radiance data for both SWIR bands (11 and 12) were extracted for this analysis and appropriate emissivity was allocated (linked) to each radiant pixel, based on its calculated predicted radiance (Table 3.3), using 'thresholding' method, to compute pixel integrated temperatures. Non-thermal radiance marked as Background (bg_{12}=3.5) is related to daytime image reflectance and was subtracted from recorded radiance data to account for thermal component only. Same Background value was subtracted from SWIR Band 11 (bg_{11}=3.5).

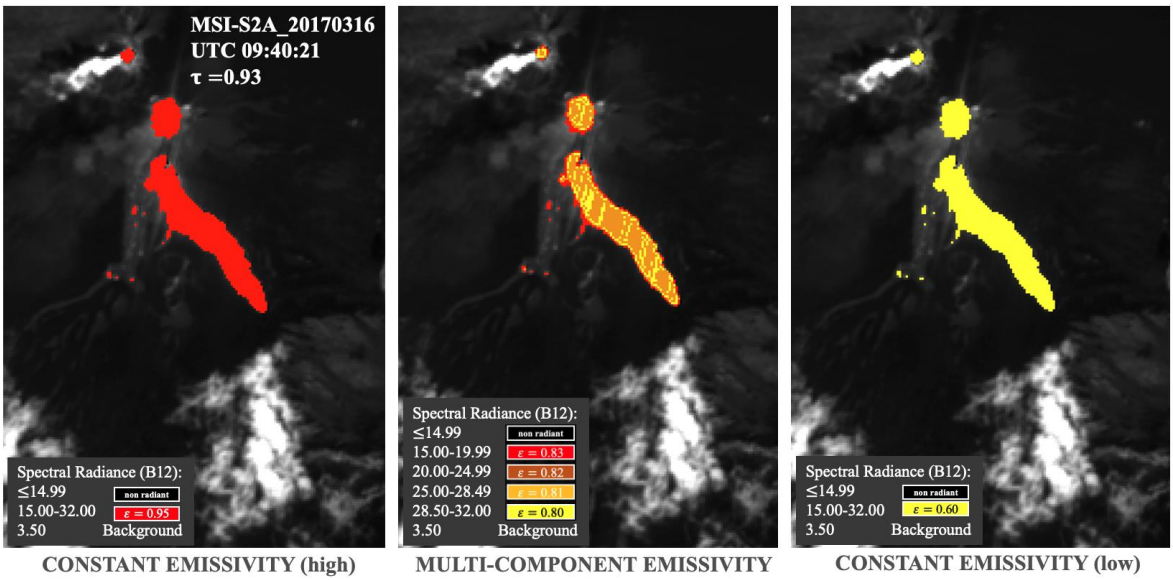

CONSTANT EMISSIVITY (high) MULTI-COMPONENT EMISSIVITY CONSTANT EMISSIVITY (low)

Figure 3.8 MSI scene (Sentinel 2A, Band 12) scene acquired on 16 March 2017, showing all radiant pixels, with recorded spectral radiance (W μm^{-1}), used for computation of total radiant heat flux at constant emissivity **(left)** 0.95 and **(right)** 0.60, as well as the **(centre)** multi-component emissivity approach (dynamic).

1200 radiant pixels extracted from the MSI scene, acquired on 16 March 2017 (Fig.3.8) were used to compute total radiant heat flux values of 2.88 GW and 3.41 GW for constant emissivity 0.95 and 0.60 respectively. In contrast, computation of total radiant heat flux using multicomponent emissivity, involved automatic allocation of correct emissivity values based on radiance thresholds indicated in Figure 3.8 centre, where emissivity of 0.83 was applied to 121 pixels, 0.82 to 103 pixels, 0.81 to 682 pixels and 0.80 to 294 pixels, producing 3.02 GW.

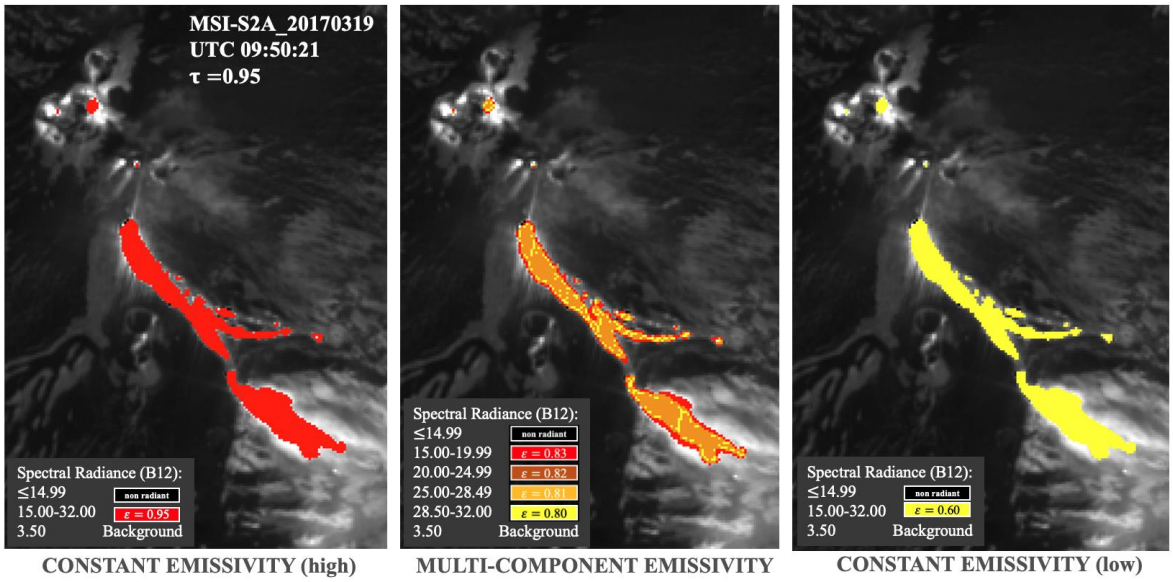

Figure 3.9 MSI scene (Sentinel 2A, Band 12) acquired on 19 March 2017, showing all radiant pixels, with recorded spectral radiance (W μm^{-1}), used for computation of total radiant heat flux at constant emissivity **(left)** 0.95 and **(right)** 0.60, as well as the **(centre)** multi-component emissivity approach (dynamic).

1390 radiant pixels extracted from the MSI scene, acquired on 19 March 2017 (Fig.3.9) were used to compute total radiant heat flux values of 3.10 GW and 3.66 GW for constant emissivity 0.95 and 0.60 respectively. In contrast, computation of total radiant heat flux using multicomponent emissivity, involved automatic allocation of correct emissivity values based on radiance thresholds indicated in Figure 3.9 centre, where emissivity of 0.83 was applied to 181 pixels, 0.82 to 155 pixels, 0.81 to 825 pixels and 0.80 to 229 pixels, producing 3.31 GW.

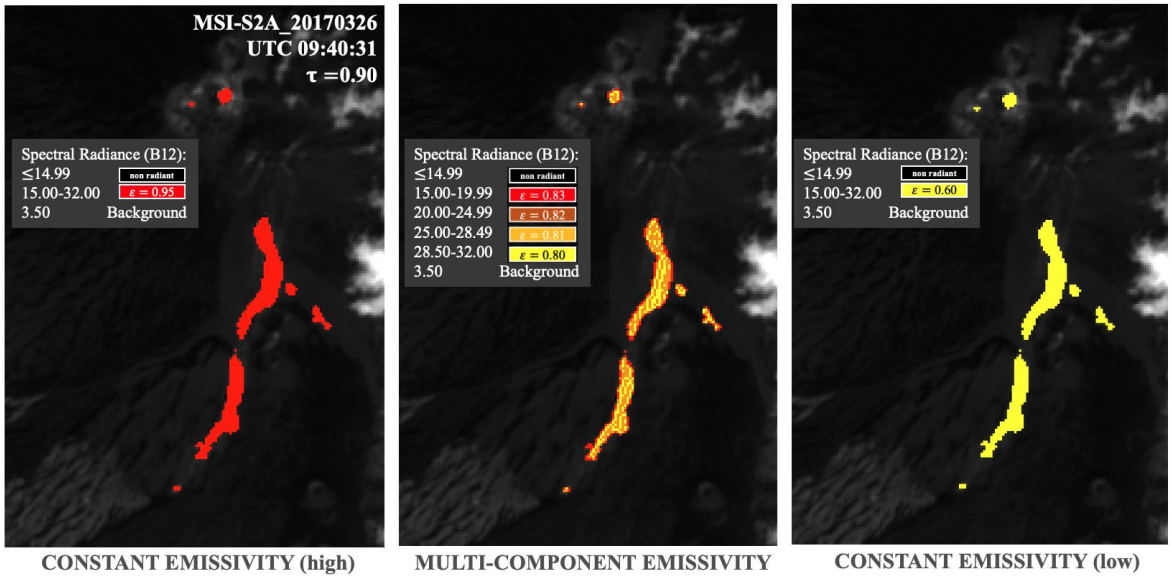

Figure 3.10 MSI scene (Sentinel 2A, Band 12) acquired on 26 March 2017, showing all radiant pixels, with recorded spectral radiance (W μm^{-1}), used for computation of total radiant heat flux at constant emissivity **(left)** 0.95 and **(right)** 0.60, as well as the **(centre)** multi-component emissivity approach (dynamic).

762 radiant pixels extracted from the MSI scene, acquired on 26 March 2017 (Fig.3.10) were used to compute total radiant heat flux values of 1.76 GW and 2.09 GW for constant emissivity 0.95 and 0.60 respectively. In contrast, computation of total radiant heat flux using multicomponent emissivity, involved automatic allocation of correct emissivity values based on radiance thresholds indicated in Figure 3.10 centre, where emissivity of 0.83 was applied to 168 pixels, 0.82 to 89 pixels, 0.81 to 285 pixels and 0.80 to 220 pixels, producing 1.87 GW.

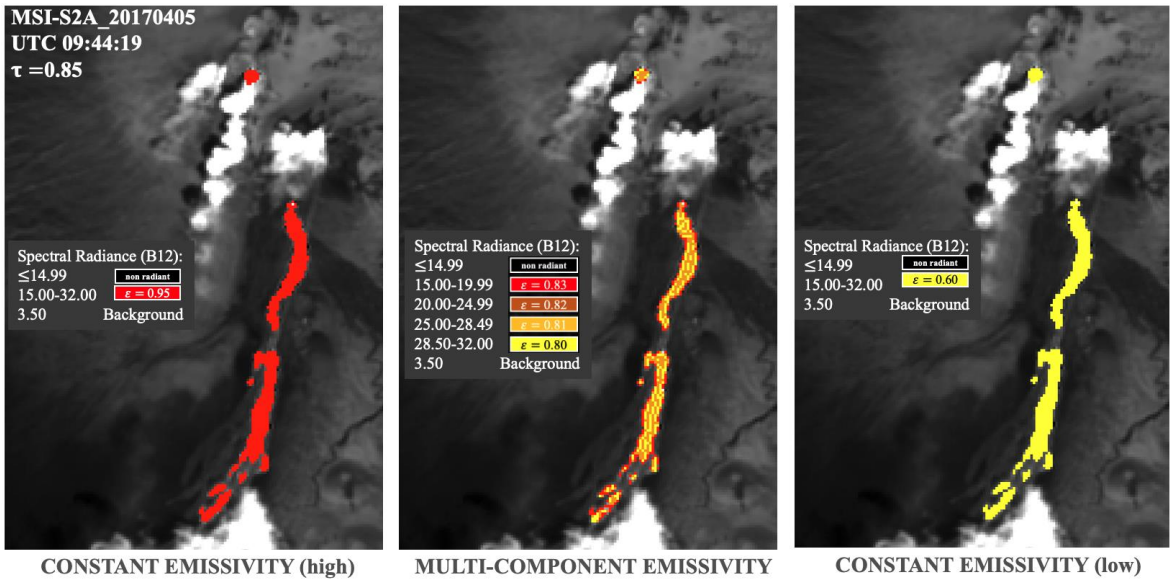

Figure 3.11 MSI scene (Sentinel 2A, Band 12) acquired on 05 April 2017, showing all radiant pixels, with recorded spectral radiance (W μm^{-1}), used for computation of total radiant heat flux at constant emissivity **(left)** 0.95 and **(right)** 0.60, as well as the **(centre)** multi-component emissivity approach (dynamic).

717 radiant pixels extracted from the MSI scene, acquired on 05 April 2017 (Fig.3.11) were used to compute total radiant heat flux values of 1.67 GW and 1.97 GW for constant emissivity 0.95 and 0.60 respectively. In contrast, computation of total radiant heat flux using multicomponent emissivity, involved automatic allocation of correct emissivity values based on radiance thresholds indicated in Figure 3.11 centre, where emissivity of 0.83 was applied to 98 pixels, 0.82 to 114 pixels, 0.81 to 272 pixels and 0.80 to 233 pixels, producing 1.78 GW.

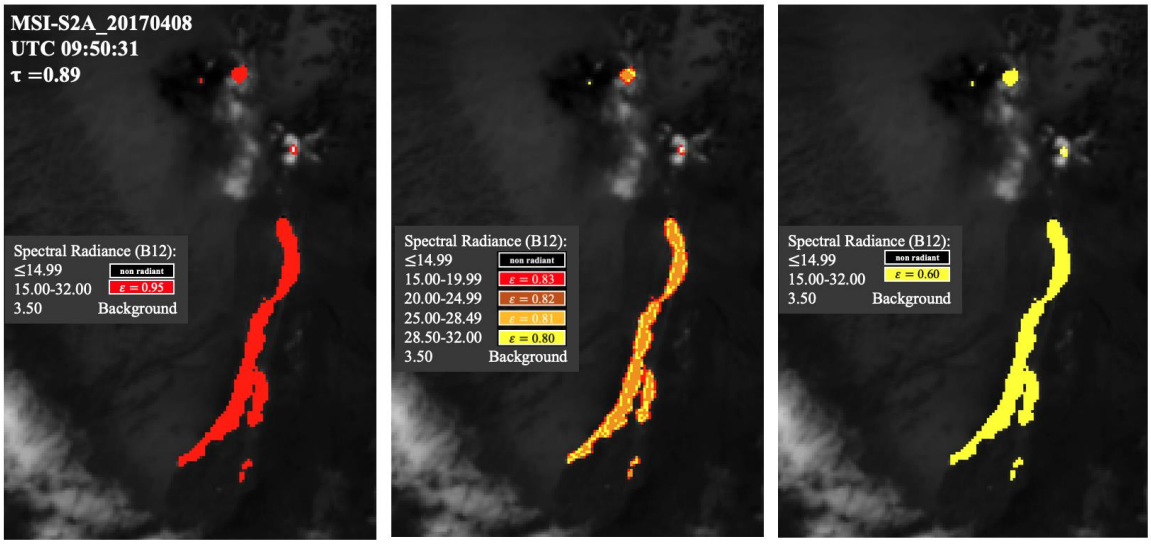

Figure 3.12 MSI scene (Sentinel 2A, Band 12) acquired on 08 April 2017, showing all radiant pixels, with recorded spectral radiance (W μm^{-1}), used for computation of total radiant heat flux using at emissivity **(left)** 0.95 and **(right)** 0.60, as well as the **(centre)** multi-component emissivity approach (dynamic).

746 radiant pixels extracted from the MSI scene, acquired on 08 April 2017 (Fig.3.12) were used to compute total radiant heat flux values of 1.75 GW and 2.07 GW for constant emissivity 0.95 and 0.60 respectively. In contrast, computation of total radiant heat flux using multicomponent emissivity, involved automatic allocation of correct emissivity values based on radiance thresholds indicated in Figure 3.12 centre, where emissivity of 0.83 was applied to 80 pixels, 0.82 to 93 pixels, 0.81 to 380 pixels and 0.80 to 193 pixels, producing 1.87 GW.

3.3.3 Radiant Heat Flux Difference

Radiant heat flux results presented in Figure 3.14 and Table 3.4 show an increase in calculated radiant heat flux of ~18.3 % (17.8-18.7 %) between endmembers (i.e., emissivity 0.95 and 0.60) for all spaceborne scenes analysed. The multicomponent results, being composed of several different emissivities, are plotting in between endmembers (i.e., emissivity 0.95 and 0.60).

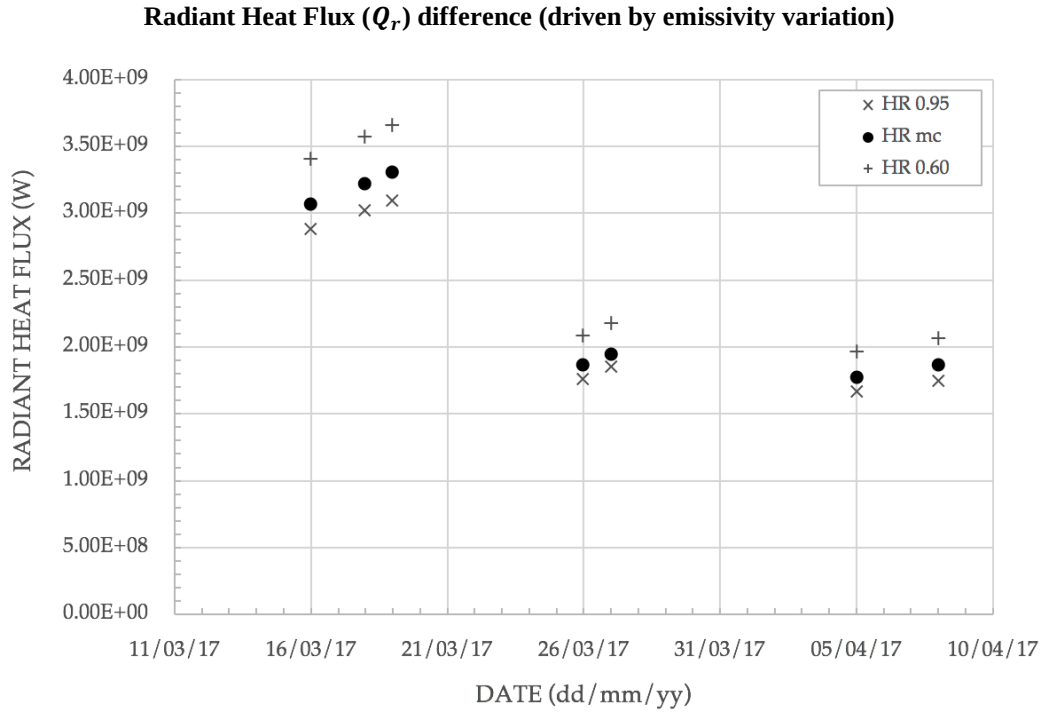

Figure 3.14 Radiant heat flux results (difference) using different emissivity values; (i) constant values (0.95 and 0.60), and (ii) multicomponent emissivity (HR mc). 'HR' signifies high-resolution data (combined OLI and Sentinel-2A spaceborne scenes).

Table 3.4 Estimation of total radiant heat flux (Q_r) using high-spatial resolution data acquired by Landsat 8 (OLI) and MSI (Sentinel 2A) during the 2017 Mt Etna eruption

Emissivity method	16 March (MSI-S2)	18 March (OLI)	19 March (MSI-S2)	26 March (MSI-S2)	27 March (OLI)	05 April (MSI-S2)	08 April (MSI-S2)
Constant 0.95	2.88	3.02	3.10	1.76	1.85	1.67	1.75
Multicomponent	3.02	3.22	3.31	1.87	1.95	1.78	1.87
Constant 0.60	3.41	3.57	3.66	2.09	2.18	2.07	2.07

*Values reported for each date indicate computed total radiant heat flux (GW) for constant or multicomponent emissivity

3.4 Discussion and conclusions

Sensors carried onboard Earth-orbiting satellites provide a means to obtain an instantaneous record of the thermal properties of an active lava flow, at regular high-to-moderate or low repeat intervals, depending on their temporal resolution capabilities (Chapter 1). High-temperature thermal anomalies (i.e., lava flows) commonly stand out in near V-NIR or SWIR wavelengths (i.e., 0.7-2.5 μm) satellite images and relatively easy to detect (Pieri and Abrams, 2005), although reflected solar radiation in daytime images can sometimes be confounding (Blackett, 2014; Harris, 2013a), thus, it was corrected here using $\mathrm{bg}_{(\mathrm{band})}$ approach (Section 3.2).

Land surface temperature and land surface emissivity are two key parameters used as satellite input parameters, because they are closely linked to the Earth's surface energy balance (Sobrino et al., 2008). As demonstrated in Figure 3.14, if emissivity corrections are neglected or simplified, the output data will result in systematic errors.

Many studies to date use predominantly TIR satellite data to provide a range of volcanic applications for (near) real-time detection and monitoring of active volcanoes, regionally or globally (discussed in Chapter 5), while here, analyses using high-spatial resolution spaceborne data in SWIR was presented.

Since 1972, the Landsat series have been providing a synoptic record of global land cover and land changes. Various studies have investigated capabilities and limitations using this platform, where its thermal information has been successfully used to identify and quantify thermal anomalies at active volcanoes for decades (Flynn et al., 2000; Francis and Rothery, 1987). Ability of Landsat platforms to provide data in two SWIR bands, which are sensitive to surfaces of magmatic temperatures means that they can be exploited to analyse lava flows using dual-band approach.

The novel technique used here, applying multicomponent emissivity to SWIR imagery acquired during the 2017 Mt Etna eruption has indicated a radiant heat flux uncertainty ≤16.8 % between constant emissivity endmembers (i.e., 0.95 and 0.60). Applying multi-component approach to compute radiant heat flux can constrain this uncertainty.

Remote sensing and laboratory based FTIR spectroscopy can be valuable tools when analysing the same target area (or sets of targets) on the ground. Spaceborne measured emissivity (ASTER GED) for the 2017 Mt Etna eruption (Section 2.3.1) was validated ('ground-truthed'), corrected and expanded, using very-high temperature FTIR thermal emission results (Section 2.3.5). Spaceborne results indicate an increase in calculated radiant heat flux of ~18.3 % between endmembers (i.e., emissivity 0.95 and 0.60) for all spaceborne scenes, whereas, multicomponent results, being composed of several different emissivities indicate more plausible radiant heat flux results.

For example, the scene acquired on 16 March 2017 (Table 3.4) produced a total calculated radiant heat flux of 2.88 gigawatts (GW) using constant emissivity of 0.95, and 3.41 GW using constant emissivity of 0.60. Conversely, a 'multi-component' emissivity approach produced a total calculated radiant heat flux value of 3.02 GW, where several emissivity values were applied to different thermal components (i.e., range of crust and melt temperatures), expected to be found in this active lava flow.

A recent study (Lombardo et al., 2020) argues that spectral emissivity of Etnean basaltic melts does not vary significantly with temperature in SWIR spectral range, when compared to its solidified counterpart. This finding is based on a new Draping algorithm for temperature-emissivity separation, taking into account the non-uniform temperature distribution of the melt surface, and compared to emissivity measured using 'lava simulator' (Lombardo et al., 2020). Nonetheless, findings presented here (Chapters 2 and 3) indicate that emissivity of Etnean basalts in SWIR varies from 0.81 at 774 K to 0.74 at 1373 K. This variation has an inherent impact on computation of radiant heat and mass fluxes, as well as 'distance to run' estimates (Chapter 4).

4 The view from above

Much of the material discussed in this chapter has been published in the papers by Rogic et al. (2019a) and Rogic et al. (2019b), which are reproduced in full as Appendices G and H.

High-spatial (low temporal) resolution of Landsat series data presented in previous chapter means that data is being acquired every 16 days, whereas MSI for Sentinel 2, provides data every 5 days, which increases observational data for the period analysed. The small number of usable cloud free data, as well as possible saturation due to sensor detection capabilities (Harris, 2013b) over high radiance targets may present additional restrictions for information extracted from high-spatial resolution data. Therefore, a data synergy (and validation), using moderate-to-low spatial resolution data, discussed in this chapter is a viable and practical option to aid the analysis, interpretation and constrain the uncertainty of computed radiant heat flux using multi-platform and multi-payload spaceborne data.

4.1.1 High-to-moderate spatial resolution data of the same target area

MODIS acquires data in 36 channels, daytime and 16 channels, night-time. Data acquired by for the 2017 Mt Etna eruption by MODIS channels (Table 4.1), onboard Terra and Aqua were processed using automated procedures 'MyMOD', detailed in (Hirn et al., 2008b). MyMOD allows the automatic detection of anomalous pixels and sequential calculation of effective temperature, radiant heat flux and effusion rate from moderate spatial/temporal resolution multispectral data acquired by MODIS. It processes an at-satellite radiance calculation, determines integrated TIR temperature (corrected for adiabatic cooling) and detects hot-spots in MIR window, using Normalized thermal Index (NTI) method (Hirn et al., 2008b). Hot-spot detection using NTI method is computed using MODIS MIR (Channel 22) and TIR (Channel 32) data, with fixed thresholds. For example, NTI larger than -0.8 is a marker for subpixel thermal anomaly for night-time data, whereas this threshold is fixed at -0.6 for daytime MODIS data (Hirn et al., 2008b).

Table 4.1 Radiometric and geometric characteristics of MODIS

MODIS Channel	Wavelength Range (μm)	Resolution at Nadir (m)	Max T* (K) Terra	Max. T* (K) Aqua
MIR 21	3.93-3.99	1000	506	513
MIR 22	3.93-3.99	1000	330	334
TIR 31	10.78-11.28	1000	388	360
TIR 32	11.77-12.27	1000	388	359

*Maximum Brightness Temperature in Kelvin (K)

Measured FTIR data (Fig. 4.1 and Table 4.2) were applied to MyMOD, as input parameters, linked to radiance, to recalculate total radiant heat fluxes for 99 MODIS files, acquired during the 2017 Mt Etna eruption between 25 February 2017 and 28 April 2017.

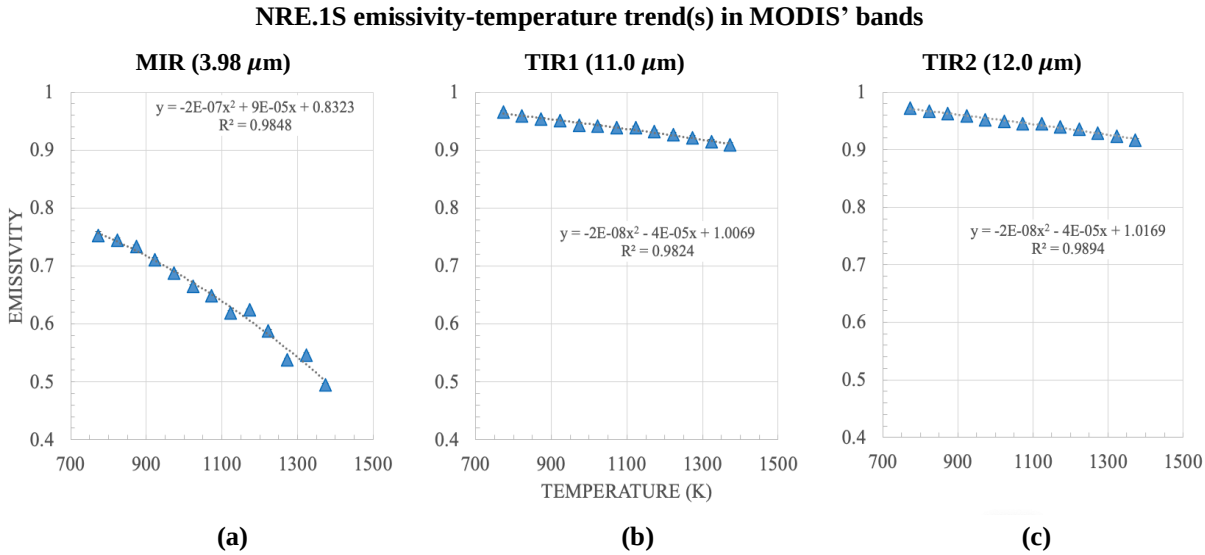

Figure 4.1 Modelled emissivity-temperature trends for MODIS' **(a)** MIR Band 21 (3.98μm) **(b)** TIR band 31 (11.0 μm) **(c)** TIR band 32 (12.0 μm)

Table 4.2 MODIS-Aqua (MYD) and MODIS-Terra (MOD) temperature and radiance data linked to measured emissivity values at MODIS' Bands 21, 31 and 32.

MODIS Band	λ (μm)		*773	873	973	1073	1173	1273	1373	MEAN
21	3.981	ε MIR	0.752	0.733	0.788	0.648	0.623	0.538	0.494	0.615
		Rad MIR	838	1408	2038	2742	3562	3965	4550	
31	11.017	ε TIR1	0.966	0.954	0.943	0.938	0.932	0.922	0.909	0.932
		Rad TIR1	160	201	244	289	333	377	419	
32	12.036	ε TIR2	0.954	0.944	0.934	0.927	0.921	0.910	0.898	0.921
		Rad TIR2	121	151	181	213	244	275	304	

*Temperature in Kelvin (K)

**Rad is satellite measured spectral radiance

Emissivity values (Table 4.2) were applied to MODIS data by reprogramming MyMOD code (courtesy of Hirn) to obtain radiant heat flux results (Fig. 4.2).

This new recalculated total radiant heat flux, using multicomponent emissivity approach was compared directly with the high-spatial resolution data (Chapter 3) and shown in Figure 4.3. Multi-platform results (OLI, Sentinel 2A and MODIS) appear to be relatively comparable, considering the marked difference in temporal and spatial resolution.

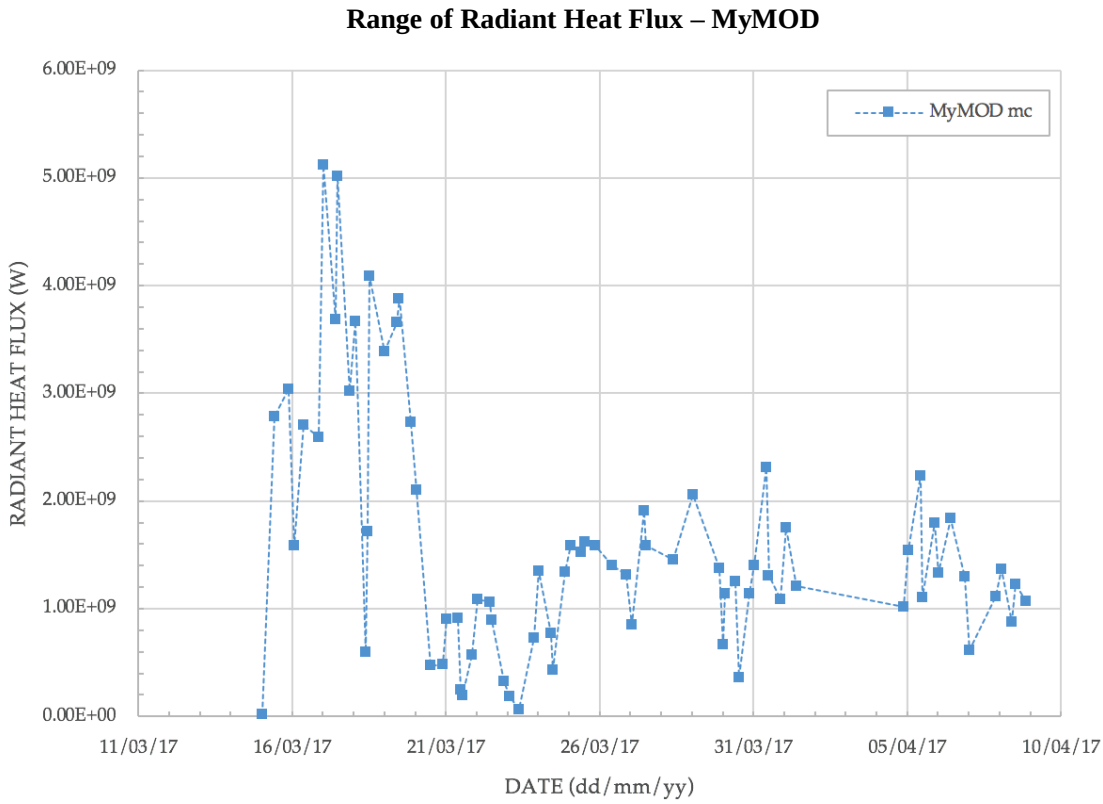

Figure 4.2 Computed total radiant heat flux results for MODIS (MyMOD), from 15 March to 10 April 2017, applying multicomponent approach.

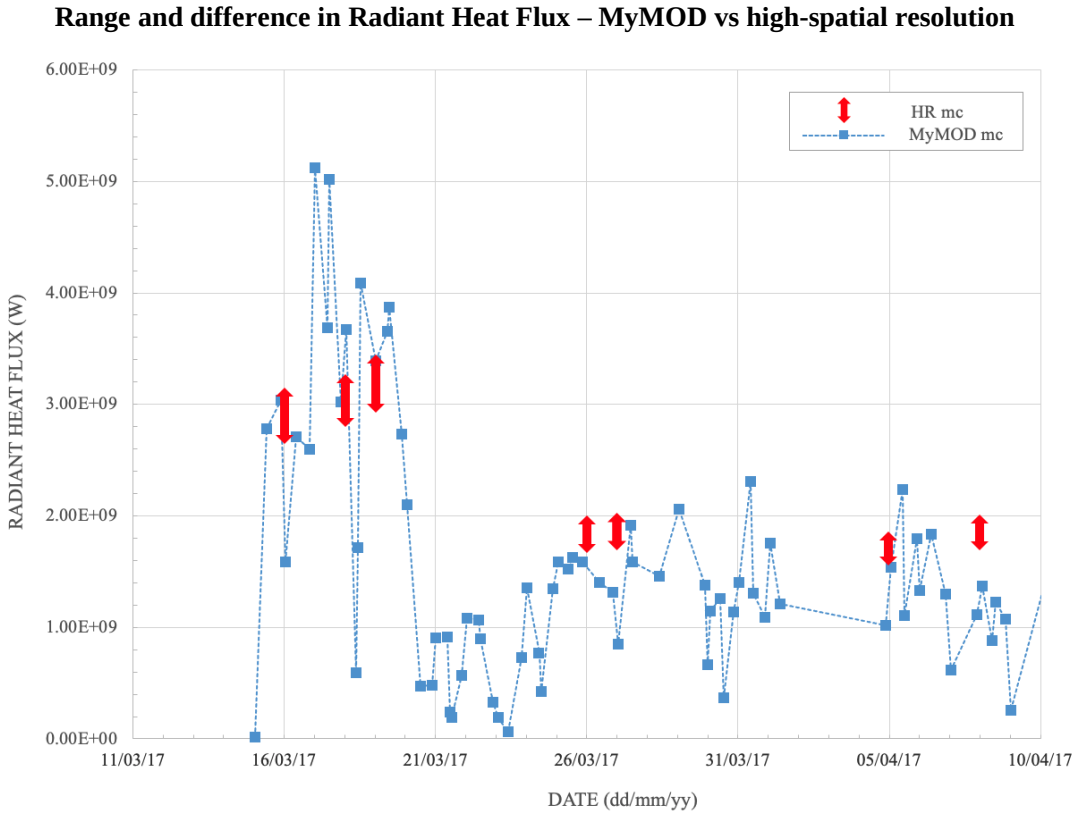

Figure 4.3 Comparison in computed radiant heat flux values from15 March to 10 April 2017, derived from high-spatial resolution (HR OLI and Sentinel-2) and MODIS data (MyMOD), using multicomponent approach.

4.1.2 Low-moderate and high-spatial resolution data of the same target area

Moderate-to-high temporal resolution satellite data processed using HOTSAT thermal monitoring system (Ganci et al., 2016, 2011), employed by the INGV (Catania, Italy) to monitor Mt Etna is used here for comparison and validation against the new multicomponent approach and determine extent of uncertainty in total radiant heat flux produced by different spaceborne platforms and different approaches (Figs. 4.4 and 4.5).

The HOTSAT system is designed to automatically provide the location of the 'hotspot' pixels, if present, and quantify their thermal anomaly by computing the associated radiant heat flux. It uses MODIS data providing images at 1.0 km spatial resolution up to four time per day and Spinning Enhanced Visible Infra-Red Imager (SEVIRI) data providing almost continuous monitoring (i.e., four times per hour and up to 5 minutes sampling interval in rapid scanning service mode) with a spatial resolution of 3.0 km at nadir (World Meteorological Organisation, n.d.). The radiant heat flux is computed for all pixels and classified as a true 'hotspot' by using the MIR radiance method (Wooster et al., 2003).

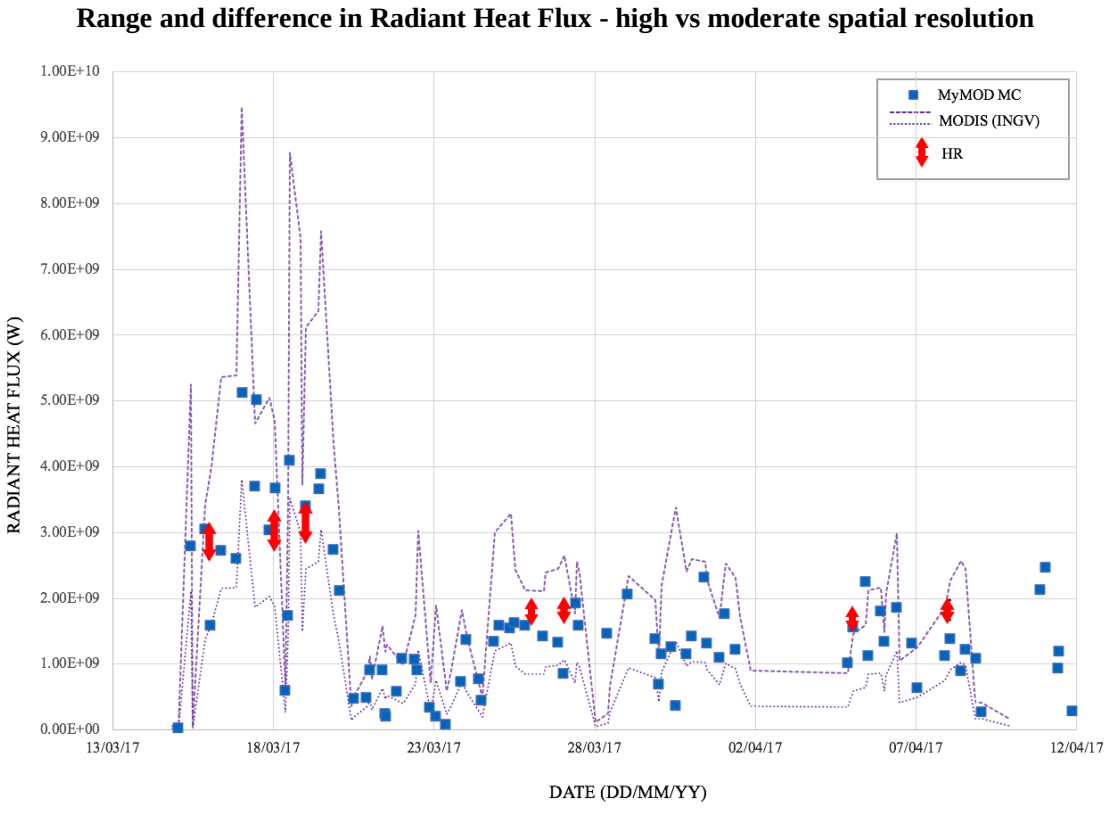

Figure 4.4 Comparison in computed radiant heat flux values from 15 March to 12 April 2017, derived from high-spatial resolution (HR OLI and Sentinel-2) and MODIS (MyMOD), using multi component approach, and MODIS (INGV), to derive min/max values, using constant emissivity (Wooster et al., 2003).

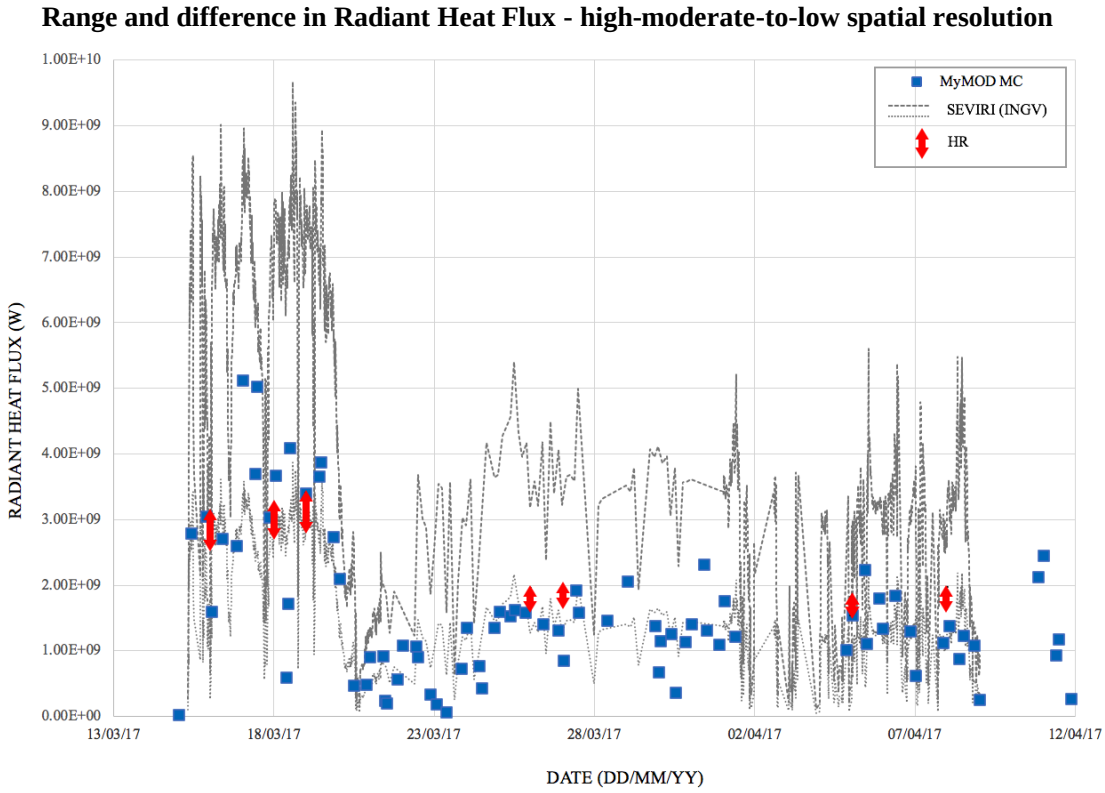

Figure 4.5 Comparison in computed radiant heat flux values from 15 March to 12 April 2017, derived from high-spatial resolution (HR OLI and Sentinel-2) and MODIS (MyMOD), using multi component approach, and SEVIRI (INGV) to derive min/max values, using constant emissivity (Wooster et al., 2003).

It is important to note that this method (Wooster et al., 2003) is using constant emissivity, hence the value of emissivity is considered equal to the emissivity in the MIR and it is usually simplified. Therefore, use of this emissivity assumption causes errors in the result when radiant heat flux is computed. It has been indicated that this approach may also introduce errors larger than 30% outside a range of temperatures ~600-1500 K (Wooster et al., 2003).

SEVIRI (INGV) and MODIS (INGV) data (Figs. 4.4 and 4.5) used to analyse the 2017 eruptive activity on Mt Etna between 14 March and 09 April 2017, show that the higher spatial resolution provided by MODIS permits detection of less intense thermal anomalies. For example, both the first and the last thermal anomalies during this eruptive event were detected by MODIS, on 14 March (20:35 GMT) and on 9 April (21:14 GMT), respectively. The peak of activity occurred within the first five days of eruption, with a maximum radiant heat flux of 9.47 GW recorded on 17 March (00.40 GMT) by MODIS and 9.67 GW on 18 March (14:15 GMT) by SEVIRI. Conversely, MyMOD approach using 'multicomponent' emissivity produced radiant heat flux value of 5.12 GW on 17 March (00:40 GMT) and 4.09

GW on 18 March (12:25 GMT). High-spatial resolution data was not available for 17 March and Landsat 8 (OLI) produced radiant heat flux of 3.22 GW on 18 March (09:41 GMT).

To illustrate the difference in computed radiant heat fluxes produced by various platforms (Figs. 4.2-4.5), data shown in Figure 4.3 indicates the range produced on a specific date/time.

Table 4.3 Total radiant heat flux (in GW) comparison data acquired by high (OLI, Sentinel-2), moderate (MODIS) and low (SEVIRI) spatial resolution payloads during the 2017 Mt Etna eruption.

Date (dd/mm/yy)	Landsat-8 (OLI)	MSI (Sentinel 2)	MODIS (MyMOD)	**MODIS min-max	**MODIS mean	**SEVIRI min-max	**SEVIRI mean
16/03/17	-	**3.02**	**2.71**	2.15-5.36	**3.76**	2.95-7.38	**5.17**
18/03/17	**3.22**	-	**1.72**	1.38-3.44	**2.41**	2.71-6.78	**4.74**
19/03/17	-	**3.31**	**3.66**	2.55-6.36	**4.46**	2.86-7.14	**5.00**
26/03/17	-	**1.87**	**1.41**	0.84.2.10	**1.47**	1.67-4.18	**2.93**
27/03/17	**1.95**	-	**1.91**	1.02-2.55	**1.79**	1.43-3.58	**2.51**
05/04/17	-	**1.78**	**2.24**	0.64-1.60	**1.12**	1.30-3.24	**2.27**
08/04/17	-	**1.87**	**1.22**	1.03-2.57	**1.80**	1.73-4.32	**3.02**

*Total radiant heat flux values (GW) computed for data acquired by all payloads ~09:30 UTM.

**MODIS and SEVIRI data processed by the INGV (Catania, Italy) using HOTSAT approach (Ganci et al., 2011, 2016) for the 2017 Mt Etna eruption (extracted for specific dates from data shown in Figs. 4.4 and 4.5)

By comparing the radiant heat flux values obtained from moderate-to-high temporal resolution, namely SEVIRI and MODIS (data courtesy of INGV, Catania), and high-spatial resolution, namely OLI and Sentinel-2A, it is evident that the latter falls inside the region of admissible values retrieved from SEVIRI and MODIS images (Figs. 4.4 and 4.5). Moreover, the fact that the high-spatial resolution data and MyMOD results are reasonably close to the lower boundaries in most cases of the SEVIRI (INGV) and MODIS (INGV) data, suggests that emissivity does play a role in the computation of accurate radiant heat flux values from spaceborne data. This may, in this example, produce 28-176 % difference in computed radiant total heat flux, based on the lowest and highest mean values for each scene (Table 4.3).

4.2 Impact on Effusion Rates and predicted ‘distance-to-run’

Varying the emissivity and wavelength will have an impact on the computation of integrated temperatures and radiant heat fluxes, and hence on the estimation of lava effusion rates and lava flow ‘distance-to-run’. This is critically important for civil defence and hazard mitigation efforts.

Empirical derivation of effusion rates (Wright et al., 2001; Pieri and Baloga, 1986) and estimation of maximum ‘aa’ lava flow length (Kilburn, 2015, 1996; Calvari and Pinkerton,

1998) involves certain assumptions. The basis for each study, Kilburn (2015, 1996) and Calvari and Pinkerton (1998) are compared here to illustrate that they are independent, as former uses a physical model, while the latter is based on multiparametric statistics. The latter performs a multiple regression analyses, using main variables in their investigation to determine the maximum length of 'aa' lava flows, specific for Mt Etna. In contrast, the former (Kilburn, 2015, 1996), uses the main controlling lava flow development factors, such as the rate of magma supply, the lava's physical properties, and the local environment.

Often, the effusion rate can be calculated by exploiting ground-based observations, where the information on how the volume of an individual flow changes in a given time interval can be quite accurate. This is achieved by using information on the rate of advance, if the cross-sectional area of the flow front is known (i.e., width × thickness × rate of advance) or if the volume and time interval are known (length × width ×thickness ÷ time). The calculated eruption rate can be used to estimate the maximum potential lava flow length (Kilburn, 2015, 1996). However, this approach is not intended to forecast the exact final length of the flow, but its maximum potential value.

The estimation of maximum lava flow length is most needed at the start of the eruption. This information would play an important role in hazard mitigation for densely populated areas in close proximity to an active volcano. An accurate estimation of effusion rate is considered to be a primary objective for monitoring efforts during on-going eruptions and studies that model lava flow propagation and development.

A simplified quantitative evaluation performed on the best-quality night-time image acquired during the 2001 eruption, selected here, was chosen to avoid pixel saturation and the reflected radiances of daytime images in SWIR. This eruption was observed by three high-spatial resolution payloads on Landsat 5 (ETM), Landsat 7 (ETM+) and Terra (ASTER). The selected image data presented here were acquired by Enhanced Thematic Mapper + (ETM+) on 5 August 2001 at 20:34 UTM (Fig. 4.5). ETM+ is the multispectral scanning radiometer onboard Landsat-7, providing high-spatial resolution data (30 m in V-NIR-SWIR and 60 m in TIR) in repeat cycles of 16 days. Launched in 1999 and still active at the time of writing, ETM+ provided very high-quality images until 2003, when the linear scan compensator developed a permanent fault affecting the whole image (black stripes).

A simplified test, using 20% variation in emissivity (i.e., 1.0 and 0.80) is used to assess the sensitivity of computed radiant heat flux to variations in emissivity (Rogic et al., 2019a).

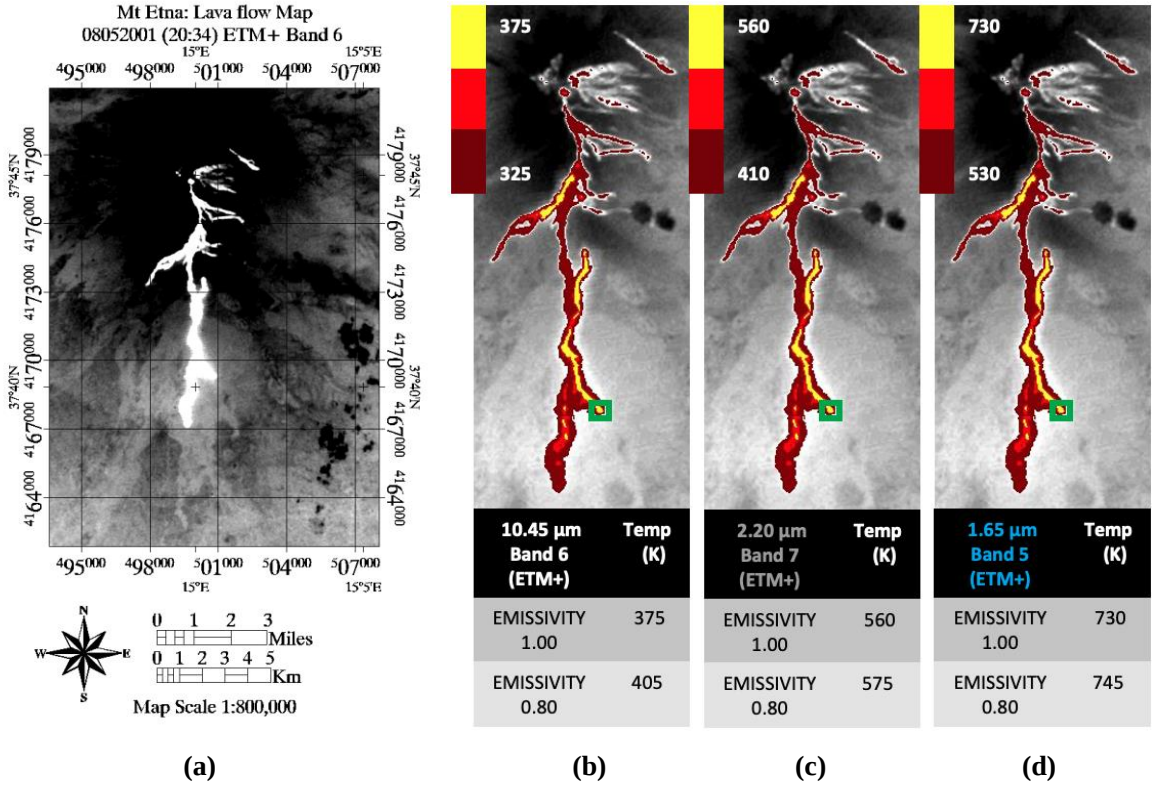

Figure 4.6 (a) High temperature thermal anomaly scene, acquired for Mt Etna on 05 August 2001 by Landsat-7 (ETM+), **(b-d)** showing fluctuation in computed pixel integrated temperatures for all radiant pixels of the same target area as in **(a)** TIR Band 6 and SWIR Bands 7 and 5 for emissivity of 1.0. The green square in **(b-d)** marks the location of the pixel (37°39′28′′N and 14°59′48′′E), used to derive temperature values with emissivity variation given below **(b-d)** (from Rogic et al.(2019a)).

After radiometric and atmospheric correction, the image (Fig. 4.6) was processed for all radiant pixels in SWIR and TIR, while applying uniform emissivity across the entire spaceborne scene (e.g., 1.0 or 0.80), following previously established procedures (Chapter 3). A marked difference in calculated pixel integrated temperatures is evident when using different emissivity values (i.e., 1.0 and 0.80) in TIR and two SWIR channels. These values are ranging from as low as 325 K (brightness temperature $\varepsilon = 1.0$ at 10.45 μm TIR wavelength) to as high as 745 K ($\varepsilon = 0.80$ and 1.65 μm SWIR). Overall, 20% emissivity change gives rise to pixel integrated temperature differences of the order of 15 K in SWIR and 30 K in TIR (shown in 4.5 b-d).

Considering that varying emissivity (i.e., 1.0 or 0.80) impacts the computation of apparent lava surface temperatures, more accurate FTIR measured emissivity-temperature data obtained for the 2001 eruption were used (Chapter 2), in an attempt to improve deduced temperatures, using the novel multicomponent emissivity approach (Chapter 3).

In this example, lower emissivity (0.60) has been used than previously (Fig. 4.6) to assess its lower boundary impact.

For each emissivity approach (i.e., 1.0, 0.60 and multicomponent), using calculated integrated temperatures, sub-resolutions were solved in SWIR (1.65 μm and 2.20 μm) to obtain the effective temperature (Eq. 9) and total radiant heat flux (Eq. 10), from which the lava effusion rate (Wright et al., 2001; Pieri and Baloga, 1986) E_{r_calc} is estimated:

$$E_{r\_calc} = \frac{Q_{r\_calc}}{\rho\left(C_p \Delta T + \Phi C_L\right)} \tag{12}$$

In Equation (Eq. 12), the ρ is the lava density (2600 kg m^{-3}); C_p is the specific heat capacity (1150 J kg^{-1}K^{-1}); ΔT is the average temperature difference throughout the active flow (100-200 K), which is a significant parameter for estimating eruption rate; Φ is the average fraction of crystals (0.4-0.5) grown in cooling through ΔT, and C_L is the latent heat of crystallization (2.9×10^5 J kg^{-1}). It is important to note that while radiant heat flux Equation (Eq. 11) includes only observables and variable emissivity, the values used to solve effusion rate Equation (Eq. 12) are average values taken from various literature sources, which are specific for this type of lava and Mt Etna (Harris et al., 2007, 2000) and relate to key relationships between the imposed parameters (Pieri and Baloga, 1986). Therefore, the Equation (Eq. 12) is dependent on the flow composition and highly sensitive to both the eruptive and 'lava-stop' (advance cessation) temperatures.

Total radiant heat flux value for the entire thermal anomaly was used in computation of instantaneous effusion rate E_{r_calc} (Eq. 12) to attempt a rapid estimation of the maximum lengths (L_m) that an individual 'aa' lava flow can reach, using Kilburn (2015, 1996), general empirical approach, which can be simplified for basalts:

$$L_m = 2.5\ {E_r}^{1/2} \tag{13}$$

where E_r is effusion rate in m^{3}s^{-1} (originally termed 'Q' representing mean rate of discharge (Kilburn, 2015, 1996) and L_m, the maximum potential length that an individual lava flow can reach is in kilometres. The maximum potential length is expected to increase with effusion rate.

The relationship shown in Equation (Eq. 13) can be used to estimate the maximum potential length of an 'aa' flow, based on certain surface criterion (e.g., velocity, solidification) but it is indicated that this approach is not valid for 'pahoehoe' or 'blocky' flows, as they are more problematic to forecast (Kilburn, 2015, 1996), because they tend to lengthen until eruption stops, hence, to forecast length, volume of magma to be erupted must

be known. It is also important to note that observation in Kilburn (2015), suggests that Mt Etna's 'aa' flows don't extend beyond approximately 60% of the theoretical maximum (L_m).

Second approach (Calvari and Pinkerton, 1998) and the equation correction stated in (Wright et al., 2001) was also tested here, which is derived specifically for Mt Etna:

$$L = 10^{3.11} E_r{}^{0.47} \tag{14}$$

where E_r is effusion rate in m^3s^{-1} (originally termed 'E' representing the mean discharge rate (Calvari and Pinkerton, 1998), normally averaged for the whole time an individual flow was active). Here, the instantaneous E_{r_calc}, derived for the 5 August 2001 ETM+ scene is used. L is the final length of the single channel-fed flow in kilometres.

Therefore, a total radiant heat flux spaceborne data results using constant (i.e., 1.0 and 0.60) and multicomponent emissivity were exploited (Fig. 4.7) to project the impact of emissivity (and uncertainty) on computed effusion rates (E_{r_calc}) and test 'distance-to-run' results to assess the effect emissivity may have on the final lava length in (Eq. 13 and Eq. 14). Figure 4.7 shows that 40% variation in emissivity would produce 340 m (8%) uncertainty in 'distance-to -run' in this example.

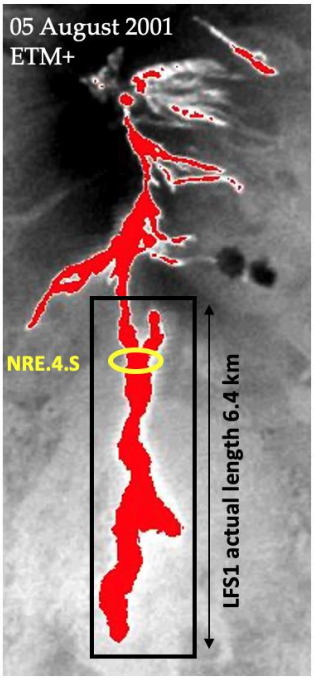

Radiant Heat Flux (Q_{r_calc}) → Effusion Rates (E_{r_calc})

$$L_m = 2.5\, E_r{}^{1/2}$$

$$L = 10^{3.11}\, E_r{}^{0.47}$$

EMISSIVITY	1.0	multicomponent	0.60
Q_{r_calc} (GW)	1.91	2.03	2.27
$E_{r\,calc}$ (m^3s^{-1})	2.43	2.57	2.88
$L_{m\,\_calc}$ (km)	**3.90**	**4.01**	**4.24**
L_{calc} (km)	1.95	2.01	2.11

Figure 4.7 Shows ETM+ scene acquired on 5 August 2001, highlighting the high-temperature thermal anomaly in red, focusing on the an individual LFS1 flow (Coltelli et al., 2007) analysed, and detailing a flow chart of procedures followed to obtain the maximum potential lengths (L_m) that LFS1 lava flow can reach, using general (Kilburn, 2015, 1996) and Mt Etna specific (Calvari and Pinkerton, 1998) empirical approaches.

The individual lava flow LFS1 analysed here reached its maximum length on or around 25 July 2001 with an estimated eruption rate of 18.33 m^3s^{-1} (Coltelli et al., 2007). According to field estimates (Table 4.4), after that date, the effusion rate dropped, so lava did not extend along the whole flow length.

Table 4.4 Volumes and effusion rates for the LFS1 2001 Mt Etna eruption (Coltelli et al., 2007)

Acquisition date	Local time	Eruption day	Acquisition Time (s)	Cumulative Volume ($\times 10^6 m^3$)	Time Span (s)	Partial Volume ($\times 10^6 m^3$)	Daily Effusion Rate ($m^3 s^{-1}$)
18/07/2001	03:00	0	0	0.00	0	0.00	0.00
18/07/2001	13:00	1	36000	0.37	36000	0.37	10.28
19/07/2001	16:00	2	133200	1.70	97200	1.33	13.68
20/07/2001	13:00	3	208800	3.50	75600	1.80	22.81
22/07/2001	11:00	5	374400	8.58	165600	5.08	30.68
26/07/2001	12:00	9	723600	14.98	349200	6.40	18.33
28/07/2001	16:00	11	910800	16.99	187200	2.01	10.74
30/07/2001	11:00	13	1065600	18.35	154800	1.37	8.85
02/08/2001	10:00	16	1321200	19.82	255600	1.47	5.75
04/08/2001	07:00	18	1483200	20.62	162000	0.80	4.94
06/08/2001	11:00	20	1670400	21.21	187200	0.59	3.15
07/08/2001	07:00	21	1742400	21.32	72000	0.11	1.53
09/08/2001	10:00	23	1926000	21.40	183600	0.08	0.44

ETM+ data from 5 August 2001 produced calculated effusion rate between 2.43 $m^3s^{-1}$and 2.88 m^3s^{-1}, which is in line with the rate drop observed for that time period, and corresponds well with field estimates of ~3 m^3s^{-1} on 6 August 2001 (Table 4.4), reported by Coltelli et al. (2007). Used here to project an impact of calculated spaceborne radiant heat flux using different emissivity, a 'snapshot' data for 5 August 2001 highlighted an increase in L_m of 9 % between emissivity endmembers (Fig. 4.7), and so may play a role in hazard mitigation at densely populated areas in close proximity to an active volcano, such as Mt Etna.

Although, this data may provide useful 'snap-shots', indicative of the current (instantaneous) state of activity at the moment in time, and relatively accurate computed radiant (and mass) flux, an instantaneous 'snap-shot' data, such as the one presented here for is based on a limited number of infrequent observations (i.e., one scene). Therefore, it may not reflect the significant peak discharge rate or dynamic flow regimes that are known to change over timescales of days or less (Bailey et al., 2006; Lautze et al., 2004; Harris et al., 2000; Wadge, 1981) and cannot be used in as a stand-alone approach to estimate final lava flow lengths. Instantaneous effusion rate computed from high-spatial resolution scenes may provide the volume flux of erupted lava that is feeding the flow at any point in time, which may help constrain high-temporal (large pixels) data. For a complete activity

overview, high-spatial resolution data must be used in tandem with moderate-to-high temporal platforms, as well as ground observations to obtain a complete activity overview (discussed further in Chapter 6).

Nonetheless, using the volume and eruption time information (Table 4.4) for period while flow was lengthening (18 to 25 July) would suggest an average effusion rate (i.e., cumulative volume divided by the acquisition time in seconds) of 22.9 m^3s^{-1} and if using Equation (Eq. 13) would produce L_m = 11.9 km. If, we then apply the observation (Kilburn, 2015) suggesting that Mt Etna's 'aa' flows do not extend beyond approximately 60% of the theoretical maximum, it will produce L_m= 7.1 km, which is greater than and therefore consistent with the maximum potential length, as the observed (actual) LFS1 length was 6.4 km. However, the second approach (Eq. 14) would produce shorter calculated length (L = 5.6 km) than the observed, hence underestimating the actual LFS1 final length.

5 Emissivity-Temperature rule and Forward modelling

5.1 'Dynamic Emissivity-Temperature Rule'

The 'emissivity-temperature trends' I measured and developed in this thesis for Mt Etna (Chapter 4), have been validated and employed by the INGV to improve on the 'static' (constant) emissivity approach to spaceborne and numerical modelling simulations, currently used operationally by the INGV (Catania, Italy). Findings presented in this thesis (Chapter 2) have provided substantial clarification on emissivity behaviour with temperature, with implications for procedures used by the INGV to monitor Mt Etna, which currently involve a constant emissivity approach (Wooster et al., 2003). A new approach, based on very-high temperature FTIR data (Section 2.3.5), providing reliable and exploitable predictive emissivity trends for both modelling and spaceborne applications at a range of temperatures and wavelengths is proposed here (Sections 5.1-5.3).

Measured emissivity data at specific wavelengths and the temperatures ('cooling-down') were used to derive a 'law' which relates emissivity to the temperature. Using a similar approach for both satellite remote sensing (Section 5.1) and lava flow modelling (Section 5.2), the INGV team modified the 'thresholds' approach presented in this thesis (Chapters 3 and 4), based on very-high temperature FTIR data (Chapter 2) to create a 'law' by computing a spectrum-integrated mean emissivity, which for any interval $(\lambda_{min}, \lambda_{max})$ can be calculated as described in the next sentence

$$\varepsilon_{[\lambda_{\min},\lambda_{\max}]}(T) = \frac{\int_{\lambda_{\min}}^{\lambda_{\max}} \varepsilon(\lambda,T) B_\lambda(\lambda,T) d\lambda}{\int_{\lambda_{\min}}^{\lambda_{\max}} B_\lambda\,(\lambda,T) d\lambda} \tag{15}$$

where $B_\lambda\,(\lambda,T)$ is Planck's Radiation law (in wavelength). Since ε(λ,T) information is not continuous (in λ), the integral is used for piecewise linear interpolation between each pair of data points, and provide an approximation justified by the fine granularity of the wavenumber sampling in the data. More sophisticated results could be achieved with higher-order reconstructions. Nonetheless, the results obtained using the simplified approach provides an uncertainty across samples that is of the same order as the FTIR measurement (experimental) error, reported in Appendix B.

For satellite remote sensing application, the spectrum-integrated mean emissivity is computed over the spectral response wavelengths of each channel. For example, MODIS' MIR channels (21 and 22) have bandwidth 3.929-3.989 μm, while the TIR channels (31 and 32) have bandwidth 10.780-11.280 μm and 11.770-12.270 μm.

Fitting quadratic polynomials to the temperature range of available data gives the following 'laws' Equations (Eq. 16-18) for the mean emissivity as a function of temperature in Kelvin (K) for the MODIS sensor:

$$\varepsilon_{MIR}(T) = 0.839079 + 0.0000970901\,T - 2.57376 \cdot 10^{-7}\,T^2 \quad (16)$$

$$\varepsilon_{TIR31}(T) = 0.912157 + 0.000152048\,T - 1.24152 \cdot 10^{-7}\,T^2 \quad (17)$$

$$\varepsilon_{TIR32}(T) = 0.92467 + 0.0001438\,T - 1.20315 \cdot 10^{-7}\,T^2 \quad (18)$$

By computing the mean and maximum relative error between derived emissivity 'laws' and the original data, observed values are within the measurement error range, thus use of the higher polynomial degrees is deemed unnecessary.

5.2 Numerical Modelling: lava flow simulation (MAGFLOW)

To evaluate impact of emissivity variation on the simulated ultimate lava flow lengths, a collaborative pilot study was undertaken (Rogic et al., 2019b, 2019a) with the INGV (Catania, Italy), which performed a sensitivity test by running a MAGFLOW cellular automaton propagator (Bilotta et al., 2016; Herault et al., 2009). The approach uses physical model accounting for both thermal and rheological evolution of flowing lavas and potential to significantly improve understanding of the dynamics of lava flow emplacement (Kereszturi et al., 2014) and assist with related hazard assessment and mitigation (Cappello et al., 2016, 2015b, 2015a; Pedrazzi et al., 2015; Del Negro et al., 2013; Negro et al., 2013).

To model the lava flow path for the 2001 Etna eruption, MAGFLOW was run on a pre-eruptive Digital Elevation Model (DEM) using field-derived effusion rates (Coltelli et al., 2007) and the typical properties of Etnean basaltic rocks (density = 2600 kg/m3; specific heat capacity = 1150 J kg−1 K−1; solidification temperature = 1173 K; extrusion temperature = 1360 K). Three model runs, each with different emissivity values (i.e., 0.80, 0.93, and 1.00) were introduced to the model, maintaining constant emissivity, unaffected by temperature changes throughout the simulation. This method was validated using the actual lava flow extent of the 2001 Mount Etna eruption (Fig. 5.1).

Whilst the actual lava flow field is quite well reproduced by the MAGFLOW model for all three emissivity values, the simulation run with $\varepsilon = 0.93$ reaches the closest flow length (6.5 km versus the actual 6.4 km), which is the most critical factor for hazard analysis (Bilotta et al., 2019, 2012).

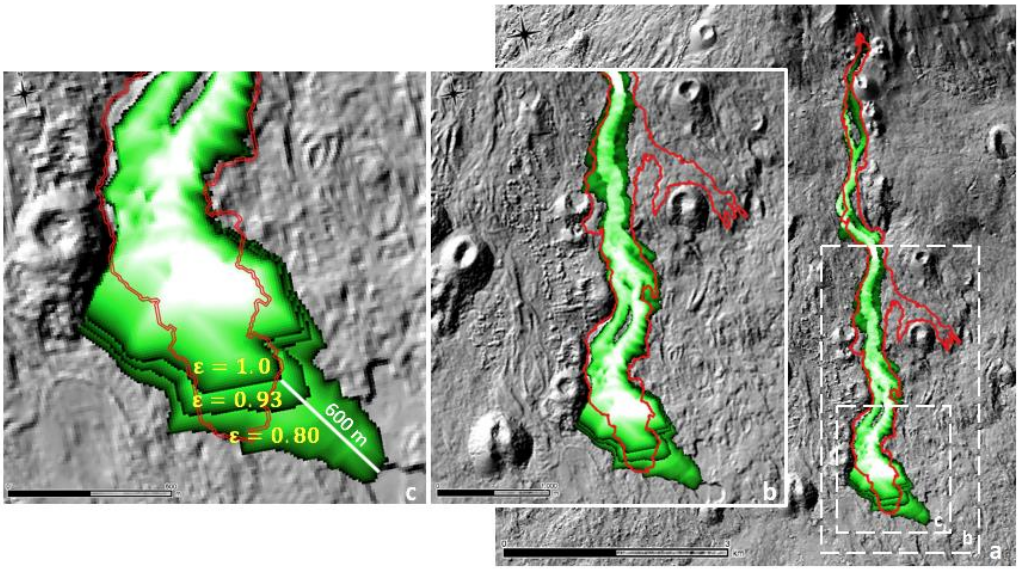

Figure 5.1 MAGFLOW simulation results with changing emissivity (i.e., 0.80, 0.93, and 1.00), showing a difference of up to 600 m (~10%) in lava flow length (from Rogic et al., (2019a)). The red outline is the actual limit of the real flow.

The pilot was expanded using very-high temperature FTIR results (Section 2.3.5), providing a better understanding of the variation of emissivity with temperature and impact of emissivity on deduced temperature during active lava flow propagation (and cooling).

For lava flow modelling, full spectrum of mean emissivity was used. Available data over SWIR-MIR-TIR range (2.17-25.0 μm) has been validated (Section 5.1) to ensure the 'stability' of mean emissivity in this range.

The mean emissivity is considered to be sufficiently stable to approximate the emissivity over the available spectrum (personal communication with Giuseppe Bilotta, INGV, Catania). By fitting a quadratic polynomial to the temperature range of available data would provide the mean emissivity of lava as a function of temperature and used in MAGFLOW simulation (INGV approach):

$$\varepsilon(T) = 0.817587 + 0.000345885\,T - 3.32996 \cdot 10^{-7}\,T^2 \qquad (19)$$

Using this approach, a synthetic test on a 20-degree inclined plane was performed (Fig. 5.2), using typical Etnean parameters (density = 2600 kg/m3; specific heat capacity = 1150 J kg−1 K−1; solidification temperature = 1173 K; extrusion temperature = 1360 K), applying a constant (0.90) and variable emissivities (modelled emissivity law).

Simulation results (personal communication with Annalisa Cappello, INGV, Catania) show that constant emissivity (Fig. 5.2a) produced a lava flow length of 5.87 km, whereas modelled variable emissivity approach (Fig. 5.2b) produced 6.53 km flow. A difference of 10.6 % in computed lava flow length (0.66 km) demonstrates that emissivity,

as an input parameter, also plays an important role in lava flow modelling applications, since it impacts ‘distance-to-run’ estimates.

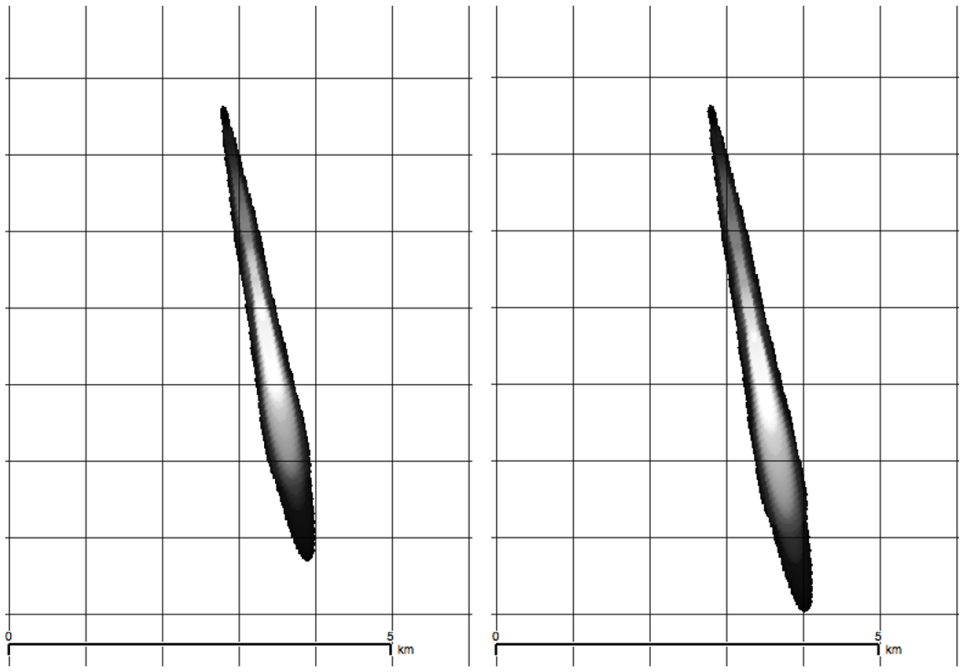

(a) **(b)**

Figure 5.2 A synthetic MAGFLOW simulation on 20-degree inclined plane using **(a)** constant emissivity (0.90) and **(b)** using a modelled emissivity law in (Eq. 19) with variable emissivity, derived FTIR from measured trends (Section 2.3.5).

5.3 Emissivity-Temperature Trends: Mt Etna and Global Application

Validation results provided by the INGV (Sections 5.1 and 5.2) are consistent with comprehensive analyses, based on FTIR data (Chapter 2), applied to the 2017 and 2001 Mt Etna eruptions using spaceborne data (Chapters 3 and 4).

Exploiting all available FTIR data (Chapter 2) for eruptions investigated, allows creation of Mt Etna ‘standard’ (3-eruptions mean) emissivity-radiance-temperature trends (Fig. 5.3) and ‘look-up’ tables (Table 5.1 and Appendix E) to serve as input parameters using ‘thresholds’ approach, for spaceborne multi-platform analyses (e.g., OLI, Sentinel-2A, MODIS), specific for Mt Etna.

Plotted ‘standard’ Mt Etna data, (Fig. 5.3), including errors (Appendix E) indicates that largest emissivity variation is in MIR (28 %), varying between 0.758 and 0.483 at 773 and 1373 K respectively, whereas emissivity variation with temperature in upper SWIR (2.17-2.35 μm) is 11% (0.817 at 773 K and 0.706 at 1373 K). Smallest emissivity variation (6%) was found in TIR, ranging from 0.964 to 0.912 at 773 K and 1373 K respectively.

Table 5.1 Mt Etna 'standard' modelled Emissivity-Temperature Trends in SWIR, MIR and TIR

SWIR (1.65 μm and 2.20 μm)

Temperature (K)	773	823	873	923	973	1023	1073	1123	1173	1223	1273	1323	1373
Emissivity	0.82	0.82	0.83	0.83	0.83	0.82	0.81	0.80	0.79	0.77	0.75	0.73	0.71
Error	0.04	0.02	0.01	0.01	0.02	0.01	0.01	0.01	0.02	0.02	0.02	0.03	0.02
RAD SWIR1	2.14	4.50	8.10	14.3	23.0	34.8	50.96	70.71	101.4	131.1	161.8	214.6	267.3
RAD SWIR2	4.30	7.60	11.4	17.5	25.4	33.4	44.8	56.3	75.8	90.5	104.4	130.8	151.3

MIR (3.98 μm)

Temperature (K)	773	823	873	923	973	1023	1073	1123	1173	1223	1273	1323	1373
Emissivity	0.76	0.74	0.72	0.70	0.69	0.67	0.65	0.62	0.60	0.57	0.54	0.51	0.48
Error	0.01	0.01	0.01	0.01	0.01	0.01	0.01	0.01	0.02	0.01	0.01	0.02	0.01
RAD MIR	873	1099	1413	1721	2020	2391	2712	3030	3462	3728	3879	4342	4460

TIR1 (11.00 μm)

Temperature (K)	773	823	873	923	973	1023	1073	1123	1173	1223	1273	1323	1373
Emissivity	0.96	0.96	0.95	0.95	0.95	0.94	0.94	0.93	0.93	0.92	0.92	0.91	0.90
Error	0.02	0.01	0.01	0.01	0.01	0.01	0.01	0.01	0.01	0.01	0.01	0.01	0.01
RAD TIR1	160	180	202	223	245	267	288	311	331	354	376	395	417

TIR2 (12.0 μm)

Temperature (K)	773	823	873	923	973	1023	1073	1123	1173	1223	1273	1323	1373
Emissivity	0.97	0.97	0.96	0.96	0.96	0.95	0.95	0.94	0.93	0.93	0.92	0.92	0.91
Error	0.01	0.01	0.01	0.01	0.01	0.01	0.01	0.01	0.01	0.01	0.01	0.01	0.01
RAD TIR2	121	136	152	167	182	198	213	229	242	259	274	288	303

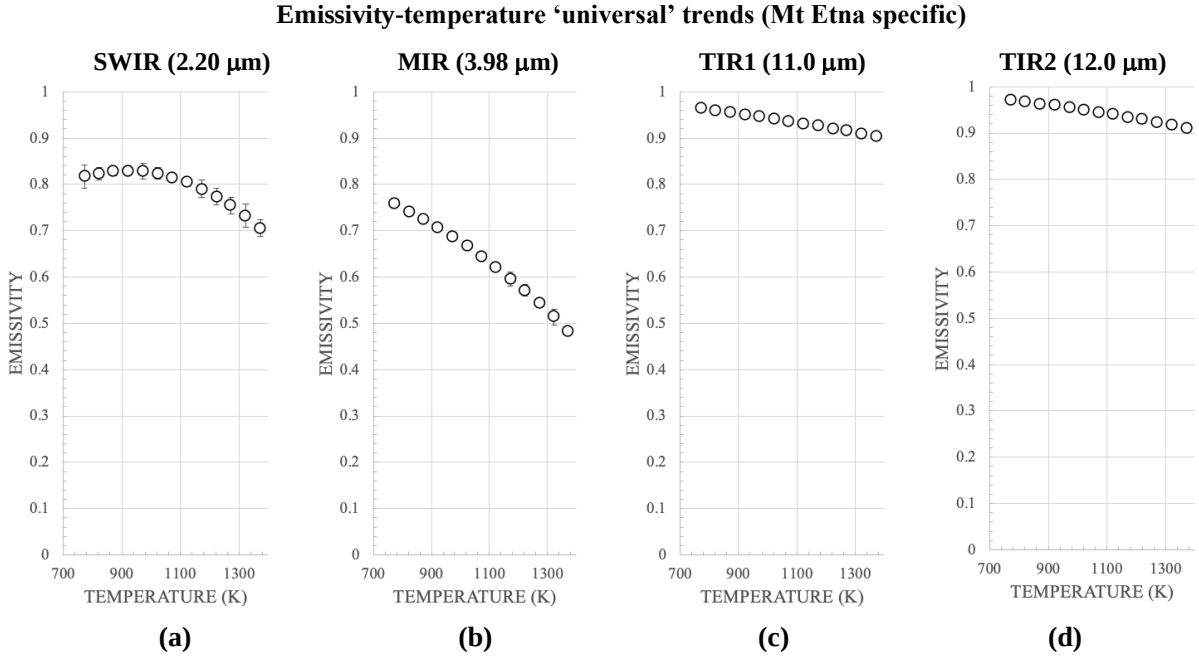

Figure 5.3 Mt Etna specific 'standard' emissivity-temperature trends, derived from all available FTIR data (3-eruptions mean) to serve as spaceborne input parameters at **(a)** high-spatial resolution SWIR, as well as **(b)** MODIS' MIR and **(c-d)** TIR bands wavelengths**.**

5.3.1 Variation in 'Dynamic Trends' driven by the composition

To assess wider applicability of multicomponent emissivity-temperature behaviour, developed here for the trachy-basaltic Mt Etna, two additional and distinctly different sites were considered; an andesitic subduction volcano, Lascar (Chile) and an intraplate tholeiitic basalt volcano, Kilauea (Hawaii).

I measured emissivity data, where emissivity was determined by means of radiance (method in Section 2.2.5) for Lascar volcano (sample courtesy of S. Self, OU, U.K.), from a 1993 lava. Lascar volcano in northern Chile is a subduction zone stratovolcano, with recent cyclic activity starting in 1984, which ended up producing its largest historical Plinian to sub-Plinian eruption in 1993 (Matthews et al., 1997). Emissivity data for Kilauea (Hawaii) were obtained from the February 2018 Puu Oo lava coastal plain lava flow field (sample data courtesy of the IVIS Laboratory, University of Pittsburgh). The lower East Rift Zone eruption and summit collapse are considered to be the largest event occurring in the last two centuries (Anderson et al., 2019).

The chemical composition for Kilauea, Mt Etna and Lascar samples (Table 5.2) have been plotted to reveal a total alkali silica (TAS) content (Fig. 5.4).

Table 5.2 Total Silica Alkali content in wt.% for volcanoes analysed

Volcano Location	Silica (SiO_2)	Alkali ($Na_2O + K_2O$)
Mt Etna, Italy	47.73	5.41
Lascar, Chile	57.70	4.83
Hawaii	49.93	2.46

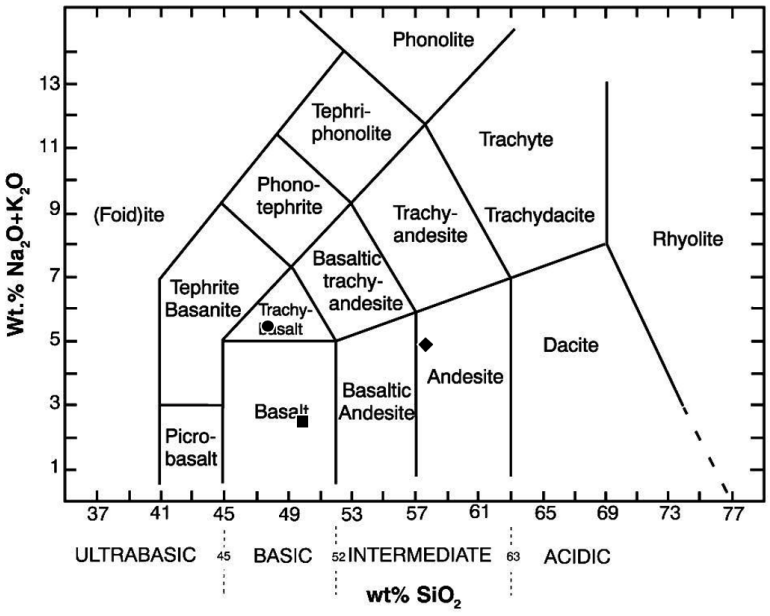

Figure 5.4 Derived total alkali silica (TAS) content for Mt Etna, Italy (filled black circle), Lascar, Chile (filled black diamond) and Kilauea, Hawaii (filled black square).

These are consistent with previous compositional findings for the three sites investigated (Robidoux et al., 2020; Giordano and Dingwell, 2003; Wolfe and Morris, 1996). The three-sample series of different composition all show comparable variation in emissivity with temperature (Fig. 5.5 and Appendix F), which may support the claim that emissivity is composition dependent. Different volcanic settings, eruption styles and lava types for samples analysed are not discussed here, as results from this analysis are used solely to compare emissivity trends with temperature change for compositionally different sites.

Emissivity-temperature trends presented here (Figs. 5.5 and 5.6), which I measured and determined by means of radiance (Section 2.2.5), have been derived for MODIS' MIR and TIR wavelengths (3.98 μm, and 11.0 μm and 12.0 μm respectively), extracted and modelled from very-high FTIR data (Appendix F).

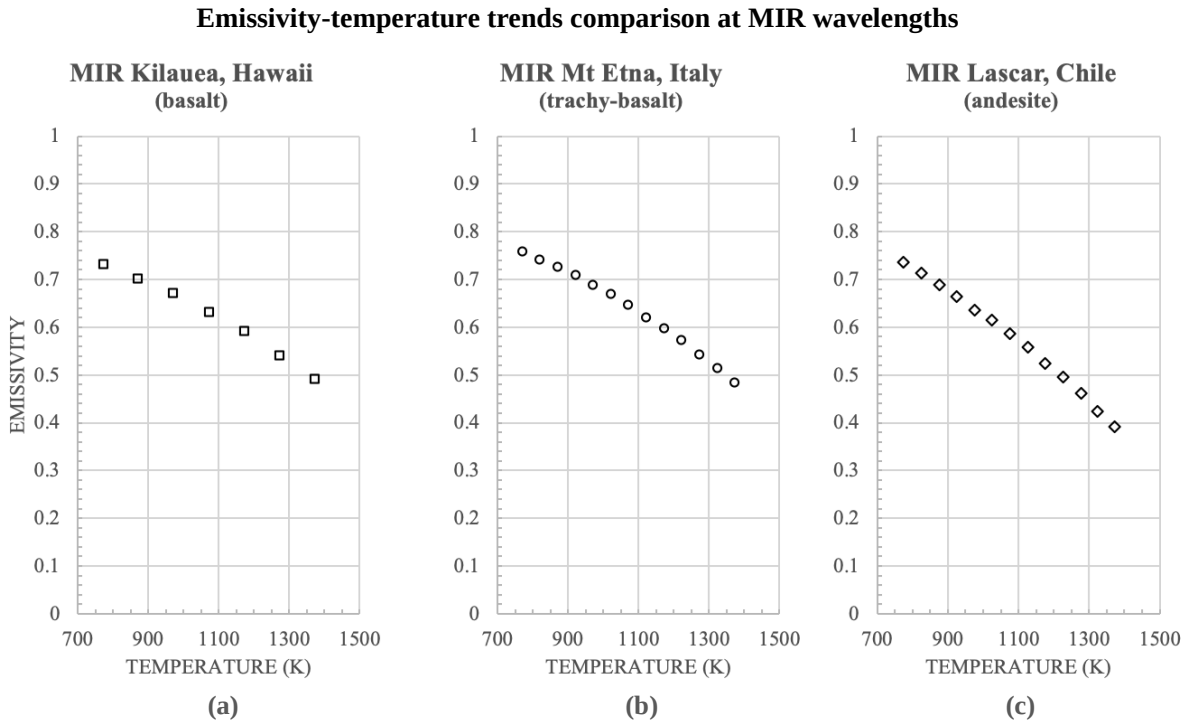

Figure 5.5 Emissivity-temperature trends in comparison in MODIS' MIR (3.98 μm wavelength) for **(b)** Mt Etna 'standard' (Table 5.1 and Fig. 5.2), **(b)** Lascar, Chile (1993 eruption) and **(c)** Kilauea**,** Hawaii (2018 eruption).

Emissivity trend (Fig. 5.5 a-c) in MODIS' MIR band 21 (3.98 μm) shows emissivity decrease with temperature increase (773-1373 K) by 24% for Kilauea (0.730-0.490), 28% (0.758-0.483) for Mt Etna and 35% for Lascar (0.735-0.390).

Emissivity-temperature trends comparison at TIR wavelengths

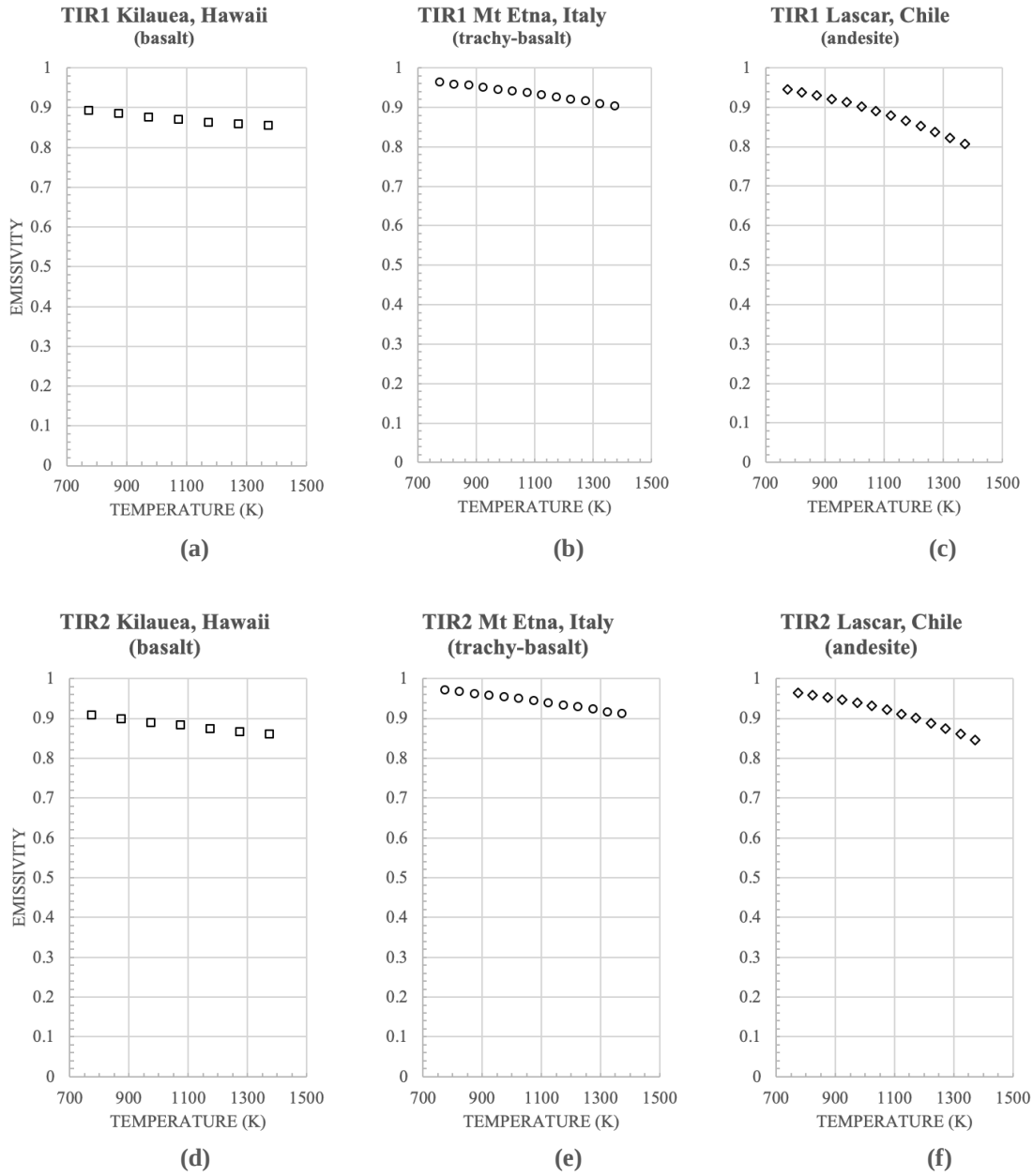

Figure 5.6 Emissivity-temperature trends in MODIS' TIR1 **(a-c)** and TIR2 **(d-f)** wavelengths (11.0 μm and 12.0 μm respectively) for **(a & d)** Mt Etna 'standard' (Table 5.1 and Fig. 5.2) **(b & e)** Lascar, Chile (1993 eruption) and **(c & f)** Kilauea**,** Hawaii (2018 eruption).

Emissivity trend (Fig. 5.6 a-c) in MODIS' TIR1 band 31 (11.0 μm) shows emissivity decrease with temperature increase (773-1373 K) by 4% for Kilauea (0.893-0.856), 6% (0.964-0.904) for Mt Etna and 14% for Lascar (0.944-0.806).

Emissivity trend (Fig. 5.6 d-f) in MODIS' TIR2 band 32 (12.0 μm) shows emissivity decrease with temperature increase (773-1373 K) by 5% for Kilauea (0.908-0.860), 6% (0.972-0.912) for Mt Etna and 12% for Lascar (0.964-0.846).

Emissivity-temperature trends comparison at MODIS' MIR and TIR wavelengths

MIR (3.98μm)

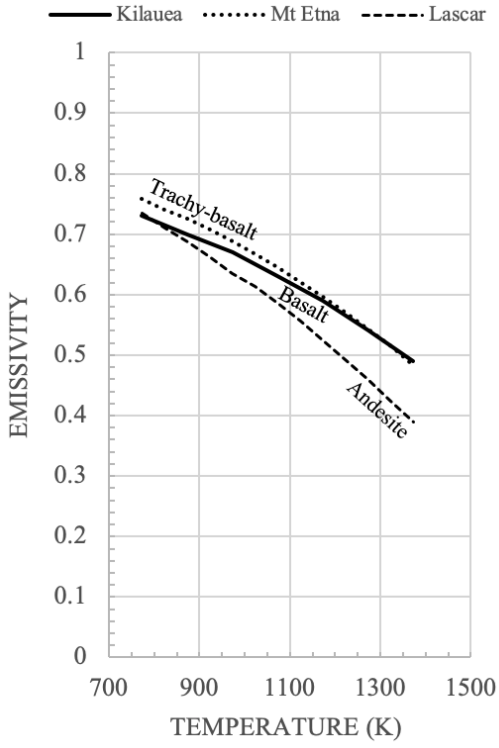

(a)

TIR1 (11.0 μm)

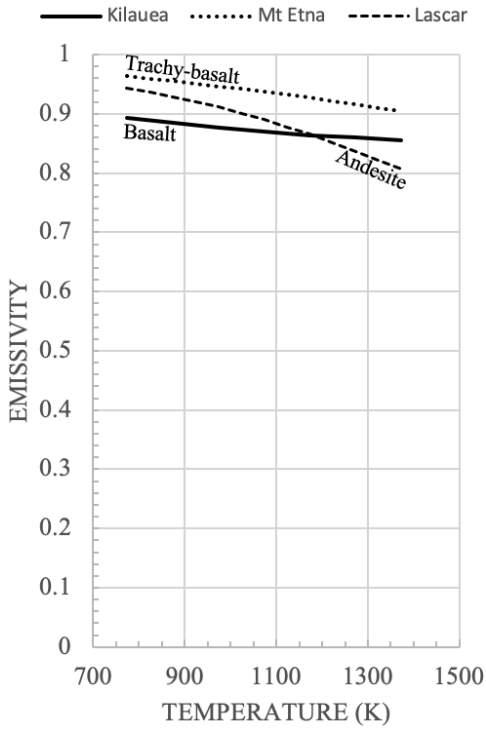

(b)

TIR2 (12.0 μm)

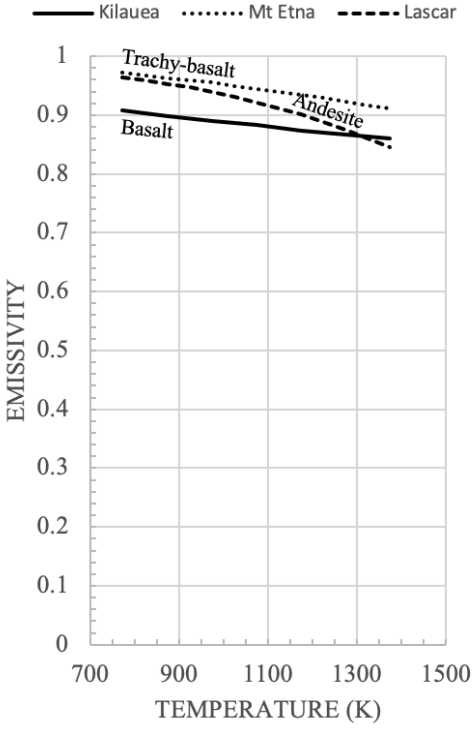

(c)

Figure 5.7 Trends diversity in MODIS' **(a)** MIR (3.98 μm) and **(b-c)** TIR bands (11.0 μm and 12.0 μmm respectively). Distinct compositional trends can be identified for trachy-basalt (Mt Etna), andesite (Lascar) and basalt (Kilauea).

In MIR (Fig. 5.7 a) trachy-basalt (Mt Etna) is comparable to the more tholeiitic basalt (Kilauea), with a maximum difference ≤ 0.03, whereas andesite shows larger difference with both (basalt and trachy-basalt), especially with temperature increase (≤ 0.1). In TIR (Figs. 5.7 b-c), silica-rich andesite follows similar trend(s) seen in MIR, when compared to trachy-basalt, showing a difference ≤ 0.1, which increases at temperatures >900 K. The tholeiitic basalt shows markedly different ('flat') trend(s) in TIR, demonstrating that emissivity is both wavelength and composition dependent, as it produced a marked distinction in spectral signatures (≤ 0.1) between compositionally different sample groups.

Since there are no reliable data available at the time of writing for Kilauea and Lascar in SWIR, this wavelength range could not be included into the compositional comparison analysis presented here. Nevertheless, this exercise clearly shows that emissivity is not only wavelength and temperature dependent, but it also depends on composition. Moreover, Figure 5.7 indicates that the most evolved lava sample, in this case andesitic Lascar, displays the largest change in emissivity with temperature, whereas the most primitive lava (Kilauea) has the smallest change.

Future work to generalize the findings presented in this section (Fig. 5.7 and Appendix F), would involve measurements from extensive suites of samples representing different volcanic settings to complement and constrain the in-depth analyses and trends developed here for Mt Etna.

6 Automated volcano monitoring systems: 2020

6.1 Space-based automated systems

Currently operational space-based automated volcano monitoring systems, and systems discussed previously (Chapter 1) are employed to search the surface of the Earth for thermal emission signatures, which may imply changes in activity, or can simply provide information on volcano's activity status (Ramsey and Harris, 2013).

A few monitoring systems are established and operated by national and international monitoring agencies (e.g., USGS, NOAA, Copernicus EMS, Eumetsat, JMA) where the focus is either on observing specific regions of interest at various spatial and temporal resolutions, or on global/supracontinental monitoring in (near) real-time, and at low-to moderate spatial resolution. These are robust and enduring systems that may not specifically address volcanic activity but have a wider scope on land and atmospheric hazards, and emergency management support. Additionally, a limited number of spaceborne systems with global volcano monitoring aimed at global volcano monitoring, mostly arising from successful research projects, have been developed and operated by universities and research institutions. Some of such systems in operation today are used for continuous and (near) real-time automated volcano monitoring.

Examples of such system, based on MODIS data, where MODVOLC (Wright et al., 2004) and MIROVA (Middle Infrared Observation of Volcanic Activity, (Coppola et al., 2016) appear to be the most used for this purpose (Coppola et al., 2020) may provide synthetic information in regions which do not have resources to operate ground networks. MODVOLC (Wright, 2016; Wright et al., 2004) uses infrared satellite data acquired by NASA's two MODIS sensors on Terra and Aqua satellites to detect and identify hot-spot pixels and measure radiant flux on a global scale by performing a single pixel fixed threshold analysis. This 'always-on' moderate-spatial and temporal resolution system has been used widely to detect and catalogue thermal emission signatures of volcanic unrests globally, by utilizing both MIR and TIR thermal channels to measure spectral radiance emitted by high-temperature thermally anomalous targets on the ground. While principally used to observe wildfires, MODIS' MIR channel has been successfully used to quantify the energy radiated by active lavas of significantly smaller dimensions than the instruments' sampling size (Wright, 2016). Similarly, MIROVA is an automated volcano hot-spot detection system, also based on MODIS' data, providing thermal flux time series for over 200 volcanoes worldwide (Coppola et al., 2020). In contrast, a spaceborne volcano monitoring system HOTVOLC (Gouhier et al., 2016), uses geostationary platforms (MSG-SEVIRI, MTSAT

and GOES-Imager), providing data every 15 minutes to monitor (near) real-time activity (hot-spots detection, lava flow volumes and discharge rates).

In addition to several automated volcano monitoring systems developed over the last 30 years to detect volcanic hotspots (Chapter 1), VAST (Higgins and Harris, 1997) and HOTSAT (Cappello et al., 2019; Del Negro et al., 2016) approaches consider the difference between the pixel's temperature and that of its surrounding pixels. The latter shows how distinctly different spatial and temporal capabilities of MODIS and SEVIRI can be exploited for automated volcano monitoring and was tested on Mt Etna's 2017 eruption (Chapter 4). One of the most successful satellite instruments, used for volcanic surveillance, ASTER (onboard Terra), has been effectively employed (2000-2008) for hotspot detection (Reath et al., 2019) and utilized its multispectral data for building the ASTER Volcano Archive (AVA, 2020) for ~1500 recently active volcanoes worldwide.

A more recent system, Monitoring Unrest from Space system (MOUNTS), based on Sentinel data (Sentinel-1, Sentinel-2 and Sentinel-5P) uses multi-platforms to provide a range of information on the unrest (Valade et al., 2019). Another new method (Massimetti et al., 2020) compares results from high-spatial resolution data with the existing operational approaches and has been developed for hot spot detection. This new approach uses high-spatial resolution Sentinel-2 with MODIS-MIROVA thermal data and shows that multi-sensors would increase monitoring capabilities if integrated into the currently operational automated systems. However, the purpose of that study using SWIR data was merely to detect the size, number and location of hot pixels of high-temperature thermal anomaly. Their approach does not involve calculation of pixel integrated temperatures or radiant heat flux.

Despite being used for decades to study discrete active volcanism, a global volcano monitoring system using high-spatial resolution sensors (e.g., Landsat-class) has not been integrated into the existing automated systems. This may predominantly be due to the limiting temporal resolution of these sensors. Nonetheless, a recent study introduced a new semi-automated platform (Layana et al., 2020b, 2020a), Volcanic Anomalies Monitoring System (VOLCANOMS), exploiting high-spatial resolution Landsat series data in NIR and SWIR to detect volcanic thermal anomalies, compute effective temperatures, and total radiant heat and mass fluxes. This approach applied well-established methods (Blackett, 2014) but it applies emissivity of a specific volcano based on ASTER 05 surface emissivity spaceborne data as an input parameter for seven volcanic sites, which has been identified as 'static' (Chapter 2).

The current and future monitoring systems can benefit from a combination of payloads with high refresh rates and high-spatial resolution, which can be balanced by moderate temporal and spatial resolutions. This could be achieved by building upon the EVOSS project (Ferrucci et al., 2014), as one of several significant systems (Chapter 1) that had marked the development of a complete and global monitoring capacity (discussed in Section 6.2).

6.2 The 'ideal' volcano monitoring system

Various RS methods and automated projects to date (Chapter 1 and section 6.1) have fulfilled some requirements (to a varying degree) necessary to establishing an 'ideal' volcano monitoring system. Nonetheless, the lack of multi-platform, multi-payload integration to overcome large pixel, single-parameter methodologies in global volcano monitoring has been identified. The closest to an advanced multi-parameter, multi-technique integration was delivered in the EC-FP7 EVOSS project (2010-2013), with the developed system kept in automated-unsupervised operation from November 2011 until July 2016.

EVOSS project demonstrated that the prospect of providing multi-parameters volcano monitoring service worldwide (and/or for specific individual targets) is feasible. The project provided a break-through in (near) real-time monitoring operations by using a multi-technique approach, which focussed on multi-parameters results delivery at high-to-very high temporal resolution framework. The blend of advanced processing techniques for detecting and simultaneously analysing high-temperature features, syn-eruptive ground deformation, volcanic gases and volcanic ash at erupting (or unresting) volcanoes in Europe, Africa, the ocean islands and the Antilles covered ~150 volcanoes.

For thermal analysis, both (i) geostationary and (ii) wide-swath LEO platforms were exploited. Most of the original platforms used for the EVOSS-style thermal, SO_2, ash and deformation retrievals are still operational and enhanced with certain upgrades, included in the outline here.

Due to very-high refresh rate requirements (15-30 min) suitable candidates in 2010 were (i) SEVIRI onboard (MSG), the Japanese Advanced Meteorological Imager (JAMI) onboard Multifunction Transport Satellite (MTSAT), and the Imager onboard Geostationary Operational Environmental Satellite (GOES). Today, SEVIRI is still operational at a time of writing and accompanied, in multispectral content, by GOES and HIMAWARI 3rd generation series, all of which are capable of EVOSS-style operations worldwide.

For (ii) polar satellites that provided daily revisits were exploited. In particular MODIS onboard Terra and Aqua, as well as Advanced Very High-Resolution Radiometer (AVHRR) onboard NOAA. In addition to these, Visible Infrared Imaging Radiometer Suite (VIIRS), also operated by NOAA with comparatively moderate-to-high spatial resolution (375-750 m) and global coverage twice daily, can be added to this category, as it has capability of detecting volcanic hot-spots and fires, among similar targets (Faruolo et al., 2020). Although, Landsat 8 and MSI's Sentinel-2A and 2B would greatly contribute and improve both spatial and spectral resolution thermal analyses.

From the work presented in this thesis, the EVOSS-style thermal procedures (i.e., radiant and mass fluxes) remain relevant and with significant scope for improvement. The EVOSS approach prioritised high-to-very high temporal resolution data, primarily exploiting instruments equipped with at least one MIR and two TIR channels. Nonetheless, procedures including high-spatial resolution SWIR data (when available) have been developed for volcanic hotspot detection and computation of physical parameters, such as radiant and mass fluxes. Combining all these results presented in this thesis would provide (near) real-time and improved quality data for volcano monitoring, with a potential to include ground deformation and gas analyses.

6.3 Discussion and Conclusions

The volcano research science and the data user community have for many years relied on coarse spatial resolution ($\geq$ 1 km) spaceborne data in MIR and TIR, overlooking the impact that input parameters, such as emissivity can have on monitoring active volcanoes (Chapters 2, 3 and 4). This may be driven both by lack of reliable information on emissivity's behaviour with temperature and by dynamic nature of volcanic hazards, favouring higher repeat interval (temporal resolution) over the greater detail (spatial resolution).

However, the large instantaneous field of view of high-temporal (low spatial) resolution sensors, such as SEVIRI for example tend not to favour target detection, as background radiance may dominate the signal from relatively small dimensions of a hot target on the ground (i.e., lava flow). For this reason, the approach developed in this thesis was not extended to geostationary platforms, as the pixels are too large and too heterogeneous, from the aspect of emissivity standpoint, in most non-desertic areas.

Current operational satellite-based volcano monitoring systems appear to be lacking in (a) spatial resolution for volcanic products of smaller dimensions, which remains a major limitation for an accurate operational and tactical volcanic crises management, and (b)

appropriate input parameters. It has been established that the majority of studies to date use constant emissivity of the target from spectral libraries (e.g., ASTER GED), neglecting the thermal component. The need for improved methods for deriving appropriate and accurate emissivity data, proposed in this thesis is driven by its demonstrated variation with wavelength and temperature (Chapter 2), as well as the variation with composition (Chapter 5).

The accuracy of spaceborne thermal estimates and computation of apparent surface temperatures relies on these input parameters, which affect subsequent analyses that rely on the accuracy of this measurement.

As pixels can also be occupied by more than one temperature component (and emissivity), an analytical (sub-resolutions) approach is commonly used to resolve effective temperatures. Therefore, sensors with high-spatial resolution SWIR data are most appropriate for monitoring applications (Chapters 3 and 4), as these they can provide improved information to constrain thermal phenomena and estimates related to volcanic radiant heat (and mass) flux, as well as other applications (Schroeder et al., 2016).

Landsat-class instruments, complemented by missions of similar scope, such as Sentinel-2, as well as VIIRS are characterized by relatively high-spatial resolution (30, 20 and 375 m respectively). Temporal resolution of these platform may vary from 16 days to twice daily but if incorporated, they have the potential of transforming an EVOSS-style data acquisition and analyses and improve volcano monitoring efforts. Collectively, the integration of appropriate available instruments can provide satellite-based spatially refined array of data at sufficient temporal and spatial resolutions to provide an improved support for volcanic hazard assessment and risk mitigation.

A multi-sensor data approach, integrating IR observation from different spaceborne platforms, including SWIR data has been suggested to improve information for an individual target (Plank et al., 2019) and detection (e.g., Hotmap) of set of targets (Murphy et al., 2016). Nonetheless, although previously proposed (Marchese et al., 2019; Murphy et al., 2016), it appears that no operational system is currently actively using high-spatial resolution SWIR-based data for volcano monitoring tasks or automated web-based volcanic detection systems, which could constrain MIR-TIR uncertainty for moderate-to-high-temporal, large pixel data (>1 km) to better interpret the thermal signals.

Solitary high-spatial resolution images have been used here (Chapters 3 and 4) to assess uncertainty in radiant heat flux produced by moderate-to high resolution instruments. It is however beneficial to exploit the enormous amount of currently available high-temporal

resolution baseline data to quantify the natural variability of the volcanic systems under investigation, as solitary ‘snap-shot’ data alone cannot produce the temporal detail needed to track and monitor dynamic volcanic activity.

Fully automated procedures currently available for (near) real-time volcano monitoring at high refresh rate is considered mandatory for maintaining consistent and reliable processing. On the other hand, fully automated processing of high-spatial resolution data may not be viewed as essential, given the acquisition rates (5-16 days). However, assimilation of results from these platforms would further improve efficiency and constrain multi-platform data uncertainty. This proposed tactical global volcano monitoring integration for automated high- moderate-to-low spatial resolution routines, previously operating (Ferrucci and Hirn, 2016; Tait and Ferrucci, 2013; Hirn et al., 2010, 2008), complete with updated information on input parameters (Chapters 2 and 5) can improve the strategic EO and monitoring efforts.

Building on findings presented in this thesis both on emissivity behaviour with temperature and its impact on spaceborne and modelling applications, a methodology expansion is proposed to enhance the existing monitoring networks. Integration of IR satellite sensors currently available in SWIR-MIR-TIR bands would improve monitoring capabilities to characterize volcanic activity with an exceptional level of accuracy and detail. The multi-sensor approach would provide a joint contribution to investigate, monitor and characterize thermal volcanic activity, where high-to-moderate temporal resolution data (e.g., SEVIRI, MODIS) allows detection and onset of eruption, and high-spatial resolution data (e.g., Landsat-8 OLI, MSI Sentinel-2) would refine geometry and detail of active flow advance. Although extensively assessed solely for Mt Etna in this thesis, input parameters for other volcanoes (Chapter 5) appear to be sufficiently stable in MIR and TIR wavelengths, thus expected to be applicable globally. Nonetheless, further assessment using laboratory and RS applications should be applied to a wider range of volcanic targets to confirm and validate this claim.

The concept of an EVOSS-style volcano monitoring system (Ferrucci et al., 2014; Tait and Ferrucci, 2013; Theys et al., 2013) outlined in Section 6.2 is paralleled with previous work on multi-platform, multi-payload high-temperature RS (Ferrucci and Hirn, 2016; Harris, 2013a; Hirn et al., 2010, 2009, 2008; Oppenheimer, 1993; Rothery et al., 1988). The existing gap in thermal RS procedures and uncertainty involving computation of radiant heat fluxes related to accuracy of spaceborne input parameters has been highlighted in this thesis. This can be rectified by an automatic processing of high-to moderate and low spatial

resolution payloads, acquiring appropriate emissivity through radiance-temperature links, according to ‘look-up’ tables or applying the ‘laws’ presented here for quantitative sub-resolution processing. This will ensure coverage in both high-temporal and high-spatial resolutions.

Remote analyses of the radiant heat flux conversion to mass flux requires a priori knowledge of several specific site dependent parameters (Wright et al., 2001), as does the ‘distance-to-run’ approach (Kilburn, 2015, 1996; Calvari and Pinkerton, 1998), thus these approaches may remain a semi-quantitative estimate, based on average behaviour of molten lavas.

Therefore, furnished with improved input parameters (multicomponent emissivity), the novel approach presented in this thesis can be tested fully by an improved version of an unsupervised EVOSS-style, multi-payload, multi-parameter volcano monitoring and modelling system. This is currently within reach for Mt Etna with a potential for global application, leveraging the sustainable data provision in the very long term by three major meteorological agencies (Eumetsat, JMA and NOAA), as well as the high-resolution USGS and Copernicus polar observing systems.

7 References

Acocella, V., Neri, M., Behncke, B., Bonforte, A., Del Negro, C., Ganci, G., 2016. Why does a mature volcano need new vents? The case of the new Southeast crater at Etna. Front. Earth Sci. 4, 1–16. https://doi.org/10.3389/feart.2016.00067

Allard, P., Behncke, B., D'Amico, S., Neri, M., Gambino, S., 2006. Mount Etna 1993-2005: Anatomy of an evolving eruptive cycle. Earth-Science Rev. 78, 85–114. https://doi.org/10.1016/j.earscirev.2006.04.002

Anderson, K.R., Johanson, I.A., Patrick, M.R., Gu, M., Segall, P., Poland, M.P., Montgomery-Brown, E.K., Miklius, A., 2019. Magma reservoir failure and the onset of caldera collapse at Kīlauea Volcano in 2018. Science (80-.). 366. https://doi.org/10.1126/science.aaz1822

Andronico, D., Branca, S., Calvari, S., Burton, M., Caltabiano, T., Corsaro, R.A., Del Carlo, P., Garfi, G., Lodato, L., Miraglia, L., Murè, F., Neri, M., Pecora, E., Pompilio, M., Salerno, G., Spampinato, L., 2005. A multi-disciplinary study of the 2002-03 Etna eruption: Insights into a complex plumbing system. Bull. Volcanol. 67, 314–330. https://doi.org/10.1007/s00445-004-0372-8

Andronico, D., Lodato, L., 2005. Effusive activity at Mount Etna volcano (Italy) during the 20th century: A contribution to volcanic hazard assessment. Nat. Hazards 36, 407–443. https://doi.org/10.1007/s11069-005-1938-2

AVA, 2020. ASTER Volcano Archive [WWW Document]. URL https://ava.jpl.nasa.gov/about.php (accessed 7.1.20).

Bailey, J.E., Harris, A.J.L., Dehn, J., Calvari, S., Rowland, S.K., 2006. The changing morphology of an open lava channel on Mt. Etna. Bull. Volcanol. 68, 497–515. https://doi.org/10.1007/s00445-005-0025-6

Ball, M., Pinkerton, H., 2006. Factors affecting the accuracy of thermal imaging cameras in volcanology. J. Geophys. Res. Solid Earth 111, n/a-n/a. https://doi.org/10.1029/2005JB003829

Barsi, J.A., Barker, J.L., Schott, J.R., 2003. Web-Based Atmospheric Correction Tool for Single Thermal Band Instrument [WWW Document]. URL https://atmcorr.gsfc.nasa.gov/ (accessed 9.25.19).

Barsi, J.A., Schott, J.R., Palluconi, F.D., Hook, S.J., 2005. Validation of a web-based atmospheric correction tool for single thermal band instruments. Earth Obs. Syst. X 5882, 58820E. https://doi.org/10.1117/12.619990

Behncke, B., Fornaciai, A., Neri, M., Favalli, M., Ganci, G., Mazzarini, F., 2016. Lidar

surveys reveal eruptive volumes and rates at Etna, 2007-2010. Geophys. Res. Lett. 43, 4270–4278. https://doi.org/10.1002/2016GL068495

Behncke, B., Neri, M., 2003. The July–August 2001 eruption of Mt. Etna (Sicily). Bull. Volcanol. 65, 461–476. https://doi.org/10.1007/s00445-003-0274-1

Bilotta, G., Cappello, A., Hérault, A., Del Negro, C., 2019. Influence of topographic data uncertainties and model resolution on the numerical simulation of lava flows. Environ. Model. Softw. 112, 1–15. https://doi.org/10.1016/j.envsoft.2018.11.001

Bilotta, G., Cappello, A., Herault, A., Ganci, G., Del Negro, C., 2016. MAGFLOW : a physics-based model for the dynamics of lava-flow emplacement. Geol. Soc. Spec. Publ. 357–373.

Bilotta, G., Cappello, A., Hérault, A., Vicari, A., Russo, G., Del Negro, C., 2012. Sensitivity analysis of the MAGFLOW Cellular Automaton model for lava flow simulation. Environ. Model. Softw. 35, 122–131. https://doi.org/10.1016/j.envsoft.2012.02.015

Blackett, M., 2017. An overview of infrared remote sensing of volcanic activity. J. Imaging 3. https://doi.org/10.3390/jimaging3020013

Blackett, M., 2014. Early analysis of landsat- 8 thermal infrared sensor imagery of volcanic activity. Remote Sens. 6, 2282–2295. https://doi.org/10.3390/rs6032282

Borgström, S., Seifert, F.M., Tampellini, L., Ratti, R., 2008. GlobVolcano project overview. Proc. 2008 2nd Work. USE Remote Sens. Tech. Monit. Volcanoes Seism. Areas, USEReST 2008 1–6. https://doi.org/10.1109/USEREST.2008.4740334

Branca, S., Coltelli, M., Groppelli, G., Lentini, F., 2011. Geological map of Etna volcano, 1:50,000 scale. Ital. J. Geosci. 130, 265–291. https://doi.org/10.3301/IJG.2011.15

Brown, S.K., Loughlin, S.C., Sparks, R.S.J., Vye-Brown, C., Barclay, J., Calder, E., Cottrell, E., Jolly, G., Komorowski, J.C., Mandeville, C., Newhall, C., Palma, J., Potter, S., Valentine, G., 2015. Global volcanic hazard and risk, Global Volcanic Hazards and Risk. https://doi.org/10.1017/CBO9781316276273.004

Calvari, S., Pinkerton, H., 1998. Formation of lava tubes and extensive flow field during the 1991-1993 eruption of Mount Etna. J. Geophys. Res. Solid Earth 103, 27291–27301. https://doi.org/10.1029/97jb03388

Cappello, A., Bilotta, G., Neri, M., Negro, C. Del, 2013. Probabilistic modeling of future volcanic eruptions at Mount Etna. J. Geophys. Res. Solid Earth 118, 1925–1935. https://doi.org/10.1002/jgrb.50190

Cappello, A., Ganci, G., Bilotta, G., Corradino, C., Hérault, A., Del Negro, C., 2019.

Changing Eruptive Styles at the South-East Crater of Mount Etna: Implications for Assessing Lava Flow Hazards. Front. Earth Sci. 7, 1–10. https://doi.org/10.3389/feart.2019.00213

Cappello, A., Ganci, G., Bilotta, G., Herault, A., Zago, V., Del Negro, C., 2018. Satellite-driven modeling approach for monitoring lava flow hazards during the 2017 Etna eruption. Ann. Geophys. Geophys. 61. https://doi.org/10.4401/ag-7792

Cappello, A., Ganci, G., Calvari, S., Perez, N.M., Hernandez, P.A., Silva, S. V, Cabral, J., Del Negro, C., 2016. Lava flow hazard modelling during the 2014-2015 Fogo eruption, Cape Verde. J. Geophys. Res. Solid Earth 2290–2303. https://doi.org/10.1002/2015JB012666

Cappello, A., Geshi, N., Neri, M., Del Negro, C., 2015a. Lava flow hazards—An impending threat at Miyakejima volcano, Japan. J. Volcanol. Geotherm. Res. 308, 1–9. https://doi.org/10.1016/j.jvolgeores.2015.10.005

Cappello, A., Zanon, V., Del Negro, C., Ferreira, T.J.L., Queiroz, M.G.P.S., 2015b. Exploring lava-flow hazards at Pico Island, Azores Archipelago (Portugal). Terra Nov. 27, 156–161. https://doi.org/10.1111/ter.12143

Cigna, F., Tapete, D., Lu, Z., 2020. Remote Sensing of Volcanic Processes and Risk. Remote Sens. 12, 2567. https://doi.org/10.3390/rs12162567

Coltelli, M., Proietti, C., Branca, S., Marsella, M., Andronico, D., Lodato, L., 2007. Analysis of the 2001 lava flow eruption of Mt. Etna from three-dimensional mapping. J. Geophys. Res. Earth Surf. 112, 1–18. https://doi.org/10.1029/2006JF000598

Coppola, D., Laiolo, M., Cigolini, C., Delle Donne, D., Ripepe, M., 2016. Enhanced volcanic hot-spot detection using MODIS IR data: Results from the MIROVA system. Geol. Soc. Spec. Publ. 426, 181–205. https://doi.org/10.1144/SP426.5

Coppola, D., Laiolo, M., Cigolini, C., Massimetti, F., Donne, D.D., Ripepe, M., Arias, H., Barsotti, S., Parra, C.B., Centeno, R.G., Cevuard, S., Chigna, G., Chun, C., Garaebiti, E., Gonzales, D., Griswold, J., Juarez, J., Costa, F., 2020. Thermal Remote Sensing for Global Volcano Monitoring : Experiences From the MIROVA System 7, 1–21. https://doi.org/10.3389/feart.2019.00362

Corradino, C., Ganci, G., Cappello, A., Bilotta, G., Herault, A., Del Negro, C., 2019. Mapping Recent Lava Flows at Mount Etna Using Multispectral Sentinel-2 Images and Machine Learning Techniques. Remote Sens. 11. https://doi.org/10.3390/rs11161916

Danilina, I., Gillespie, A., Balick, L., Mushkin, A., Smith, M., O'Neal, M., 2009. Subpixel

roughness effects in spectral thermal infrared emissivity images. WHISPERS '09 - 1st Work. Hyperspectral Image Signal Process. Evol. Remote Sens. 1–4. https://doi.org/10.1109/WHISPERS.2009.5288976

Del Negro, C., Cappello, A., Ganci, G., 2016. Quantifying lava flow hazards in response to effusive eruption. Bull. Geol. Soc. Am. 128, 1–13. https://doi.org/10.1130/B31364.1

Del Negro, C., Cappello, A., Neri, M., Bilotta, G., Hérault, A., Ganci, G., 2013. Lava flow hazards at Mount Etna: Constraints imposed by eruptive history and numerical simulations. Sci. Rep. 3, 1–8. https://doi.org/10.1038/srep03493

Di Bello, G., Filizzola, C., Lacava, T., Marchese, F., Pergola, N., Pietrapertosa, C., Piscitelli, S., Scaffidi, I., Tramutoli, V., 2004. Robust satellite techniques for volcanic and seismic hazards monitoring. Ann. Geophys. 47.

Dozier, J., 1981. A method for satellite identification of surface temperature fields of subpixel resolution. Remote Sens. Environ. 11, 221–229. https://doi.org/10.1016/0034-4257(81)90021-3

ESA, n.d. Copernicus Open Access Hub [WWW Document]. URL https://scihub.copernicus.eu/ (accessed 10.9.19).

Faruolo, M., Lacava, T., Pergola, N., Tramutoli, V., 2020. The VIIRS-Based RST-FLARE configuration: The Val d'Agri Oil Center Gas Flaring Investigation in between 2015-2019. Remote Sens. 12. https://doi.org/10.3390/rs12050819

Ferrari, S., Nestola, F., Massironi, M., Maturilli, A., Helbert, J., Alvaro, M., Domeneghetti, M.C., Zorzi, F., 2014. In-situ high-temperature emissivity spectra and thermal expansion of C 2 / c pyroxenes : Implications for the surface of Mercury. Am. Mineral. 99, 786–792.

Ferrucci, F., Hirn, B., 2016. Automated monitoring of high-temperature volcanic features: From high-spatial to very-high-temporal resolution. Geol. Soc. Spec. Publ. 426, 159–179. https://doi.org/10.1144/SP426.25

Ferrucci, F., Theys, N., Hirn, B., Clarisse, L., Valks, P., Laneve, G., van der A, R., Tait, S., Di Bartola, C., Brenot, H., 2014. Operational Integration of Spaceborne Measurements of Lava Discharge Rates and Sulfur Dioxide Concentrations for Global Volcano Monitoring, in: Wenzel, F., Zschau, J. (Eds.), Early Warning for Geological Disasters: Scientific Methods and Current Practice. Springer Berlin Heidelberg, Berlin, Heidelberg, pp. 307–331. https://doi.org/10.1007/978-3-642-12233-0_16

Flynn, L.P., Harris, A.J.L., Rothery, D.A., Oppenheimer, C., 2000. High-spatial-resolution thermal remote sensing of active volcanic features using landsat and hyperspectral

data. Geophys. Monogr. Ser. 116, 161–177. https://doi.org/10.1029/GM116p0161

Flynn, L.P., Harris, A.J.L., Wright, R., 2001. Improved identification of volcanic features using Landsat 7 ETM+. Remote Sens. Environ. 78, 180–193. https://doi.org/10.1016/S0034-4257(01)00258-9

Francis, P., Rothery, D., 2000. Remote Sensing of Active Volcanoes. Annu. Rev. Earth Planet. Sci. 28, 81–106. https://doi.org/10.1146/annurev.earth.28.1.81

Francis, P.W., Rothery, D.A., 1987. Using the Landsat Thematic Mapper to detect and monitor active volcanoes: an example from Lascar volcano, northern Chile. Geology 15, 614–617. https://doi.org/10.1130/0091-7613(1987)15<614:UTLTMT>2.0.CO;2

Ganci, G., Bilotta, G., Cappello, A., Herault, A., Del Negro, C., 2016. HOTSAT: A multiplatform system for the thermal monitoring of volcanic activity using satellite data. Geol. Soc. Spec. Publ. 426, 207–221. https://doi.org/10.1144/SP426.21

Ganci, G., Cappello, A., Bilotta, G., Corradino, C., 2019. Satellite-Based Reconstruction of the Volcanic Deposits during the December 2015 Etna Eruption. MDPI J. Data 6–13. https://doi.org/10.3390/data4030120

Ganci, G., Vicari, A., Cappello, A., Del Negro, C., 2012. An emergent strategy for volcano hazard assessment: From thermal satellite monitoring to lava flow modeling. Remote Sens. Environ. 119, 197–207. https://doi.org/10.1016/j.rse.2011.12.021

Ganci, G., Vicari, A., Fortuna, L., del Negro, C., 2011. The HOTSAT volcano monitoring system based on combined use of SEVIRI and MODIS multispectral data. Ann. Geophys. 54, 544–550. https://doi.org/10.4401/ag-5338

Gillespie, A., Rokugawa, S., Matsunaga, T., Steven Cothern, J., Hook, S., Kahle, A.B., 1998. A temperature and emissivity separation algorithm for advanced spaceborne thermal emission and reflection radiometer (ASTER) images. IEEE Trans. Geosci. Remote Sens. 36, 1113–1126. https://doi.org/10.1109/36.700995

Giordano, D., Dingwell, D.B., 2003. Viscosity of hydrous Etna basalt: Implications for Plinian-style basaltic eruptions. Bull. Volcanol. 65, 8–14. https://doi.org/10.1007/s00445-002-0233-2

Glaze, L., Francis, P.W., Rothery, D.A., 1989. Measuring thermal budgets of active volcanoes by satellite remote sensing. Nature 338, 144–146. https://doi.org/10.1038/338144a0

Gouhier, M., Guéhenneux, Y., Labazuy, P., Cacault, P., Decriem, J., Rivet, S., 2016. HOTVOLC: A web-based monitoring system for volcanic hot spots. Geol. Soc. Spec. Publ. 426, 223–241. https://doi.org/10.1144/SP426.31

Griffiths, P.R., 1975. Chemical infrared Fourier transform spectroscopy. Wiley, New York.

Guest, J.E., Duncan, A.M., 1981. Internal plumbing of Mount Etna. Nature 290, 584–586. https://doi.org/10.1038/290584a0

Hamilton, V.E., Christensen, P.R., 2000. Determining the modal mineralogy of mafic and ultramafic igneous rocks using thermal emission spectroscopy. J. Geophys. Res. E Planets 105, 9717–9733. https://doi.org/10.1029/1999JE001113

Hamilton, V.E., Wyatt, M.B., McSween, H.Y., Christensen, P.R., 2001. Analysis of terrestrial and Martian volcanic compositions using thermal emission spectroscopy 2. Application to Martian surface spectra from the Mars Global Surveyor Thermal Emission Spectrometer. J. Geophys. Res. E Planets 106, 14733–14746. https://doi.org/10.1029/2000JE001353

Harris, A., Dehn, J., Patrick, M., Calvari, S., Ripepe, M., Lodato, L., 2005. Lava effusion rates from hand-held thermal infrared imagery: An example from the June 2003 effusive activity at Stromboli. Bull. Volcanol. 68, 107–117. https://doi.org/10.1007/s00445-005-0425-7

Harris, A., Favalli, M., Steffke, A., Fornaciai, A., Boschi, E., 2010. A relation between lava discharge rate, thermal insulation, and flow area set using lidar data. Geophys. Res. Lett. 37, 1–6. https://doi.org/10.1029/2010GL044683

Harris, A., Steffke, A., Calvari, S., Spampinato, L., 2011. Thirty years of satellite-derived lava discharge rates at Etna: Implications for steady volumetric output. J. Geophys. Res. Solid Earth 116, 1–15. https://doi.org/10.1029/2011JB008237

Harris, A.J.L., 2013a. Thermal remote sensing of active volcanoes: A user's manual. Cambridge University Press. https://doi.org/10.1017/CBO9781139029346

Harris, A.J.L., 2013b. Electronic Supplement 1: Detection capabilities of thermal sensors. Therm. Remote Sens. Act. Volcanoes A User's Man. 1–57.

Harris, A.J.L., 2013c. Electronic Supplement 4: Notes on application of emissivity , atmospheric and surface re fl ection corrections. Therm. Remote Sens. Act. Volcanoes A User's Man. 1–104.

Harris, A.J.L., 2013d. Electronic Supplement 5: The dual-band method : A history of its application to volcanic hot spots. Therm. Remote Sens. Act. Volcanoes A User's Man. 1–26.

Harris, A.J.L., 2013e. Electronic Supplement 6: The dual-band method : Worked examples. Therm. Remote Sens. Act. Volcanoes A User's Man. 1–25.

Harris, Andrew J L, Butterworth, A.L., Carlton, R.W., Downey, I., Miller, P., Navarro, P., Rothery, D.A., 1997. Low- cost volcano surveillance from space: case studies from Etna, Krafla, Cerro Negro, Fogo, Lascar and Erebus. Bull Volcanol 59, 49–64. https://doi.org/10.1007/s004450050174

Harris, A.J.L., Dehn, J., Calvari, S., 2007. Lava effusion rate definition and measurement: A review. Bull. Volcanol. 70, 1–22. https://doi.org/10.1007/s00445-007-0120-y

Harris, A.J.L., Flynn, L.P., Keszthelyi, L., Mouginis-Mark, P.J., Rowland, S.K., Resing, J.A., 1998. Calculation of lava effusion rates from Landstat TM data. Bull. Volcanol. 60, 52–71. https://doi.org/10.1007/s004450050216

Harris, Andrew J.L., Keszthelyi, L., Flynn, L.P., Mouginis-Mark, P.J., Thornber, C., Kauahikaua, J., Sherrod, D., Trusdell, F., Sawyer, M.W., Flament, P., 1997. Chronology of the episode 54 eruption at Kilauea Volcano, Hawaii, from GOES-9 satellite data. Geophys. Res. Lett. 24, 3281–3284. https://doi.org/10.1029/97GL03165

Harris, A.J.L., Murray, J.B., Aries, S.E., Davies, M.A., Flynn, L.P., Wooster, M.J., Wright, R., Rothery, D.A., 2000. Effusion rate trends at Etna and Krafla and their implications for eruptive mechanisms. J. Volcanol. Geotherm. Res. 102, 237–269. https://doi.org/10.1016/S0377-0273(00)00190-6

Harris, A.J.L., Pilger, E., Flynn, L.P., Garbeil, H., Mouginis-Mark, P.J., Kauahikaua, J., Thornber, C., 2001. Automated, high temporal resolution thermal analysis of Kilauea volcano, Hawai'i, using GOES satellite data. Int. J. Remote Sens. 22, 945–967. https://doi.org/10.1080/014311601300074487

Henderson, B.G., Lucey, P.G., Jakosky, B.M., 1996. New laboratory measurements of mid-IR emission spectra of simulated planetary surfaces. J. Geophys. Res. 101, 14969–14975.

Herault, A., Vicari, A., Ciraudo, A., Del Negro, C., 2009. Forecasting lava flow hazards during the 2006 Etna eruption: Using the MAGFLOW cellular automata model. Comput. Geosci. 35, 1050–1060. https://doi.org/10.1016/j.cageo.2007.10.008

Higgins, J., Harris, A., 1997. Vast: A program to locate and analyse volcanic thermal anomalies automatically from remotely sensed data. Comput. Geosci. 23, 627–645. https://doi.org/10.1016/S0098-3004(97)00039-3

Hill, L.J., Sparks, R.S., Rougier, J.C., 2011. Risk assessment and uncertainty in natural hazards. Risk Uncertain. Assess. Nat. Hazards 9781107006, 1–18. https://doi.org/10.1017/CBO9781139047562.002

Hirn, Barbara, Bartola, C. Di, Ferro, F., 2008a. MODIS BORNE ANALYSIS OF LONG

SERIES OF RADIANT FLUXES AT ACTIVE LAVA LAKES IES Consulting Ltd . - Intelligence for Environment and Security , Rome (Italy) Università della Calabria – Department of Earth Sciences , Rende (CS), Italy Istituto Nazionale . Sperimentale 4, 370–373.

Hirn, B., Di Bartola, C., Ferrucci, F., 2010. Synergetic exploitation of meteorological geostationary payloads «SEVIRI» and «JAMI» for quantitative, real-time, global volcano monitoring. Int. Geosci. Remote Sens. Symp. 1549–1552. https://doi.org/10.1109/IGARSS.2010.5652794

Hirn, B., Di Bartola, C., Ferrucci, F., 2009. Combined use of SEVIRI and MODIS for detecting, measuring, and monitoring active lava flows at erupting volcanoes. IEEE Trans. Geosci. Remote Sens. 47, 2923–2930. https://doi.org/10.1109/TGRS.2009.2014224

Hirn, Barbara, Di Bartola, C., Ferrucci, F., 2008b. Spaceborne monitoring 2000-2005 of the Pu'u 'O'o-Kupaianaha (Hawaii) eruption by synergetic merge of multispectral payloads ASTER and MODIS. IEEE Trans. Geosci. Remote Sens. 46, 2848–2856. https://doi.org/10.1109/TGRS.2008.2001033

Hirn, B, Di Bartola, C., Laneve, G., Cadau, E., Ferrucci, F., 2008. Seviri onboard meteosat second generation, and the quantitative monitoring of effusive volcanoes in Europe and Africa. Int. Geosci. Remote Sens. Symp. 3, III-374-III–377. https://doi.org/10.1109/IGARSS.2008.4779361

Hirn, B.R., Bartola, C. Di, Laneve, G., Cadau, E., Ferrucci, F., 2008. Seviri onboard meteosat second generation, and the quantitative monitoring of effusive volcanoes in Europe and Africa, in: International Geoscience and Remote Sensing Symposium (IGARSS). pp. 374–377. https://doi.org/10.1109/IGARSS.2008.4779361

Hulley, G.C., Hook, S.J., 2013. The ASTER Global Emissivity Database (ASTER GED). Data set [37/38/39.0.12-0-15.0001] from NASA Land Processes Distributed Active Archive Center (LP DAAC). USGS/Earth Resources Observation and Science (EROS) Center [WWW Document]. URL https://lpdaac.usgs.gov (accessed 6.1.18).

Hulley, G.C., Hook, S.J., Abbott, E., Malakar, N., Islam, T., Abrams, M., 2015. The ASTER Global Emissivity Dataset (ASTER GED): Mapping Earth's emissivity at 100 meter spatial scale. Geophys. Res. Lett. 42, 7966–7976. https://doi.org/10.1002/2015GL065564

Jin, M., Liang, S., 2006. An improved land surface emissivity parameter for land surface models using global remote sensing observations. J. Clim. 19, 2867–2881.

https://doi.org/10.1175/JCLI3720.1

Kahl, M., Chakraborty, S., Pompilio, M., Costa, F., 2014. Constraints on the nature and evolution of the magma plumbing system of Mt. Etna volcano (1991-2008) from a combined thermodynamic and kinetic modelling of the compositional record of minerals. J. Petrol. 56, 2025–2068. https://doi.org/10.1093/petrology/egv063

Kahle, A.B., Alley, R.E., 1992. Separation of Temperature and Emittance in Remotely Sensed Radiance Measurements *. Remote Sens. Environ. 107–111.

Kereszturi, G., Cappello, A., Ganci, G., Procter, J., Németh, K., Negro, C. Del, Cronin, S.J., 2014. Numerical simulation of basaltic lava flows in the auckland volcanic field, New Zealand—implication for volcanic hazard assessment. Bull. Volcanol. 76, 1–17. https://doi.org/10.1007/s00445-014-0879-6

Kilburn, C.R.J., 2015. Lava Flow Hazards and Modeling, in: The Encyclopedia of Volcanoes. https://doi.org/10.1016/b978-0-12-385938-9.00055-9

Kilburn, C.R.J., 1996. Patterns and Predictability in the Emplacement of Subaerial Lava Flows Fields, in: Monitoring and Mitigation of Volcano Hazards. Springer, Berlin, pp. 491–537. https://doi.org/10.1007/978-3-642-80087-0_15

King, P.L., Ramsey, M.S., McMillan, P.F., Swayze, G., 2004. Laboratory Fourier transform infrared spectroscopy methods for geologic samples. Infrared Spectrosc. Geochemistry, Explor. Geochemistry Remote Sens. 57–91.

Kirkland, L.E., Herr, K.C., Adams, P.M., 2003. Infrared stealthy surfaces: Why TES and THEMIS may miss some substantial mineral deposits on Mars and implications for remote sensing of planetary surfaces. J. Geophys. Res. E Planets 108, 11–1. https://doi.org/10.1029/2003je002105

Komorowski, J.C., Jenkins, S., Baxter, P.J., Picquout, A., Lavigne, F., Charbonnier, S., Gertisser, R., Preece, K., Cholik, N., Budi-Santoso, A., Surono, 2013. Paroxysmal dome explosion during the Merapi 2010 eruption: Processes and facies relationships of associated high-energy pyroclastic density currents. J. Volcanol. Geotherm. Res. 261, 260–294. https://doi.org/10.1016/j.jvolgeores.2013.01.007

Korb, R., Salisbury, W., Aria, D.M.D., 1999. Thermal-infrared remote sensing and Kirchhoff ' s measurements infrared imagery of the Earth in various spectral. J. Geophys. Res. 104, 1533915350.

Kotthaus, S., Smith, T.E.L., Wooster, M.J., Grimmond, C.S.B., 2014. Derivation of an urban materials spectral library through emittance and reflectance spectroscopy. ISPRS J. Photogramm. Remote Sens. 94, 194–212.

https://doi.org/10.1016/j.isprsjprs.2014.05.005

Lautze, N.C., Harris, A.J.L., Bailey, J.E., Ripepe, M., Calvari, S., Dehn, J., Rowland, S.K., Evans-Jones, K., 2004. Pulsed lava effusion at Mount Etna during 2001. J. Volcanol. Geotherm. Res. 137, 231–246. https://doi.org/10.1016/j.jvolgeores.2004.05.018

Layana, S., Aguilera, F., Rojo, G., Vergara, Á., Salazar, P., Quispe, J., Urra, P., Urrutia, D., 2020a. Volcanic Anomalies Monitoring System (VOLCANOMS), a low-cost volcanic monitoring system based on Landsat images. Remote Sens. 12. https://doi.org/10.3390/rs12101589

Layana, S., Aguilera, F., Rojo, G., Vergara, Á., Salazar, P., Quispe, J., Urra, P., Urrutia, D., 2020b. VOLCANOMS [WWW Document]. Volcan. Anomalies Monit. Syst. (VOLCANOMS), a Low-Cost Volcan. Monit. Syst. Based Landsat Images. URL http://volcanoms.ckelar.org/ (accessed 9.14.20).

Lee, R.J., King, P.L., Ramsey, M.S., 2010. Spectral analysis of synthetic quartzofeldspathic glasses using laboratory thermal infrared spectroscopy. J. Geophys. Res. Solid Earth 115, n/a-n/a. https://doi.org/10.1029/2009JB006672

Lee, R.J., Ramsey, M.S., King, P.L., 2013. Development of a new laboratory technique for high-temperature thermal emission spectroscopy of silicate melts. J. Geophys. Res. Solid Earth 118, 1968–1983. https://doi.org/10.1002/jgrb.50197

LeMaitre, R.W., Bateman, P., Dudek, A., Keller, J., Lameyre LeBas, M.J., Sabine, P.A., Schmid, R., Sorensen, H., Streckeisen, A., Woolley, A.R., Zanettin, B., 1989. A classification and glossary of terms. Int. Union Geol. Sci. Subcomm. Syst. Igneous Rocks 193 pp.

Lombardo, V., Pick, L., Spinetti, C., Tadeucci, J., Zakšek, K., 2020. Temperature and Emissivity Separation 'Draping' Algorithm Applied to Hyperspectral Infrared Data. Remote Sens. 12, 2046. https://doi.org/10.3390/rs12122046

Marchese, F., Genzano, N., Neri, M., Falconieri, A., Mazzeo, G., Pergola, N., 2019. A multi-channel algorithm for mapping volcanic thermal anomalies by means of sentinel-2 MSI and Landsat-8 OLI data. Remote Sens. 11. https://doi.org/10.3390/rs11232876

Marchese, F., Neri, M., Falconieri, A., Lacava, T., Mazzeo, G., Pergola, N., Tramutoli, V., 2018. The contribution of multi-sensor infrared satellite observations to monitor Mt. Etna (Italy) Activity during May to August 2016. Remote Sens. 10. https://doi.org/10.3390/rs10121948

Massimetti, F., Coppola, D., Laiolo, M., Valade, S., Cigolini, C., Ripepe, M., 2020.

Volcanic Hot-Spot detection using SENTINEL-2: A comparison with MODIS-MIROVA thermal data series. Remote Sens. 12. https://doi.org/10.3390/rs12050820

Matson, M., Dozier, J., 1981. Identification of subresolution high temperature sources using a thermal IR sensor. Photogramm. Eng. Remote Sensing 47, 1311–1318.

Matthews, S.J., Gardeweg, M.C., Sparks, R.S.J., 1997. The 1984 to 1996 cyclic activity of Lascar Volcano, northern Chile: Cycles of dome growth, dome subsidence, degassing and explosive eruptions. Bull. Volcanol. 59, 72–82. https://doi.org/10.1007/s004450050176

Maturilli, A., Helbert, J., 2014. Characterization, testing, calibration, and validation of the Berlin emissivity database. J. Appl. Remote Sens. 8. https://doi.org/10.1117/1.JRS.8.084985

Maturilli, A., Helbert, J., D'Amore, M., Varatharajan, I., Rosas Ortiz, Y., 2018. The Planetary Spectroscopy Laboratory (PSL): wide spectral range, wider sample temperature range. Infrared Remote Sens. Instrum. 11. https://doi.org/10.1117/12.2319944

MIDAC corporation, 2003. MIDAC M2000 series FTIR spectrometer [WWW Document].

Murcray, F.H., Murcray, D.G., Williams, W.J., 1970. Infrared Emissivity of Lunar Surface Features. J. Geophys. Res. 75, 2662–2669.

Murphy, S.W., de Souza Filho, C.R., Wright, R., Sabatino, G., Correa Pabon, R., 2016. HOTMAP: Global hot target detection at moderate spatial resolution. Remote Sens. Environ. 177, 78–88. https://doi.org/10.1016/j.rse.2016.02.027

Murphy, S.W., Wright, R., Oppenheimer, C., Filho, C.R.S., 2013. MODIS and ASTER synergy for characterizing thermal volcanic activity. Remote Sens. Environ. 131, 195–205. https://doi.org/10.1016/j.rse.2012.12.005

Nash, D.B., Salisbury, J.W., Conel, J.E., Lucey, P.G., Christensen, P.R., 1993. Evaluation of infrared emission spectroscopy for mapping the Moon's surface composition from lunar orbit. J. Geophys. Res. 98. https://doi.org/10.1029/93je02604

Negro, C. Del, Cappello, A., Neri, M., Bilotta, G., Hérault, A., Ganci, G., 2013. Lava flow hazards at Mount Etna: Constraints imposed by eruptive history and numerical simulations. Sci. Rep. 3, 1–8. https://doi.org/10.1038/srep03493

Neri, M., Acocella, V., Behncke, B., Maiolino, V., Ursino, A., Velardita, R., 2005. Contrasting triggering mechanisms of the 2001 and 2002-2003 eruptions of Mount Etna (Italy). J. Volcanol. Geotherm. Res. 144, 235–255. https://doi.org/10.1016/j.jvolgeores.2004.11.025

Oppenheimer, C., 1998. Review article: Volcanological applications of meteorological satellites. Int. J. Remote Sens. 19, 2829–2864. https://doi.org/10.1080/014311698214307

Oppenheimer, C., 1993. Thermal distributions of hot volcanic surfaces constrained using three infrared bands of remote sensing data. Geophys. Res. Lett. 20, 431–434. https://doi.org/10.1029/93GL00500

Osterloo, M.M., Hamilton, V.E., Anderson, F.S., 2012. A laboratory study of the effects of roughness on the thermal infrared spectra of rock surfaces. Icarus 220, 404–426. https://doi.org/10.1016/j.icarus.2012.04.020

Pallister, J., Papale, P., Eichelberger, J., Newhall, C., Mandeville, C., Nakada, S., Marzocchi, W., Loughlin, S., Jolly, G., Ewert, J., Selva, J., 2019. Volcano observatory best practices (VOBP) workshops - A summary of findings and best-practice recommendations. J. Appl. Volcanol. 8. https://doi.org/10.1186/s13617-019-0082-8

Pedrazzi, D., Cappello, A., Zanon, V., Del Negro, C., 2015. Impact of effusive eruptions from the Eguas-Carvão fissure system, São Miguel Island, Azores Archipelago (Portugal). J. Volcanol. Geotherm. Res. 291, 1–13. https://doi.org/10.1016/j.jvolgeores.2014.12.012

Pieri, D., Abrams, M., 2005. ASTER observations of thermal anomalies preceding the April 2003 eruption of Chikurachki volcano, Kurile Islands, Russia. Remote Sens. Environ. 99, 84–94. https://doi.org/10.1016/j.rse.2005.06.012

Pieri, D.C., Baloga, S.M., 1986. Eruption Rate, Area, and Length relationships for some Hawaiian lava flows. J. Volcanol. Geotherm. Res. 30, 29–45.

Pieri, D.C., Glaze, L.S., Abrams, M.J., 1990. Thermal radiance observations of an active lava flow during the June 1984 eruption of Mount Etna. Geology 18, 1018–1022. https://doi.org/10.1130/0091-7613(1990)018<1018:TROOAA>2.3.CO;2

Plank, S., Marchese, F., Filizzola, C., Pergola, N., Neri, M., Nolde, M., Martinis, S., 2019. The July/August 2019 Lava Flows at the Sciara del Fuoco, stromboli-analysis from multi-sensor infrared satellite imagery. Remote Sens. 11. https://doi.org/10.3390/rs11232879

Ramsey, M., Chevrel, M., Coppola, D., Harris, A., 2019. The influence of emissivity on the thermo-rheological modeling of the channelized lava flows at Tolbachik volcano. Ann. Geophys. 61. https://doi.org/10.4401/ag-8077

Ramsey, M., Dehn, J., 2004. Spaceborne observations of the 2000 Bezymianny,

Kamchatka eruption: The integration of high-resolution ASTER data into near real-time monitoring using AVHRR. J. Volcanol. Geotherm. Res. 135, 127–146. https://doi.org/10.1016/j.jvolgeores.2003.12.014

Ramsey, Michael S., Fink, J.H., 1999. Estimating silicic lava vesicularity with thermal remote sensing: A new technique for volcanic mapping and monitoring. Bull. Volcanol. 61, 32–39. https://doi.org/10.1007/s004450050260

Ramsey, M. S., Fink, J.H., 1999. Estimating silicic lava vesicularity with thermal remote sensing: a new technique for volcanic mapping and monitoring. Bull. Volcanol. 61, 32–39. https://doi.org/10.1016/b978-0-12-385938-9.00065-1

Ramsey, M.S., Harris, A.J.L., 2013. Volcanology 2020: How will thermal remote sensing of volcanic surface activity evolve over the next decade? J. Volcanol. Geotherm. Res. 249, 217–233. https://doi.org/10.1016/j.jvolgeores.2012.05.011

Reath, K., Pritchard, M.E., Moruzzi, S., Alcott, A., Coppola, D., Pieri, D., 2019. The AVTOD (ASTER Volcanic Thermal Output Database) Latin America archive. J. Volcanol. Geotherm. Res. 376, 62–74. https://doi.org/10.1016/j.jvolgeores.2019.03.019

Robidoux, P., Rizzo, A.L., Aguilera, F., Aiuppa, A., Artale, M., Liuzzo, M., Nazzari, M., Zummo, F., 2020. Petrological and noble gas features of Lascar and Lastarria volcanoes (Chile): Inferences on plumbing systems and mantle characteristics. Lithos 370–371, 105615. https://doi.org/10.1016/j.lithos.2020.105615

Rogic, N., Cappello, A., Ferrucci, F., 2019a. Role of Emissivity in Lava Flow 'Distance-to-Run' Estimates from Satellite-Based Volcano Monitoring. Remote Sens. 11, 662. https://doi.org/10.3390/rs11060662

Rogic, N., Cappello, A., Ganci, G., Maturilli, A., Rymer, H., Blake, S., Ferrucci, F., 2019b. Spaceborne EO and a combination of inverse and forward modelling for monitoring lava flow advance. Remote Sens. 11. https://doi.org/10.3390/rs11243032

Rolim, S.B.A., Grondona, A., Hackmann, C.L., Rocha, C., 2016. A Review of Temperature and Emissivity Retrieval Methods: Applications and Restrictions. Am. J. Environ. Eng. 6(4A), 119–128. https://doi.org/10.5923/s.ajee.201601.18

Rothery, D.A., Francis, P.W., Wood, C.A., 1988. Volcano monitoring using short wavelength infrared data from satellites. J. Geophys. Res. 93, 7993–8008. https://doi.org/10.1029/JB093iB07p07993

Ruff, S.W., Christensen, P.R., Barbera, P.W., Anderson, D.L., 1997. Quantitative thermal emission spectroscopy of minerals: A laboratory technique for measurement and

calibration. J. Geophys. Res. Solid Earth 102, 14899–14913. https://doi.org/10.1029/97jb00593

Sabol, D.E., Gillespie, A.R., Abbott, E., Yamada, G., 2009. Field validation of the ASTER Temperature-Emissivity Separation algorithm. Remote Sens. Environ. 113, 2328–2344. https://doi.org/10.1016/j.rse.2009.06.008

Salisbury, J.W., Eastes, J.W., 1985. The effect of particle size and porosity on spectral contrast in the mid-infrared. Icarus 64, 586–588. https://doi.org/10.1016/0019-1035(85)90078-8

Schroeder, W., Oliva, P., Giglio, L., Quayle, B., Lorenz, E., Morelli, F., 2016. Active fire detection using Landsat-8/OLI data. Remote Sens. Environ. 185, 210–220. https://doi.org/10.1016/j.rse.2015.08.032

Siebert, L., Simkin, T., Kimberly, T., 2010. Data Criteria and Context, in: Volcanoes of the World. University of California Press, pp. xi–46.

Sigurdsson, H., McNutt, S.R., Rymer, H., Stix, J., Houghton, B., 2015. The Encyclopedia of Volcanoes, 2nd ed. Academic Press.

Sobrino, J.A., Jiménez-Muñoz, J.C., Sòria, G., Romaguera, M., Guanter, L., Moreno, J., Plaza, A., Martínez, P., 2008. Land surface emissivity retrieval from different VNIR and TIR sensors. IEEE Trans. Geosci. Remote Sens. 46, 316–327. https://doi.org/10.1109/TGRS.2007.904834

Solikhin, A., Thouret, J.C., Gupta, A., Harris, A.J.L., Liew, S.C., 2012. Geology, tectonics, and the 2002-2003 eruption of the Semeru volcano, Indonesia: Interpreted from high-spatial resolution satellite imagery. Geomorphology 138, 364–379. https://doi.org/10.1016/j.geomorph.2011.10.001

Spampinato, L., Calvari, S., Oppenheimer, C., Lodato, L., 2008. Shallow magma transport for the 2002-3 Mt. Etna eruption inferred from thermal infrared surveys. J. Volcanol. Geotherm. Res. 177, 301–312. https://doi.org/10.1016/j.jvolgeores.2008.05.013

Sparks, R.S., Aspinall, W.P., Crosweller, H.S., Hincks, T.K., 2011. Risk and uncertainty assessment of volcanic hazards, Risk and Uncertainty Assessment for Natural Hazards. https://doi.org/10.1017/CBO9781139047562.012

Tait, S., Ferrucci, F., 2013. A real-time, space borne volcano observatory to support decision making during eruptive crises: European volcano observatory space services. Proc. - UKSim 15th Int. Conf. Comput. Model. Simulation, UKSim 2013 283–289. https://doi.org/10.1109/UKSim.2013.121

Tarquini, S., Isola, I., Favalli, M., Mazzarini, F., Bisson, M., Pareschi, M.T., Boschi, E.,

2007. TINITALY/01: A new Triangular Irregular Network of Italy. Ann. Geophys. 50, 407–425. https://doi.org/10.4401/ag-4424

Theys, N., Campion, R., Clarisse, L., Brenot, H., Van Gent, J., Dils, B., Corradini, S., Merucci, L., Coheur, P.F., Van Roozendael, M., Hurtmans, D., Clerbaux, C., Tait, S., Ferrucci, F., 2013. Volcanic SO2 fluxes derived from satellite data: A survey using OMI, GOME-2, IASI and MODIS. Atmos. Chem. Phys. 13, 5945–5968. https://doi.org/10.5194/acp-13-5945-2013

Thompson, J.O., Ramsey, M.S., 2020. Uncertainty Analysis of Remotely-Acquired Thermal Infrared Data to Extract the Thermal Properties of Active Lava Surfaces.

U.S. Department of the Interior, U.S. Geological Survey, 2005. Global Visualisation (GloVis) Viewer [WWW Document]. URL https://glovis.usgs.gov/ (accessed 9.1.19).

USGS, 2019. Landsat 8 Data Users Handbook [WWW Document]. URL https://www.usgs.gov/land-resources/nli/landsat/landsat-8-data-users-handbook (accessed 11.1.19).

USGS, n.d. Commitee on Earth Observation Satellites (CEOS) [WWW Document]. URL https://www.usgs.gov/centers/eros/science/committee-earth-observation-satellites-ceos?qt-science_center_objects=0#qt-science_center_objects (accessed 7.1.20).

Valade, S., Ley, A., Massimetti, F., D'Hondt, O., Laiolo, M., Coppola, D., Loibl, D., Hellwich, O., Walter, T.R., 2019. Towards global volcano monitoring using multisensor sentinel missions and artificial intelligence: The MOUNTS monitoring system. Remote Sens. 11, 1–31. https://doi.org/10.3390/rs11131528

Vicari, A., Ganci, G., Behncke, B., Cappello, A., Neri, M., Del Negro, C., 2011. Near-real-time forecasting of lava flow hazards during the 12-13 January 2011 Etna eruption. Geophys. Res. Lett. 38, 1–7. https://doi.org/10.1029/2011GL047545

Wadge, G., 1981. The variation of magma discharge during basaltic eruptions. J. Volcanol. Geotherm. Res. 11, 139–168. https://doi.org/10.1016/0377-0273(81)90020-2

Wadge, G., Guest, J.E., 1981. Steady-state magma discharge at Etna 1971-81. Nature 294, 548–550. https://doi.org/10.1038/294548a0

Walter, L.S., Salisbury, J.W., 1989. Spectral characteristics of igneous rocks in the 8- to 12-μm region. J. Geophys. Res. B Solid Earth 94, 9203–9213.

WMO, n.d. Moderate-resolution Imaging Spectro-radiometer (MODIS) [WWW Document]. URL https://www.wmo-sat.info/oscar/instruments/view/modis (accessed 7.1.20a).

WMO, n.d. Observing Systems Capability Analysis and Review Tool - MSI [WWW

Document]. URL https://www.wmo-sat.info/oscar/instruments/view/312 (accessed 9.25.19b).

Wolfe, E.W., Morris, J., 1996. Sample data for the geologic map of the island of Hawaii. U.S. Geol. Surv. Misc. Investig. Ser. Map I-2524-B 3. https://doi.org/10.3133/i2524B

Wooster, M.J., Rothery, D.A., 1997. Time-series analysis of effusive volcanic activity the using ERS Along Track Scanning Radiometer: The 1995 eruption of Fernandina Volcano, Galapagos Islands. Remote Sens. Environ. 62, 109–117. https://doi.org/10.1016/S0034-4257(97)00087-4

Wooster, M.J., Zhukov, B., Oertel, D., 2003. Fire radiative energy for quantitative study of biomass burning: Derivation from the BIRD experimental satellite and comparison to MODIS fire products. Remote Sens. Environ. 86, 83–107. https://doi.org/10.1016/S0034-4257(03)00070-1

World Meteorological Organisation, n.d. Observing Systems Capability Analysis and Review Tool - Sinning Enhanced Visible Infra-Red Imager (SEVIRI) [WWW Document]. URL https://www.wmo-sat.info/oscar/instruments/view/503 (accessed 7.1.20).

World Metheorological Organisation, n.d. Observing Systems Capability Analysis and Review Tool - Landsat 8 [WWW Document]. URL https://www.wmo-sat.info/oscar/satellites/view/227 (accessed 9.25.19).

Wright, R., 2016. MODVOLC: 14 years of autonomous observations of effusive volcanism from space. Geol. Soc. Spec. Publ. 426, 23–53. https://doi.org/10.1144/SP426.12

Wright, Robert, Blake, S., Harris, A.J.L., Rothery, D.A., 2001. A simple explanation for the space-based calculation of lava eruption rates. Earth Planet. Sci. Lett. 192, 223–233. https://doi.org/10.1016/S0012-821X(01)00443-5

Wright, R., Flynn, L., Garbeil, H., Harris, A., Pilger, E., 2002. Automated volcanic eruption detection using MODIS. Remote Sens. Environ. 82, 135–155. https://doi.org/10.1016/S0034-4257(02)00030-5

Wright, R., Flynn, L.P., Garbeil, H., Harris, A.J.L., Pilger, E., 2004. MODVOLC: Near-real-time thermal monitoring of global volcanism. J. Volcanol. Geotherm. Res. 135, 29–49. https://doi.org/10.1016/j.jvolgeores.2003.12.008

Wright, R., Flynn, L.P., Harris, A.J.L., 2001. Evolution of lava flow-fields at Mount Etna, 27-28 October 1999, observed by Landsat 7 ETM+. Bull. Volcanol. 63, 1–7. https://doi.org/10.1007/s004450100124

Wright, R., Pilger, E., 2008. Radiant flux from Earth's subaerially erupting volcanoes. Int. J. Remote Sens. 29, 6443–6466. https://doi.org/10.1080/01431160802168210

Wright, S.P., Ramsey, M.S., 2006. Thermal infrared data analyses of Meteor Crater, Arizona: Implications for Mars spaceborne data from the Thermal Emission Imaging System. J. Geophys. Res. E Planets 111, 1–16. https://doi.org/10.1029/2005JE002472

8 Appendices

8.1 Appendix A: Surface variation: Rough vs Smooth

Naturally occurring 'rough' vs cut 'smooth sample surfaces

In an attempt to confirm the hypothesis that samples' surface mineralogy is responsible for different spectral shapes observed (Section 2.3.3, Fig. 2.8 – Fig. A2.1 repeated here), thin sections for NRE.1.4 samples' naturally occurring 'rough' and cut 'smooth' surfaces were created to help identify features (Fig. A2.1 b & d) and clarify the cause of spectral discrepancy observed for the same samples' surface types.

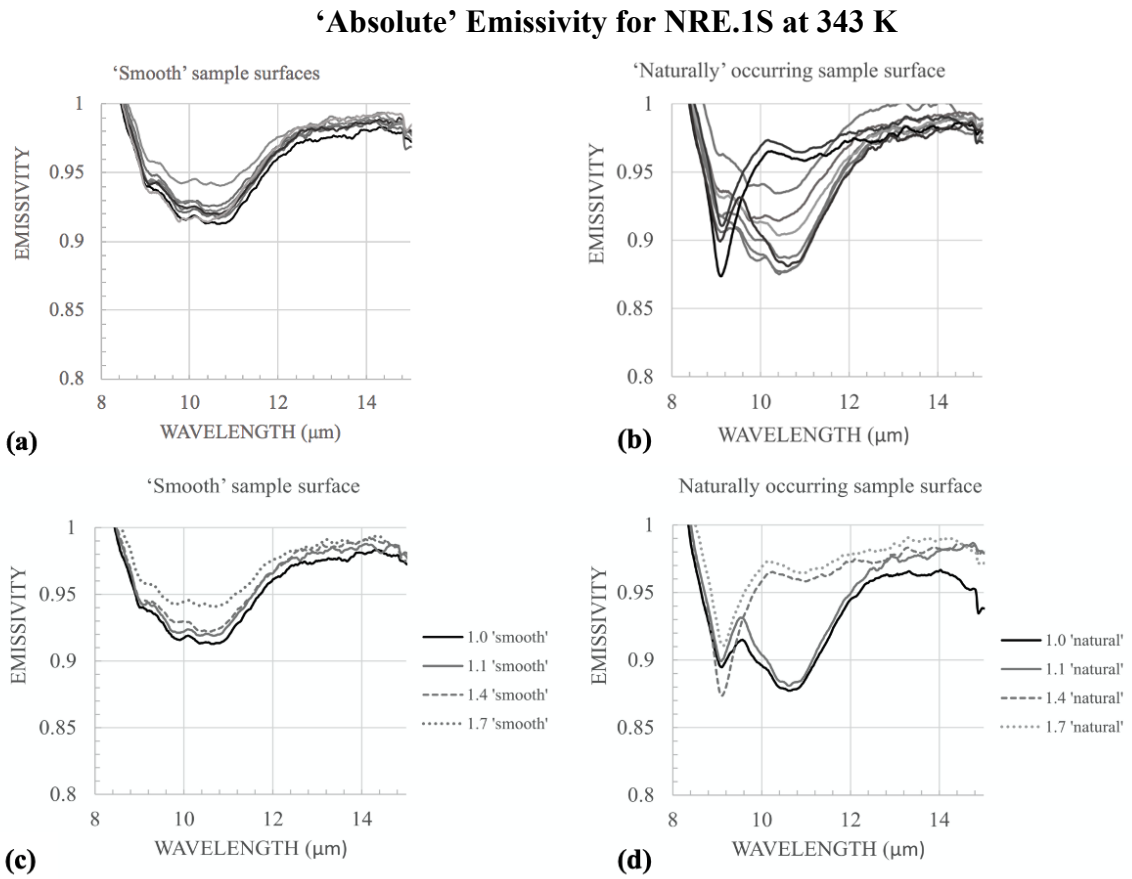

Figure (2.8) A2.1 (a & c) An example of NRE.1S emissivity results variation for cut 'smooth' sample surfaces and **(b & d)** 'naturally rough' sample surfaces, where 'naturally rough' surface samples display a range of spectral contrast (lower emissivity) and different spectral signature shapes from that of their cut 'smooth' counterparts.

Figure A2.2 shows an example of naturally occurring 'rough' **(i)** and **(ii)** cut 'smooth' for NRE.1.4 sample at low magnification. Surfaces in plane polarized light (PPL) and in cross polarized light (XPL) are also shown. Images were taken using optical microscope Leica Wild MZ8, equipped with polarizing filters and rotating stage for geological samples. It works both in reflected and/or transmitted modes.

The low power view in Figure A2.3 **(a)** shows that this is a fine-grained rock with micro phenocrysts (500-2000 μm) of plagioclase and olivine **(g & h)**, which are enclosed in a fine-grained (< 1 mm) groundmass of minerals typical for basalt (plagioclase feldspar, clinopyroxene and olivine). A higher magnification view of the same slide **(f-h)** show details of the olivine mineral. The different orientation in which olivine crystals are cut shown by the range of biofringence interference colours (purple blue) in cross-polarized views **(f & h)**.

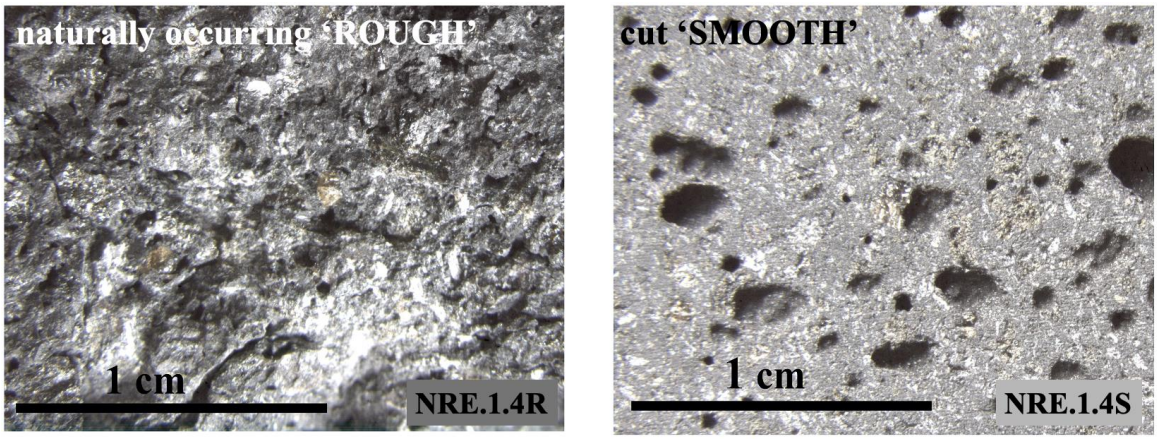

(i) **(ii)**

Figure A2.2 An example of naturally occurring 'rough' **(i)** and **(ii)** cut 'smooth' for NRE.1.4 sample at low magnification.

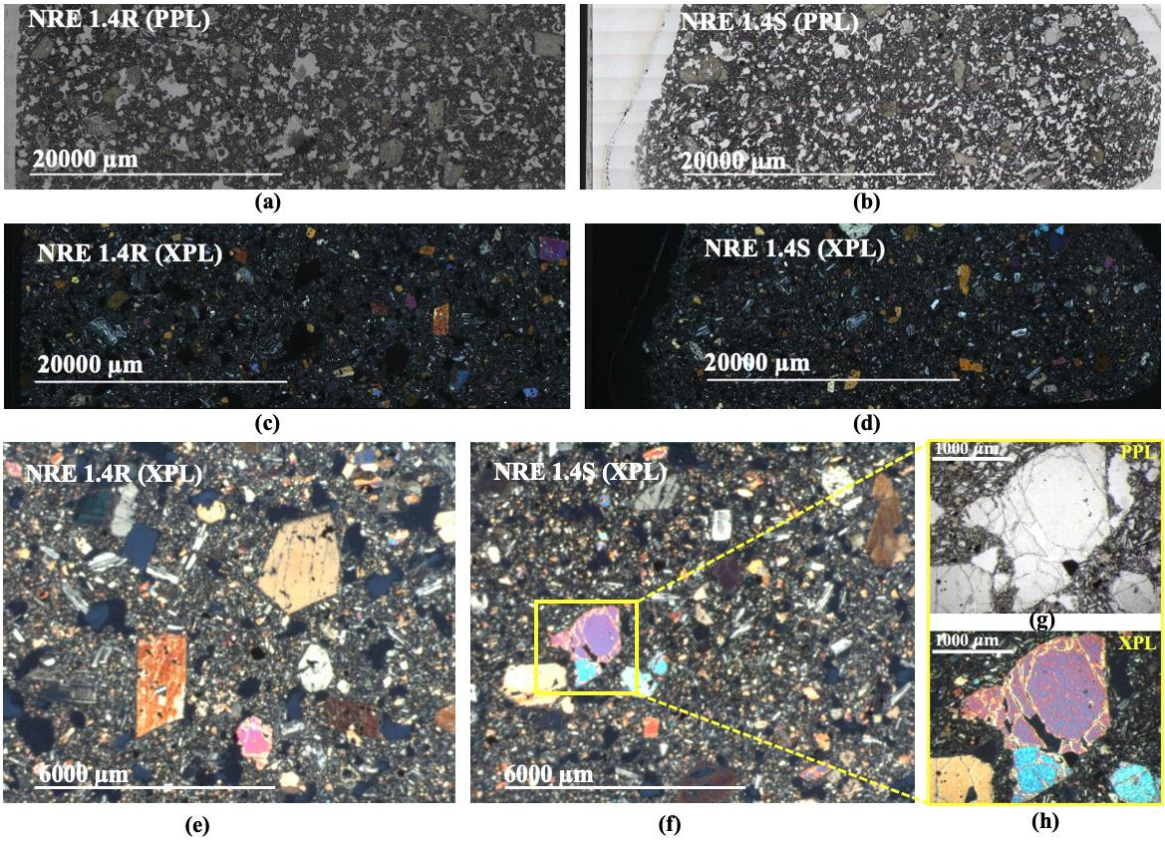

(a) **(b)** **(c)** **(d)** **(e)** **(f)** **(g)** **(h)**

Figure A2.3 (a & c) An example of NRE.1S emissivity results variation for cut 'smooth' sample surfaces and **(b & d)** 'naturally rough' sample surfaces, where 'naturally rough' surface samples display a range of spectral contrast (lower emissivity) and different spectral signature shapes from that of their cut 'smooth' counterparts.

Nonetheless, no firm evidence was found to confirm that the surface mineralogy for NRE.1.4 sample was responsible for producing inconsistent emissivity features identified. This may be due to the technique used (thin section), which potentially removed surface evidence (could not preserve it) or it could be due to insufficient expertise that I have in petrological investigation of geological samples.

Although, this analysis could not confirm with confidence that the samples' surface mineralogical variation may be responsible for producing the features identified in Figure A1 (b & d), it is evident that the shape and position of spectral signatures are markedly different for the two types of surfaces.

8.2 Appendix B: FTIR Experimental Error

Experimental Error Data

Data presented here shows the percentage errors associated with the data acquired at the University of Pittsburgh IVIS Laboratory with a FTIR spectrometer using the furnace experiment. (Chapter 2, Sections 2.2.5 and 2.3.5) Errors were calculated for each wavenumber (converted to wavelength) and account for all random and systematic errors, following (Ruff et al., 1997) method.

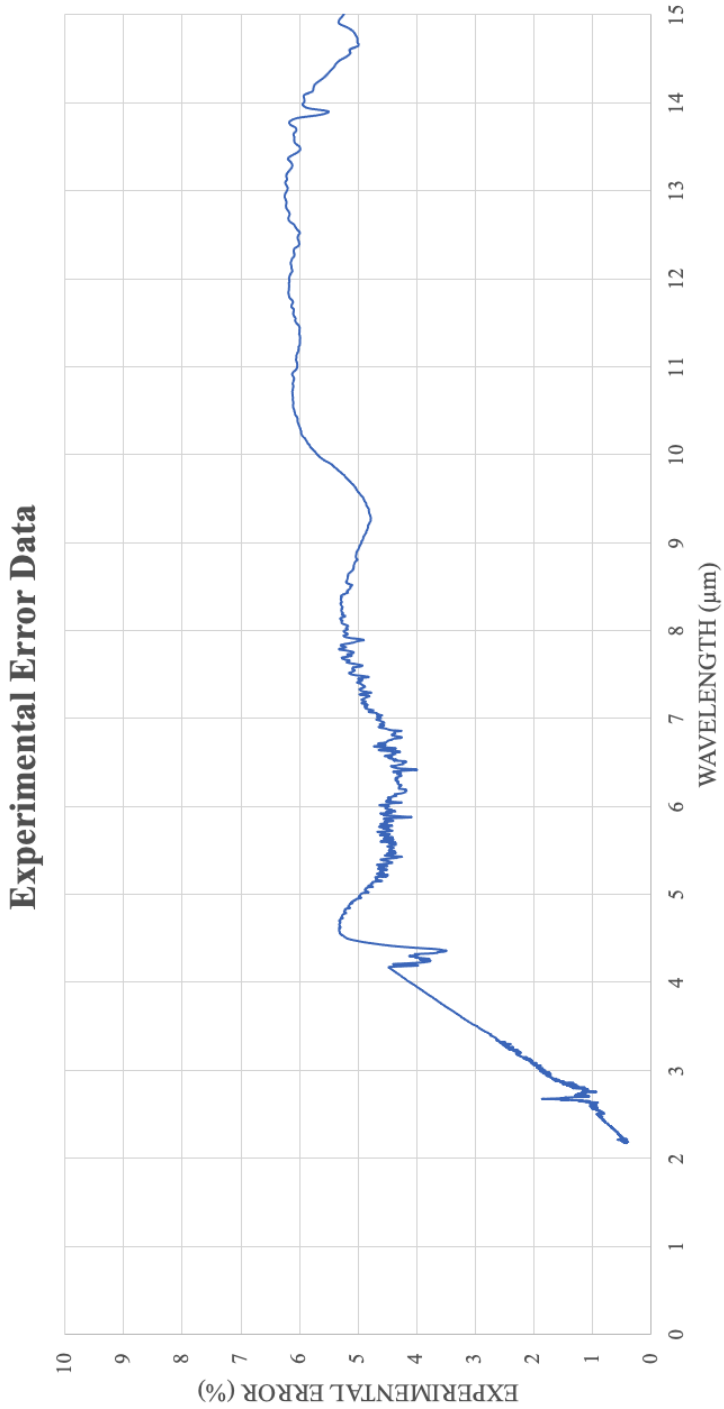

8.3 Appendix C: Thermal Anomalies: the 2017 Mt Etna data

From the data of the isolated thermally anomalous pixels extracted for each spaceborne scene acquired between 16 March to 08 August 2017, radiances in OLI's (Figure C1 a-b) and Sentinel-2A SWIR Bands (Fig. C1 c-g). These follow similar trends (Fig. C1 a-g). SWIR and 6 and 11 (c.w. 1.61 μm and 1.65 μm) are plotted on the horizontal and Bands 7 and 12 on the vertical axis (c.w. 2.22 μm and 2.20 μm).

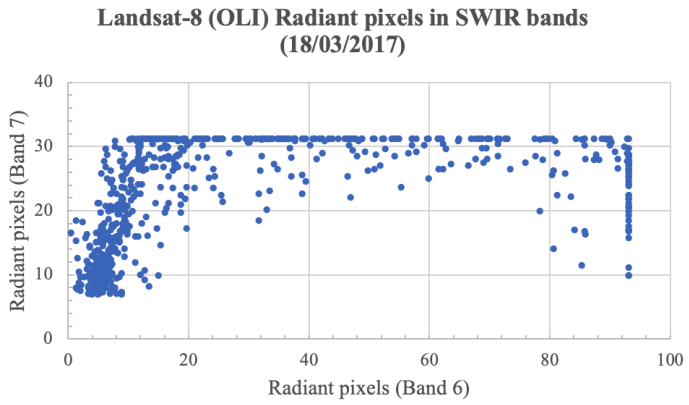

(a)

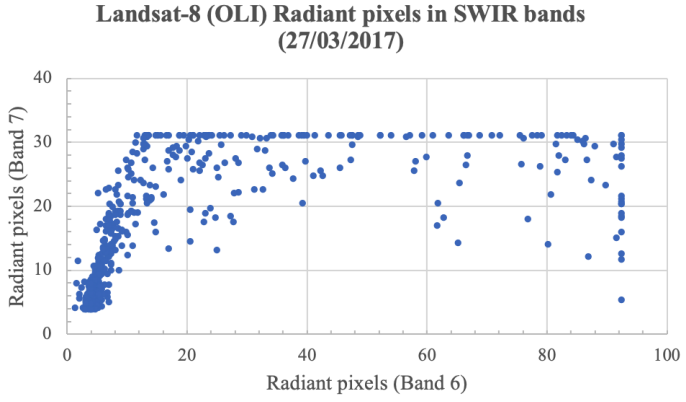

(b)

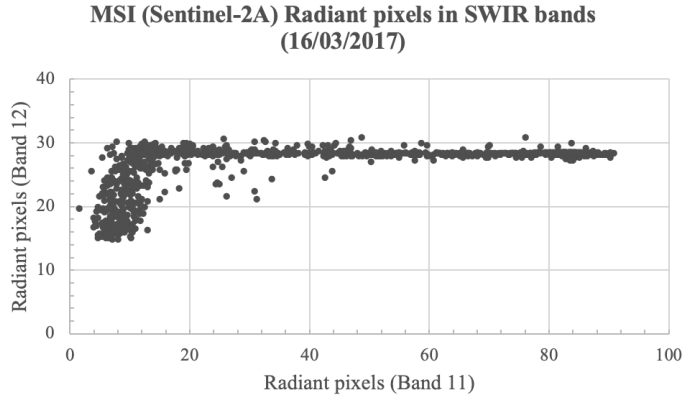

(c)

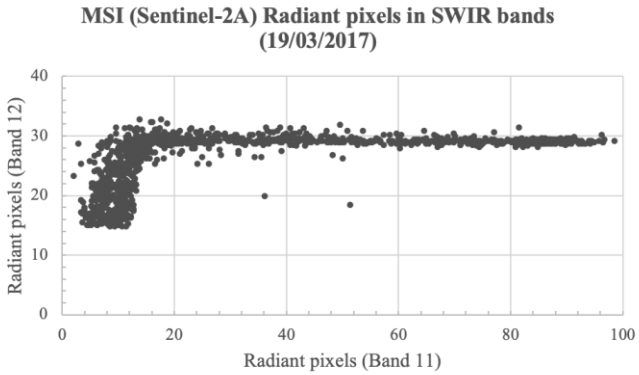

(d)

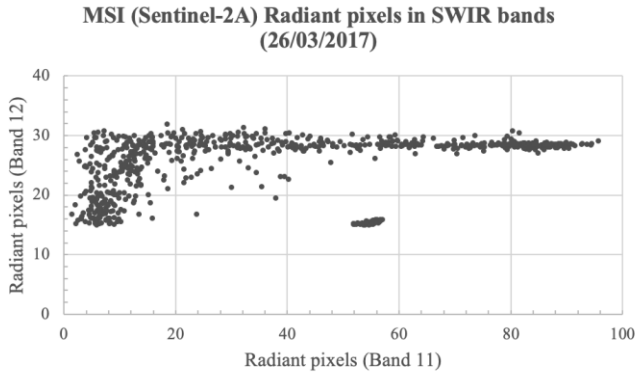

(e)

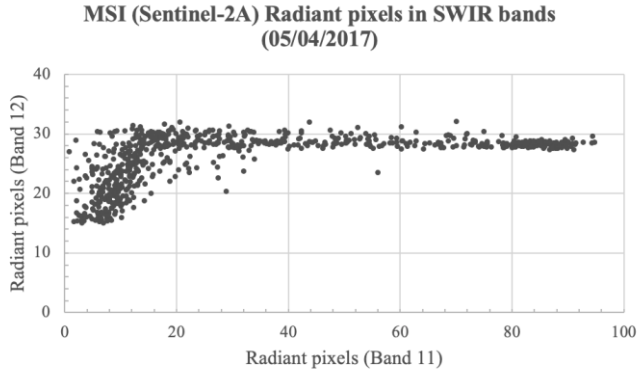

(f)

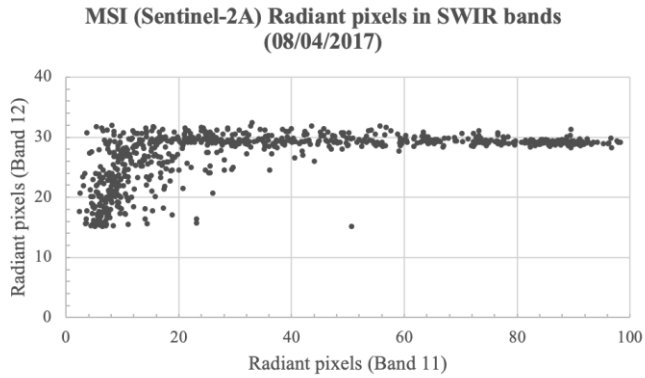

(g)

Figure C1 Spectral radiance trend(s) plotted using all isolated radiant pixels in the high-temperature thermal anomaly observed in **(a-b)** OLI's SWIR Bands (6 and 7) and **(c-g)** Sentinel-2A SWIR Bands (11 and 12), acquired between 16 March 2017 and 08 April during the 2017 Mt Etna eruption.

8.4 Appendix D: Total Radiant Heat Flux: computation method

The mean spectral radiance measured by a satellite sensor as a digital number (DN) is converted into 'at-satellite' spectral radiance R_λ. In SWIR region (1.5 and 2.5 μm) upwelling path radiance ($R_{\lambda,U}$) contribution is low, whereas the surface reflected radiation $\left(R_{\lambda,D}\right)$ can be estimated by subtracting the mean spectral radiance (R_λ) value of surrounding, clearly non-volcanic background pixels ($\mathrm{bg}_{(\mathrm{band})}$) from the thermally anomalous pixels.

Therefore, only pixels with radiance greater than $(3\times \mathrm{bg}_7)+ \mathrm{bg}_7$ for OLI's SWIR Band 7 were extracted as thermally anomalous, within the region of interest. Same approach is applied to both SWIR OLI's bands (Band 6 and Band 7) and Sentinel-2A (Band 11 and Band 12).

The total radiant heat fluxes (Q_{r_calc} in W), associated with the thermally anomalous pixels isolated were computed using the Stephan Boltzmann Equation (Eq. 10).

Spaceborne data were processed using three approaches; firstly by applying a constant emissivity, where an assumed value (e.g., 0.95 or 0.60) is applied to the entire thermal anomaly; and secondly, multicomponent emissivity is used, derived from very-high temperature laboratory FTIR data, in SWIR (Chapter 2, Section 2.3.5).

Volcanic anomalies are unlikely to entirely fill the 30-m SWIR pixel (e.g., OLI) with a single source at a specific temperature, thus, two or more thermal components would likely be present and should be accounted for. So, after radiometric and atmospheric data correction, 'dual-band' procedure, with some modifications related to emissivity as input parameter were employed.

Here, radiance data in SWIR (OLI's Bands 6, 7 and Sentinel-2 Bands 11, 12) are linked to an appropriate, measured emissivity value to compute pixel integrated temperature (T_i) for each band, enabling derivation of an effective temperature (T_e) for each radiant pixel of the high-temperature thermal anomaly analysed (Eq. 8). This 'thersholding' approach, detailed in Figure D1 (and Fig. 3.3 in main text), uses radiant pixels segmentation to link specific radiance range to an appropriate emissivity value to compute pixel integrated temperature (T_i). Considering that emissivity also varies as a function of wavelength, the absence of FTIR data at 1.65 μm and the close proximity of OLI and Sentinel-2 SWIR bands (1.65 and 2.20 μm), similar behaviour is anticipated based on preliminary reflectance data.

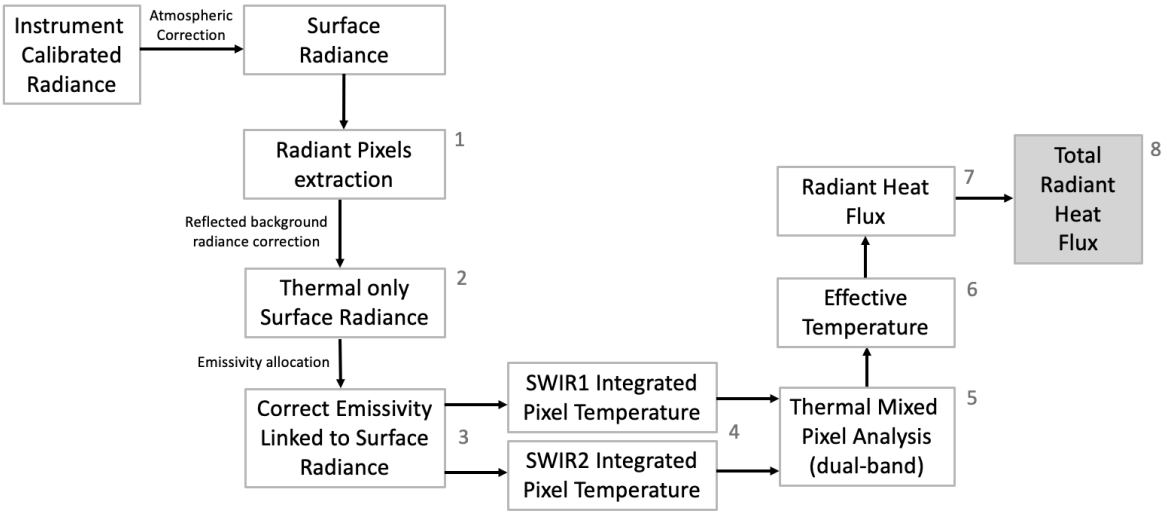

Figure D1 (and Fig. 3.3 repeated here) A flowchart illustrating the semi-automated (steps 1-8) methods used to derive total radiant heat flux using high-spatial resolution data in two SWIR bands (Appendix D).

Having obtained the Effective Temperature (T_e) for each radiant pixel, the remotely sensed radiant heat flux (Q_{r_calc}) was computed (Eq. 10).

The code presented here (courtesy of S. Eriksen, personal communication), was used to compute total radiant heat fluxes from the extracted radiant pixels (ENVI+IDL). The code was created in Jupyter Notebook, running on Python 3 platform.

Notes:

Starting equations of note;

$$R_{A,thermal=\tau_A[f_h L(\lambda_A,T_h)+(1-f_h)L(\lambda_A,T_c)]}$$
$$R_{A,thermal=\tau_B[f_h L(\lambda_B,T_h)+(1-f_h)L(\lambda_B,T_c)]}$$
$$R_{A,thermal=\tau_C[f_h L(\lambda_C,T_h)+(1-f_h)L(\lambda_C,T_c)]}$$

Modified equations used here to cteate the code have been shown and discussed in the main text (Chapter 1)

Equation 1:

$$L_{\lambda,T}\frac{\varepsilon \times C_1 \times \lambda^{-5}}{\pi \times (e^{\frac{C_2}{\lambda \times T_i}}-1)}$$

Equation 2: Surface fraction

$$f_h = \frac{K - L(\lambda, T_c)}{L(\lambda, T_{melt}) - L(\lambda, T_{c\,min})}$$

$$K = \frac{R}{\tau}$$

Equation 3: Integrated Temperature

$$T_i = \frac{C_2}{\lambda \times \ln(\frac{\tau\varepsilon C_1}{\pi\lambda^{-5}R}+1)}$$

Equation 4: Effective Temperature:

$$T_e = [f_h \times {T_h}^4 + (1 - f_h){T_c}^4]^{\frac{1}{4}}$$

where,

τ = atmospheric spectral transmission coefficient
f_h = surface fraction
ε = emissivity of radiative surface
C_x = constants
T = temperature (K)
R = thermal radiance

***Table D1 Emissivity-temperature 'Look-up' table**

using 'therholds' approach for OLI and Sentinel-2 input parameters in SWIR

λ (μm)	Mode	*773	823	873	923	973	1023	1073	1123	1173	1223	1273	1323	1373
1.65	εFTIR	0.80	0.87	0.83	0.84	0.86	0.81	0.81	0.78	0.82	0.78	0.73	0.76	0.73
	εmodel	**0.83**	**0.83**	**0.83**	**0.83**	**0.83**	**0.82**	**0.82**	**0.81**	**0.79**	**0.77**	**0.76**	**0.74**	**0.72**
	Error	0.02	0.05	0.01	0.01	0.01	0.01	0.01	0.01	0.01	0.01	0.01	0.01	0.01
	Rad	2.2	4.4	8.1	14.4	23.0	35.3	51.2	71.5	101.7	131.9	162.3	215.8	271.2
2.22	εFTIR	0.80	0.87	0.83	0.84	0.86	0.81	0.81	0.78	0.82	0.78	0.73	0.76	0.73
	εmodel	**0.83**	**0.83**	**0.83**	**0.83**	**0.83**	**0.82**	**0.81**	**0.80**	**0.79**	**0.77**	**0.76**	**0.74**	**0.72**
	Error	0.02	0.05	0.01	0.01	0.01	0.01	0.01	0.01	0.01	0.01	0.01	0.01	0.01
	Rad	4.3	7.6	11.4	17.5	25.4	33.4	44.8	56.3	75.8	90.5	104.4	130.8	151.3

*Table 3.3 in main text repeated here for guidance on input parameters

Example of input parameters (emissivity-radiance link) using 'thresholding' approach in the code:

```
"""Calculate emissivity based on radiance values
"""
if band == '6':
    if r <= 5:
        emissivity = 0.83
    elif r > 5 and r <= 21:
        emissivity = 0.83
    elif r > 21 and r <= 51:
        emissivity = 0.82
    elif r > 51 and r <= 71:
        emissivity = 0.81
    elif r > 71 and r <= 101:
        emissivity = 0.79
```

```
elif band == '7':
    if r <= 5:
        emissivity = 0.85
    elif r > 5 and r <= 15:
        emissivity = 0.85
    elif r > 15 and r <= 25:
        emissivity = 0.83
    elif r > 25 and r <= 28.50:
        emissivity = 0.81
    elif r > 28.50 and r <= 34:
        emissivity = 0.80
```

Define global constants

In [1]:

```
#emissivity = Varied
transmissivity = 0.95
c_1 = 374200000.0
c_2 = 14388.0
t_melt = 1323.0

# arbitrary small number
epsilon = 1e-6
```

Equations as functions

In [2]:

```
import numpy as np

def L(lam, temp, emissivity):
    """
    Equation 1 above
    @param lam wavelength
    @param temp temperature in K
    @param emissivity
    """
    numerator = emissivity * c_1 * lam **-5
    denominator = np.pi * (np.exp(c_2 / (lam * temp)) - 1)
    return numerator / denominator

def R(lam, temp, emissivity):
    """Not actually used
    Equation 1 times transmissivity
    @param lam wavelength
    @param temp temperature in K
    @param emissivity
    """
    return transmissivity * L(lam, tempm, emissivity)

def calculate_fh(K, L_lam_T_c, L_lam_T_melt):
    """
    Equation 2 above
    @param K therm / transmissivity
    @param L_lam_T_c L(lam, T_c_min)
    @param L_lam_5_T_melt L(lam_5, T_melt)
    """
    numerator = K - L_lam_T_c
    denominator = L_lam_T_melt - L_lam_T_c
    return numerator / denominator

def calculateTi(r_therm, lam, emissivity):
```

```
    """Caculate integrated temperature
    Equation 3 above.
    @param R_therm therm
    @param lam wavelength
    @param emissivity
    """
    log_num = transmissivity * emissivity * c_1
    log_den = np.pi * lam**5 * r_therm
    if log_num/log_den < 0 :
        return None
    return c_2 / (lam * np.log(np.fabs(log_num/log_den) + 1))

def calculateTe(f_h, t_h, t_c):
    """Calculate the effective temperature
    Equation 4 above.
    @param f_h surface fraction
    @param t_h magmatic temperature
    @param t_c average temperature
    """
    a = f_h * t_h ** 4
    b = (1 - f_h) * t_c ** 4
    return (a + b) ** 0.25

def calculateQ(A, e, sigma, t):
    """Calculate total radiant flux
    """
    return A * e * sigma * t ** 4

def same_sign(x, y):
    """
    @param x
    @param y
    @return True is x and y are of the same sign, else False
    """
    return (x > 0 and y > 0) or (x < 0 and y < 0)

def find_tc(t_c_min, t_c_max,
            l_tmelt_A, l_tmelt_B,
            lambda_A, lambda_B,
            k_A, k_B,
            fh_min_A, fh_max_A,
            fh_min_B, fh_max_B,
            emissivity_A, emissivity_B):
    """Recursive approach to finding tc
    """
    if abs(t_c_min - t_c_max) > epsilon:
        t_c_mid = (t_c_max + t_c_min) / 2.0 # Calculate mid point
        fh_A_mid = calculate_fh(k_A, L(lambda_A, t_c_mid, emissivity_A), l_tmelt_A)
```

```
        fh_B_mid = calculate_fh(k_B, L(lambda_B, t_c_mid, emissivity_B), l_tmelt_B)

        # If the both fh are the same sign
        if same_sign(fh_A_mid - fh_B_mid, fh_min_A - fh_min_B):
            # True if...
            # Case 1: Both negative; fh_B_mid > fh_A_mid and fh_B_min > fh_A_min
            # Case 2: Both positive; fh_A_mid > fh_B_mid and fh_A_min > fh_B_min
            # Set low point to mid point
            fh_min_A = fh_A_mid
            fh_min_B = fh_B_mid
            t_c_min = t_c_mid
        else:
            # If False
            # Set high point to be mid point
            fh_max_A = fh_A_mid
            fh_max_B = fh_B_mid
            t_c_max = t_c_mid

        # Here is the recursion
        t_c_min, t_c_max, fh_min_A, fh_max_A, fh_min_B, fh_max_B = find_tc(t_c_min, t_c_max,
                                                                           l_tmelt_A, l_tmelt_B,
                                                                           lambda_A, lambda_B,
                                                                           k_A, k_B,
                                                                           fh_min_A, fh_max_A,
                                                                           fh_min_B, fh_max_B,
                                                                          emissivity_A, emissivit
y_B)

    return t_c_min, t_c_max, fh_min_A, fh_max_A, fh_min_B, fh_max_B

def calculateTh(lambda_A, tau_A, t_c, r_A, f_h, emissivity):
    """Rearrange starting equations to calculate t_h
    @param lambda_A wavelength
    @param tau_A
    @param t_c
    @param r_A
    @param f_h
    @param emissivity
    """
    l_a = L(lambda_A, t_c)
    l_th = ((r_A / tau_A) - (1 - f_h) * l_a) / f_h
    t_h =  (c_2 / np.pi) * np.log((emissivity * c_1 * lambda_A ** -5) / (np.pi * l_th ) + 1)
    return t_h
```

```
def getEmissivity(r, band):
    """Calculate emissivity based on radiance values
    """
    if band == '6':
        if r <= 5:
            emissivity = 0.83
        elif r > 5 and r <= 21:
            emissivity = 0.83
        elif r > 21 and r <= 51:
            emissivity = 0.82
        elif r > 51 and r <= 71:
            emissivity = 0.81
        elif r > 71 and r <= 101:
            emissivity = 0.79
        else:
            print('r_6 out of range. r =', r)

    elif band == '7':
        if r <= 5:
            emissivity = 0.85
        elif r > 5 and r <= 15:
            emissivity = 0.85
        elif r > 15 and r <= 25:
            emissivity = 0.83
        elif r > 25 and r <= 28.50:
            emissivity = 0.81
        elif r > 28.50 and r <= 34:
            emissivity = 0.80
        else:
            print('r_7 out of range. r =', r)
    else:
        print('band', band, 'not defiend')

    return emissivity
```

Handle Output CSV

In [3]:

```
import csv # slightly easier to use than xlrd

def create_csv(outname):
    """Fill a row with titles
    NOTE will overwrite any existing csv with the same name
    Uses global variable row_titles
    @param outname csv output name
    """
    with open(outname, 'w', newline='') as csvfile:
        thewriter = csv.writer(csvfile, delimiter=',')
        thewriter.writerow(row_titles)
```

```
def insert_row(outname, rowinfo):
    """Just insert info on the next line
    @param outname csv output name
    @param rowinfo list of information to fill that row with
    """
    with open(outname, 'a', newline='') as csvfile:
        thewriter = csv.writer(csvfile, delimiter=',')
        thewriter.writerow(rowinfo)
```

Dual Band

In [4]:

```
def pixelDualBand(rad_A, rad_B):
    """Original code
    Slightly rewritten to make easier to read
    Loop over arrays and fill a row
    Made generic by A and B
    @param rawA array of radient pixel values
    @param rawB array of radient pixel values
    """

    for i in range(rad_A.size):

        # Have to reset these after each loop
        t_c_min =  356.0
        t_c_max = 650.0

        # raw_A
        rad_pixel_A = rad_A[i]
        rad_thermal_A = rad_pixel_A - bg_A # subtract background to leave thermal radience
        emissivity_A = getEmissivity(rad_pixel_A, '5')
        ti_A = calculateTi(rad_thermal_A, lambda_A, emissivity_A) # calculate integrated temperat
ure
        r_A_saturated = rad_thermal_A > r_A_max # Determine if saturated
        r_A_too_small = rad_thermal_A < r_A_min # Determine if too small
        l_tmelt_A = L(lambda_A, t_melt, emissivity_A) # Do once as used multiple times
        k_A = rad_thermal_A / transmissivity # Do once as used multiple times

        # raw_B
        rad_pixel_B = rad_B[i]
        rad_thermal_B = rad_pixel_B - bg_B # subtract background to leave thermal radience
        emissivity_B = getEmissivity(rad_pixel_B, '7')
        ti_B = calculateTi(rad_thermal_B, lambda_B, emissivity_B) # calculate integrated temperat
ure
        r_B_saturated = rad_thermal_B > r_B_max # Determine if saturated
        r_B_too_small = rad_thermal_B < r_B_min # Determine if too small
        l_tmelt_B = L(lambda_B, t_melt, emissivity_B) # Do once as used multiple times
        k_B = rad_thermal_B / transmissivity # Do once as used multiple times
```

```
        # Starting points
        fh_min_A = calculate_fh(k_A, L(lambda_A, t_c_min, emissivity_A), l_tmelt_A)
        fh_max_A = calculate_fh(k_A, L(lambda_A, t_c_max, emissivity_A), l_tmelt_A)

        fh_min_B = calculate_fh(k_B, L(lambda_B, t_c_min, emissivity_B), l_tmelt_B)
        fh_max_B = calculate_fh(k_B, L(lambda_B, t_c_max, emissivity_B), l_tmelt_B)

        # Find mid point
        # Definately could be replaced by a scipy function
        # Halve search region each time
        t_c_min, t_c_max, fh_min_A, fh_max_A, fh_min_B, fh_max_B = find_tc(t_c_min, t_c_max,
                                                                           l_tmelt_A, l_tmelt_B,
                                                                           lambda_A, lambda_B,
                                                                           k_A, k_B,
                                                                           fh_min_A, fh_max_A,
                                                                           fh_min_B, fh_max_B,
                                                                          emissivity_A, emissivit
y_B)

        # Once difference < epsilon
        # t_c = midpoint
        t_c = (t_c_min + t_c_max) / 2.0
        t_c_min, t_c_max = 356.0, 650.0 # Reset variables

        # Determine if there is convergence
        if min(abs(t_c - t_c_min), abs(t_c - t_c_max)) < 2*epsilon:
            # If No Convergence
            # ie t_c - t_c_min/max < 2*epsilon
            # Dual band solution fails
            f_h = 0.0

            if not r_A_saturated and not r_B_saturated and not r_B_too_small:
                # If both bands are unsaturated and rad B is not too small
                # t_central is integrated T of band B
                t_c = ti_B
            else:
                # Else set t_c to integrated T of band A
                t_c = ti_A

        else:
            # If Convergence
            # Calculate fraction
            fh_A = calculate_fh(k_A, L(lambda_A, t_c, emissivity_A), l_tmelt_A)
            fh_B = calculate_fh(k_B, L(lambda_B, t_c, emissivity_B), l_tmelt_B)
            f_h = (fh_A + fh_B) / 2.0

        # Calculate effective temperature
```

```
        if f_h > 0.0: # Solution found
            t_h = t_melt
            t_e = calculateTe(f_h, t_h, t_c)
        else:
            t_e = t_c

        # Calculate Q
        q = calculateQ(A, e_q, sigma, t_e)

        # Create Row
        rowinfo = []
        rowinfo.append(rad_pixel_A)
        rowinfo.append(rad_pixel_B)
        rowinfo.append(emissivity_A)
        rowinfo.append(emissivity_B)
        rowinfo.append(rad_thermal_A)
        rowinfo.append(rad_thermal_B)
        rowinfo.append(ti_A)
        rowinfo.append(ti_B)
        rowinfo.append('yes' if r_A_saturated else 'no')
        rowinfo.append('yes' if r_B_saturated else 'no')
        rowinfo.append('yes' if r_A_too_small else 'no')
        rowinfo.append('yes' if r_B_too_small else 'no')
        rowinfo.append(f_h)
        rowinfo.append(1.0 - f_h)
        rowinfo.append(t_c)
        rowinfo.append(t_e)
        rowinfo.append(q)

        insert_row(outfile, rowinfo)
```

Determine Pixel

In [6]:

```
def determinePixel(outfile, radA, radB, radC=[]):
    """Control sequence allowing for situations where there
    are two or three values
    @param outfile name of csv to output
    @param radA array of values
    @param radB array of values
    @param radC array of values or None
    """
    global row_titles

    if len(radC) > 0:
        row_titles = ['RawA', 'RawB', 'RawC','R_A', 'R_B', 'R_C', 'T_i_A', 'T_i_B', 'T_i_C', 'R_A
_sat', 'R_B_sat', 'R_C_sat',
                      'R_A_too_small', 'R_B_too_small', 'R_C_too_small', 'f_h', 'f_c', 'T_c', 'T_
e', 'Q']
```

```
        create_csv(outfile)
        pixelTriBand(radA, radB, radC)
    else:
        row_titles = ['Raw_5', 'Raw_7', 'Emissivity_5', 'Emissivity_7','R_5', 'R_7', 'T_i_5', 'T_
i_7', 'R_5_sat', 'R_7_sat', 'R_5_too_small', 'R_7_too_small',
                      'f_h', 'f_c', 'T_c', 'T_e', 'Q']
        create_csv(outfile)
        pixelDualBand(radA, radB)
```

Running

Dual Band

In [7]:

```
import pandas as pd

data = pd.read_excel('data.xls')
print(data)

# Info is in column 5 and 6 named 'Unnamed: 5' and 'Unnamed: 6'
# Use arrays (Can impliment most of the above in array form which will be much faster)
rad_5 = data['Unnamed: 5'].dropna().to_numpy()
rad_7 = data['Unnamed: 6'].dropna().to_numpy()

# First 2 enteries are the titles so remove them
rad_5_array = rad_5[2:].flatten()
rad_7_array = rad_7[2:].flatten()
```

```
     Unnamed: 0  Unnamed: 1  Unnamed: 2  Unnamed: 3  Unnamed: 4 Unnamed: 5  \
0           NaN         NaN         NaN         NaN         NaN         NaN
1           NaN         NaN         NaN         NaN         NaN         NaN
2           NaN         NaN         NaN         NaN         NaN         NaN
3           NaN         NaN         NaN         NaN         NaN         NaN
4           NaN         NaN         NaN         NaN         NaN         NaN
..          ...         ...         ...         ...         ...         ...
678         NaN         NaN         NaN         NaN         NaN      5.0033
679         NaN         NaN         NaN         NaN         NaN      5.3071
680         NaN         NaN         NaN         NaN         NaN      5.7123
681         NaN         NaN         NaN         NaN         NaN      6.2525
682         NaN         NaN         NaN         NaN         NaN      5.7322

    Unnamed: 6
0          NaN
1          NaN
2          NaN
3          NaN
4          NaN
..         ...
678     7.3846
679     7.4208
680     8.1217
```

```
681    10.1023
682     8.8158

[683 rows x 7 columns]
```

Set parameters for Bands 5 and 7 ETM+ (6 and 7 OLI or 11 and 12 Sentinel-2)

In [8]:

```
lambda_A = 1.65; r_A_min = -7.67183; r_A_max = 92.90148; bg_A = 1.5
lambda_B = 2.22; r_B_min = -2.58582; r_B_max = 31.31277; bg_B = 1.5

# Not sure what to set these to
e_q = 1
sigma = 0.0000000567
A = 900

outfile = 'output2.csv'

determinePixel(outfile, rad_5_array, rad_7_array)
```

In [9]:

```
xl = pd.read_csv('output2.csv')
print(xl)
```

```
       Raw_5    Raw_7  Emissivity_5  Emissivity_7      R_5      R_7  \
0     8.8016  10.4282           0.6           0.6   7.3016   8.9282
1    17.1888  23.5415           0.6           0.6  15.6888  22.0415
2    34.5969  31.3130           0.6           0.6  33.0969  29.8130
3     9.2989  14.1339           0.6           0.6   7.7989  12.6339
4    62.1923  26.6192           0.6           0.6  60.6923  25.1192
..       ...      ...           ...           ...      ...      ...
667   5.0033   7.3846           0.6           0.6   3.5033   5.8846
668   5.3071   7.4208           0.6           0.6   3.8071   5.9208
669   5.7123   8.1217           0.6           0.6   4.2123   6.6217
670   6.2525  10.1023           0.6           0.6   4.7525   8.6023
671   5.7322   8.8158           0.6           0.6   4.2322   7.3158

          T_i_5       T_i_7 R_5_sat R_7_sat R_5_too_small R_7_too_small  \
0    643.947170  546.617225      no      no            no            no
1    682.496010  591.717077      no      no            no            no
2    724.845970  608.495346      no      no            no            no
3    647.095758  563.105011      no      no            no            no
4    763.320702  598.863356      no      no            no            no
..          ...         ...     ...     ...           ...           ...
667  610.820875  528.051308      no      no            no            no
668  614.399985  528.315293      no      no            no            no
669  618.809788  533.177913      no      no            no            no
670  624.154234  544.908287      no      no            no            no
671  619.016827  537.586478      no      no            no            no

          f_h       f_c         T_c         T_e             Q
```

```
0    0.000000  1.000000  546.617225  546.617225  4.555739e+06
1    0.002038  0.997962  497.474883  509.462309  3.437746e+06
2    0.000000  1.000000  608.495346  608.495346  6.996077e+06
3    0.001001  0.998999  502.730938  508.536652  3.412830e+06
4    0.000000  1.000000  598.863356  598.863356  6.563516e+06
..        ...       ...         ...         ...           ...
667  0.000450  0.999550  477.936442  481.013118  2.731827e+06
668  0.000493  0.999507  469.155423  472.712020  2.548075e+06
669  0.000544  0.999456  474.503798  478.296747  2.670640e+06
670  0.000604  0.999396  499.147275  502.752761  3.260194e+06
671  0.000542  0.999458  488.757341  492.207850  2.995158e+06

[672 rows x 17 columns]
```

8.5 Appendix E: Mt Etna 'Standard' emissivity-temperature trends

Mt Etna 'standard' input parameters

Using all available FTIR data for the three Mt Etna eruptions investigated (2001, 2002-2003 and 2017), allowed creation of a 'standard' (mean) emissivity-temperature spectral signatures (Fig. E1). from these trends and 'look-up' tables (Tables E1 and 5.2 in main text) were extracted in SWIR (2.22 μm), MIR (3.98μm) and TIR (11.0 μm and 12.0 μm) wavelengths which can be applied to spaceborne multi-platform analyses for Mt Etna (e.g., OLI, Sentinel-2A, MODIS).

Table E.1 Mt Etna 'standard' Emissivity-Temperature Trends

SWIR (2.20 μm)

Temperature (K)	773	823	873	923	973	1023	1073	1123	1173	1223	1273	1323	1373
FTIR NRE.4S	0.802	0.833	0.83	0.859	0.847	0.836	0.815	0.794	0.814	0.779	0.724	0.743	0.739
FTIR NRE.3S	**0.755**	**0.848**	**0.812**	**0.84**	**0.827**	**0.811**	**0.797**	**0.774**	**0.789**	**0.753**	**0.701**	**0.709**	**0.703**
FTIR NRE.1S	0.804	0.875	0.83	0.846	0.861	0.818	0.815	0.784	0.826	0.788	0.737	0.76	0.739
FTIR 'standard'	0.787	0.852	0.824	0.848	0.845	0.822	0.809	0.784	0.810	0.773	0.721	0.737	0.727
'standard' modelled	**0.817**	**0.824**	**0.828**	**0.830**	**0.828**	**0.824**	**0.815**	**0.805**	**0.791**	**0.774**	**0.755**	**0.733**	**0.706**
'standard' error	0.025	0.021	0.009	0.010	0.017	0.013	0.009	0.010	0.019	0.018	0.018	0.026	0.018
'std' Rad SWIR1	2.14	4.51	8.10	14.27	23.0	34.80	50.96	70.71	101.38	131.13	161.81	214.6	267.3
'std' Rad SWIR2	4.29	7.59	11.42	17.45	25.37	33.43	44.78	56.33	75.76	90.52	104.42	130.79	151.27

MIR (3.98 μm)

Temperature (K)	773	823	873	923	973	1023	1073	1123	1173	1223	1273	1323	1373
FTIR NRE.4S	0.753	0.733	0.736	0.713	0.677	0.672	0.634	0.608	0.594	0.562	0.518	0.513	0.480
FTIR NRE.3S	0.746	0.742	0.739	0.718	0.680	0.673	0.641	0.611	0.601	0.567	0.523	0.518	0.480
FTIR NRE.1S	0.752	0.744	0.734	0.711	0.688	0.665	0.648	0.619	0.624	0.587	0.538	0.547	0.495
FTIR 'standard'	0.750	0.740	0.736	0.714	0.682	0.670	0.641	0.613	0.606	0.572	0.526	0.526	0.485
'standard' modelled	**0.758**	**0.741**	**0.725**	**0.707**	**0.688**	**0.667**	**0.645**	**0.621**	**0.596**	**0.571**	**0.543**	**0.514**	**0.483**
'standard' error	0.004	0.006	0.003	0.004	0.005	0.004	0.007	0.006	0.015	0.013	0.010	0.017	0.008
'std' Rad MIR	837	1099	1413	1721	2020	2391	2712	3030	3462	3728	3879	4342	4460

TIR1 (11.0 μm)

Temperature (K)	773	823	873	923	973	1023	1073	1123	1173	1223	1273	1323	1373
FTIR NRE.4S	0.970	0.966	0.962	0.955	0.952	0.949	0.940	0.938	0.928	0.927	0.922	0.913	0.912
FTIR NRE.3S	0.959	0.954	0.952	0.946	0.940	0.938	0.930	0.926	0.916	0.912	0.909	0.897	0.893
FTIR NRE.1S	0.966	0.958	0.954	0.951	0.943	0.941	0.938	0.938	0.931	0.927	0.922	0.915	0.908
FTIR 'standard'	0.965	0.959	0.956	0.951	0.945	0.943	0.936	0.934	0.925	0.922	0.918	0.908	0.904
'standard' modelled	**0.964**	**0.959**	**0.956**	**0.951**	**0.946**	**0.942**	**0.937**	**0.932**	**0.927**	**0.921**	**0.916**	**0.910**	**0.904**
'standard' error	0.006	0.006	0.005	0.005	0.006	0.006	0.005	0.006	0.008	0.008	0.007	0.009	0.010
'std' Rad TIR 1	159.9	180.6	202.4	223.4	244.8	267.1	288.4	311.2	331.5	353.9	375.7	395.4	417.4

TIR2 (12.0 μm)

Temperature (K)	773	823	873	923	973	1023	1073	1123	1173	1223	1273	1323	1373
FTIR NRE.4S	0.976	0.972	0.969	0.962	0.958	0.956	0.947	0.945	0.936	0.934	0.927	0.920	0.917
FTIR NRE.3S	0.966	0.962	0.961	0.954	0.949	0.946	0.938	0.934	0.925	0.921	0.915	0.906	0.901
FTIR NRE.1S	0.973	0.967	0.963	0.959	0.952	0.949	0.946	0.945	0.940	0.936	0.928	0.924	0.917
FTIR 'standard'	0.972	0.967	0.964	0.958	0.953	0.950	0.944	0.941	0.934	0.930	0.923	0.917	0.912
'standard' modelled	**0.972**	**0.967**	**0.963**	**0.959**	**0.955**	**0.950**	**0.945**	**0.940**	**0.934**	**0.929**	**0.923**	**0.917**	**0.912**
standard error	0.005	0.005	0.004	0.004	0.005	0.005	0.005	0.005	0.007	0.008	0.007	0.009	0.008
'std' Rad TIR 2	121.4	136.3	151.8	166.8	182.1	197.8	212.8	228.7	242.3	258.9	273.6	288.0	302.9

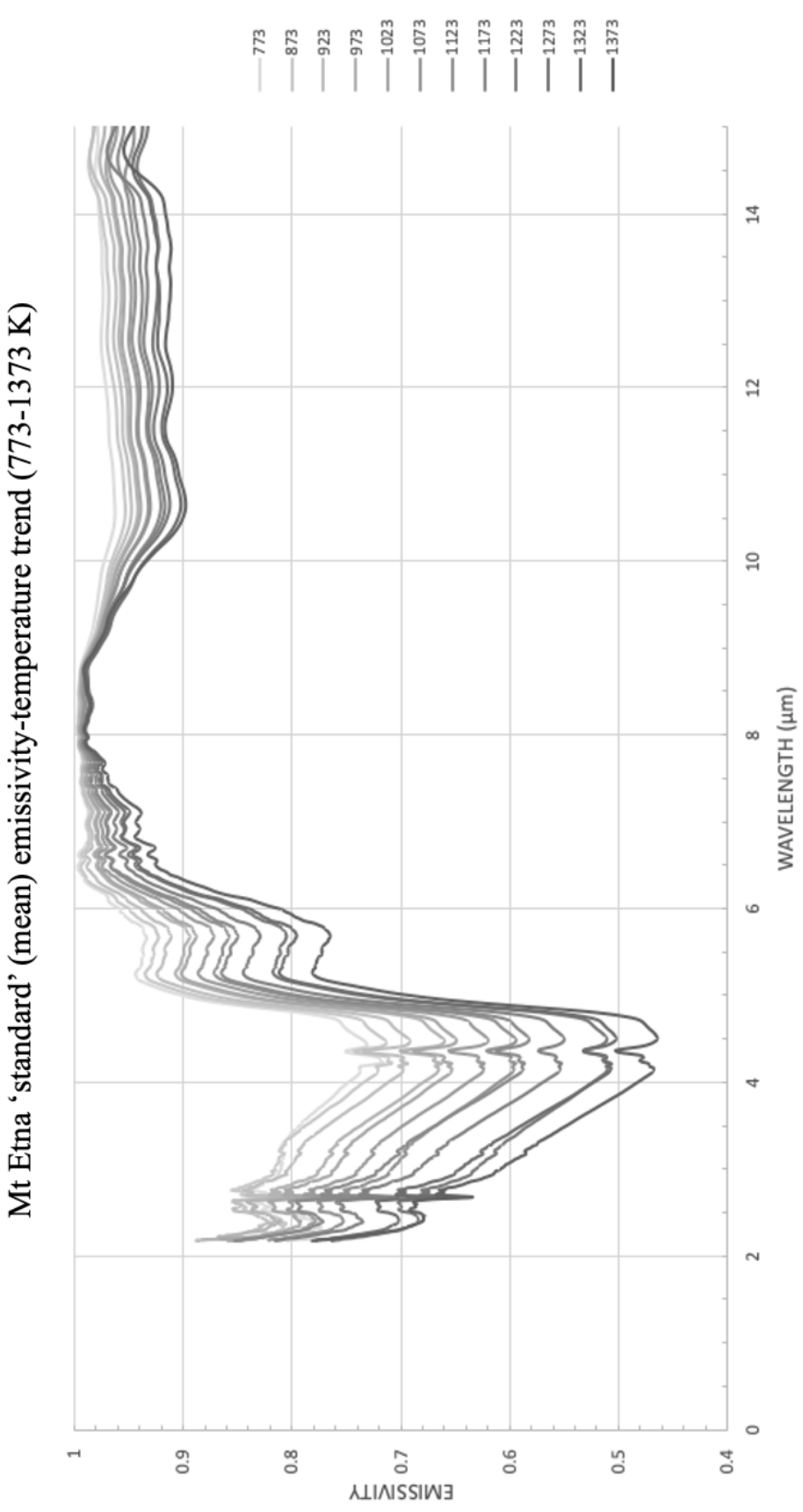

Figure E1 Mt Etna 'standard' (mean) absolute emissivity spectral signatures at a range of temperature (773-1373 K) and wavelength (2.17-15.0 µm)

8.6 Appendix F: Variation driven by the composition

To assess wider applicability of multi-component emissivity-temperature behaviour, developed here for the trachy-basaltic Mt Etna, two additional and distinctly different sites were considered; an andesitic subduction volcano, Lascar (Chile) and an intraplate tholeiitic basalt volcano, Kilauea (Hawaii).

Figure F1 shows measured and modelled emissivity-temperature data for Mt Etna ('standard' mean), Lascar volcano, Chile (sample courtesy of S. Self, OU, U.K.) from a 1993 lava and Kilauea (Hawaii) for sample obtained from the February 2018 Puu Oo lava coastal plain lava flow field (data courtesy of J. O. Thompson, the IVIS Laboratory, University of Pittsburgh). Modelled only results are shown in the main text (Table 5.2). Figure 5.7 in main text is repeated here for clarity showing distinct compositional trends identified for trachy-basalt (Mt Etna), andesite (Lascar) and basalt (Kilauea) from modelled data (Table F1 and 5.7).

Table F1 measured and modelled emissivity comparison: Mt Etna – Lascar – Kilauea

Temperature (K)	773	823	873	923	973	1023	1073	1123	1173	1223	1273	1323	1373
MIR Mt Etna FTIR	0.750	0.740	0.736	0.714	0.682	0.670	0.641	0.613	0.606	0.572	0.526	0.526	0.485
MIR Mt Etna model	0.758	0.741	0.725	0.707	0.688	0.667	0.645	0.621	0.596	0.571	0.543	0.514	0.483
MIR Lascar FTIR	0.727	0.708	0.702	0.675	0.636	0.628	0.584	0.554	0.530	0.495	0.451	0.432	0.402
MIR Lascar model	0.735	0.710	0.687	0.663	0.635	0.613	0.585	0.557	0.523	0.493	0.460	0.423	0.390
MIR Kilauea FTIR	0.727	-	0.703	-	0.669	-	0.627	-	0.621	-	0.506	-	0.516
MIR Kilauea model	0.730	-	0.700	-	0.670	-	0.630	-	0.590	-	0.540	-	0.490
TIR1 Mt Etna FTIR	0.965	0.959	0.956	0.951	0.945	0.943	0.936	0.934	0.925	0.922	0.918	0.908	0.904
TIR1 Mt Etna model	0.964	0.959	0.956	0.951	0.946	0.942	0.937	0.932	0.927	0.921	0.916	0.910	0.904
TIR1 Lascar FTIR	0.951	0.938	0.933	0.922	0.914	0.910	0.893	0.888	0.865	0.854	0.852	0.816	0.813
TIR1 Lascar model	0.944	0.937	0.929	0.921	0.912	0.901	0.890	0.878	0.866	0.852	0.837	0.822	0.806
TIR1 Kilauea FTIR	0.893	-	0.888	-	0.877	-	0.867	-	0.857	-	0.877	-	0.850
TIR1 Kilauea model	0.893	-	0.885	-	0.877	-	0.870	-	0.864	-	0.860	-	0.856
TIR2 Mt Etna FTIR	0.972	0.967	0.964	0.958	0.953	0.950	0.944	0.941	0.934	0.930	0.923	0.917	0.912
TIR2 Mt Etna model	0.972	0.967	0.963	0.959	0.955	0.950	0.945	0.940	0.934	0.929	0.923	0.917	0.912
TIR2 Lascar FTIR	0.966	0.957	0.955	0.945	0.938	0.935	0.920	0.915	0.898	0.888	0.882	0.854	0.848
TIR2 Lascar model	0.964	0.959	0.953	0.947	0.940	0.931	0.922	0.911	0.901	0.888	0.875	0.861	0.846
TIR2 Kilauea FTIR	0.908	-	0.902	-	0.890	-	0.879	-	0.870	-	0.879	-	0.855
TIR2 Kilauea model	0.908	-	0.899	-	0.890	-	0.883	-	0.874	-	0.867	-	0.860

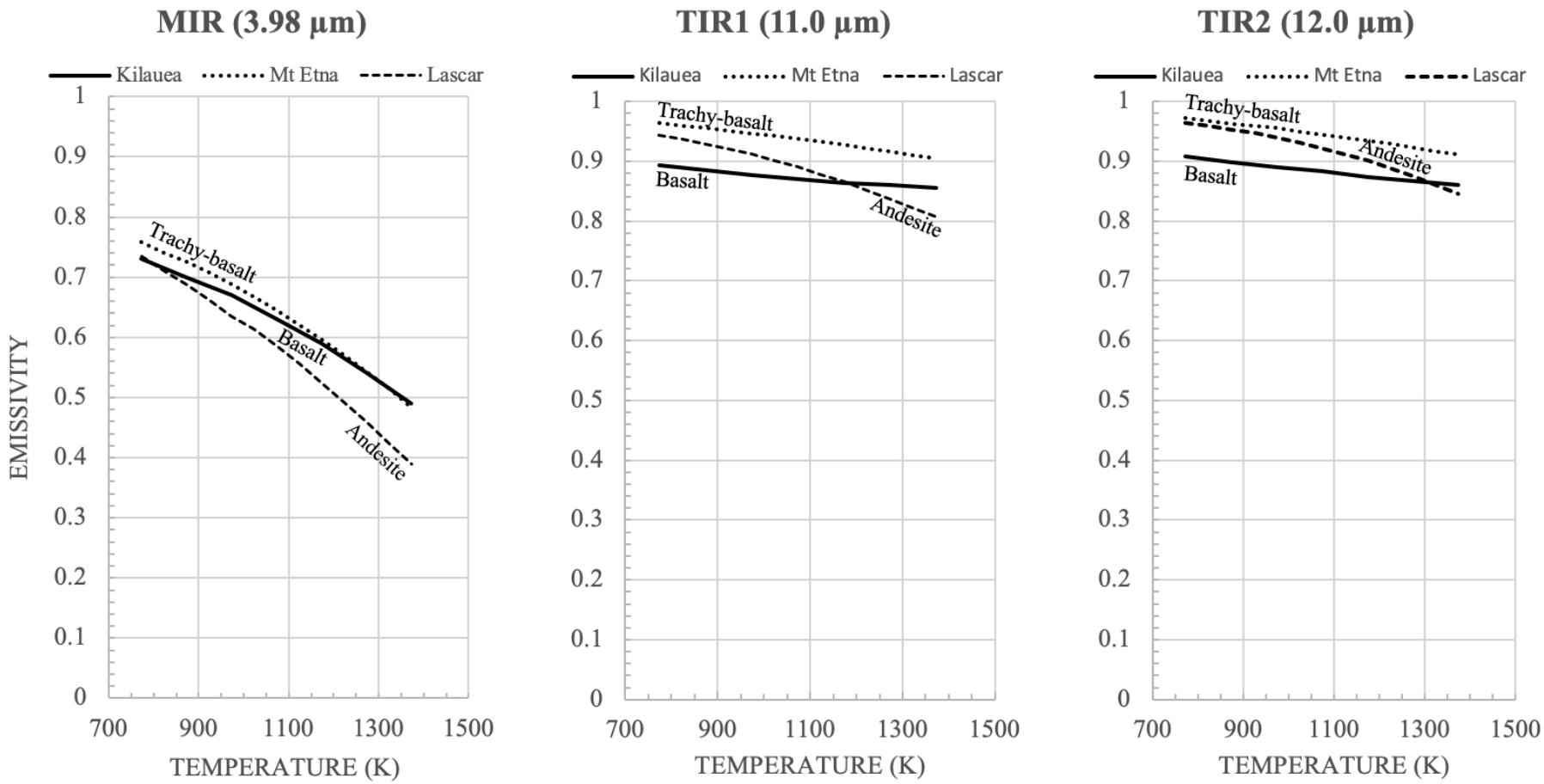

8.7 Appendix G: Publication: (Rogic et al., 2019a)

remote sensing

MDPI

Article

Role of Emissivity in Lava Flow 'Distance-to-Run' Estimates from Satellite-Based Volcano Monitoring

Nikola Rogic [1,*], Annalisa Cappello [2] and Fabrizio Ferrucci [1,3]

1 School of Environment, Earth and Ecosystem Sciences, The Open University, Milton Keynes MK7 6AA, UK; fabrizio.ferrucci@unical.it
2 Istituto Nazionale di Geofisica e Vulcanologia, Osservatorio Etneo, 95125 Catania, Italy; annalisa.cappello@ingv.it
3 Department of Environmental and Chemical Engineering, University of Calabria, 87036 Rende (CS), Italy
* Correspondence: nikola.rogic@open.ac.uk; Tel.: +44-077-313-02424

Received: 30 January 2019; Accepted: 14 March 2019; Published: 19 March 2019

Abstract: Remote sensing is an established technological solution for bridging critical gaps in volcanic hazard assessment and risk mitigation. The enormous amount of remote sensing data available today at a range of temporal and spatial resolutions can aid emergency management in volcanic crises by detecting and measuring high-temperature thermal anomalies and providing lava flow propagation forecasts. In such thermal estimates, an important role is played by emissivity—the efficiency with which a surface radiates its thermal energy at various wavelengths. Emissivity has a close relationship with land surface temperatures and radiant fluxes, and it impacts directly on the prediction of lava flow behavior, as mass flux estimates depend on measured radiant fluxes. Since emissivity is seldom measured and mostly assumed, we aimed to fill this gap in knowledge by carrying out a multi-stage experiment, combining laboratory-based Fourier transform infrared (FTIR) analyses, remote sensing data, and numerical modeling. We tested the capacity for reproducing emissivity from spaceborne observations using ASTER Global Emissivity Database (GED) while assessing the spatial heterogeneity of emissivity. Our laboratory-satellite emissivity values were used to establish a realistic land surface temperature from a high-resolution spaceborne payload (ETM+) to obtain an instant temperature–radiant flux and eruption rate results for the 2001 Mount Etna (Italy) eruption. Forward-modeling tests conducted on the 2001 'aa' lava flow by means of the MAGFLOW Cellular Automata code produced differences of up to ~600 m in the simulated lava flow 'distance-to-run' for a range of emissivity values. Given the density and proximity of urban settlements on and around Mount Etna, these results may have significant implications for civil protection and urban planning applications.

Keywords: emissivity; lava flow modeling; remote sensing; volcano monitoring

1. Introduction

As less than 10% of the ~1500 active subaerial volcanoes around the world are monitored regularly on the ground, remote sensing (RS) provides an opportunity to increase coverage. A combination of laboratory-based analyses, RS data, and numerical modeling could bridge critical gaps in volcanic hazard assessment and risk mitigation.

The prediction of lava flow 'distance-to-run' (ultimate length) is viewed as the key activity in support of risk mapping and planning the emergency response and crisis management of effusive volcanic events. The impact of volcanic eruptions and distances to which erupted lava will flow depend on several physical and chemical parameters [1–4].

It is widely recognized that RS data can be integrated with ground-based observations during volcanic crisis to facilitate the estimation of thermal anomalies and—depending on spatial and temporal resolutions—forecast the geographic extent of active lava flows. However, a developing lava flow is a complex surface to observe using remote techniques, due to the moving material exhibiting a range of temperatures, textures, vesicularities [5], and thicknesses. Furthermore, the evolution of thermal anomalies may involve continuous changes in energy emitted as surfaces cool, as well as variations that depend on viewing angles [6].

Several automated processes for the detection and measurement of volcanic 'hot-spots'—such as VAST [7], MODVOLC [8,9], RAT [10], MyVOLC and MyMOD [11], among others—have been developed, tested, and run to date. In particular, three projects have marked the development and awareness for a complete and global monitoring capacity: (i) the European Space Agency's (ESA) pilot project GLOBVOLCANO (2008–2011), using high-spatial resolution RS; (ii) the European Commission's European Volcano Observatory Space Services (EVOSS, 2010–2014), centered on high to very-high temporal resolutions, and (iii) the Disaster Risk Management volcano pilot project of the Committee on Earth Observation Satellite (CEOS), focusing on the continuous monitoring of volcanic activity in the whole of Latin America and the Caribbean. These projects, among others, have demonstrated how access to RS data over volcanic regions can enhance the understanding of volcanic activity, enabling hazard mitigation and the identification of developing trends in volcanic activity [12,13].

A focus of this study is emissivity, which is defined as the efficiency of radiating thermal energy at a specific wavelength. Although it is a critical variable in the interpretation of passive RS for accurate surface temperature estimation, emissivity is seldom measured and mostly assumed or estimated to be a fixed value, which does not change as a function of temperature and wavelength.

The fundamental laws of Planck, Stefan-Boltzmann, and Wien demonstrate that surfaces radiate in different regions of the electromagnetic spectrum, depending on their temperature. Planck's radiation law defines the radiation released to be that of a perfect radiator, a blackbody: however, very few terrestrial surfaces would act as near-perfect blackbodies. The ability of non-blackbody surfaces to emit radiation is defined by their emissivity. Emissivity may be defined as the ratio of the radiation emittance of a sample relative to that of a blackbody at the same temperature.

Volcanic surfaces, such as the basalts analyzed here, may be characterized as selective radiators, since their emissivity varies with wavelength and would be less than unity (blackbody). A variety of approaches have been used to derive surface temperatures from RS data, where emissivity is either assumed to be unity, or a fixed 'look up' value. This value for basaltic surfaces is estimated to be 0.90 to 0.95 [14], or it is estimated directly from reflectance data [15] (e.g., 0.80). The motivation of this study is to establish the significance of emissivity variations in the derivation of lava surface temperatures from RS data, and assess the impact of such variations on the estimation of eruption rates and the prediction of lava flow 'distance-to-run' using high spatial resolution spaceborne data.

2. Materials and Methods

2.1. Rock Samples

Due to its persistent activity, Mount Etna (Italy) is frequently targeted for studies involving the application of RS data to detect high-temperature thermal features and measure eruptive products [9,16]. The 2001 eruption presents three main features: (i) despite lasting only 23 days (18 July to 09 August 2001), it gave rise to an outstanding pattern of seven different (Figure 1) fast-developing lava flows [17]; (ii) the total lava flow volume is significant in the recent eruptive history of Etna, and (iii) this eruption could be observed by three high spatial resolution multispectral payloads (TM onboard Landsat 5, ETM+ onboard Landsat 7, and ASTER onboard Terra).

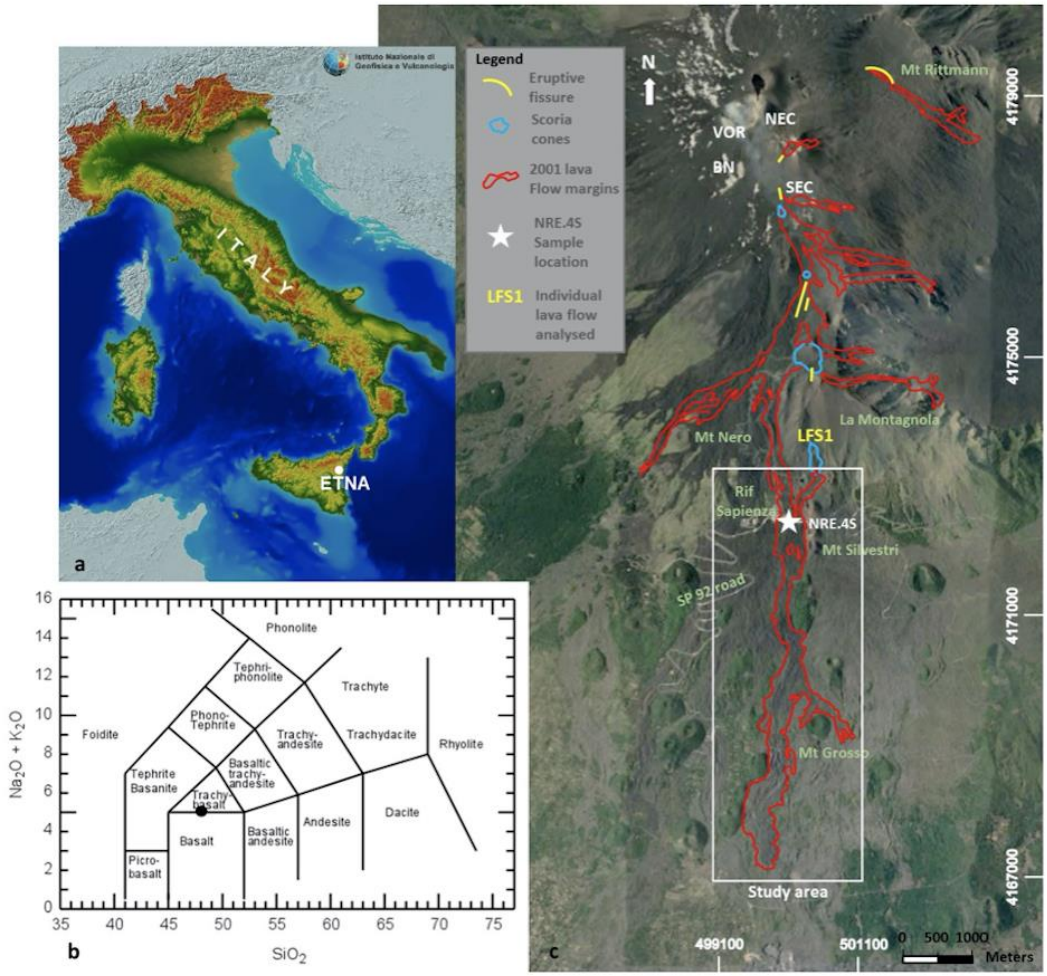

Figure 1. (**a**) A geological map of Italy and the location of Mount Etna [18]; (**b**) Derived silica versus alkalis, superimposed on the chemical classification scheme for NRE.4S; (**c**) The 2001 eruption lava flow margins are highlighted in red and superimposed on the target area in Google Earth. Eruptive fissures are marked in yellow, scoria cones in light blue (after [17]) and within the individual flow study area (LFS1), the approximate sample locations are indicated by the star symbol.

To measure the emissivity of exposed lavas, we collected 10 rock samples termed the NRE.4 Series (NRE.4S) across the main flow (LFS1) (Figure 1), in a grid scaled to the spatial resolution of the ASTER TIR bands (~90 m). Samples were initially investigated using Fourier transform infrared (FTIR) spectroscopy to derive emissivity from both reflectance and radiance data at ambient/low and high temperatures. Existing spaceborne data (ASTER Global Emissivity Database) and numerical modeling (MAGFLOW) are used for data validation.

The chemical composition of the samples (average values for the entire series) and their approximate locations are provided in Table 1 and shown in Figure 1. Previously published information on volumes and effusion rates for the 2001 Mount Etna eruption [17] are also provided in Table 2.

Table 1. X-Ray Fluorescence major elements content, as a component oxide weight percent (wt%).

SiO_2	TiO_2	Al_2O_3	Fe_2O_3	MnO	MgO	CaO	Na_2O	K_2O	P_2O_5	SO_3	LOI	Total
48.15	1.53	16.49	11.19	0.17	5.71	10.49	3.52	1.70	0.53	0.005	−0.30	99.18

Table 2. Volumes and effusion rates for the LFS1 2001 Mount Etna eruption (from [17]).

Acquisition Date	Local Time	Eruption Day	Acquisition Time (s)	Cumulative Volume ($\times 10^6$ m^3)	Time Span (s)	Partial Volume ($\times 10^6$ m^3)	Daily Effusion Rate (m^{3}s^{-1})
18/07/2001	03:00	0	0	0.00	0	0.00	0.00
18/07/2001	13:00	1	36,000	0.37	36,000	0.37	10.28
19/07/2001	16:00	2	133,200	1.70	97,200	1.33	13.68
20/07/2001	13:00	3	208,800	3.50	75,600	1.80	22.81
22/07/2001	11:00	5	374,400	8.58	165,600	5.08	30.68
26/07/2001	12:00	9	723,600	14.98	349,200	6.40	18.33
28/07/2001	16:00	11	910,800	16.99	187,200	2.01	10.74
30/07/2001	11:00	13	1,065,600	18.35	154,800	1.37	8.85
02/08/2001	10:00	16	1,321,200	19.82	255,600	1.47	5.75
04/08/2001	07:00	18	1,483,200	20.62	162,000	0.80	4.94
06/08/2001	11:00	20	1,670,400	21.21	187,200	0.59	3.15
07/08/2001	07:00	21	1,742,400	21.32	72,000	0.11	1.53
09/08/2001	10:00	23	1,926,000	21.40	183,600	0.08	0.44

2.2. Laboratory-Based Data Acquisition

We carried out laboratory Fourier transform infrared (FTIR) analyses on solidified volcanic rock samples from the major 2001 eruption of Mount Etna to derive emissivity at a range of wavelengths and temperatures.

2.2.1. Emissivity from Surface Reflectance Spectra

We collected reflectance spectra of samples measured at an ambient temperature (~295 K) at the Planetary Emissivity Laboratory (DLR, Germany) by the Bruker Vertex 80v FTIR spectrometer, using a gold integration sphere hemispherical reflectance accessory.

The experimental setup [19] measures the reflectance of samples in the visible, the near infrared bands, and medium infrared (MIR) ranges. Reflectances are converted into approximate emissivity. For MIR measurements, a wide-range Mercury Cadmium Telluride (MCT) detector is used (1000–400 cm^{-1}) in tandem with a wide-range germanium (Ge) on potassium bromide (KBr) beam splitter (12,500–420 cm^{-1}). For V-NIR measurements, conversely, an InGaAs Diode detector was used (12,500–5800 cm^{-1}) in tandem with a silicon (Si) on calcium fluoride (CaF_2) beam splitter (15,000–1200 cm^{-1}).

Samples (grain size 500–1000 µm) were placed into individual sample cups, which were placed on the hemispherical reflectance accessory, and aligned. Prior to measuring samples, a gold reference target was used to calibrate the instrument. Finally, individual sample spectra were normalized to the gold reference target spectrum results to obtain reflectance values.

The apparent emissivity (ε') values were derived using the measured reflectance (R) data using Kirchhoff's law (Equation (1)). This approach provides an expected result precision of 0.005 [20].

$$\varepsilon' = 1 - R \quad (1)$$

It is important to note that Kirchhoff's law (1) is only valid for hemispherical reflectance measurements, and is used to approximate emissivity from reflectance data [21]; thus, the term 'apparent' emissivity (ε') is used in contrast to the 'true' emissivity (ε).

2.2.2. Emissivity from Surface Radiance Spectra

The thermal emission spectra of the samples were measured in a vacuum (0.7 mbar) at temperature and wavelength ranges of 400 to 900 K and 5.0 to 16.0 µm, respectively. The experimental setup [19] used an external simulation chamber attached to the FTIR spectrometer measuring the emissivity of solid samples (grain size 100–3000 µm). The emissivity chamber was equipped with an internal web-cam, and several temperature sensors to measure the sample/cup temperature, monitor the

equipment, and record chamber temperatures. Both the cup and the sample are heated uniformly by induction, and the temperature of the emitting surface is measured using a thermophile sensor in contact with the surface. The resulting data are calibrated using the emissivity spectrum of the blackbody material [19] to provide the set of 'true' emissivity (ε) data.

2.3. Emissivity from High-Spatial Resolution Satellite Data

The Global Emissivity Database

The Global Emissivity Database (GED v.3) built by NASA's Jet Propulsion Laboratory (JPL) [22] is the most detailed emissivity product available for Earth's land surface. Emissivity, rescaled to 100 m from the original 90-m ASTER TIR pixels, is an average of data acquired at five TIR central wavelengths (8.30 µm, 8.65 µm, 9.10 µm, 10.60 µm, and 11.30 µm) every 16 days, from 2000 to 2008. It was obtained by NASA JPL by combining temperature emissivity separation (TES) algorithms and water vapor scaling (WVS) atmospheric corrections coincident with MODIS MOD07 atmospheric profiles and the MODTRAN 5.2 radiative transfer code [23].

In this study, we examined 12 1° × 1° ASTER GEDv3 data 'tiles' downloaded from the NASA EOSDIS Land Processes DAAC [24], centered on Sicily (Italy) and Mount Etna.

3. Emissivity Results

3.1. Emissivity from Reflectance

As a preliminary estimate of surface emissivity, we used FTIR reflectance data measured at ambient temperature. The spectral signatures were consistent with those from previous research on basaltic rocks [14,25], confirming that representative emissivity data can be obtained this way (Figure 2). To extend the observable spectral range, two detectors (KBr at 0.66 to 2.50 µm and MCT at 2.50 to 16.00 µm) were used, so that the data could be merged at 2.63 µm to provide the best signal-to-noise (STN) ratio result for the entire range from visible near-infrared (VNIR) to TIR wavelength. The maximum difference in emissivity at any wavelength between the NRE.4 series samples was 0.02.

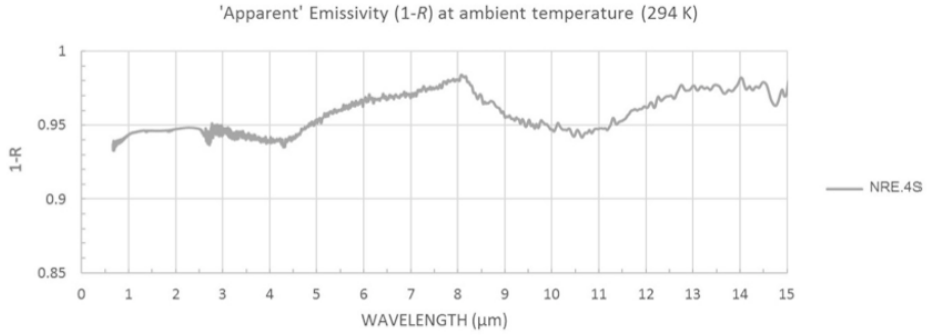

Figure 2. 'Apparent' emissivity (ε') spectral signatures measured and derived from reflectance Fourier transform infrared (FTIR) data (1-*R*) at ambient temperature for NRE.4S.

3.2. Emissivity from Radiance

The spectral signatures for samples analyzed using thermal emission analysis at 400 K (Figure 3a) display emissivity values consistent with the preliminary reflectance data (Figure 2) in the TIR region (8.0–15.0 µm), with a significantly improved STN ratio and optimal error range (<0.01) for NRE.4 Series. In contrast to ambient/low-temperature data, high-temperature results (Figure 3b) show a steady decrease in emissivity with every temperature increase step (400–900 K). However, this trend could not be observed between 5.0–6.0 µm. This is because of the instrument sensitivity limitations and

for this reason, only the results in TIR wavelengths (8.0–15.0 μm) should be used in further analyses. An additional 'cooling test' was performed by measuring the emissivity of the same series in the opposite direction (cooling), by decreasing temperature steps (i.e., 900–400 K), maintaining consistent sample conditions. The deviance in emissivity values during the temperature increase (heating) is shown in Figure 3b and the temperature decrease (cooling) was ≤0.02 with no hysteresis deviation trend in either direction.

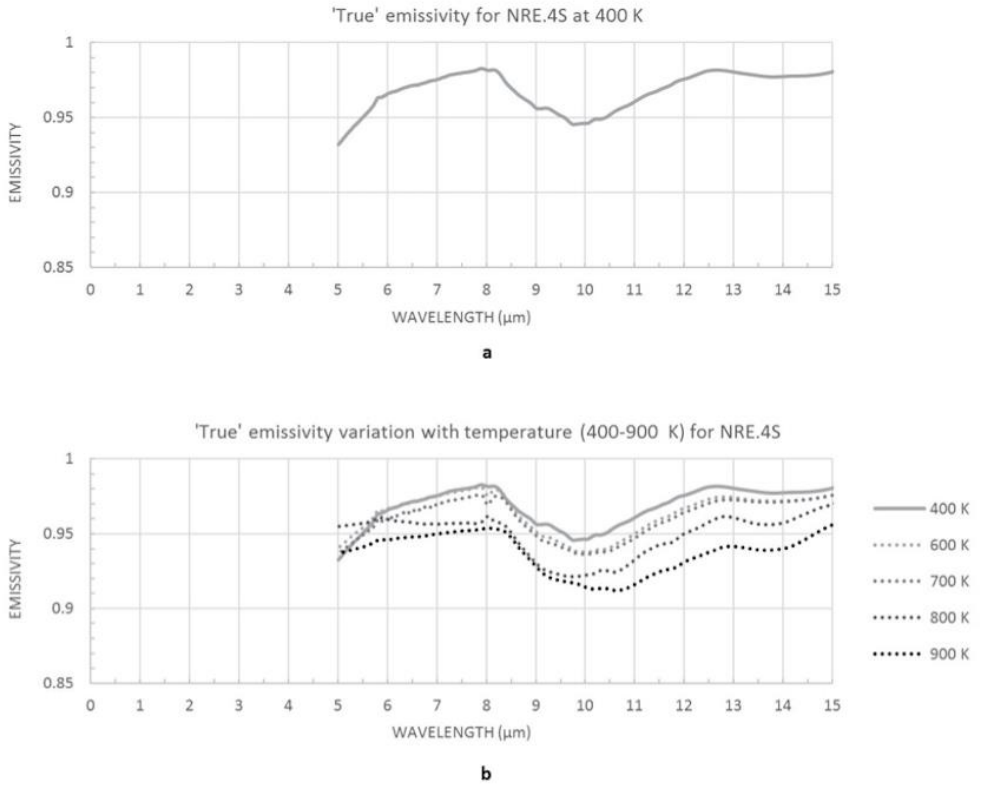

Figure 3. (**a**) 'True' emissivity (ε) spectral signatures at 400 K using thermal emission FTIR for NRE.4S; and (**b**) 'true' emissivity (ε) spectral signature variation with temperature change between 400–900 K.

3.3. Comparison with Emissivity from Satellite Data

The emissivity map (Figure 4) created using existing spaceborne ASTER GEDv3 data [22] over Sicily (Italy) and Mount Etna, displays a mean emissivity variation of the NRE.4S targets analyzed. The highest emissivities are shown in dark blue; these correspond to the Mt Etna region, which is consistent with the emissivity signatures of basaltic volcanic surfaces. Sicily is geologically complex due to its regional tectonics; thus, green and red areas on the map with lower emissivities would represent compositionally different geological units of non-volcanic origin.

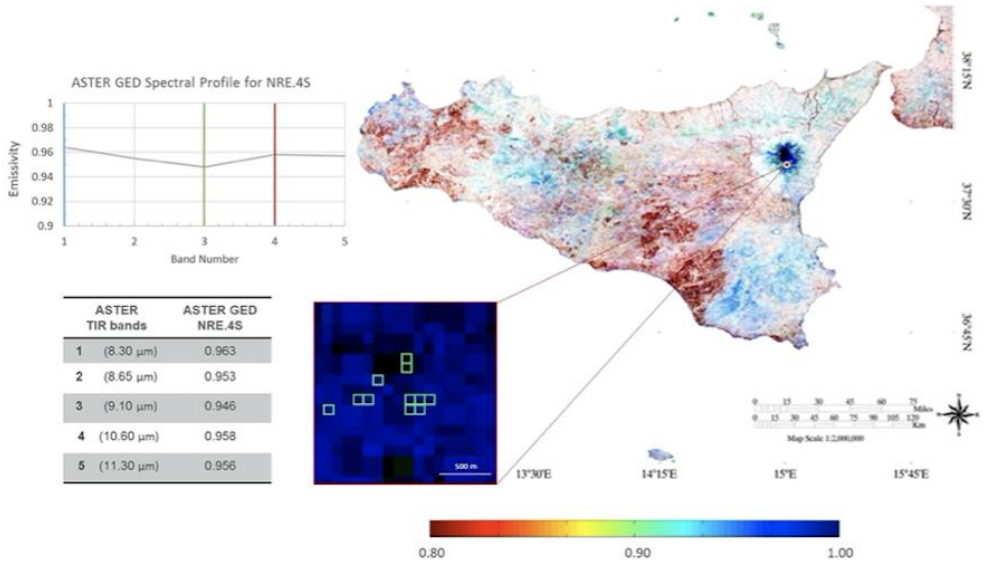

Figure 4. (Map) ASTER Global Emissivity Database (ASTER GED) over Sicily, Italy at 100-m pixel resolution at 10.60 µm and 4-3-1 band red–green–blue (RGB) view. The color ramp indicates the mean emissivity values (0.8–1.0). Inset shows samples' pixel locations for NRE.4S. Emissivity spectral profile plot and the table show emissivity variation with wavelength, extracted from ASTER GED for NRE.4S.

For a direct comparison, spaceborne emissivity data (Figures 4 and 5a) and laboratory FTIR results (Figures 2 and 3a) of the same area targets (NRE.4S) are shown at ASTER TIR operating central-wavelength bands (8.30 µm, 8.65 µm, 9.10 µm, 10.60 µm, and 11.30 µm). A relatively comparable trend can be observed (Figure 5b), exhibiting the best data fit at 9.10 µm ($\leq$0.01) and data range/error of $\leq$0.03 at other wavelengths. Accounting for different methodologies used in this study and their limitations (discussed in Section 5), the emissivity range/error is expected. This may suggest that, despite being a nine-year average (2000–2008), the ASTER GED mean emissivity data for the 2001 lava flow area can fit reasonably well with our results obtained using ambient/low-temperature FTIR laboratory measurements. However, the high-temperature FTIR results (Figure 3b) indicate a trend (Figure 5c,d) that suggest an emissivity decrease with temperature increase.

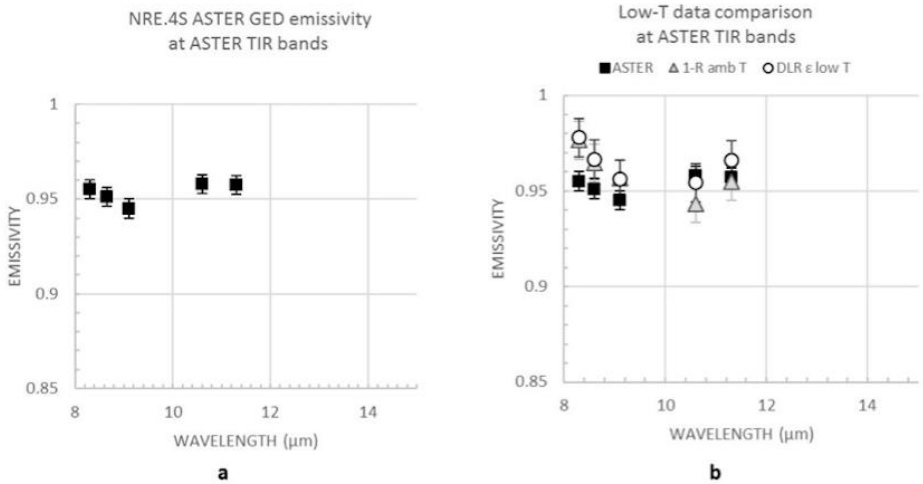

Figure 5. *Cont.*

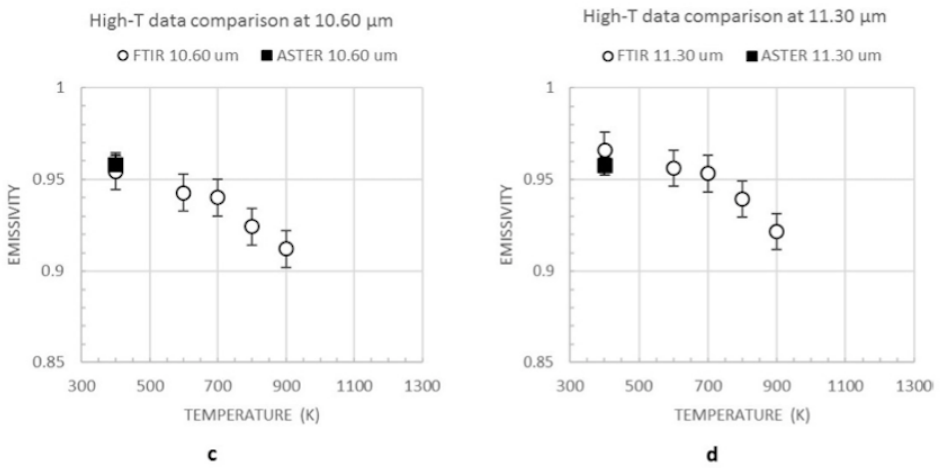

Figure 5. (**a**) ASTER GED mean emissivity values (black squares) plotted at ASTER TIR bands for NRE.4S; (**b**) ASTER GED mean emissivity values (black squares) compared to the 'apparent' (1-*R*) emissivity (grey triangles) and 'true' low-temperature (400 K) emissivity data (empty circles) for NRE.4S; (**c**,**d**) ASTER GED mean emissivity (static) for NRE.4S (black square) at 10.60 µm and 11.30 µm (ASTER TIR bands 4 and 5 respectively), superimposed on the emissivity/temperature trend 400–900 K (empty circles). Error bars represent maximum emissivity difference between NRE.4S samples measured.

4. Emissivity versus Effusion Rate and 'Distance-to-Run'

4.1. From Spaceborne Data

Varying the emissivity and wavelength will have an impact on the computation of integrated temperatures and radiant fluxes, and hence on the estimation of lava effusion rates and 'distance-to-run'. To perform a quantitative evaluation, we selected the best-quality night-time image acquired during the 2001 eruption, aimed to avoid both pixel saturation and the reflected radiances of daytime images in SWIR.

This eruption was observed by three high-spatial resolution payloads on Landsat 5 (ETM), Landsat 7 (ETM+), and Terra (ASTER). The selected image data presented here was acquired by ETM+ on 5 August 2001 at 20:34 (Figure 6a). ETM+ is the multispectral scanning radiometer onboard Landsat 7, providing high-spatial resolution data (30 m in V-NIR-SWIR and 60 m in TIR) in repeat cycles of 16 days. Launched in 1999 and still active at the date of writing, ETM+ provided very high-quality images until 2003, when the linear scan compensator developed a permanent fault affecting the whole image (black stripes).

To assess the sensitivity to variations in emissivity, we selected three values. One end-member is a blackbody (1.0), and the second value (0.80) has been used in published research [15]. The third value (0.93) that was selected for our assessment is the minimum emissivity value at 10.60 µm from our reflectance data (Figure 2), which is also a mean emissivity estimate for basalt [14].

The image was processed for all of the radiant pixels in SWIR and TIR using the three emissivities (1.0, 0.93, and 0.80), following previously established procedures [26]. After radiometric and atmospheric correction [27,28], integrated temperatures are calculated and sub-resolutions were solved in SWIR (1.65 µm and 2.20 µm) to obtain the total radiant flux Q_{r_calc}.

$$Q_{r\_calc} = A\varepsilon\sigma\tau\Phi'(T_e^4 - T_a^4) \quad (2)$$

from which the lava effusion rate [16,29,30] E_{r_calc} is estimated:

$$E_{r\_calc} = \frac{Q_{r\_calc}}{\rho[C_P\Delta T + \Phi\, C_L]} \quad (3)$$

In Equation (2), A is the pixel surface area, ε is the emissivity, σ is the Stefan–Boltzmann's constant, τ is atmospheric transmissivity, and Φ' is the shape of the radiating surface. Note that the symbol Φ' in Equation (2) is not the same symbol representing the percentage of crystals grown (Φ) in Equation (3) or the fitness function (ϕ) in Table 3. The equation for radiative heat transfer has term $T_e^4 - T_a^4$, where T_e^4 is the effective temperature to the fourth, power and T_a^4 is the ambient temperature to the fourth power. The difference in temperature from the hot material to the ambient temperature has a control on the rate of transfer. As we are dealing with very small changes in emissivity, this small difference in temperature will play an important role.

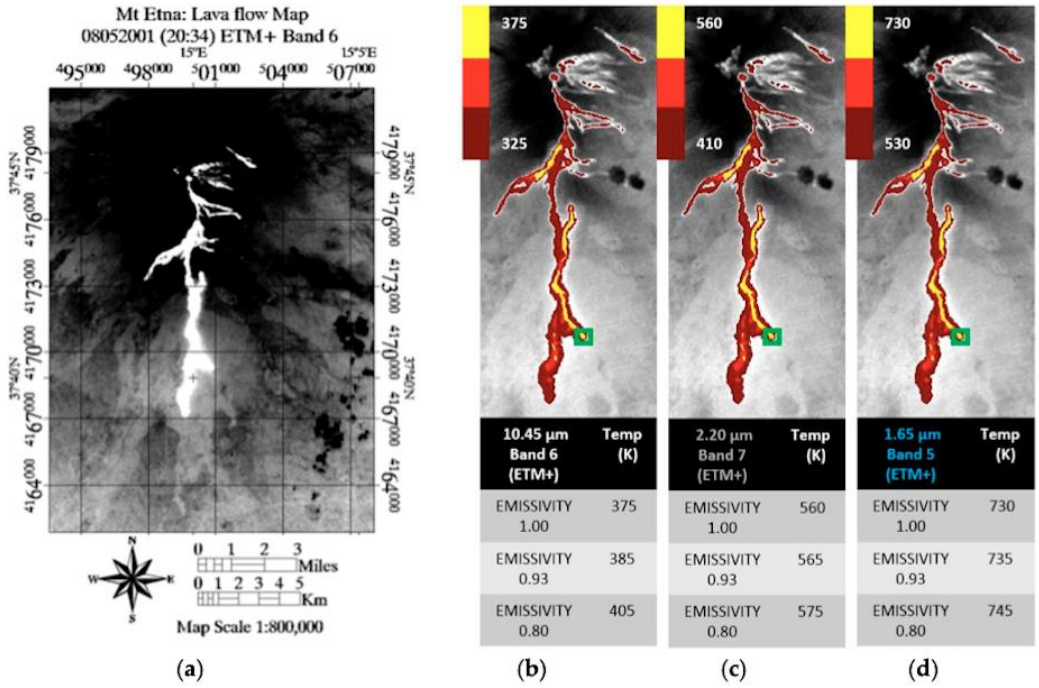

Figure 6. (**a**) Mount Etna high-temperature thermal anomaly scene acquired on 5 August 2001 by Landsat 7 (ETM+); (**b–d**) are all radiant pixel integrated temperatures of the same target area as in (**a**) TIR Band 6 and SWIR bands 7 and 5 for emissivity of 1.0; The green square in (**b–d**) marks the location of the pixel (37°39′28″N 14°59′48″E) used to derive temperature with emissivity variation given below (**b–d**).

In Equation (3), ρ is the lava density (2600 kg m^{-3}); C_P the specific heat capacity (1150 J kg^{-1} K^{-1}); ΔT is the average temperature difference throughout the active flow (100 to 200 K), which is a significant parameter in estimating eruption rate; Φ is the average mass fraction of crystals (0.4 to 0.5) grown in cooling through ΔT, and C_L is the latent heat of crystallization (2.9×10^5 J kg^{-1}).

Note that while Equation (2) includes only observables and variable emissivity, the values used to solve Equation (3) are average values taken from various literature sources, which are specific for this type of lava and Mount Etna [31,32].

We observe that the TIR (Figure 6b) and two SWIR channels (Figure 6c,d) display significantly different integrated pixel temperatures on the active flow, ranging from as low as 325 K (brightness temperature $\varepsilon = 1$ at 10.45 µm TIR wavelength) to as high as 745 K ($\varepsilon = 0.8$ and 1.6 µm SWIR). Overall, 20% emissivity change may give rise to integrated pixel temperature differences in the order of 15 K in SWIR and 25 K in TIR (shown in 6b-d), which is consistent with previous research [15].

We used the instantaneous effusion rate E_{r_calc} derived from high-spatial resolution RS data to attempt a rapid estimation of the maximum lengths that individual lava flow can reach (Figure 7).

By implementing the empirical law $L_{max} = 2E_r^{\frac{1}{2}}$ [33,34] we observe that a moderate difference in emissivity will influence calculated eruption rates and may impact the L_{max} 'distance-to-run' by as much as ±300 m.

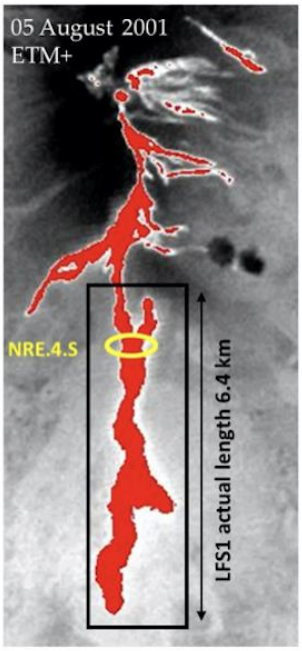

[26] Radiant Flux (Q_{r_calc}) all radiant SWIR pixels

[29] Effusion Rates (E_{r_calc})

[33] $L_{max} = 2(E_r)^{0.5}$

Emissivity	1.00	0.93	0.80
$E_{r\ calc}$ $(m^3 s^{-1})$	2.0	1.9	1.6
L_{max_calc} (km)	2.8	2.7	2.5

Figure 7. ETM+ scene obtained on 5 August 2001 highlighting the high-temperature thermal anomaly, focusing on an individual LFS1 flow analyzed in this study and detailing a flow chart of procedures followed to obtain the maximum lengths that LFS1 lava flow can reach using the empirical approach [33,34]. The table shows the difference in results using various emissivity values (0.80, 0.93, and 1.0).

Often, the effusion rate can be calculated by exploiting ground-based observations, where the information on how the volume of an individual flow has changed in a given time interval can be quite accurate. This is achieved by using information on the rate of advance, if the cross-sectional area of the flow front is known (i.e., width × thickness × rate of advance) or if the volume and time interval are known (length × width × thickness ÷ time). The calculated eruption rate is used in the L_{max} equation to estimate the maximum length that the lava flow can achieve. This approach provides an estimated maximum lava flow length, and is not intended to forecast the exact final length of the flow.

The individual lava flow LFS1 analyzed here reached its maximum length on or around 25 July 2001 with an estimated eruption rate of 18.33 m^3s^{-1} [17]. According to field estimates, after that date, the effusion rate dropped, so lava did not extend along the whole flow length. Our ETM+ data from 5 August 2001 produced an effusion rate of ~2 m^3s^{-1}, which is in line with the rate drop observed for that time period, and corresponds well with field estimates of ~3 m^3s^{-1} on 6 August 2001 (Table 2).

The total volume [17] up to the end of the eruption (Table 2) would suggest an average effusion rate (i.e., cumulative volume divided by the acquisition time in seconds) of 11.1 m^3s^{-1} and L_{max} = 6.7 km, which is slightly greater than and consistent with the observed $L_{max} = 6.4\ km$. Nonetheless, the L_{max} estimation is most needed at the start of the eruption. Our ETM+ calculated effusion rate for 5 August 2001 also highlighted an increase in L_{max} of 5% between emissivity end-members (i.e., 0.80 and 1.0), which may play a role in hazard mitigation at densely populated areas in close proximity to an active volcano.

4.2. From Straightforward Modelling

To reproduce the lava flow path for the 2001 Mount Etna eruption, we used the MAGFLOW cellular automaton propagator [35,36], which uses a physical model accounting for both thermal and rheological evolution of flowing lavas. It is argued that this model has the potential to significantly improve understanding of the dynamics of lava flow emplacement [37] and assist with related hazard assessment and mitigation [38–42]. MAGFLOW sensitivity analyses show that the main controlling factors are topography, rheology, and vent location, while temporal changes in effusion rates will also strongly influence the accuracy of the predictive lava-flow modeling [43,44].

To model the lava flow path for the 2001 Etna eruption, MAGFLOW was run on a pre-eruptive Digital Elevation Model (DEM) using field-derived effusion rates [17] and the typical properties of basaltic rocks (density = 2600 kg/m^3; specific heat capacity = 1150 J kg^{-1} K^{-1}; solidification temperature = 1173 K; extrusion temperature = 1360 K), and we varied the emissivity.

To evaluate its impact on the simulated ultimate lava flow lengths, we carried out a sensitivity test where three different emissivity values (i.e., 0.80, 0.93, and 1.00) were introduced to the model, maintaining constant emissivity, unaffected by temperature changes throughout the simulation. This method was validated using the actual lava flow extent of the 2001 Mount Etna eruption.

The MAGFLOW simulations obtained using the various emissivity values (i.e., 0.80, 0.93, and 1.00) are shown in Figure 8. There is good overall agreement between the actual and the simulated lava flows, but major discrepancies occurred for all simulations and reality due to the neglecting of the ephemeral vent opening that fed the minor, southeastern branch of the flow [17].

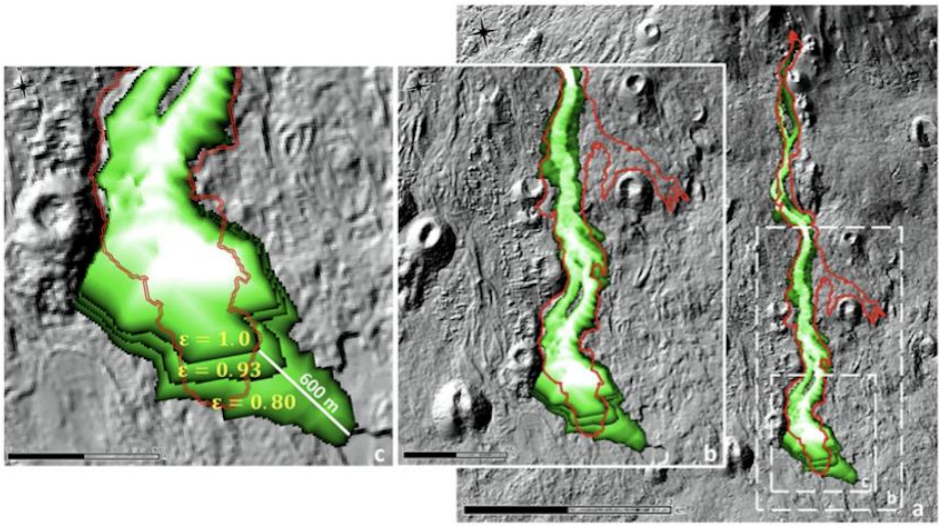

Figure 8. MAGFLOW simulation results with changing emissivity (i.e., 0.80, 0.93, and 1.00), showing a difference of up to 600 m in lava flow length.

The quality of fit was quantified using a fitness function (ϕ) computed as the square root of A (sim $\cap$ real)/A (sim $\cup$ real), where A (sim $\cap$ real) and A (sim $\cup$ real) are the areas of the intersection and union between the simulated and actual lava flows, respectively. The lower and upper limits for ϕ are zero and one, with zero indicating the maximum error (i.e., lack of common areas between the simulated and actual lava flows), and one corresponding to a complete overlap (i.e., the simulated area coincides totally with the actual lava flow field).

The main morphological features (area, length, and average thickness) of actual and simulated lava flows, as well as the results of the fitness function (ϕ) are reported in Table 3.

Table 3. Comparison between the morphological properties (length, area, and average thickness) of the 2001 Etna lava flow derived by field measurements [17] and numerical simulations.

	Length [km]	Area [km^2]	Average Thickness [m]	Fitness [ϕ]
Actual lava flow	6.4	1.95	11	-
Simulation with $\varepsilon = 0.8$	6.9	1.94	12.4	0.76
Simulation with $\varepsilon = 0.93$	6.5	1.83	13.1	0.78
Simulation with $\varepsilon = 1.0$	6.3	1.78	13.5	0.77

The closest approximate values for the area covered and the average distribution were obtained by the MAGFLOW simulation run with an emissivity of 0.8 (1.94 km^2 and 12.4 m, respectively). However, having almost the same extent does not guarantee a best fit (areas may not overlap wholly or in part). This is confirmed by the values of the fitness function ϕ. Whilst the actual lava flow field is quite well reproduced by the MAGFLOW model, with ϕ always higher than 0.75, the maximum value (0.78) is obtained by the simulation run with $\varepsilon = 0.93$, demonstrating that it better reflects the actual field. The MAGFLOW simulation run with $\varepsilon = 0.93$ also reaches the closest flow length (6.5 versus 6.4 km), which is the most critical factor for hazard analysis.

5. Discussion

The land surface temperature derivation and the estimation of eruption rates from spaceborne data rely on assumptions of lava flow emissivity. The majority of research on emissivity to date has been carried out on solid lava at ambient temperatures [14], and it is anticipated that under certain conditions, target radiation emission in the TIR region of the electromagnetic spectrum is inversely proportional to its reflectance [45]. However, there are several drawbacks in using reflectance to derive emissivity values, as the temperature of the sample is not taken into account, and its spatial variation is not recorded. Nonetheless, reflectance data (1-*R*) can be used to provide a first approximation estimate in the absence of 'true emissivity' information.

The 'apparent' emissivity data for the 2001 Mount Etna eruption, which was derived from reflectance data at ambient temperature, is comparable to that of the low-temperature (400 K) emission FTIR data ('true' emissivity), with a range/error of emissivity $\leq$0.03, which is consistent with previous research on basaltic rock spectral signatures [25]. A certain amount of spectral contrast is observed and can be attributed to the instrument's sensitivity and/or the methodology used, which has been acknowledged in previous research [46].

The spaceborne ASTER GED mean emissivity data obtained for the same target area was also relatively consistent with our FTIR results at ambient/low temperatures, producing an emissivity range/error of $\leq$0.03. However, using this satellite-based approach, incorrect emissivity as an input could result in an error in retrieving lava flow surface temperatures, which will have an inherent impact on the computation of the radiant flux, estimates of the mass eruption rate, and lava flow 'distance-to-run' forecasts. Our 5 August 2001 example for the ETM+ satellite scene was used to compute radiant flux show variances in the calculated eruption rate, which has an impact of ~300 m in derived 'distance-to-run' between the emissivity end members (0.8 and 1.0). Similarly, a simple emissivity assessment using numerical forward modeler (MAGFLOW) by means of varying its value (i.e., 0.80, 0.93, and 1.0) showed that emissivity has an impact on simulated lava flow 'distance-to-run' results of up to ~600 m between the emissivity end-members (0.8 and 1.0).

The computation of Q_{r_calc} term in [3] using spaceborne data also involves convection (Q_c) and conduction (Q_k) of the flow. It has been argued that for flows that are not crusted over, Q_{r_calc} is much larger than Q_c and Q_k. However, in case of flows with crusts, Q_c can have as large a heat loss effect as Q_{r_calc} [47]. Etnean 'aa' lava flows, which have been discussed here, have crusts and very rough surfaces as they advance away from their vents and channels; thus, their heat transfer through convection can be as large as that of radiation for the medial and distal parts of the flow. Since the crust may act as an insulator, it limits convection and radiation by the amount of heat conducted

from the flow through the crust to the outer surface. This effect may be considered as the most likely contributor to the longer flow lengths. Therefore, emissivity variation may indicate flow phase changes by insulation, allowing it to flow father than a simple effusion rate model would predict. Thus, a model that includes all of the thermal components may be able to account for changes in the thermal conditions (and rheology of the flow). Similarly, if emissivity variation is considered when producing the best dual-band solution using the multi-component approach [48] from spaceborne data, it should also involve applying several different emissivities within a single pixel.

The emissivity variation may also be seen as a proxy for crusting the lava flow, which will insulate the flow, allowing it to flow for longer, and thus further. This approach may provide a means of identifying changes in the insulation properties of an active lava flow by using apparent emissivity. Therefore, it can be argued that a change in the apparent emissivity of the surface of the flow does have an indirect effect on the 'distance-to-run'.

The emissivity data derived from reflectance, low-temperature emission FTIR analyses and/or ASTER GED provide 'static' emissivity values, which may be related to the solidified (cooled) product. However, the high-temperature thermal anomaly observed on Mount Etna has an extrusion temperature of ~1360 K, so there is a need to account for emissivity changes with temperature, as evident from our high-temperature FTIR results. This is consistent with several thermal emission studies of silicate glasses and basaltic lavas, which suggest that the emissivity of molten material is significantly lower than that of the same material in a solid state [49]. Therefore, our preliminary results from high-temperature data imply that it is essential to expand this study to assess the role and significance of emissivity, not only as a 'static' and uniform value across all wavelengths and temperatures, but also taking its response to thermal gradient into account. This will determine the emissivity variation with temperature change, and will provoke further investigation into the role and impact of emissivity in lava flow dynamic modeling and hazard mitigation.

6. Conclusions

Our reflectance and emission FTIR results at ambient/low temperature indicate that emissivity is wavelength-dependent. Both laboratory (FTIR) and spaceborne (ASTER GED) data correspond well for the same target area, and show good correlation at specific TIR wavelengths by exhibiting an emissivity range/error of $\leq$0.03. However, this emissivity information is 'static', relating to the solidified (cooled) product, not reflecting the range of temperatures involved at an active lava flow or the emissivity/temperature trend seen in our high-temperature FTIR results. Furthermore, the theoretical empirical approaches and modeling used in this study indicate that a variation of 0.2 in emissivity may result in significant changes to the prediction of lava flow 'distance-to-run' estimates.

A reliable and exploitable predictive emissivity trend is needed for both modeling and spaceborne applications for a range of temperatures and wavelengths to improve our understanding of the variation of emissivity with temperature. Further, a better understanding of the impact of emissivity on deduced temperature during active lava flow propagation (and cooling) is needed to improve spaceborne data interpretation, which relies on emissivity as an input in computations of lava surface temperatures, radiant fluxes, and ultimately lava flow length estimations.

Author Contributions: F.F. and N.R. led the conception and design of the work. N.R. and A.C. acquired the data. N.R., A.C., F.F. were responsible for analysis, modelling and interpretation of data. All authors participated in drafting and revising the article and have given final approval of the submitted and revised versions.

Funding: This research (and the APC) was fully funded by the Open University, Milton Keynes, U.K.

Acknowledgments: This project and manuscript were improved through invaluable guidance and support of the Open University, School of Environment, Earth and Ecosystem Sciences, Milton Keynes, U.K. (H. Rymer and S. Blake). The authors are grateful to the Natural Environment Research Council (NERC) Field Spectroscopy Facility, University of Edinburgh, U.K. (C. MacLellan and A. Gray) and Clarendon Laboratory, University of Oxford, U.K. (N. Bowles) for accommodating preliminary FTIR pilot studies. Special thanks to the DLR, Institute of Planetary Research, Planetary Emissivity Laboratory, Berlin, Germany (A. Maturilli) for accommodating FTIR measurements and helpful discussions. MAGFLOW simulations were performed within the framework

of Tecnolab, the Laboratory for Technological Advance in Volcano Geophysics of the INGV in Catania, Italy. The editor Arlene Cui and the three anonymous reviewers are acknowledged for their constructive and supportive comments, which helped improve this manuscript.

Conflicts of Interest: The authors declare no conflict of interest. The funders had no role in the design of the study; in the collection, analyses, or interpretation of data; in the writing of the manuscript, or in the decision to publish the results.

References

1. Garel, F.; Kaminski, E.; Tait, S.; Limare, A. An experimental study of the surface thermal signature of hot subaerial isoviscous gravity currents: Implications for thermal monitoring of lava flows and domes. *J. Geophys. Res. Solid Earth* **2012**, *117*, B02205. [CrossRef]
2. Vicari, A.; Alexis, H.; Del Negro, C.; Coltelli, M.; Marsella, M.; Proietti, C. Modeling of the 2001 lava flow at Etna volcano by a Cellular Automata approach. *Environ. Model. Softw.* **2007**, *22*, 1465–1471. [CrossRef]
3. McGuire, W.J.; Kilburn, C.R.J.; Murray, J.B. *Monitoring Active Volcanoes: Strategies, Procedures, Techniques*; University of London Press: London, UK, 1995; p. 421.
4. Harris, A.J.L. *Thermal Remote Sensing of Active Volcanoes: A User's Manual*; Cambridge University Press: Cambridge, UK, 2013; p. 736.
5. Ramsey, M.S.; Fink, J.H. Estimating silicic lava vesicularity with thermal remote sensing: A new technique for volcanic mapping and monitoring. *Bull. Volcanol.* **1999**, *61*, 32–39. [CrossRef]
6. Ball, M.; Pinkerton, H. Factors affecting the accuracy of thermal imaging cameras in volcanology. *J. Geophys. Res. Solid Earth* **2006**, *111*, B11203. [CrossRef]
7. Higgins, J.; Harris, A. VAST: A program to locate and analyse volcanic thermal anomalies automatically from remotely sensed data. *Comput. Geosci.* **1997**, *23*, 627–645. [CrossRef]
8. Wright, R.; Flynn, L.; Garbeil, H.; Harris, A.; Pilger, E. Automated volcanic eruption detection using MODIS. *Remote Sens. Environ.* **2002**, *82*, 135–155. [CrossRef]
9. Wright, R.; Flynn, L.P.; Garbeil, H.; Harris, A.J.; Pilger, E. MODVOLC: Near-real-time thermal monitoring of global volcanism. *J. Volcanol. Geotherm. Res.* **2004**, *135*, 29–49. [CrossRef]
10. Di Bello, G.; Filizzola, C.; Lacava, T.; Marchese, F.; Pergola, N.; Pietrapertosa, C.; Piscitelli, S.; Scaffidi, I.; Tramutoli, V. Robust satellite techniques for volcanicand seismic hazards monitoring. *Ann. Geophys.* **2004**, *47*. [CrossRef]
11. Hirn, B.R.; Di Bartola, C.; Laneve, G.; Cadau, E.; Ferrucci, F. SEVIRI Onboard Meteosat Second Generation, and the Quantitative Monitoring of Effusive Volcanoes in Europe and Africa. In Proceedings of the IGARSS 2008, 2008 IEEE International Geoscience and Remote Sensing Symposium, Boston, MA, USA, 7–11 July 2008; pp. 374–377.
12. Wooster, M.J.; Rothery, D.A. Time-series analysis of effusive volcanic activity using the ERS along track scanning radiometer: The 1995 eruption of Fernandina volcano, Galápagos Islands. *Remote Sens. Environ.* **1997**, *62*, 109–117. [CrossRef]
13. Coppola, D.; Macedo, O.; Ramos, D.; Finizola, A.; Delle Donne, D.; Del Carpio, J.; White, R.; McCausland, W.; Centeno, R.; Rivera, M.; et al. Magma extrusion during the Ubinas 2013–2014 eruptive crisis based on satellite thermal imaging (MIROVA) and ground-based monitoring. *J. Volcanol. Geotherm. Res.* **2015**, *302*, 199–210. [CrossRef]
14. Harris, A.J.L. Thermal remote sensing of active volcanism: Principles. In *Thermal Remote Sensing of Active Volcanoes: A User's Manual*; Cambridge University Press: Cambridge, UK, 2013; pp. 70–112.
15. Rothery, D.A.; Francis, P.W.; Wood, C.A. Volcano monitoring using short wavelength infrared data from satellites. *J. Geophys. Res.* **1988**, *93*, 7993–8008. [CrossRef]
16. Harris, A.J.; Butterworth, A.L.; Carlton, R.W.; Downey, I.; Miller, P.; Navarro, P.; Rothery, D.A. Low- cost volcano surveillance from space: Case studies from Etna, Krafla, Cerro Negro, Fogo, Lascar and Erebus. *Bull. Volcanol.* **1997**, *59*, 49–64. [CrossRef]
17. Coltelli, M.; Proietti, C.; Branca, S.; Marsella, M.; Andronico, D.; Lodato, L. Analysis of the 2001 lava flow eruption of Mt. Etna from three-dimensional mapping. *J. Geophys. Res. Earth Surf.* **2007**, *112*, F02029. [CrossRef]
18. Tarquini, S.; Isola, I.; Favalli, M.; Mazzarini, F.; Bisson, M.; Pareschi, M.T.; Boschi, E. TINITALY/01: A new triangular irregular network of Italy. *Ann. Geophys.* **2007**, *50*, 407–425.

19. Maturilli, A.; Helbert, J.; D'Amore, M.; Varatharajan, I.; Ortiz, Y.R. The Planetary Spectroscopy Laboratory (PSL): Wide spectral range, wider sample temperature range. In Proceedings of the SPIE 10765: Infrared Remote Sensing and Instrumentation, San Diego, CA, USA, 18 September 2018.
20. Korb, A.R.; Salisbury, J.W.; Aria, D.M. Thermal-infrared remote sensing and Kirchhoff's law 2. Field measurements. *J. Geophys. Res. Solid Earth* **1999**, *104*, 15339–15350. [CrossRef]
21. Maturilli, A.; Helbert, J.; Witzke, A.; Moroz, L. Emissivity measurements of analogue materials for the interpretation of data from PFS on Mars Express and MERTIS on Bepi-Colombo. *Planet. Space Sci.* **2006**, *54*, 1057–1064. [CrossRef]
22. NASA; JPL. *ASTER Global Emissivity Dataset 100-meter HDF5[37/38/39.012-0-15.0001]*; NASA EOSDIS Land Processes DAAC: Sioux Falls, SD, USA, 2014.
23. Hulley, G.C.; Hook, S.J.; Abbott, E.; Malakar, N.; Islam, T.; Abrams, M. The ASTER Global Emissivity Dataset (ASTER GED): Mapping Earth's emissivity at 100 meter spatial scale. *Geophys. Res. Lett.* **2015**, *42*, 7966–7976. [CrossRef]
24. NASA; JPL. LP DAAC: Land Processes Distributed Active Archive Center. 2014. Available online: https://lpdaac.usgs.gov/dataset_discovery/community/community_products_table/ag100_v003 (accessed on 1 June 2018).
25. Wyatt, M.B.; Hamilton, V.E.; McSween, H.Y.; Christensen, P.R.; Taylor, L.A. Analysis of terrestrial and Martian volcanic compositions using thermal emission spectroscopy: 1. Determination of mineralogy, chemistry, and classification strategies. *J. Geophys. Res.* **2001**, *106*, 14711–14732. [CrossRef]
26. Hirn, B.; Di Bartola, C.; Ferrucci, F. Spaceborne monitoring 2000-2005 of the Pu'u 'O'o-Kupaianaha (Hawaii) eruption by synergetic merge of multispectral payloads ASTER and MODIS. *IEEE Trans. Geosci. Remote Sens.* **2008**, *46*, 2848–2856. [CrossRef]
27. Barsi, J.A.; Barker, J.L.; Schott, J.R. An Atmospheric Correction Parameter Calculator for a single thermal band earth-sensing instrument. In Proceedings of the IGARSS 2003, 2003 IEEE International Geoscience and Remote Sensing Symposium, Toulouse, France, 21–25 July 2003; pp. 3014–3016.
28. Barsi, J.A.; Barker, J.L.; Schott, J.R. Atmospheric Correction Parameter Calculator. 2003 IGARSS03. Available online: https://atmcorr.gsfc.nasa.gov/ (accessed on 1 June 2018).
29. Pieri, D.C.; Baloga, S.M. Eruption rate area, and length relationships for some Hawaiian lava flows. *J. Volcanol. Geotherm. Res.* **1986**, *30*, 29–45. [CrossRef]
30. Wright, R.; Blake, S.; Harris, A.J.; Rothery, D.A. A simple explanation for the space-based calculation of lava eruption rates. *Earth Planet. Sci. Lett.* **2001**, *192*, 223–233. [CrossRef]
31. Harris, A.J.L.; Murray, J.B.; Aries, S.E.; Davies, M.A.; Flynn, L.P.; Wooster, M.J.; Wright, R.; Rothery, D.A. Effusion rate trends at Etna and Krafla and their implications for eruptive mechanisms. *J. Volcanol. Geotherm. Res.* **2000**, *102*, 237–269. [CrossRef]
32. Harris, A.; Dehn, J.; Calvari, S. Lava effusion rate definition and measurement: A review. *Bull. Volcanol.* **2007**, *70*, 1–22. [CrossRef]
33. Kilburn, C.R.J.; Pinkerton, H.; Wilson, L. Forecasting the behaviour of lava flows. In *Monitoring Active Volcanoes*; McGuire, W.J., Kilburn, C.R.J., Murray, J., Eds.; UCL Press: Londin, UK, 1995; pp. 346–368.
34. Kilburn, C.R.J.; Ballard, R.D. *Lava Flows and Flow Fields*; Sigurdsson, H., Ed.; Academic Press: San Diego, CA, USA, 2000; pp. 291–305.
35. Herault, A.; Vicari, A.; Ciraudo, A.; Del Negro, C. Forecasting lava flow hazards during the 2006 Etna eruption: Using the MAGFLOW cellular automata model. *Comput. Geosci.* **2009**, *35*, 1050–1060. [CrossRef]
36. Cappello, A.; Hérault, A.; Bilotta, G.; Ganci, G.; Del Negro, C. MAGFLOW: A physics-based model for the dynamics of lava-flow emplacement. *Geol. Soc. Spec. Publ.* **2016**, *426*, 357–373. [CrossRef]
37. Kereszturi, G.; Cappello, A.; Ganci, G.; Procter, J.; Németh, K.; Del Negro, C.; Cronin, S.J. Numerical simulation of basaltic lava flows in the Auckland Volcanic Field, New Zealand—Implication for volcanic hazard assessment. *Bull. Volcanol.* **2014**, *76*, 1–17. [CrossRef]
38. Del Negro, C.; Cappello, A.; Neri, M.; Bilotta, G.; Hérault, A.; Ganci, G. Lava flow hazards at Mount Etna: Constraints imposed by eruptive history and numerical simulations. *Sci. Rep.* **2013**, *3*, 3493. [CrossRef]
39. Cappello, A.; Geshi, N.; Neri, M.; Del Negro, C. Lava flow hazards—An impending threat at Miyakejima volcano, Japan. *J. Volcanol. Geotherm. Res.* **2015**, *308*, 1–9. [CrossRef]
40. Cappello, A.; Zanon, V.; Del Negro, C.; Ferreira, T.J.; Queiroz, M.G. Exploring lava-flow hazards at Pico Island, Azores Archipelago (Portugal). *Terra Nova* **2015**, *27*, 156. [CrossRef]

41. Pedrazzi, D.; Cappello, A.; Zanon, V.; Del Negro, C. Impact of effusive eruptions from the Eguas–Carvão fissure system, São Miguel Island, Azores Archipelago (Portugal). *J. Volcanol. Geotherm. Res.* **2015**, *291*, 1–13. [CrossRef]
42. Cappello, A.; Ganci, G.; Calvari, S.; Pérez, N.M.; Hernández, P.A.; Silva, S.V.; Cabral, J.; Del Negro, C. Lava flow hazard modeling during the 2014–2015 Fogo eruption, Cape Verde. *J. Geophys. Res. Solid Earth* **2016**, *121*, 2290–2303. [CrossRef]
43. Bilotta, G.; Cappello, A.; Hérault, A.; Vicari, A.; Russo, G.; Del Negro, C. Sensitivity analysis of the MAGFLOW Cellular Automaton model for lava flow simulation. *Environ. Model. Softw.* **2012**, *35*, 122–131. [CrossRef]
44. Bilotta, G.; Cappello, A.; Hérault, A.; Del Negro, C. Influence of topographic data uncertainties and model resolution on the numerical simulation of lava flows. *Environ. Model. Softw.* **2019**, *112*, 1–15. [CrossRef]
45. Rolim, S.B.A.; Grondona, A.; HACKMANN, C.; Rocha, C. A Review of Temperature and Emissivity Retrieval Methods: Applications and Restrictions. *Am. J. Environ. Eng.* **2016**, *6*, 119–128.
46. Sabol, D.E., Jr.; Gillespie, A.R.; Abbott, E.; Yamada, G. Field validation of the ASTER Temperature– Emissivity Separation algorithm. *Remote Sens. Environ.* **2009**, *113*, 2328–2344. [CrossRef]
47. Patrick, M.R.; Dehn, J.; Dean, K. Numerical modeling of lava flow cooling applied to the 1997 Okmok eruption: Approach and analysis. *J. Geophys. Res. Solid Earth* **2004**, *109*, B03202. [CrossRef]
48. Wright, R.; Flynn, L.P. On the retrieval of lava-flow surface temperatures from infrared satellite data. *Geology* **2003**, *31*, 893–896. [CrossRef]
49. Lee, R.J.; Ramsey, M.S.; King, P.L. Development of a new laboratory technique for high-temperature thermal emission spectroscopy of silicate melts. *J. Geophys. Res. Solid Earth* **2013**, *118*, 1968–1983. [CrossRef]

8.8 Appendix H: Publication: (Rogic et al., 2019b)

remote sensing

MDPI

Article

Spaceborne EO and a Combination of Inverse and Forward Modelling for Monitoring Lava Flow Advance

Nikola Rogic [1,*], Annalisa Cappello [2], Gaetana Ganci [2], Alessandro Maturilli [3], Hazel Rymer [1], Stephen Blake [1] and Fabrizio Ferrucci [1,4]

1 School of Environment, Earth and Ecosystem Sciences, The Open University, Milton Keynes MK7 6AA, UK; hazel.rymer@open.ac.uk (H.R.); stephen.blake@open.ac.uk (S.B.); fabrizio.ferrucci@open.ac.uk (F.F.)
2 Istituto Nazionale di Geofisica e Vulcanologia, Osservatorio Etneo, 95125 Catania, Italy; annalisa.cappello@ingv.it (A.C.); gaetana.ganci@ingv.it (G.G.)
3 German Aerospace Center, (DLR), Institute of Planetary Research, 12489 Berlin, Germany; alessandro.maturilli@dlr.de
4 Department of Environmental and Chemical Engineering, University of Calabria, 87036 Rende (CS), Italy
* Correspondence: nikola.rogic@open.ac.uk; Tel.: +44-77-313-02424

Received: 1 November 2019; Accepted: 13 December 2019; Published: 16 December 2019

check for updates

Abstract: We aim here to improve the understanding of the relationship between emissivity of the lava and temperature by carrying out a multi-stage experiment for the 2017 Mt Etna (Italy) eruption. We combine laboratory, spaceborne, and numerical modelling data, to quantify the emissivity–temperature relationship. Our laboratory-based Fourier-transform infrared (FTIR) results indicate that emissivity and temperature are inversely correlated, which supports the argument that emissivity of molten material is significantly lower than that of the same material in its solid state. Our forward-modelling tests using MAGFLOW Cellular Automata suggest that a 35% emissivity variation (0.95 to 0.60) can produce up to 46% overestimation (for constant emissivity 0.60) in simulated/forecasted lava flow lengths (compared to actual observed). In comparison, our simulation using a 'two-component' emissivity approach (i.e., different emissivity values for melt and cooled lava) and constant emissivity 0.95 compares well (≤10% overestimation) with the actual 2017 lava flow lengths. We evaluated the influence of variable emissivity on lava surface temperatures using spaceborne data by performing several parametrically controlled assessments, using both constant ('uniform') and a 'two-component' emissivity approach. Computed total radiant fluxes, using the same spaceborne scene (Landsat 8 Operational Land Imager (OLI)), differ ≤15% depending on emissivity endmembers (i.e., 0.95 and 0.60). These results further suggest that computed radiant flux using high-spatial resolution data is bordering at lower boundary (range) values of the moderate-to-high temporal resolution spaceborne data (i.e., Moderate Resolution Imaging Spectroradiometer (MODIS) and Spinning Enhanced Visible and Infrared Imager (SEVIRI)), acquired for the same target area (and the same time interval). These findings may have considerable impact on civil protection decisions made during volcanic crisis involving lava flows as they approach protected or populated areas. Nonetheless, the laboratory work, reported here, should be extended to include higher volcanic eruptive temperatures (up to 1350 K).

Keywords: remote sensing; volcanic hazard modelling; emissivity uncertainty; FTIR spectroscopy; Mount Etna

1. Introduction

A small fraction of the active subaerial volcanoes around the world are monitored regularly [1]. There is variety in local practices used for volcano surveillance [2,3], and fewer than 10% of the potentially active volcanoes worldwide (erupted at least once in the last 10,000 years) are monitored with the appropriate quality, frequency, and timeliness [1,4]. This poses an objective and significant threat to communities [5], especially in countries lacking in infrastructure and with limited financial resources [6], creating a critical gap in hazard assessment and risk management [7].

Satellite remote sensing is an established technological solution for bridging critical gaps in volcanic hazard and risk mitigation, as it offers cost effective and global volcano surveillance at a wide range of spatial and temporal resolutions [8–10]. It can significantly contribute to operational eruption forecasting and hazard assessment [11–15].

Remote sensing offers the potential of gathering valuable data without the risks and the cost associated with ground-based volcanic fieldwork. None of the spaceborne sensors to date, such as the low-to-moderate spatial resolution Moderate Resolution Imaging Spectroradiometer (MODIS) onboard Terra and Aqua satellites, Spinning Enhanced Visible and Infrared Imager (SEVIRI) onboard the Meteosat Second Generation (MSG) geostationary platform, or the higher spatial resolution Landsat 8 OLI (Operational Land Imager), were designed specifically to observe volcanic thermal emission during effusive eruptions. Nonetheless, some of these sensors have the ability to record high-temperature surface anomalies, such as those that occur during volcanic effusive activity. The thermal emission of an active volcanic surface relates directly to the volcanic activity at a specific time and can be detected and measured from space to identify physical processes occurring on the ground.

All objects above absolute zero (0 K) emit electromagnetic radiation at a wavelength and intensity that are functions of the characteristics of the surface temperature and emissivity (radiating efficiency). Therefore, there is a direct relationship between thermal emissions and thermal volcanic activity. According to the Stefan–Boltzmann law, the radiance emitted by the surface will increase, as the temperature of the surface rises. As a hotter volcanic surface will radiate more energy and higher radiant flux density, any variation observed radiance will reflect a variation in volcanic activity on the ground. Sensors having channels in the mid-infrared (MIR) and thermal infrared (TIR) bands (e.g., MODIS) have been used widely for decades to detect volcanic thermal anomalies [16,17] and have proven to be a valuable tool for identifying trends and monitoring volcanic activity [18–25]. On the other hand, sensors such as the Multi-Spectral Imager (MSI) aboard Sentinel-2 satellites and OLI, having channels in the short-wave infrared (SWIR), and providing data at medium-high spatial resolution, enable a better identification of high-temperature thermal anomalies (e.g., lava flows) [23,26]. This approach is explored further in this study, using high-spatial resolution data (Landsat 8 OLI).

Satellite data analysis and interpretation rely on certain assumptions and input parameters, some of which, such as emissivity, are not well quantified for molten and hot volcanic rocks. Several recent thermal emission studies of silicate glasses and basaltic lava [27] suggest that the emissivity of molten material is significantly lower than that of the same material in its solid state. Thus, emissivity is not only wavelength dependent but also temperature dependent [25,28].

The computation of surface temperature from spaceborne data and models that rely on computed temperatures to track cooling with time, introduce errors due to uncertainties in emissivity as an input parameter. It has been recognized previously [24] that an uncertainty in emissivity gives rise to errors in pixel-integrated temperatures (i.e., lava surface temperatures) that may consequently affect estimates of total and maximum radiant fluxes. The need to quantify the emissivity–temperature relationship, often neglected in both spaceborne and modelling applications was illustrated using 'distance-to-run' forecasts for the 2001 Mt Etna eruption [28]. A recent study investigating the application of thermo-rheological models to forecast lava flow emplacement, used a 'two-component' emissivity model [25], assuming the fraction of molten lava and cooled crust. The study concluded that the emissivity of molten lava may be as low as 0.60, while an emissivity of 0.95 corresponded to the crusted fraction of the lava.

The motivation for the present study is to assess the role of emissivity in the determination of radiant fluxes obtained from spaceborne data. To achieve this, we compared the results from spaceborne data with models using three approaches; firstly by applying a constant 'standard' emissivity, where an assumed value (e.g., 0.95) is applied to the entire thermal anomaly; secondly by applying a constant but lower value for emissivity (0.60), known to be more appropriate for molten lava temperatures; and thirdly we applied a modification of the 'two-component' emissivity approach [25], by applying a specific emissivity parameterization (0.60 for melt and 0.95 for crust).

Mt Etna (Sicily, Italy) was chosen as a perfect candidate for this study due to its persistent activity, displaying a range of eruptive products and styles [29,30] and the availability of spaceborne data with a range of temporal and spatial resolutions. Considering that it is surrounded by almost one million people, the implications of volcanic activity monitoring are significant for civil protection and urban planning in the region.

Out of several significant, long- [31] and short-lived [29] effusive events on Mt Etna, the most recent, longest eruptive episode (Figure 1) started from the old "saddle" (V_1) between the South-East Crater (SEC) and the New Southeast Crater (NSEC) on the morning of 15 March 2017 and continued from a pit crater, opening on the south flank of the saddle (V_2). The lava flow expanded to both southeast and southwest, diverted by the eruptive cones formed during the 2002–2003 flank eruption. At the beginning of April 2017, the lava started flowing from two ephemeral vents that opened downstream (V_3 and V_4). This eruption, which ended on 9 April 2017, emitted 7.96×10^6 m^3 of lava [8] over an area of 1.782 km^2 (Figure 1).

The location and chemical composition of collected samples (filled blue circles) for the 2017 Mt Etna eruption are shown in Figure 1 and Table 1, respectively.

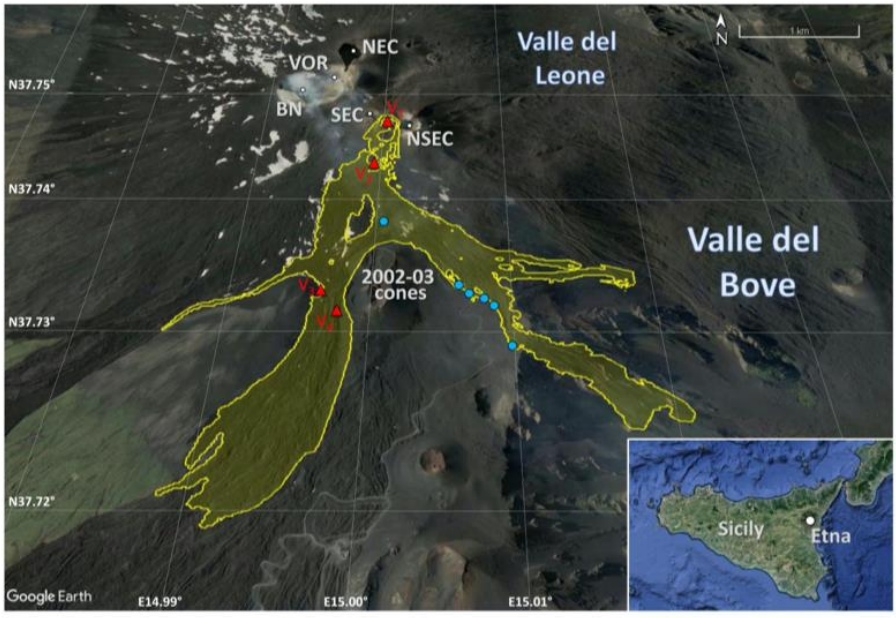

Figure 1. Main Figure: Google Earth three-dimensional (3D) view (from south) of Etna's summit area. The active craters are indicated, North-East Crater (NEC), Voragine (VOR), Bocca Nuova (BN), South-East Crater (SEC), and New South-East Crater (NSEC), together with the 2002–2003 cones that diverted the lava flow emitted by the March–April 2017 eruption. "Valle del Leone" is the NE part of Valle del Bove, a large horseshoe-shaped depression located on the eastern side of the volcano. The location and opening times (see text) of the 2017 eruptive vents are indicated by filled red triangles, and the location of collected samples (NRE.1S) by filled blue circles. The actual lava flow field (in yellow) was retrieved from the Sentinel-2A image acquired on 8 April 2017. Inset: Location of Mt Etna volcano on the island of Sicily, Italy.

Table 1. X-ray fluorescence (XRF) major elements content, as a component oxide weight percent (wt%) for the NRE.1 Series (NRE.1S).

SiO_2	TiO_2	Al_2O_3	Fe_2O_3	MnO	MgO	CaO	Na_2O	K_2O	P_2O_5	LOl	Total
47.49	1.63	17.71	11.26	0.17	4.81	10.362	3.65	1.72	0.55	−0.35	99.02

2. Materials and Methods

2.1. Rock Samples

To measure the emissivity of the exposed 2017 lava flow, we collected six rock samples (Figure 1; Table 1), termed NRE.1 Series (NRE.1S). These were initially investigated using Fourier transform infrared (FTIR) spectroscopy, to derive absolute emissivity from radiance at a range of temperatures (400–900 K) and wavelengths (5.0–15.0 μm).

Bulk chemical analyses of major elements for the NRE.1S samples were processed using X-ray fluorescence (XRF) technique (Table 1). XRF results indicate silica (SiO_2) and alkali ($Na_2O + K_2O$) content of 47.49 and 5.37, respectively. This is consistent with previous research on Etnean lavas [32], categorizing them as basalts to transitional trachy-basalts.

2.2. Laboratory-Based Data Acquisition

2.2.1. Emissivity from Surface Radiance Spectra

Thermal emission spectra of the samples were measured at the Planetary Spectroscopy Laboratory (PSL) of the German Aerospace Center (DLR) in Berlin, in a vacuum (0.7 mbar), over a temperature range of 400–900 K, in the 5.0 to 15.0 μm wavelength range. The experimental set up [33,34] uses an external 'simulation chamber', attached to the FTIR spectrometer (Figure 2), measuring the emissivity of solid crushed samples (grain size 1000–3000 μm). The emissivity chamber is equipped with an internal webcam and several temperature sensors to measure the sample/cup temperature, monitor the equipment, and record chamber temperatures. Both the cup and the sample are heated uniformly by induction, and the temperature of the emitting surface is measured using a thermophile sensor in contact with the surface. The resulting data are calibrated using the emissivity spectrum of the blackbody material [34] to provide the set of absolute emissivity data.

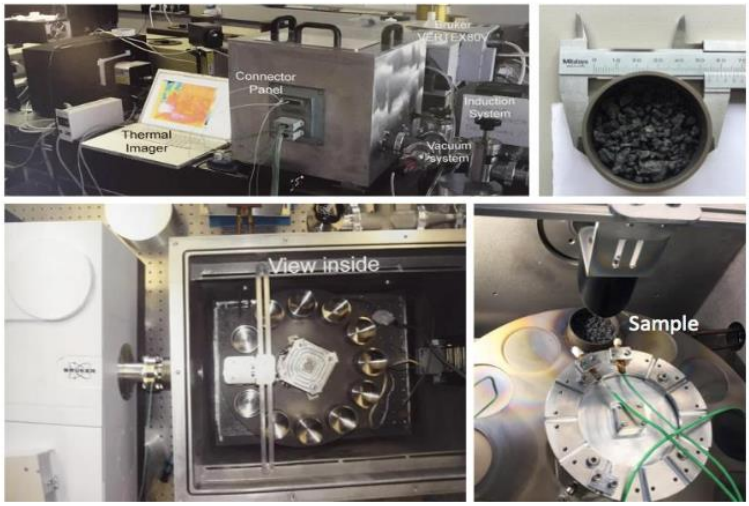

Figure 2. Experimental set up ([34] and this study) to measure emissivity of the NRE.1S, using Bruker VERTEX 80 V instrument.

2.3. Thermal Surveillance Using Spaceborne Data

2.3.1. High-Spatial Resolution Data

In this study, we selected a platform hosting decametric resolution sensors operating at the time of the 2017 Mt Etna eruption: the Landsat 8 (Landsat Continuity Mission), launched by National Aeronautics and Space Administration (NASA) in April 2013. Landsat 8 hosts two payloads, the Operational Land Imager (OLI) and the Thermal Infrared Sensor (TIRS), with the overall capability of collecting data in 11 spectral bands (0.44–12.00 μm), 30 m to 100 m spatial resolution global coverage, and equatorial repeat cycle of 16 days [35].

General aspects of physics and techniques of thermal remote sensing of active volcanoes can be found in [22] among others. Here, we used the specific approach described in [23]. The mean spectral radiance measured by a satellite sensor as a digital number (DN) can be converted into 'at-satellite' spectral radiance R_λ ($W\ m^{-2}\mu m^{-1}sr^{-1}$), which is composed of the surface reflected radiance ($R_{\lambda,\ D}$), the upwelling path radiance ($R_{\lambda,\ U}$) and the surface thermal radiance $L(\lambda,\ T)$

$$\begin{aligned} R_\lambda &= \tau_\lambda L(\lambda, T) + \tau_\lambda \rho_\lambda R_{\lambda,D} + R_{\lambda,\ U} \\ &= R_{\lambda,\ thermal} + R_{\lambda,\ nonthermal} \end{aligned} \quad (1)$$

where, τ_λ is the atmospheric spectral transmission coefficient; ρ_λ is the spectral reflectivity of the target; $R_{\lambda,\ thermal}$ is composed of $\tau_\lambda L(\lambda, T)$ and $R_{\lambda,\ nonthermal}$ is composed of $\tau_\lambda \rho_\lambda R_{\lambda,D} + R_{\lambda,\ U}$.

The upwelling path radiance ($R_{\lambda,\ U}$) contribution in the short wavelength infrared (SWIR) region, such as in OLI's Band 6 (1.60 μm) and Band 7 (2.20 μm) was very low, so it was ignored and the radiation reflected by the surface ($R_{\lambda,\ D}$) in daytime images were estimated by subtracting the mean spectral radiance (R_λ) value of surrounding nonthermally anomalous pixels, from the thermally anomalous pixels. If available, the nighttime images would be preferable, as they contain only the thermal component. However, in this study, we analysed all available daytime images acquired during the 2017 Mt Etna Eruption, distributed by the Global Visualization (GloVis) Viewer [36].

The overall spectral radiance L_λ, emitted by a blackbody at a particular temperature (T) and wavelength (λ), is given by Planck's radiation law. This quantifies Wien's displacement law which states that the spectral radiance emitted from a surface will increase with temperature while at the same time, the highest emissions will become of shorter wavelength.

Based on Planck's radiation law, the spectral radiance of a pixel (Equation (2)) is a function of its integrated temperature (T_i) :

$$\mathrm{L}(\lambda,\ \mathrm{T}) = \frac{\varepsilon_\lambda\ \mathrm{c}_1 \lambda^{-5}}{\pi\left[\exp\left(\frac{\mathrm{c}_2}{\lambda \mathrm{T}_{\mathrm{i},\lambda}}\right) - 1\right]} \quad (2)$$

where, c_1 and c_2 are related constants; $c_1 = 1.19 \times 10^{-16}\ W\ m^{-2}\ sr^{-1}$ and $c_2 = 1.44 \times 10^{-2}\ m\ K$, respectively. $c_1 = 2\pi\, h\, c_2$ where h is Planck's constant and c is the speed of light; $c_2 = h\,\frac{c}{k}$ where k is the Stefan–Boltzmann constant; λ is the wavelength in micrometers; ε_λ is the emissivity of the radiative surface, and $T_{i,\ \lambda}$ is the integrated pixel temperature at a specific wavelength.

Assuming that the pixel was thermally pure (i.e., isothermal surface), the pixel integrated temperature (T_i) should be the temperature of the target surface after being corrected for emissivity, atmospheric, and sensor response effects. However, a scene recorded over an active lava flow surface may contain a wide range of temperatures (and emissivities), so a single pixel will be a mixture of several thermal components. Therefore, after radiometric and atmospheric data correction [37–39], and following procedures outlined in [23], the fundamentals of 'dual-band' approaches [20,24,40–43] were employed using unsaturated radiance data in SWIR (OLI's Bands 6 and 7) to derive an effective temperature (T_e) for each radiant pixel of the high-temperature thermal anomaly analysed:

$$\mathrm{T_e} = \left[\mathrm{f_h}\ \mathrm{T_h}^4 + (1 - \mathrm{f_h})\ \mathrm{T_c}^4\right]^{\frac{1}{4}} \quad (3)$$

In the case of high-spatial resolution spaceborne data, pixel radiance values can be computed as the weighted average of subpixel radiance emitted by two distinctly different temperature components: the hot component at temperature T_h representing melt, occupying a surface fraction f_h of the pixel and the cooler, crusted component, at temperature T_c occupying the remainder of the pixel (i.e., $1 - f_h$).

Having obtained the effective temperature (T_e) for each radiant pixel by solving sub-resolutions [23], the remotely sensed radiant heat flux (Q_{R_calc}) was acquired [23,44,45]:

$$Q_{R\_calc} = A\ \varepsilon\ \sigma\ \tau\ (T_e{}^4 - T_a{}^4) \quad (4)$$

where, A is the pixel surface area; ε is emissivity; σ is the Stefan–Boltzmann constant; τ is atmospheric transmissivity, and $T_e{}^4$ is the effective temperature to the fourth power, and the $T_a{}^4$ is the ambient temperature to the fourth power.

The retrieval of radiant heat flux (power) for the thermally anomalous pixels using high-spatial resolution spaceborne radiance data was calculated using two OLI's SWIR bands (Band 6 located at 1.65 µm and B7 at 2.20 µm central wavelengths) and these radiance values, extracted from thermally anomalous pixels, were used to compute total radiant flux values for each scene analysed.

Total radiant fluxes were computed by applying constant emissivity values (i) 0.95 and (ii) 0.60, uniformly to the entire thermal anomaly, and (iii) using a 'two-component' emissivity approach by creating a 'threshold' within the thermal anomaly, based on pixel radiance values for assumed cooler crust radiant pixels ($\varepsilon = 0.95$) and for assumed melt ($\varepsilon = 0.60$). Landsat 8 OLI's Band 7 recorded radiance values were used to create 'thresholds', based on sensor's minimum and maximum operating limits [46], minimum radiance value selected was 5.0 (to exclude background radiance) and maximum radiance selected was 32.00 (~ maximum radiance in Band 7). Assumed crust (5.0–24.99) and assumed melt (25.00–32.00) radiance limits were applied in our 'two-component' emissivity computation.

2.3.2. Moderate-to-High Temporal Resolution Data

Moderate-to-high temporal resolution satellite data were processed using the HOTSAT thermal monitoring system [47,48]. In particular, the system ingests MODIS data, which provides images at 1 km spatial resolution up to four times per day and SEVIRI data, which enables almost continuous monitoring (i.e., four times per hour and up to a 5 min sampling interval in rapid scanning service mode) with a spatial resolution of 3 km at nadir. The system is designed to automatically provide the location of the 'hotspot' pixels, if present, and to quantify their thermal anomaly by computing the associated radiant heat flux.

The algorithm implemented in HOTSAT firstly detects clouds in the analysed images, by applying the texton technique [49], then looks for thermal anomalies by using a contextual approach. An adaptive threshold is retrieved in a 'non-active volcanic' portion of the image to be analysed and a potential 'hotspot' pixel is found if the threshold is overcome in the 'volcanic' portion of the image. Those potential 'hotspot' pixels are then classified as a true 'hotspot' after successfully passing several statistical tests.

The radiant heat flux is computed for all the pixels classified as a true 'hotspot'. This is accomplished by using the MIR radiance method [50], where the radiant heat flux is computed by approximating the Planck law in MIR to the 4th order power law, thus obtaining:

$$Q_{MIR} = \frac{A_{sampl}\varepsilon\sigma}{a\varepsilon_{MIR}} L_{MIR,h} \quad (5)$$

where, Q_{MIR} is the radiant heat flux (W), A_{sampl} is the ground sampling area (m^2), ε is the emissivity, σ is the Stefan–Boltzmann constant (5.67×10^{-8} J s^{-1} m^{-2} K^{-4}), $L_{MIR,h}$ and ε_{MIR} are the hot pixel spectral radiance and surface spectral emissivity in the appropriate MIR spectral band. The constant a (W m^{-4} sr^{-1} $\mu m^{-1} K^{-4}$) is determined from empirical best-fit relationships. This approach may introduce errors larger than 30% outside a range of temperatures ~600–1500 K, where that approximation holds [50].

According to this formulation, the value of emissivity is considered equal to the emissivity in the MIR and it is usually simplified. So, emissivity has no impact on the Q_{MIR} computation if it is the assumed constant (0.95 or 0.60) and wavelength independent. However, if we consider that emissivity can vary with wavelength, Equation (5) cannot be reduced, and the emissivity values in MIR (ε_{MIR}) and the total emissivity (ε) should be taken into account. Based on recent work [51–53], we assumed that the total variation of ε_{MIR} with respect to ε, is ±45%.

The total radiant heat flux, obtained summing up the Q_{MIR} for the hotspot pixels of each image, was then converted into time averaged discharge rate (TADR) according to [54].

2.4. Numerical Modelling Approach

2.4.1. MAGFLOW

To forward model the lava flow path of the 2017 Mt Etna eruption, we used the latest version of MAGFLOW, which has been implemented on graphic processing units (GPUs) using CUDA (Compute Unified Device Architecture), a parallel computing architecture provided by NVIDIA for the deployment of the latest generation of GPUs as high-performance parallel computing hardware [13,55]. Thanks to its fast execution, MAGFLOW on GPU [13] has become the core of the satellite-driven modelling strategy 'Lav@Hazard' for the production of real-time eruptive scenarios and the forecasting of lava flow hazards [54,56,57].

For the 2017 Mt Etna eruption, we ran MAGFLOW using the HOTSAT-derived TADRs on a 5 m digital elevation model (DEM) of Mt Etna derived from a tri-stereo Pléiades imagery acquired on 18 July 2016 [58,59]. The three-dimensional (3D) processing of the tri-stereo Pléiades imagery was performed using the free and open source MicMac photogrammetric library [60], developed by the French Institut Géographique National.

The location and opening times of the eruptive vents (V_1, V_2, V_3, and V_4) are reported in Figure 1. Given the chemical composition of the lava (Table 1), we used the typical properties of Mt Etna's basaltic rocks (density = 2600 kg/m^3; specific heat capacity = 1150 J kg^{-1} K^{-1}; solidification temperature = 1173 K; extrusion temperature = 1360 K), while varying the emissivity to assess the impact on the final emplacement of the lava flow. We ran three MAGFLOW simulations: two with a static, constant emissivity value (0.60 or 0.95) and another with a temperature-dependent emissivity (i.e., 'two- components': 0.60 for molten lava and 0.95 for cooled crust).

3. Results

3.1. Emissivity from Radiance

Spectral signatures for the NRE.1S samples (Figure 3) obtained using thermal emission FTIR are consistent and comparable with previous laboratory-based research of basaltic rocks [61] and Etnean lavas [28]. This clearly demonstrates that emissivity is not only wavelength, but also temperature-dependent, as measured emissivity decreases with every temperature increase step (400–900 K). However, this trend could not be observed clearly between 5.0–6.0 μm. This is because of the instrument sensitivity limitations. Emissivity spectral curves at low-to-moderate temperatures (400–700 K) show a maximum variation of ≤0.0074. However, a considerably larger decrease in emissivity (≤0.0346) occurs at moderate-to-high temperature (700–900 K). The emissivity decrease with temperature increase does not appear to be linear. The maximum measured emissivity variation between 400 and 900 K is ≤0.0377 (at 11.8 μm), which may suggest that emissivity would tend to decrease more substantially with any further temperature increase.

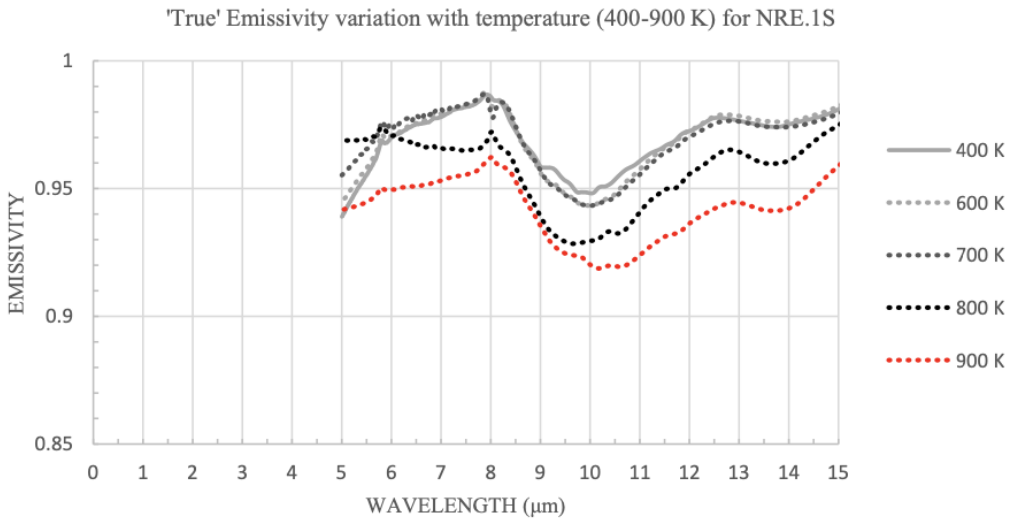

Figure 3. Emissivity spectral signatures for NRE.1S at 400–900 K and 5.0–15.0 μm, using thermal emission Fourier-transform infrared spectroscopy (FTIR).

An additional 'cooling test' was performed by measuring emissivity of the same series in the opposite direction (cooling), by decreasing temperature steps (i.e., 900–400 K), while maintaining consistent sample conditions. The deviance in emissivity values during the temperature increase (heating), shown in Figure 3 and the temperature decrease (cooling) was ≤0.0050 with no hysteresis deviation trend in either direction.

For a direct comparison with spaceborne data and to obtain a clearer emissivity trend with temperature, laboratory-measured FTIR emissivity results are shown at Landsat 8 TIR wavelengths (Figure 4). Emissivity values at 10.80 μm are lower (≥0.02) than those at 12.00 μm, displaying steady negative trend(s) at both wavelengths with temperature increase at 400–700 K and more significant decrease at 700–900 K.

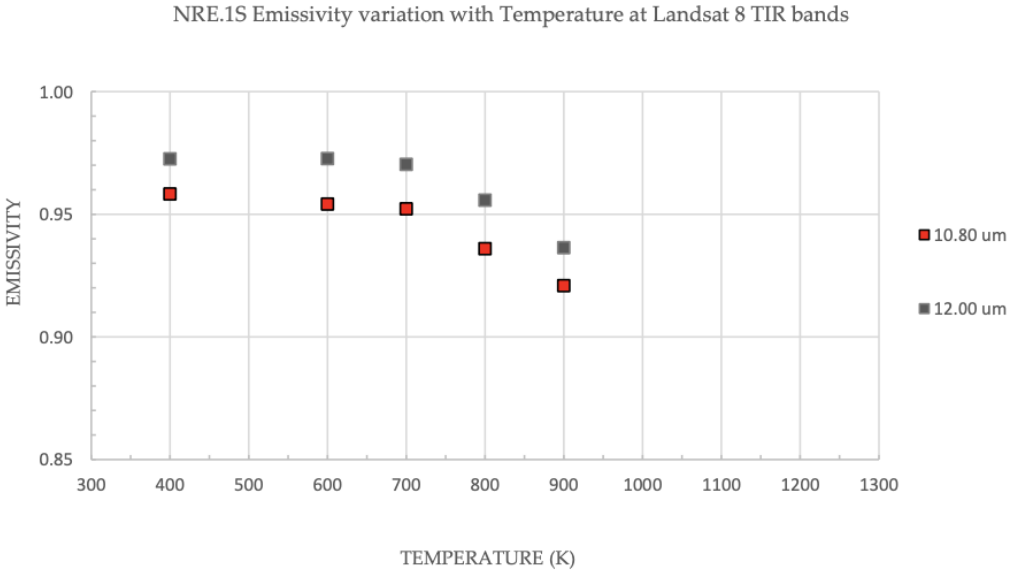

Figure 4. Emissivity variation with temperature increase of 400–900 K shown at Landsat 8 (TIRS) thermal infrared (TIR) bands.

3.2. From Spaceborne Data

Varying the emissivity and wavelength will have an impact on the computation of integrated temperatures and the consequent total radiant heat flux of any high-temperature thermal anomaly investigated.

To perform a quantitative evaluation on the impact of emissivity on computation of lava surface temperatures, we selected two high-spatial (low temporal) resolution images, acquired by Landsat 8 (OLI), during the 2017 eruption on 18 and 27 March.

3.2.1. High-Spatial (Low-Temporal) Resolution Data

According to Planck's law, high-temperature thermal anomalies are best observed in SWIR. This region is most sensitive to the temperatures found in an active lava flow (i.e., ~900 to 1300 K) [22]. According to the Wien's displacement law, the wavelength of maximum radiance shifts to shorter wavelengths with increasing temperature. The temperature of volcanic features varies widely, ranging between 600 and 1500 K, and thus can be observed in TIR, MIR, and SWIR portions of the spectrum. SWIR radiation is mainly emitted in detectable quantities from very hot surfaces (e.g., molten lava), while MIR and TIR detect cooler volcanic surfaces. Hotspot pixels on the ground, within the thermal anomaly are likely to be occupied by more than one temperature component, so an alternative approach is employed, as spaceborne data can provide only integrated pixel temperatures. By applying a fixed threshold test to Landsat 8 OLI's Band 7 radiance, hotspot pixels were detected. To estimate the fraction of cooled (crusted) and/or molten material in each pixel, an analytical approach (e.g., dual band) was employed [23] and shown in Figure 5, for the dates analysed (18 and 27 March 2017). Table 2 compares the total radiant heat flux values calculated using constant emissivity (0.95 and 0.60) values and the 'two-component' approach described in Section 2.3.1.

Table 2. Estimation of total radiant flux (Q_R) from Landsat 8 (OLI) data during the 2017 Mt Etna effusive event.

Date/Time	Emissivity	(ε)	# Radiant Pixels	Total Radiant Flux Q_R (GW)
	Constant	0.95	672	3.12
18/03/2017	Constant	0.60	672	3.68
09:41:54	**Two**	0.95 *	379	
	Components	0.60 **	293	**3.41**
	Constant	0.95	421	1.68
27/03/2017	Constant	0.60	421	1.97
09:35:38	**Two**	0.95 *	263	
	Components	0.60 **	158	**1.82**

* Component 1 (assumed crust); ** Component 2 (assumed melt).

3.2.2. Moderate-to-High Temporal Resolution

SEVIRI and MODIS data were used here (Figure 6) to analyse the 2017 eruptive activity on Mt Etna, between 14 March and 09 April. The high temporal resolution, with up to five minutes sampling interval in rapid scanning service (RSS) mode, offered by SEVIRI, enables a near-continuous monitoring of volcanic thermal activity. The higher spatial resolution of 1 km (as opposed to 3 km for SEVIRI), a good spectral resolution, and high signal-to-noise (STN) ratio offered by MODIS, permits detection of less intense thermal anomalies. For these reasons, both the first and the last thermal anomalies during this eruptive event were detected by MODIS, on 14 March (20:35 GMT) and on 9 April (21:14 GMT), respectively. The peak of activity occurred within the first five days of eruption, with a maximum radiant heat flux of 9.47 gigawatts GW recorded on 17 March (00:40 GMT) by MODIS and 9.67 GW on 18 March (14:15 GMT) by SEVIRI. Thermal activity was quite stable after 20 March 2017, with an

average radiant heat flux of ~2 GW. Converting the radiant heat flux curve into TADR and integrating this information, we obtain the final erupted lava volume of 7.96 ± 3.5 million cubic meters.

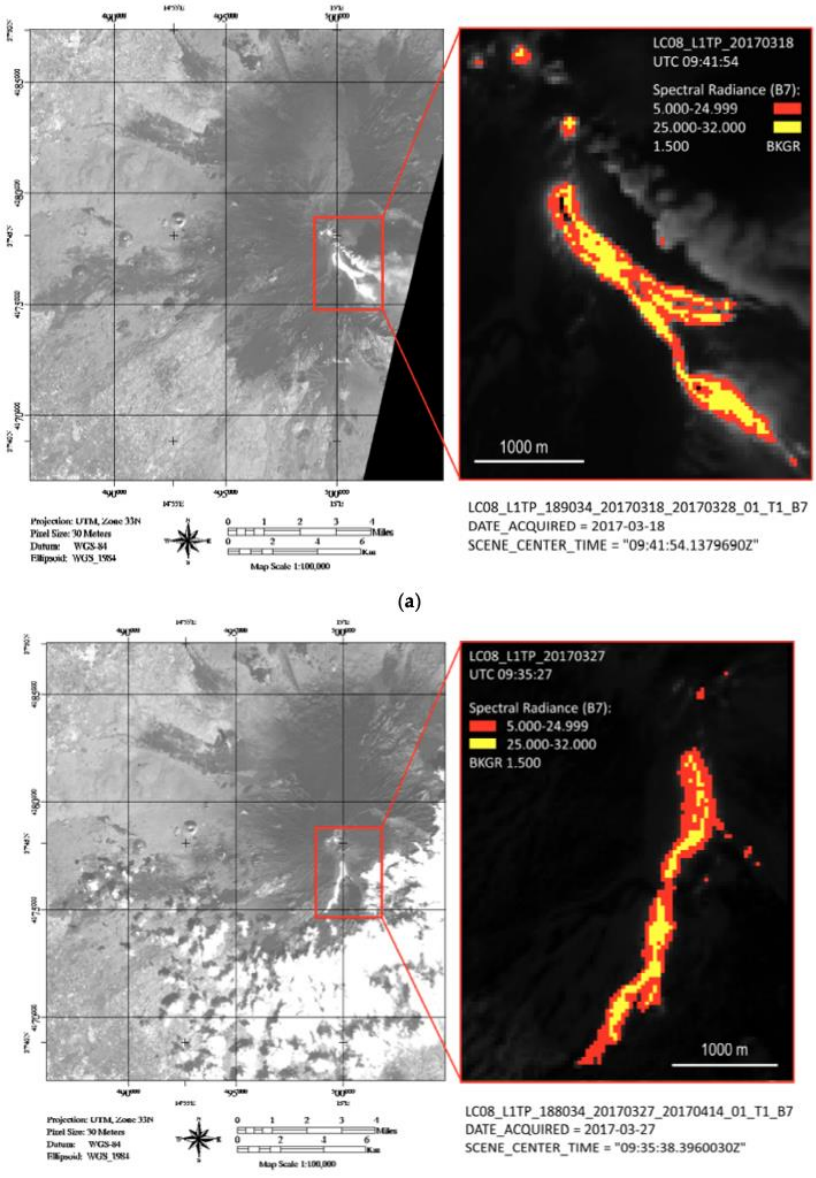

Figure 5. (**a**) Effusive activity recorded by Landsat 8 (Operational Land Imager (OLI)) on 18 March 2017 and; (**b**) 27 March 2017. Following the 'two-component' approach, cut outs in (a,b) contain 'threshold' values used in this study (Section 2.3.1) , based on radiance values, where radiant pixels in red are used for computation of crust temperatures (i.e., emissivity 0.95) and radiant pixels in yellow, relating to the melt temperatures (i.e., emissivity 0.60). Background (BKGR) value (averaged radiance value of the pixels surrounding thermally anomalous pixels) was subtracted from radiance data (all thermally anomalous pixels), so that thermal component alone (excluding reflected radiances of daytime images in short-wave infrared (SWIR)) can be analysed.

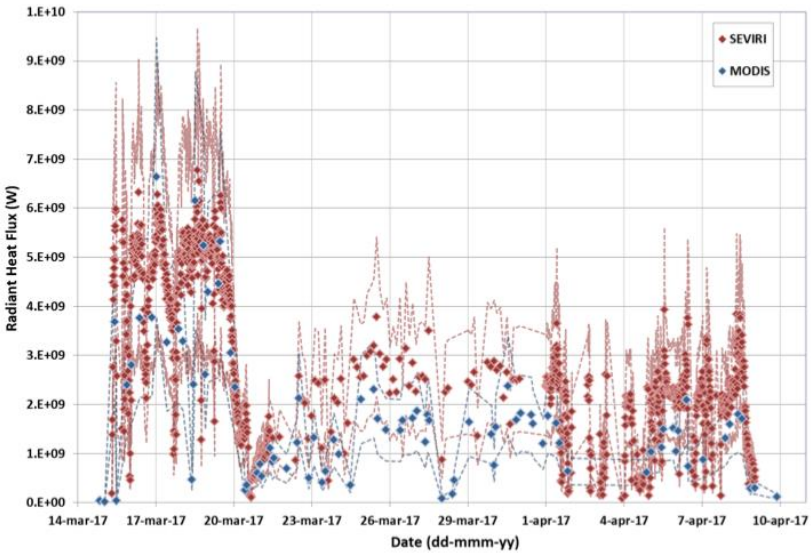

Figure 6. Radiant heat flux computed from Spinning Enhanced Visible and Infrared Imager (SEVIRI) (red diamonds) and Moderate Resolution Imaging Spectroradiometer (MODIS) (blue diamonds) data at Mt Etna from 15 March to 9 April 2017. Dashed lines, in the respective colours, include the range of variation of each time series.

3.2.3. Spaceborne Data Comparison and Validation

By comparing the radiant heat flux values obtained from moderate-to-high temporal resolution, namely SEVIRI and MODIS, and high-spatial resolution, namely Landsat-8 OLI data, we found that the latter falls inside the region of admissible values retrieved from SEVIRI and MODIS images (Figure 7). Moreover, the fact that the Landsat-8 results are quite close to the lower boundaries of the SEVIRI and MODIS, suggests $\varepsilon < \varepsilon_{MIR}$.

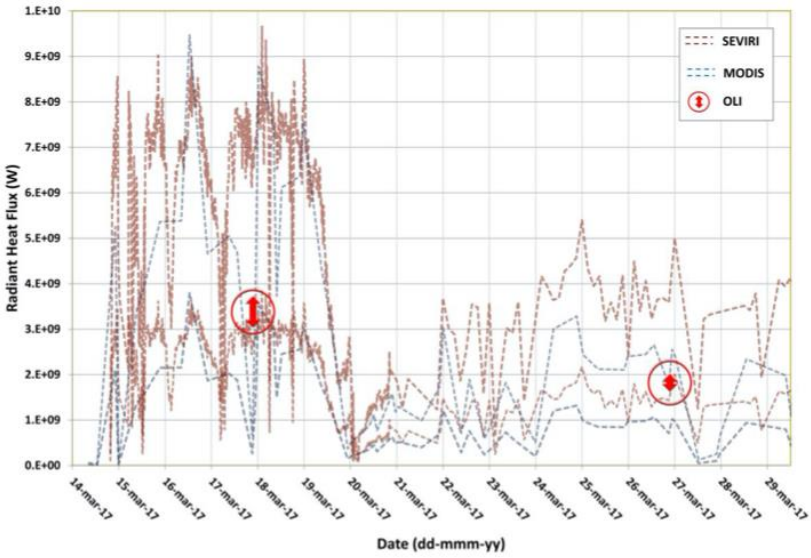

Figure 7. Range of radiant flux variation recorded between 14–29 March 2017 and retrieved by MODIS (blue dashed lines), SEVIRI (purple dashed lines), and Landsat-8 OLI (red circled bars).

3.2.4. From Straightforward Modelling

Figure 8 shows a comparison between the actual lava flow field (white contour outline) and three MAGFLOW simulations run with a constant emissivity of 0.60 (Figure 8a), a constant emissivity of 0.95 (Figure 8b), and with the 'two-component' emissivity approach (Figure 8c).

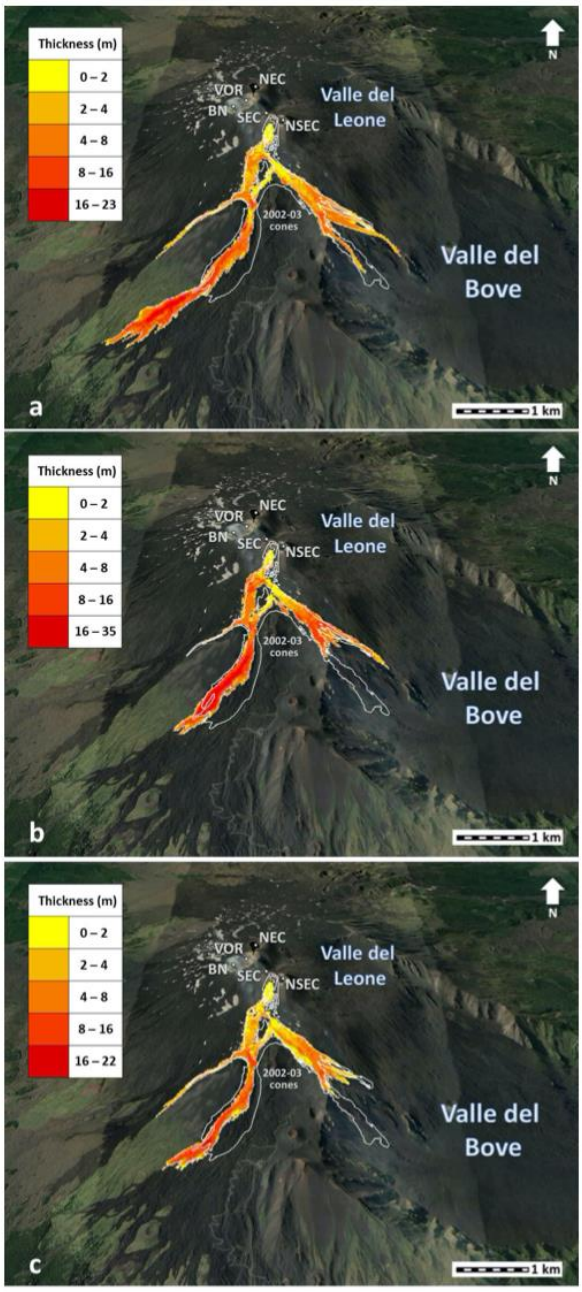

Figure 8. Eruptive scenarios obtained by using a constant emissivity of (**a**) 0.60 and (**b**) 0.95, as well as (**c**) the 'two-component' emissivity approach. The colours indicate deposit thickness in meters. The white contour highlights the actual lava flow field retrieved from the Sentinel-2A image acquired on 8 April 2017.

The best simulated scenarios are those run with the constant emissivity of 0.95 and with the 'two-component' emissivity approach. The lava flows modelled, using a constant emissivity of 0.60, overestimated significantly (46 %) in terms of maximum length, especially for the south-west branch.

This is verified by the accuracy, calculated as the square root of the intersection over union areas of the simulated and actual lava flows [10,62–64]. Although the actual lava flow field is quite well reproduced by all three MAGFLOW simulations with an accuracy always higher than 0.6, the simulations with the constant emissivity of 0.95 and the 'two-component' emissivity approach reach an accuracy of about 0.7, against 0.6 reached by the other MAGFLOW simulation.

4. Discussion

Land surface temperature (LST) and land surface emissivity (LSE) are two key parameters used in many studies and as satellite input parameters, because they are closely linked to the Earth's surface energy balance [65]. Normally, corrections are needed to estimate LST using spaceborne sensors, such as surface emissivity. If these corrections are neglected, the output data will result in systematic errors.

Remote sensing and laboratory-based FTIR spectroscopy are valuable tools when analysing the same target (or sets of targets) area on the ground. Spaceborne sensor measuring spectral emissivity of a surface can be validated ('ground-truthed') using a laboratory-based thermal emission spectroscopy technique [61,66].

Our laboratory-based FTIR results indicate that emissivity decreases with temperature increase, which is a trend that supports the argument that emissivity of molten material is significantly lower than that of the same material in its solid state [27]. Emissivity results presented here involve a temperature range of 400–900 K, which can be related to cooling and crusted flows. For the molten portion of the flow, we used emissivity values retrieved from literature [25].

The best simulated scenarios using MAGFLOW are those run with the constant emissivity of 0.95 and using the 'two-component' emissivity approach. The lava flows modelled, using a constant emissivity of 0.60 overestimates significantly, in terms of maximum length, especially for the south-west branch. The terrain can attenuate the observed spectral radiance, and hence the LST, because it can act as an obstacle to function of the mutual angle between the sensor plane of the satellite instrument and the normal direction to each cell of the DEM. LSE is an indicator of material composition and can vary with viewing angle and surface roughness. In our case study (i.e., the 2017 Etna eruption), the median slope is about 6° and there are no shadows due to the topography, so the terrain contribution can be neglected.

Our spaceborne results for both constant emissivity (i.e., 0.95 and 0.60) and a 'two-component' approach [25] produced comparable radiant flux results (Table 2), bordering at the lower boundaries of SEVIRI and MODIS acquired values. These indicate a maximum ≤16% variation in calculated total radiant flux between the two emissivity end members (i.e., 0.95 and 0.60). For example, the scene acquired on 18 March 2017 (Table 2) produced a total radiant flux of 3.12 GW using a constant uniform emissivity of 0.95, and 3.68 GW using an emissivity of 0.60. Conversely, a 'two-component' emissivity approach produced a total radiant flux value of 3.41 GW, perhaps a more realistic value, where two different emissivity values were applied to different components (i.e., crust and melt), expected to be found in an active lava flow.

Furthermore, the variation and magnitude of radiant flux (power) for thermally anomalous pixels gathered by the high-spatial resolution spaceborne data (this study) and MODIS and SEVIRI (this study and [8]), show a marked difference (i.e., overestimation), which may be driven by the difference in spatial resolution (pixel size) and instrument sensitivity capabilities.

Given such data, previous workers have often gone on to calculate lava effusion rates [67,68] or 'distance-to-run'[28]. This is not done here as the high-spatial resolution data are based on a limited number of infrequent observations (scenes), which may or may not correspond to significant peak discharge rates. Equally, research shows [69] that variations in lava effusion rates may occur over short

timescales, and flow regimes are known to change over timescales of days or less [70–72]. This may suggest that such instantaneous readings might not be truly representative.

Nonetheless, our results highlight the uncertainty in accuracy, as data comparison in this study shows that high-spatial resolution radiant flux results (e.g., from OLI) fall at the lower boundary of values retrieved from MODIS and SEVIRI.

5. Conclusions

Laboratory-based FTIR results presented in this study provide a clear indication that the measured emissivity of volcanic samples, investigated here, decreases non-linearly with temperature increase between 400 and 900 K. The current work should now be extended to include higher eruptive temperatures (~1350 K for Etna's lavas), using an alternative laboratory-based approach, which would allow heating of samples to this temperature. This is essential to increase our understanding of the behaviour of emissivity at molten rock temperatures. The synergy of high-spatial and high-temporal resolution two-component, radiant flux data has the potential to support more accurate effusion rate estimates, that are critical in supporting operational 'distance-to-run' forecasts. We propose then that the emissivity–temperature relationship be quantified and linked to the range of temperatures found in an active lava flow, by creating a 'Dynamic Emissivity–Temperature Rule'. This would significantly improve the accuracy of lava surface temperatures derivation (from spaceborne data) and operational lava flow forecasting (through modelling applications), which will contribute to hazard assessment and mitigation.

Author Contributions: F.F. and N.R. led the conception and design of the work. N.R., A.C., G.G., and A.M. acquired the data. N.R., A.C., G.G., A.M., and F.F. were responsible for analysis, modelling, and interpretation of data. All authors (N.R., A.C., G.G., A.M., H.R., S.B., and F.F.) participated in drafting and revising the article and have given final approval of the submitted and revised versions.

Funding: The Open University, Milton Keynes, U.K. provided studentship funding for N.R.

Acknowledgments: MAGFLOW simulations were performed within the framework of Tecnolab, the Laboratory for Technological Advance in Volcano Geophysics of the INGV in Catania, Italy. The anonymous reviewers are acknowledged for their constructive and supportive comments, which helped improve this manuscript.

Conflicts of Interest: The authors declare no conflicst of interest. The funders had no role in the design of the study; in the collection, analyses, or interpretation of data; in the writing of the manuscript, or in the decision to publish the results.

References

1. Sigurdsson, H.; McNutt, S.R.; Rymer, H.; Stix, J.; Houghton, B. *The Encyclopedia of Volcanoes*, 2nd ed.; Sigurdsson, H., Houghton, B., McNutt, S.R., Rymer, H., Stix, J., Eds.; Academic Press: Cambridge, MA, USA, 2015.
2. Sparks, R.S.; Aspinall, W.P.; Crosweller, H.S.; Hincks, T.K. *Risk and Uncertainty Assessment of Volcanic Hazards*; 2011; Volume 9781107006, ISBN 9781139047562.
3. Ramsey, M.S.; Harris, A.J.L. Volcanology 2020: How will thermal remote sensing of volcanic surface activity evolve over the next decade? *J. Volcanol. Geotherm. Res.* **2013**, *249*, 217–233. [CrossRef]
4. Tait, S.; Ferrucci, F. A real-time, space borne volcano observatory to support decision making during eruptive crises: European volcano observatory space services. In Proceedings of the 2013 UKSim 15th International Conference on Computer Modelling and Simulation, Cambridge, UK, 10–12 April 2013; pp. 283–289.
5. Komorowski, J.C.; Jenkins, S.; Baxter, P.J.; Picquout, A.; Lavigne, F.; Charbonnier, S.; Gertisser, R.; Preece, K.; Cholik, N.; Budi-Santoso, A.; et al. Paroxysmal dome explosion during the Merapi 2010 eruption: Processes and facies relationships of associated high-energy pyroclastic density currents. *J. Volcanol. Geotherm. Res.* **2013**, *261*, 260–294. [CrossRef]
6. Pallister, J.; Papale, P.; Eichelberger, J.; Newhall, C.; Mandeville, C.; Nakada, S.; Marzocchi, W.; Loughlin, S.; Jolly, G.; Ewert, J.; et al. Volcano observatory best practices (VOBP) workshops—A summary of findings and best-practice recommendations. *J. Appl. Volcanol.* **2019**, *8*. [CrossRef]

7. Hill, L.J.; Sparks, R.S.; Rougier, J.C. Risk assessment and uncertainty in natural hazards. *Risk Uncertain. Assess. Nat. Hazards* **2011**, *9781107006*, 1–18.
8. Cappello, A.; Ganci, G.; Bilotta, G.; Herault, A.; Zago, V.; Del Negro, C. Satellite-driven modeling approach for monitoring lava flow hazards during the 2017 Etna eruption. *Ann. Geophys. Geophys.* **2018**, *61*. [CrossRef]
9. Ganci, G.; Cappello, A.; Bilotta, G.; Corradino, C.; Del Negro, C. Satellite-Based Reconstruction of the Volcanic Deposits during the December 2015 Etna Eruption. *MDPI J. Data* **2019**, *4*, 120. [CrossRef]
10. Corradino, C.; Ganci, G.; Cappello, A.; Bilotta, G.; Herault, A.; Del Negro, C. Mapping Recent Lava Flows at Mount Etna Using Multispectral Sentinel-2 Images and Machine Learning Techniques. *Remote Sens.* **2019**, *11*, 1916. [CrossRef]
11. Cappello, A.; Geshi, N.; Neri, M.; Del Negro, C. Lava flow hazards—An impending threat at Miyakejima volcano, Japan. *J. Volcanol. Geotherm. Res.* **2015**, *308*, 1–9. [CrossRef]
12. Cappello, A.; Zanon, V.; Del Negro, C.; Ferreira, T.J.L.; Queiroz, M.G.P.S. Exploring lava-flow hazards at Pico Island, Azores Archipelago (Portugal). *Terra Nov.* **2015**, *27*, 156–161. [CrossRef]
13. Bilotta, G.; Cappello, A.; Herault, A.; Ganci, G.; Del Negro, C. MAGFLOW: a physics-based model for the dynamics of lava-flow emplacement. *Geol. Soc. Spec. Publ.* **2016**, 357–373.
14. Del Negro, C.; Cappello, A.; Neri, M.; Bilotta, G.; Hérault, A.; Ganci, G. Lava flow hazards at Mount Etna: Constraints imposed by eruptive history and numerical simulations. *Sci. Rep.* **2013**, *3*, 1–8.
15. Del Negro, C.; Cappello, A.; Ganci, G. Quantifying lava flow hazards in response to effusive eruption. *Bull. Geol. Soc. Am.* **2016**, *128*, 1–13. [CrossRef]
16. Ramsey, M.; Dehn, J. Spaceborne observations of the 2000 Bezymianny, Kamchatka eruption: The integration of high-resolution ASTER data into near real-time monitoring using AVHRR. *J. Volcanol. Geotherm. Res.* **2004**, *135*, 127–146. [CrossRef]
17. Solikhin, A.; Thouret, J.C.; Gupta, A.; Harris, A.J.L.; Liew, S.C. Geology, tectonics, and the 2002-2003 eruption of the Semeru volcano, Indonesia: Interpreted from high-spatial resolution satellite imagery. *Geomorphology* **2012**, *138*, 364–379. [CrossRef]
18. Wright, R.; Flynn, L.P.; Garbeil, H.; Harris, A.J.L.; Pilger, E. MODVOLC: Near-real-time thermal monitoring of global volcanism. *J. Volcanol. Geotherm. Res.* **2004**, *135*, 29–49. [CrossRef]
19. Wooster, M.J.; Rothery, D.A. Time-series analysis of effusive volcanic activity the using ERS Along Track Scanning Radiometer: The 1995 eruption of Fernandina Volcano, Galapagos Islands. *Remote Sens. Environ.* **1997**, *62*, 109–117. [CrossRef]
20. Oppenheimer, C. Thermal distributions of hot volcanic surfaces constrained using three infrared bands of remote sensing data. *Geophys. Res. Lett.* **1993**, *20*, 431–434. [CrossRef]
21. Harris, A.; Steffke, A.; Calvari, S.; Spampinato, L. Thirty years of satellite-derived lava discharge rates at Etna: Implications for steady volumetric output. *J. Geophys. Res. Solid Earth* **2011**, *116*, 1–15. [CrossRef]
22. Harris, A.J.L. *Thermal Remote Sensing of Active Volcanoes: A User's Manual*; Cambridge University Press: Cambridge, UK, 2013; Volume 9780521859, ISBN 9781139029346.
23. Hirn, B.; Di Bartola, C.; Ferrucci, F. Spaceborne monitoring 2000-2005 of the Pu'u 'O'o-Kupaianaha (Hawaii) eruption by synergetic merge of multispectral payloads ASTER and MODIS. *IEEE Trans. Geosci. Remote Sens.* **2008**, *46*, 2848–2856. [CrossRef]
24. Rothery, D.A.; Francis, P.W.; Wood, C.A. Volcano monitoring using short wavelength infrared data from satellites. *J. Geophys. Res.* **1988**, *93*, 7993–8008. [CrossRef]
25. Ramsey, M.; Chevrel, M.; Coppola, D.; Harris, A. The influence of emissivity on the thermo-rheological modeling of the channelized lava flows at Tolbachik volcano. *Ann. Geophys.* **2019**, *61*. [CrossRef]
26. Marchese, F.; Neri, M.; Falconieri, A.; Lacava, T.; Mazzeo, G.; Pergola, N.; Tramutoli, V. The contribution of multi-sensor infrared satellite observations to monitor Mt. Etna (Italy) Activity during May to August 2016. *Remote Sens.* **2018**, *10*, 1948. [CrossRef]
27. Lee, R.J.; Ramsey, M.S.; King, P.L. Development of a new laboratory technique for high-temperature thermal emission spectroscopy of silicate melts. *J. Geophys. Res. Solid Earth* **2013**, *118*, 1968–1983. [CrossRef]
28. Rogic, N.; Cappello, A.; Ferrucci, F. Role of Emissivity in Lava Flow 'Distance-to-Run' Estimates from Satellite-Based Volcano Monitoring. *Remote Sens.* **2019**, *11*, 662. [CrossRef]
29. Cappello, A.; Bilotta, G.; Neri, M.; Del Negro, C. Probabilistic modeling of future volcanic eruptions at Mount Etna. *J. Geophys. Res. Solid Earth* **2013**, *118*, 1925–1935. [CrossRef]

30. Cappello, A.; Ganci, G.; Bilotta, G.; Corradino, C.; Hérault, A.; Del Negro, C. Changing Eruptive Styles at the South-East Crater of Mount Etna: Implications for Assessing Lava Flow Hazards. *Front. Earth Sci.* **2019**, *7*, 1–10. [CrossRef]
31. Del Negro, C.; Currenti, G.; Napoli, R.; Vicari, A. Volcanomagnetic changes accompanying the onset of the 2002-2003 eruption of Mt. Etna (Italy). *Earth Planet. Sci. Lett.* **2004**, *229*, 1–14. [CrossRef]
32. Giordano, D.; Dingwell, D.B. Viscosity of hydrous Etna basalt: Implications for Plinian-style basaltic eruptions. *Bull. Volcanol.* **2003**, *65*, 8–14. [CrossRef]
33. Maturilli, A.; Helbert, J.; D'Amore, M.; Varatharajan, I.; Rosas Ortiz, Y. The Planetary Spectroscopy Laboratory (PSL): wide spectral range, wider sample temperature range. *Infrared Remote Sens. Instrum.* **2018**, 11.
34. Maturilli, A.; Helbert, J. Characterization, testing, calibration, and validation of the Berlin emissivity database. *J. Appl. Remote Sens.* **2014**, *8*. [CrossRef]
35. World Metheorological Organisation Observing Systems Capability Analysis and Review Tool—Landsat 8. Available online: https://www.wmo-sat.info/oscar/satellites/view/227 (accessed on 25 September 2019).
36. U.S. Department of the Interior. U.S. Geological Survey Global Visualisation (GloVis) Viewer. Available online: https://glovis.usgs.gov/ (accessed on 1 September 2019).
37. Barsi, J.A.; Barker, J.L.; Schott, J.R. An Atmospheric Correction Parameter Calculator for a Single Thermal Band Earth-Sensing Instrument. *Int. Geosci. Remote Sens. Symp.* **2003**, *5*, 3014–3016.
38. Barsi, J.A.; Barker, J.L.; Schott, J.R. Web-Based Atmospheric Correction Tool for Single Thermal Band Instrument. Available online: https://atmcorr.gsfc.nasa.gov/ (accessed on 25 September 2019).
39. Barsi, J.A.; Schott, J.R.; Palluconi, F.D.; Hook, S.J. Validation of a web-based atmospheric correction tool for single thermal band instruments. *Earth Obs. Syst. X* **2005**, *5882*, 58820E.
40. Dozier, J. A method for satellite identification of surface temperature fields of subpixel resolution. *Remote Sens. Environ.* **1981**, *11*, 221–229. [CrossRef]
41. Francis, P.W.; Rothery, D.A. Using the Landsat Thematic Mapper to detect and monitor active volcanoes: an example from Lascar volcano, northern Chile. *Geology* **1987**, *15*, 614–617. [CrossRef]
42. Glaze, L.; Francis, P.W.; Rothery, D.A. Measuring thermal budgets of active volcanoes by satellite remote sensing. *Nature* **1989**, *338*, 144–146. [CrossRef]
43. Flynn, L.P.; Harris, A.J.L.; Wright, R. Improved identification of volcanic features using Landsat 7 ETM+. *Remote Sens. Environ.* **2001**, *78*, 180–193. [CrossRef]
44. Pieri, D.C.; Glaze, L.S.; Abrams, M.J. Thermal radiance observations of an active lava flow during the June 1984 eruption of Mount Etna. *Geology* **1990**, *18*, 1018–1022. [CrossRef]
45. Wright, R.; Pilger, E. Radiant flux from Earth's subaerially erupting volcanoes. *Int. J. Remote Sens.* **2008**, *29*, 6443–6466. [CrossRef]
46. USGS Landsat 8 Data Users Handbook. Available online: https://www.usgs.gov/land-resources/nli/landsat/landsat-8-data-users-handbook (accessed on 1 November 2019).
47. Ganci, G.; Bilotta, G.; Cappello, A.; Herault, A.; Del Negro, C. HOTSAT: A multiplatform system for the thermal monitoring of volcanic activity using satellite data. *Geol. Soc. Spec. Publ.* **2016**, *426*, 207–221. [CrossRef]
48. Ganci, G.; Vicari, A.; Fortuna, L.; del Negro, C. The HOTSAT volcano monitoring system based on combined use of SEVIRI and MODIS multispectral data. *Ann. Geophys.* **2011**, *54*, 544–550.
49. Ganci, G.; Vicari, A.; Bonfiglio, S.; Gallo, G.; del Negro, C. A texton-based cloud detection algorithm for MSG-SEVIRI multispectral images. *Geomat. Nat. Hazards Risk* **2011**, *2*, 279–290. [CrossRef]
50. Wooster, M.J.; Zhukov, B.; Oertel, D. Fire radiative energy for quantitative study of biomass burning: Derivation from the BIRD experimental satellite and comparison to MODIS fire products. *Remote Sens. Environ.* **2003**, *86*, 83–107. [CrossRef]
51. Ramsey, M.S.; Harris, A.J.L. Modelling the thermal and infrared spectral properties of active vents: Comparing basaltic lava flows of Tolbachik, Russia to Arsia Mons, Mars. In Proceedings of the AGU Fall Meeting, San Francisco, CA, USA, 12–16 December 2016.
52. Lee, R.J.; Ramsey, M.S. What is the emissivity of active basaltic lava flows? In Proceedings of the AGU Fall Meeting, San Francisco, CA, USA, 12–16 December 2016.
53. Lee, R.J.; King, P.L.; Ramsey, M.S. Spectral analysis of synthetic quartzofeldspathic glasses using laboratory thermal infrared spectroscopy. *J. Geophys. Res. Solid Earth* **2010**, *115*, n/a-n/a. [CrossRef]

54. Ganci, G.; Vicari, A.; Cappello, A.; Del Negro, C. An emergent strategy for volcano hazard assessment: From thermal satellite monitoring to lava flow modeling. *Remote Sens. Environ.* **2012**, *119*, 197–207. [CrossRef]
55. Bilotta, G.; Rustico, E.; Hérault, A.; Vicari, A.; Russo, G.; del Negro, C.; Gallo, G. Porting and optimizing MAGFLOW on CUDA. *Ann. Geophys.* **2011**, *54*, 580–591.
56. Vicari, A.; Ganci, G.; Behncke, B.; Cappello, A.; Neri, M.; Del Negro, C. Near-real-time forecasting of lava flow hazards during the 12–13 January 2011 Etna eruption. *Geophys. Res. Lett.* **2011**, *38*, 1–7. [CrossRef]
57. Vicari, A.; Bilotta, G.; Bonfiglio, S.; Cappello, A.; Ganci, G.; Hérault, A.; Rustico, E.; Gallo, G.; del Negro, C. Lav@hazard: A web-gis interface for volcanic hazard assessment. *Ann. Geophys.* **2011**, *54*, 662–670.
58. Ganci, G.; Cappello, A.; Bilotta, G.; Herault, A.; Zago, V.; Del Negro, C. Mapping volcanic deposits of the 2011–2015 etna eruptive events using satellite remote sensing. *Front. Earth Sci.* **2018**, *6*, 1–12. [CrossRef]
59. Ganci, G.; Cappello, A.; Zago, V.; Bilotta, G.; Hérault, A.; Del Negro, C. 3D lava flow mapping of the 17–25 may 2016 ETNA eruption using tri-stereo optical satellite data. *Ann. Geophys.* **2019**, *62*, 1–6. [CrossRef]
60. French Institut Géographique National MicMac Photogrammetric Library. Available online: http://micmac.ensg.eu (accessed on 1 November 2019).
61. Hamilton, V.E.; Wyatt, M.B.; McSween, H.Y.; Christensen, P.R. Analysis of terrestrial and Martian volcanic compositions using thermal emission spectroscopy 2. Application to Martian surface spectra from the Mars Global Surveyor Thermal Emission Spectrometer. *J. Geophys. Res. E Planets* **2001**, *106*, 14733–14746. [CrossRef]
62. Kereszturi, G.; Cappello, A.; Ganci, G.; Procter, J.; Németh, K.; Del Negro, C.; Cronin, S.J. Numerical simulation of basaltic lava flows in the auckland volcanic field, New Zealand—implication for volcanic hazard assessment. *Bull. Volcanol.* **2014**, *76*, 1–17. [CrossRef]
63. Kereszturi, G.; Németh, K.; Moufti, M.R.; Cappello, A.; Murcia, H.; Ganci, G.; Del Negro, C.; Procter, J.; Zahran, H.M.A. Emplacement conditions of the 1256 AD Al-Madinah lava flow field in Harrat Rahat, Kingdom of Saudi Arabia—Insights from surface morphology and lava flow simulations. *J. Volcanol. Geotherm. Res.* **2016**, *309*, 14–30. [CrossRef]
64. Bilotta, G.; Cappello, A.; Hérault, A.; Del Negro, C. Influence of topographic data uncertainties and model resolution on the numerical simulation of lava flows. *Environ. Model. Softw.* **2019**, *112*, 1–15. [CrossRef]
65. Sobrino, J.A.; Jiménez-Muñoz, J.C.; Sòria, G.; Romaguera, M.; Guanter, L.; Moreno, J.; Plaza, A.; Martínez, P. Land surface emissivity retrieval from different VNIR and TIR sensors. *IEEE Trans. Geosci. Remote Sens.* **2008**, *46*, 316–327. [CrossRef]
66. King, P.L.; Ramsey, M.S.; McMillan, P.F.; Swayze, G. Laboratory Fourier transform infrared spectroscopy methods for geologic samples. *Infrared Spectrosc. Geochem. Explor. Geochem. Remote Sens.* **2004**, *33*, 57–91.
67. Pieri, D.C.; Baloga, S.M. Eruption Rate, Area, and Length relationships for some Hawaiian lava flows. *J. Volcanol. Geotherm. Res.* **1986**, *30*, 29–45. [CrossRef]
68. Wright, R.; Blake, S.; Harris, A.J.L.; Rothery, D.A. A simple explanation for the space-based calculation of lava eruption rates. *Earth Planet. Sci. Lett.* **2001**, *192*, 223–233. [CrossRef]
69. Bailey, J.E.; Harris, A.J.L.; Dehn, J.; Calvari, S.; Rowland, S.K. The changing morphology of an open lava channel on Mt. Etna. *Bull. Volcanol.* **2006**, *68*, 497–515. [CrossRef]
70. Wadge, G. The variation of magma discharge during basaltic eruptions. *J. Volcanol. Geotherm. Res.* **1981**, *11*, 139–168. [CrossRef]
71. Harris, A.J.L.; Murray, J.B.; Aries, S.E.; Davies, M.A.; Flynn, L.P.; Wooster, M.J.; Wright, R.; Rothery, D.A. Effusion rate trends at Etna and Krafla and their implications for eruptive mechanisms. *J. Volcanol. Geotherm. Res.* **2000**, *102*, 237–269. [CrossRef]
72. Lautze, N.C.; Harris, A.J.L.; Bailey, J.E.; Ripepe, M.; Calvari, S.; Dehn, J.; Rowland, S.K.; Evans-Jones, K. Pulsed lava effusion at Mount Etna during 2001. *J. Volcanol. Geotherm. Res.* **2004**, *137*, 231–246. [CrossRef]